Electromagnetic Compatibility in Power Systems

Edited by:
Francesco Lattarulo

Electromagnetic Compatibility in Power Systems

This page intentionally left blank

Electromagnetic Compatibility in Power Systems

Edited by
Francesco Lattarulo

ELSEVIER

Amsterdam • Boston • Heidelberg • London • New York • Oxford
Paris • San Diego • San Francisco • Singapore • Sydney • Tokyo

To my Family:

Gabriella,
Like a lily among thorns

Maria Teresa and Nicola,
like arrows in a soldier's hand

This page intentionally left blank

CONTENTS

Preface

The number of natural or artificially produced physical phenomena exploited for practical applications is relatively high, even though several of them give rise to unpleasant consequences. These ultimately manifest themselves in the form of malfunction or definitive failure of components and systems, or environmental hazard. So far, manifold categories of inadvertent or deliberate sources have been discovered to simultaneously produce useful effects in some but adverse ones in others. In fact, it is quite likely to occur that a useful agent assumes the character of a threat or pollutant for surrounding victims, since its influence on them easily exceeds pre-established thresholds of tolerability.

Incidentally, the progressive miniaturisation and sensitivity of electronic components and circuits, often operating in close proximity to relatively powerful sources of electromagnetic interference have been responsible for the growing interest in the last decades for Electromagnetic Compatibility (EMC). EMC is founded on a body of knowledge elaborated and systematised with the object of estimating and mitigating electromagnetic interference. *Stricto sensu*, no theory is distinctive of EMC, which rather appearing as a guide to profitably apply a number of principles, theories, models and methods enunciated and elaborated in different, often contiguous, realms of applied science. Since its appearance as an organic assembly of wide-ranging notions and procedures, nowadays largely included in higher education teaching, EMC fully deserves to be qualified as a doctrine or discipline.

On the other hand, potential authors of books on the subject matter are fully aware of the serious difficulties which could "loom ahead". In fact, planning the production of manageable handbooks capable of treating all the EMC case studies of practical and long-lasting interest could result in a questionable and difficult undertaking. Therefore, in addition to textbooks providing a thorough background on basic aspects, thus being well-tailored for students and those who want to pursue this discipline, the most that can be made to jointly sustain a helpful and practicable publishing activity is to supply specialised monographs or miscellanies of selected topics. Such resources are preferentially addressed to post-graduate students, researchers and designers, often employed in the forefront of research or engaged in remodelling design paradigms. Hence, the prerequisite for such a class of publications should consist in arousing critical sense and promoting new ideas.

Even this book will try, to the best of the contributors' ability, to rather discuss unusual subjects, or throwing out suggestions for reformulating conventional approaches, than to appear as a reference text. A common motivation encouraged the authors involved

to bring together a number of accounts of their research that they have undertaken over the recent years: willing to fill the important need of covering EMC topics pertaining to power systems. The above-mentioned accounts form as many chapters, the arguments of which are summarised here.

Chapter 1 deals with the study of lightning pre-stroke phase and acknowledges its important role in determining the reliability of structural protection systems adopted for buildings. Even the efficiency of the supplementary protection system, to which the task of mitigating induced effects on inner victims is assigned, ultimately depends on the striking performances. Therefore, special attention is paid to the so far overlooked electro-dynamic mechanism involved in the attachment process, since a pure electrostatics-based method, traditionally applied to air termination placement, is verified to be only partially satisfactory.

Somehow complementary to the above material is the subject of Chapter 2 which analyses the lightning return-stroke phase and related electromagnetic scenario lightning electro-magnetic pulse (LEMP). Thereby, induced effects on the canonical victim represented by an overhead horizontal line positioned nearby a flash are investigated. The more surprising coupling feature emerged here is that the LEMP quasistatic component is not involved substantially, in spite of the assumed proximity to the return-stroke channel. The very reasons explaining such an unexplored behaviour are to be enquired into the combinative electromagnetic performances of the wet earth plane, channel and upper cloud, all together envisioned to form an interconnected discharging system.

Geomagnetic-storm-originated electromagnetic disturbance on power transmission lines is the subject of Chapter 3. Distinctive of the special threat under examination is anomalous excitation of the power system and, in turn, generation of a number of detrimental consequences to system security and service quality. The authors take the present opportunity to outline an effective mitigating strategy based on a suitable co-ordination of static VAR compensators.

In contrast to the subjects treated in Chapters 2 and 3, where the line assumes the character of a victim, in Chapter 4 the above system becomes an interfering source. This typically happens when most utility infrastructures are gathered in a unique corridor, in which case one or more overhead high voltage (HV) power transmission lines can coexist with an underground natural gas pipeline (the victim). The interference has been theoretically analysed by a simple and reliable "universal approach", according to the terminology adopted here. A comparison with some databases, relative to a critical real case, permitted the vindicated properties of the method to be evaluated and exhaustively commented upon.

Chapter 5 gives a detailed description of the degradation mechanisms affecting the shielding properties of a generic conducting enclosure under critical exposure conditions, namely when such a thin-walled structure is introduced into a quasistatic magnetic field. The canonical elliptic geometry, largely adopted elsewhere in conjunction with the magnetic dipole theory, is extended here to the case of inner field-point placed nearby a hole, even when the latter is loaded. Such an analytically unamenable example has been rigorously resolved in the case of isolated holes, while the mutual influence among

shortly spaced holes, forming a perforated structure or a grid, has been taken into account by a supplementary numerical approach restricted to a 2D field computation.

Chapter 6 offers an electrostatic description of a human body, for EMC applications, by a set of partial capacitances. The diakoptic theory is used and recommended owing to its special property of ensuring errors within the uncertainty affecting the problems at work in spite of employing low-partitioning approach. The human body either plays the role of a victim subject to the induced effects of extremely low frequency (ELF) electric field, or electrostatic discharge (ESD) source. Since capacitances instead of Maxwell coefficients are directly involved, the method could be especially useful to those who need assistance for design and performing experimental procedures.

Power quality (PQ) monitoring is a very complex task and recently it is assuming a growing importance because of the large diffusion of non-linear and time-varying loads and their interactions with the power supply system. As a consequence, the distributor/customer responsibility question is currently challenging the EMC community. After a brief description of the PQ scenario and an overview on the disturbances affecting electrical power systems and related international standards, Chapter 7 describes a new procedure capable of evaluating the PQ at the point of common coupling in terms of harmonic distortion. The value of the procedure is sustained even by a comparison with other harmonic assessment procedures.

In order to avoid/compensate the harmonic distortion on distribution lines, the use of line-connected Pulse Width Modulation (PWM) converters such as front-end active converters and active filters is also recommended. The harmonic rejection performed by these converters and the influence on their control of system non-idealities, grid unbalance, dead time and unmodelled delays, form the subject matter of Chapter 8.

Chapter 9 models the non-idealities treated in the previous chapter using a "virtual circuit approach". The latter substantially consists of using passive elements to model the digital control. The value of this approach consists in being especially straightforward for the technicians involved in the study of the harmonic propagation in industrial plants.

Chapter 10 offers a detailed analysis of the propagation of harmonics in an industrial plant. In particular, a harmonic load flow approach, especially addressed to designing passive filters and selecting their installation points in the industrial plant, is described. A case study is also presented to evaluate the practical usefulness of the proposed analysis in a better manner.

The effectiveness of passive filters to mitigate harmonic flow in an industrial plant, as discussed in the previous chapter, can be compromised by detuning problems. A possible alternative solution is represented by the employment of active filters. In Chapter 11, single-phase, three-phase and four-wire shunt active filters are reviewed in respect to both control and implementation issues in the case of microcontrollers.

As the reader can appreciate by hindsight, most chapters directly embrace important topics involving power lines (Chapters 2–4 and 7–11). In fact, similar to more usual areas of EMC concerned with electronic products, there is a general need to investigate

EMC features of complex and distributed systems. This is because the compliance with the EMC directive of a single component or sub-system of an apparatus could not adequately ensure EMC performances once they are inserted there. Chapters 5 and 6 are indirectly connected to power lines since these are assumed as sources of interfering magnetic and electric fields, respectively. Even Chapter 1 is ultimately concerned with a large system, in this case the latter is devoted to lightning protection. Last, some attempts have been made to connect (by "percolation", according to an attractive terminology adopted by Stauffer[1]) apparently separate topics. The most striking example of percolation is expressed in Chapter 6, an example which has permitted a model of human body to be presented as a main subject, even though apparently different EMC topics are treated as possible applications (radiation hazard and ESD).

Finally, it should be stressed that a further motivation, passed over deliberately in silence up to now, drove the authors to the compilation of this book: showing that relying on a restricted group of individuals, all operating in a sole Institution[2], is by itself not detrimental to promising results, provided cooperative efforts are generously made and fruitfully managed. However, this would not have been possible without the sympathising disposition of our families and the encouraging and valuable assistance of the publishing editors, to which I express, even on behalf of the single contributors, my everlasting gratitude.

Francesco Lattarulo
Bari, Italy

---

[1] Stauffer, D., "*Introduction to percolation theory*", Taylor and Francis, London, 1985.
[2] Dipartimento di Elettrotecnica ed Elettronica – Politecnico di Bari (Italy).

CHAPTER 1

A Combined Electrostatic–Electrodynamic Approach to Lightning Pre-Stroke Phenomena and Related EMC Problems

F. Lattarulo and V. Amoruso

Abstract

In essence, this chapter provides a subsidiary but important body of knowledge especially useful to deal with the problem of mitigating the interference of a LEMP (lightning electromagnetic pulse) with the sensitive circuitry placed inside a building. Even though such a victim can be equipped with largely available lightning protection devices, applying reliable guidelines to the primary protection system still turns out to be the prerequisite for a successful EMC design of the secondary protection system. Several subjects are methodically treated and stimulating arguments, for ultimately exploring more reliable estimation methods applied to the interception efficiency of air terminals, are provided. To this end, the crucial development of the attachment process, during the late instants of a pre-stroke phase, is investigated and previously overlooked electrodynamic effects, in conjunction with those of electrostatic nature, are introduced. Even the electrostatic approach will be re-examined with application to the models of thundercloud cell and leader corona.

1.1 Preliminary Remarks

In lightning physics, the stepped leader attachment process and determination of the point where a lightning flash will strike are subjects of paramount importance for safety/security and EMC problems. Nowadays, increasingly sensitive, and innumerable electric and electronic components are involved in a variety of conductive and electromagnetic coupling modes when a lightning flash strikes a structural protection system

or an outer point in the surroundings. Therefore, the diversion mode actually assumed by the lightning current before discharging through the earth system depends on the location of the striking point. Even features of the induced current and voltage surges, appearing in the circuits to be protected by the above-mentioned devices, are significantly affected.

A correlation between the attachment process and the striking point is accounted for by observing that the latter is exactly positioned on the inception and launch location of an attaching leader in response to an advancing stepped leader. Unfortunately, the striking point is unpredictable, even though the attachment phenomenon is confined to the late instants of the pre-stroke phase, namely when the physical and geometrical properties of the striking object and its surroundings are expected to play an influencing role. In general, the struck structure can be a natural or man-made terrestrial object, or an aircraft. With regard to the former class of victims, a considerable amount of models and experimental methods have been adopted for evaluating the induced effects on detecting the loops placed inside a building. In these investigations, the lightning flash is assumed to strike a metallic part of a protected building or outer points, for instance lying on the earth plane (see Ianoz, 2003). In both the case studies, a theoretical evaluation of the induced mechanism is preceded by a lightning electromagnetic pulse (LEMP) prediction, which of course carefully takes into account the shielding properties of the protection system. Specifically, the so-called primary protection system is configured as a pair of air (rods, catenary wires or meshed conductors) and earth terminations connected to the opposite ends of an interposed set of down conductors. Such an all-metal structural protection system, whose effectiveness against fire, explosion and injury to occupants has long been verified, can also be effective against inner LEMPs. However, a secondary protection, generally involving surge protective devices, is often additionally needed (by the way, owing to a persistent lack of scientific evidence, any discussion on experimental, or even commercially available, non-conventional protection techniques is deliberately omitted here).

The evaluation of the induced effects requires a direct or indirect lightning event to occur, namely that the striking point is assigned, respectively, on or outside the primary protection system. This implies that an attachment process has successfully developed in correspondence with that crucial point. In general, the greater the number of indirect events (compared to the direct ones) involving a premise is, the higher is the probability that the inner sensitive equipment can consequently experience permanent damage or malfunction. The persistent lack of knowledge on the physical mechanisms governing the stepped leader attachment process turns out to be an important cause of the observed vulnerability. Risk assessment methods, performed by making recourse to probabilistic mathematics, are currently available for optimising the design of an integrated protection system (see Mazzetti, 2003; Horvát, 2004). The methods in question, which are iterative in nature, consist in assuming a given global protection system and then evaluating the relevant risk of damage. The design of the protection system is subject to continuous improvements until the given risk is reduced to a quantity equal to or less than an assigned risk threshold. Incidentally, the guidelines for designing protection systems directly as a function of an accepted risk are not available. Therefore, a significant part of the design consists in tentatively selecting the more suitable air termination and its placement. D'Alessandro and Gumley (2000) offer an exhaustive categorisation of air

termination placement methods, which can be summarised as follows:

(a) pure geometrical construction;

(b) mesh width;

(c) rolling sphere;

(d) leader progression; and

(e) collection volume.

After Horvát (2004), a good practice for the designer could be that of first selecting some of the methods from the above list for the design section (the same author suggests methods (a)–(c)) and using the remaining ones (namely, (d) and (e)) for a subsidiary risk evaluation section. Indeed, regardless of the procedures and practical solutions adopted, investigators and users are not fully satisfied with the predicted protection efficiency, as claimed elsewhere (see again Horvát, 2004 and, for example, Berta, 2005). The possible reasons explaining the difficulties raised are analysed hereinafter and substantial arguments promoting a revision of the subject are also given. To this end, electrostatics- and electrodynamics-based concepts will be used extensively. However, a few words of clarification are appropriate to dispel possible misinterpretations of terminological nature. Electrostatic and quasi-electrostatic sources considered here are two classes of free charges, respectively motionless charges deposited somewhere in electrostatic equilibrium and moving charges along a conducting route (thereby, producing a current). In the latter case, where electrodynamic (Amperian) effects arise simultaneously, a more appropriate adjective sometimes adopted in substitution of "quasi-electrostatic" is "Coulombian".

1.2 Thundercloud Electrostatic Modelling

One of the basic topics in atmospheric electricity is a charged thundercloud. The knowledge of electrostatic performances of a thundercloud is important for investigating the lightning precursory phenomena and the related protection systems. In its mature stage, which often represents the condition preliminary to the genesis of a stepped leader, a thundercloud cell can generally decompose into a pair of superimposed columnar regions filled by a volumetric distribution of predominantly negative (N-region) and predominantly positive (P-region) charges (Rakov and Uman, 2003; Williams, 2003). In absolute value, the total charge deposited in each region is of the order of tens of coulombs. The N-region occupies the lower portion of the cell and, therefore, is responsible for a prevailing electrostatic influence towards the earth surface. In fact, the counterparts deposited in electrostatic equilibrium on the earth's surface are positive charges. An additional region of positive charge, usually referred to as p-region, could be embedded in, and rather flush-positioned on, the bottom of the N-region.

Some space charge distributions below and above the described cell are originated, respectively by corona activity at some terrestrial sites and by cosmic radiation at higher altitudes. Such classes of charges are deliberately ignored here, even though some investigators interpret the p-region as the deposition of positive charges which, after being

originated by corona activity on some sharpened points and edges on the earth surface, have travelled up to the bottom of the thundercloud cell. The overall height of a cell could attain 20 km, while the lowermost layer is rarely positioned at an altitude greater than 2 km at non-equatorial latitudes. The relatively short altitude of the cloud bottom in specific geographical regions is considered responsible for the higher incidence of ground flashes with respect to the total number of lightning events. The radius of a cylindrical representation of a cell is in the range of 1–5 km (smaller values are more frequent in nature), even though extensive banks of thunderclouds, resulting from aggregates of cells in different stages of maturation, are commonly observed. The overall electrical morphology described is erratic, especially because of severe wind pressures on the water droplets. The substantial instabilities affecting the charge distribution of a thundercloud cell and the uncertain nature of the physical phenomena responsible for the charging process are reasons enough to discourage more detailed descriptions, and restrict the degree of sophistication applied to the electrostatic model. In spite of this, finding an efficient and convenient formulation of the electrostatic field, the source of which is a continuous volume distribution of charge, is difficult and debatable. All conditions considered, preference could be given for an analytical approach allowing both costly and time-consuming numerical procedures to be waived and physical properties to be interpreted.

Dipole and multiple-dipole structures of a cell, as a result of oversimplified point concentrations of volumetrically large distributions of charges, have extensively been described or adopted elsewhere (see, for example, Ette *et al*., 1977; Carpenter and Drabkin, 1999; Rakov and Uman, 2003). The point sources and their electrical images (the earth plane is assumed to be a perfect conductor) are positioned on roughly established geometric centres and simultaneously contribute to the field calculation. In order to avoid field infinities when the observation point is in proximity to the singular points occupied by the charge concentrations, the calculation is restricted to distanced locations of practical interest, generally to the earth plane. Distinctive of arbitrary concentrations of spatially extended regions of the charge is the introduction of geometrical quantities associated with the space positions of the above unphysical point charges into the model. As discussed later, the geometrical variables in question can significantly influence the calculation of the electric field, which is often performed to reproduce, by trial-and-error, experimental field profiles on the earth plane.

A theoretical investigation suitable for the design of preventing/intercepting effectiveness of protection systems could be decomposed into two parts: clarifying whether the unstable electrostatic scenario, prior to a lightning stroke, could be reproduced by an appropriate model and, in the affirmative case, whether this model can offer convincing arguments to support the preventing/intercepting effectiveness of air terminals. Accordingly, as an alternative to suspended single or multiple-dipole models, the use of a three-level set of charged circular discs representing a generic cell is recommended (Amoruso and Lattarulo, 2002). The model is depicted in Fig. 1.1 with the main parameters annotated. Specifically, the charge region at a height h_B above the ground is a circular disc of dipolar charge. The above description of a cell can be appreciated if an introductory treatment of the electrostatic performances of volume charge distributions, reported in Appendix A is referred. Accordingly, a rigorous and so far underestimated field formulation is adopted, whose attractive feature consists in leading to a final approximate electrostatic
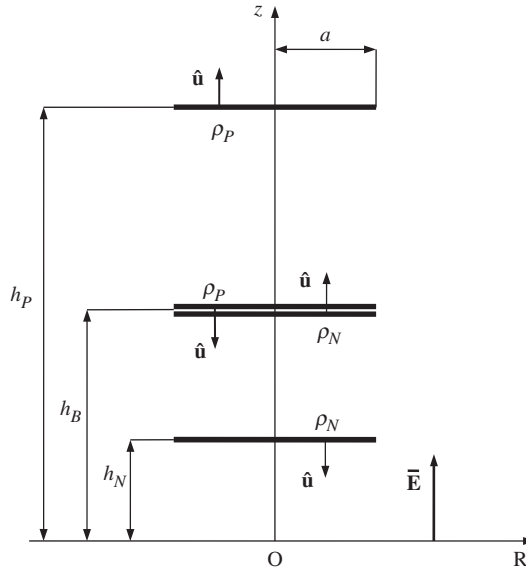
Fig. 1.1. Three-level electrostatic model of a thunderstorm cell above the ground (ρ_N and ρ_P are uniformly distributed over the upper and lower single layers and the intermediate double layer).

representation, especially appropriate to the treatment of charge distributions affected by a significant degree of uncertainty.

1.3 Electric Field at the Plane

The profiles of the electric field at ground level have been calculated using Eqs. 1.6 and 1.8 in Appendix A and traced in Fig. 1.2 for $h_N = 1.5$ km (constant parameter throughout the set of examples given here), $h_P = 10$ km, three heights h_B (as indicated), and disc radius $a = 1$ and 5 km for the curves in (a) and (b), respectively. The charge densities ρ_N and ρ_P have, respectively, been set to -1 and $+1$ nC/m^3 which are realistic values. In spite of the opposite signs assigned to the two charge densities, the partial electric fields produced by the upper and lower layers are additive and upwardly oriented (thus negative, according to the currently adopted usage in atmospheric electrostatics). This is because of the opposite orientations of the associated unit vectors. Even the pair of oppositely oriented and opposite polarity charge distributions, on the intermediate double layer, contributes with additive fields whose overall amount is, however, minor and opposite to the previous one. With the exception of the example with $h_B = 3.5$ km, the given maximum electric field remains, in absolute value, of the order of 10^4 V/m for a disc radius $a = 1$ km (Fig. 1.2(a)), as extensively verified by detection. On the other hand, Fig. 1.2(b) permits the discovery that physically the less usual maximum of 10^5 V/m is attainable by setting $a = 5$ km, which is rather an unusually large radius for a thundercloud cell. Even the polarity inversion occurs at distances similar to those

(a)

(b)
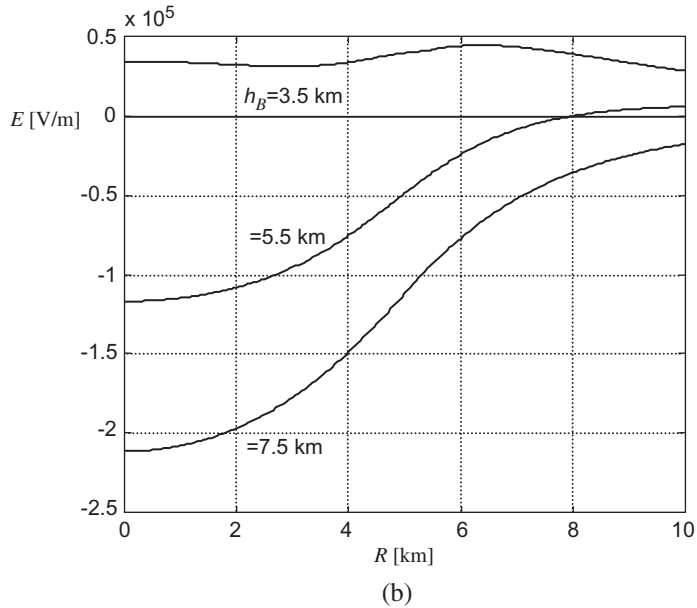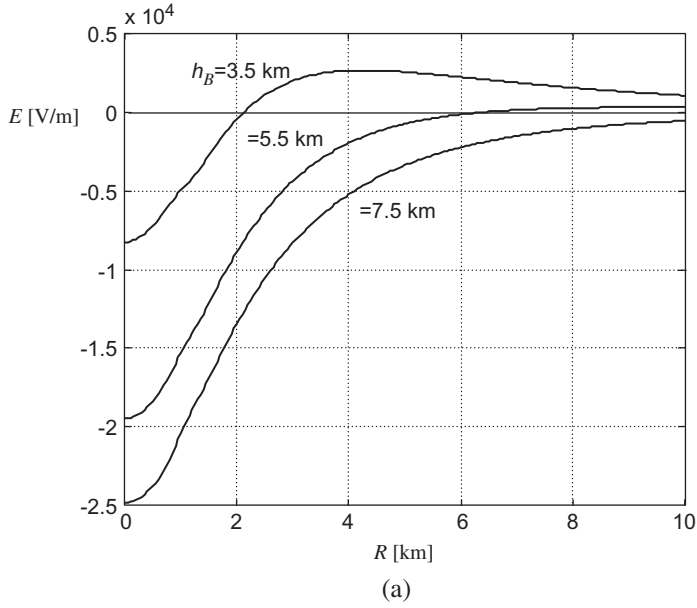
Fig. 1.2. (a) and (b) On-ground electric field distributions for three heights h_B of the intermediate double layer, as indicated; $h_N =1.5$ km, $h_P =10$ km, $-\rho_N = \rho_P =1$ nC/m^3. Curves in (a) and (b) for disc radius $a = 1$ and 5 km, respectively.

recorded experimentally. The unexpected results for $h_B = 3.5$ km are considered in Section 4, where the predictive character of the model will be especially appreciated with reference to a discussion on the on-axis field.

The electric field profiles obtained by lowering $|\rho_N|$ are illustrated in Fig. 1.3 (unchanged radii; remaining parameters as specified in the figure). In particular, the curves indicate estimation of the transitional post-stroke field disturbance caused by abrupt lowering of charge. The optional introduction of a lower p-region has been considered in Fig. 1.4, where $a = 1$ km, $\rho_N = -1$, and $\rho_P = -1$ and 1 nC/m^3, respectively, have been set. According to the present model's basic features, the p-region is merely represented by a distribution of positive charge density $\rho_L = 1 - 9$ nC/m^3 carried by a 0.5-km radius disc. The latter may be envisioned as being embedded into and centred on the larger lower disc. Even if a finite ρ-gradient is permissible within the annulus of unspecified radial thickness at the cloud base (between the p-region, where ρ_L is constant, and the surrounding N-region), the influence of the ρ-gradient on the on-ground electric field is invariably negligible. The curves show the increasing influence of the p-region in terms of the parameter ρ_L. For $\rho_L = |\rho_N|$, the curve exhibits a polarity inversion at or around a radial distance of 1.5 km. Finally, because of the excess of positive charge derived from setting $\rho_L > |\rho_N|$, the curve is unrealistically positive throughout.

Real electric field distributions at the plane could significantly depart from the regular curves discussed above owing to the influence of contiguous cumulating cells, thus forming an extended bank, of different characteristics. Figure 1.5 reproduces an experimental example, which has been reconstructed by Amoruso and Lattarulo (2003) by using an arbitrary five-cell system (see Table 1.1 for a detailed description of the quantities involved, all given by trial-and-error). Likewise arbitrary is, for example, the multiple-dipole arrangement adopted by Elle *et al.* (1997) to give a similar good fitting. However, the latter customary model invariably necessitates the introduction of inclined dipoles, a practice leading to a debatable out-of-axis arrangement of the electrostatic centres associated with the pair of N–P regions of a thundercloud cell. It is worth bearing in mind that inclined dipoles above the plane cause the appearance of a significant horizontal component of the electric field in the cloud-to-plane interspace. As an expected consequence, such questionable field component could be considered as being responsible for the remarkable inclination often exhibited by stepped leaders just emerging downwards from the cloud bottom. In a more extended sense, the investigator could be prone to overestimate the guiding role of the background field for the leader advancement (the question will be extensively treated later). Instead, the above fitting test proves that the E-field profile is given by a realistic aggregate of upright cell models involving horizontally extended uniform distribution of charges. As a result, the electrostatic centres of the P- and N-regions are collinear with the vertical axis of the cylindrical cell configuration, thus giving rise to moderate horizontal components of the electric field, even on the periphery of the cell bottom. Thereby, the investigator is tacitly invited to find more appropriate reasons explaining the typically odd-shaped space geometry exhibited by a descending leader and, ultimately, to approach the striking problem in a better way.

(a)

(b)
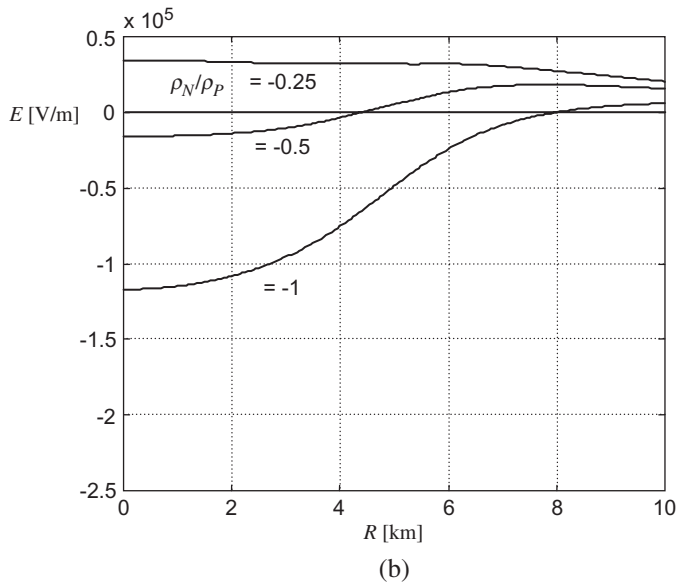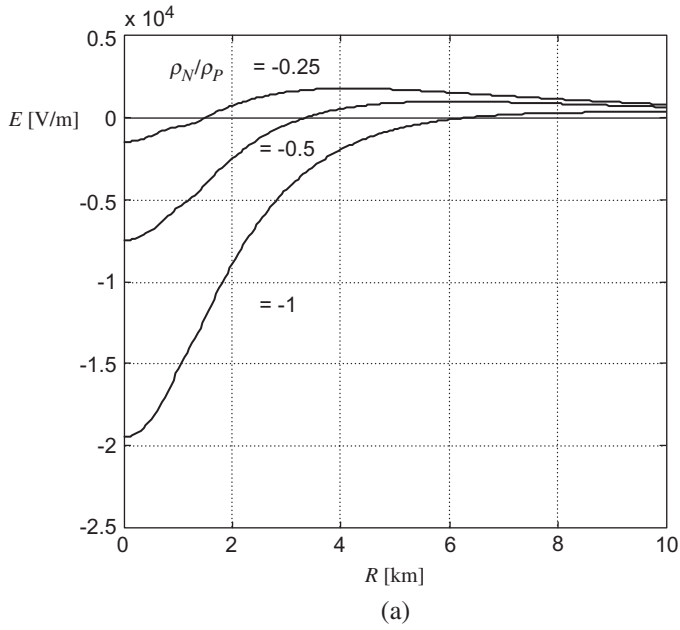
Fig. 1.3. (a) and (b) As Fig. 1.2, but with $h_B = 5.5$ km, $\rho_P = 1$ nC/m^3 and changing ρ_N as indicated.
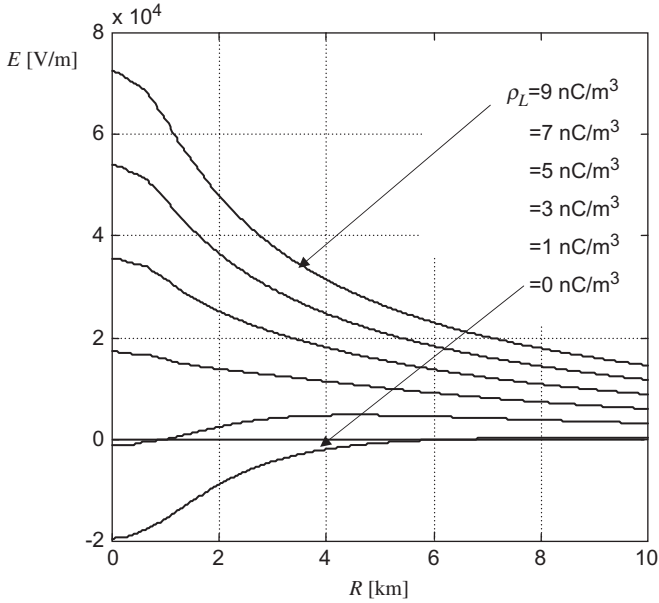
Fig. 1.4. On-ground electric field distributions with p-region included (in the form of 0.5-km radius positive layer with $\rho_L = 0$–9 nC/m^3 embedded in the centre of the lower negative layer); $h_N = 1.5$ km, $h_B = 5.5$ km, $h_P = 10$ km, $a = 1$ km, $-\rho_N = \rho_P = 1$ nC/m^3.
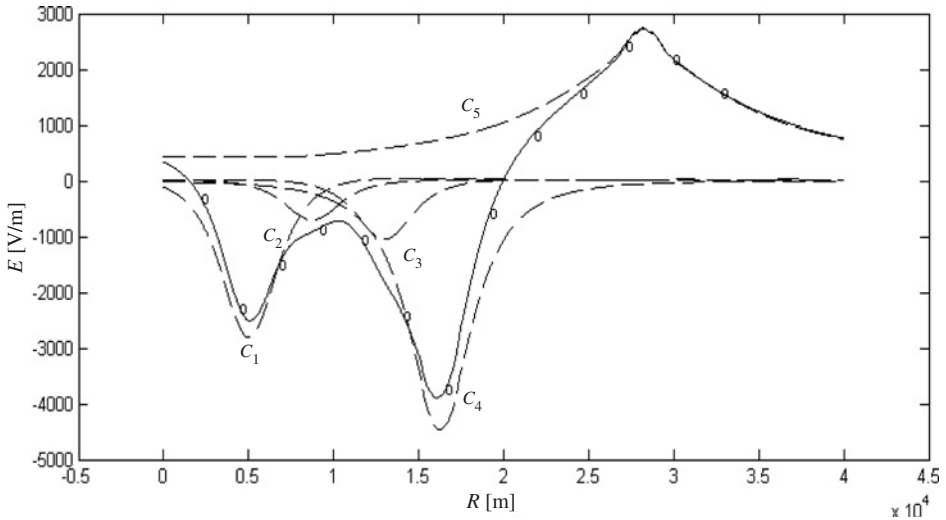
Fig. 1.5. Electric field at the ground level obtained by five cylindrical thundercloud cells (dashed lines denote the electric field caused by each cell C_i ($i = 1$–5); solid line denotes the total potential gradient; zeroes denote the experimental data after Ette *et al.* (1977)); $h_{Ni} = 1500$ m, $h_{Bi} = 5500$ m; $h_{Pi} = 10\,000$ m; cell radii $a_i = 1000$ m ($i = 1$–5). Volume charge densities and axis lateral distances R_i of each cell are reported in Table 1.1. The cell C_5 presents a p-region of radius equal to 500 m and a volume charge density ρ_L, as indicated in Table 1.1.

Table 1.1. Five-cell model parameters relative to Fig. 1.5.

Cell number	Distance R_i (m)	$|\rho_N| = |\rho_P|$ (C/m^3)	ρ_L (C/m^3)
C_1	5100	1.6×10^{-10}	–
C_2	9000	0.4×10^{-10}	–
C_3	13 000	0.6×10^{-10}	–
C_4	16 500	2.0×10^{-10}	–
C_5	27 500	1.5×10^{-10}	6.5×10^{-10}

1.4 On-Axis Electric Field

Using Eq. 1.9 in Appendix A, three families ((a)–(c)) of curves, relating to the parameters ρ_P, a and h_B, are shown in Figs. 1.6 and 1.7 (lower p-region is neglected). Essentially, the model helps to discover that at the cloud bottom, the strength of the upwardly directed fields is such that it cannot hold much greater than the one at the ground-level. Therefore, even though an increase in the electric field strength is expected when an observer approaches a charge source, the order of magnitude of such field strength remains unchanged, as experimentally detected (see, for example, Rust and Moore, 1977). Moderate on-ground field change occurs when the cell radius is very large or a bank of closely assembled cells in the same stage of maturation is incidentally formed. Conversely, field increases far exceeding the realistic ones can occur when unrealistic point concentrations of source charges, according to the earlier dipolar models, are assumed. Such convincing arguments lead to vindicate

- the slight influence of the background field on the stepped leader's inclination and tortuosity; and

- the substantial influence of natural or man-made terrestrial structures on the final stepped leader attachment process.

Knowledge of the on-axis field is helpful if the descending phase of a leader is investigated, especially when the leader has emerged from the cloud bottom. During the final phase of the leader development towards the ground, first-order errors due to the uncertain and unspecified ρ-gradient pattern are expected to only produce second-order perturbations on the outer background field, as stated earlier. Additionally, during the pre-stroke phase, ρ_N is presumed to be unchanged from significant changes, while ρ_P could even be considered unaltered throughout the flash duration.

The special combination of geometrical and electrical variables adopted permits the discovery that surprisingly positive, thus unrealistic, on-axis electric field curves are theoretically obtainable. These occur for $\rho_P = 3$ nC/m^3 in Fig. 1.7(a) and $h_B = 3.5$ km in Fig. 1.7(c). The case represented by Fig. 1.7 has been deliberately included to better appreciate the suggestive character of the present investigation applied to cell modelling, namely to a class of problems whose input parameters are known with a large degree of uncertainty. In fact, it seems clear by now that ρ_P approaching a value three times greater than $|\rho_N|$ is, as expected, an impractical occurrence. It is also expected that the P–N

(a)

(b)
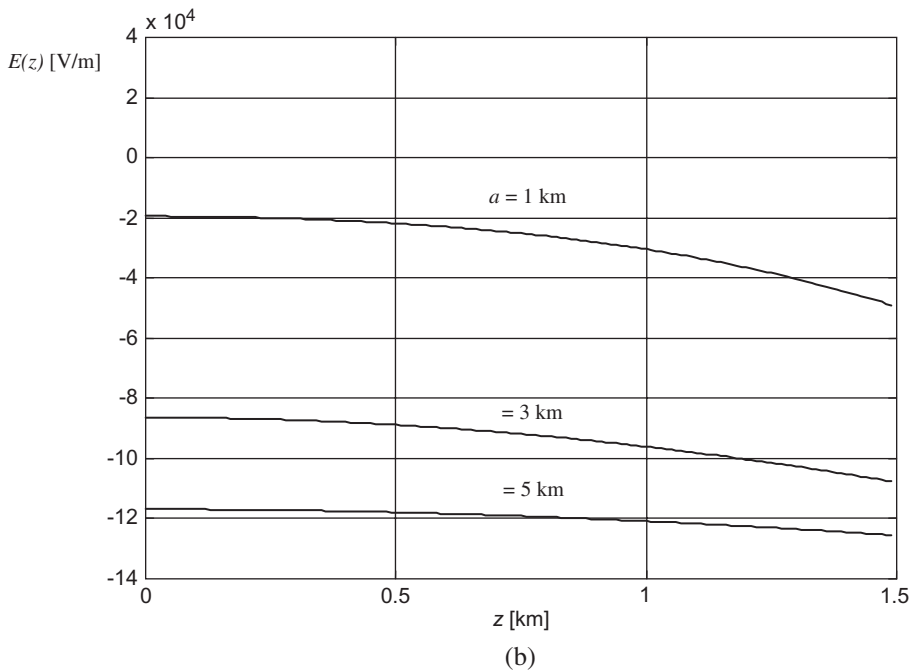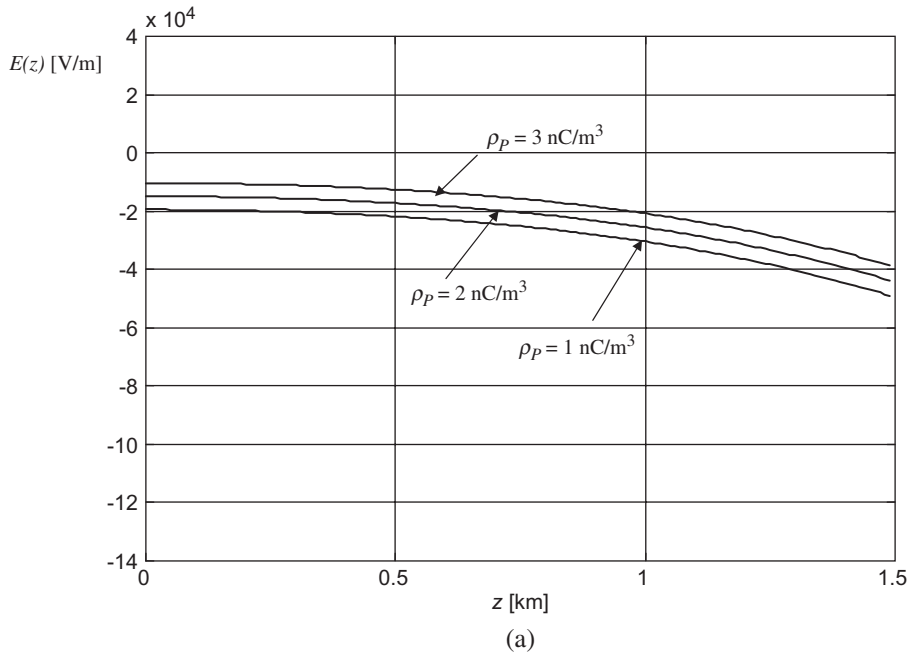
Fig. 1.6. On-axis electric field with $h_N = 1.5$ and $h_P = 10$ km, $\rho_N = -1$ nC/m^3. (a) ρ_P as indicated, $h_B = 5.5$ km, $a = 1$ km; (b) $\rho_P = -\rho_N$, $h_B = 5.5$ km, a as indicated; and (c) $\rho_P = -\rho_N$, h_B as indicated, $a = 1$ km.
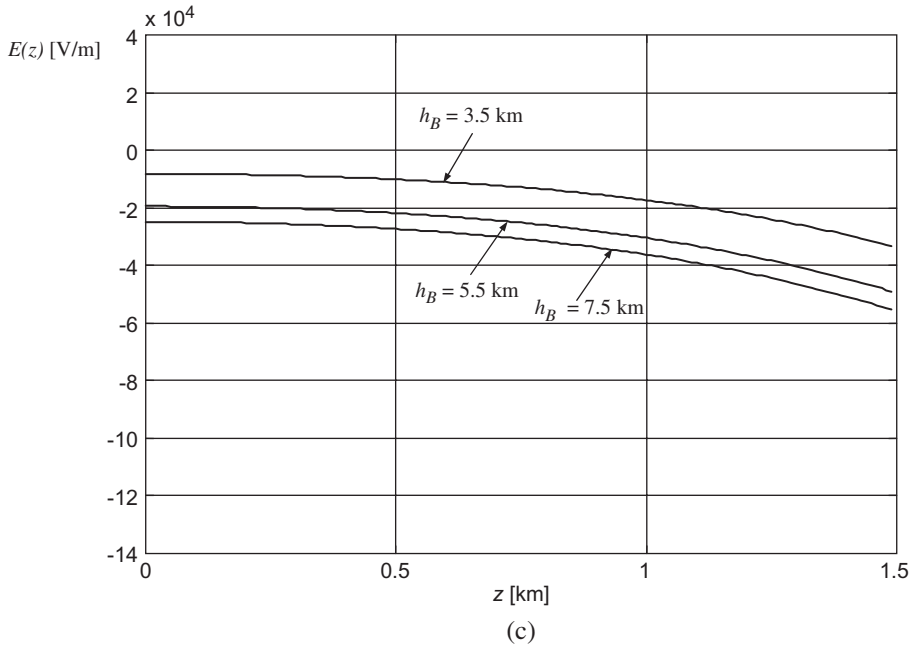
Fig. 1.6. continued.

double layer is interposed approximately mid-way between the lower and upper single layers at the cell bases.

Both the above predictions lead to the presumption that the cell model is a discharged (zero net-charge) structure with $|\rho|$ invariant throughout and the constituent P and N regions occupying equal volumes. Such a statement is also supported by Fig. 1.3(b) which clearly shows how field inversion occurs at the experimentally expected radial distance of about 8 km if $\rho_P = |\rho_N|$. To strengthen the assumption that the double-layer elevation h_B should not be significantly lower than the mid-way elevation of the thundercloud cell, note that the curves in Fig. 1.2 for $h_B = 3.5$ km are exactly similar to those recognised as being unrealistic.

1.5 Pre-Stroke Electrostatics

As restricted to an electrostatic approach, the present section can only be aimed at:

- supporting further the crucial approximation of removing the volume integral in Eq. 1.5;

- giving a preliminary but incomplete evaluation of the perturbation caused by a charged elongating leader on the background field; and

- paying special attention to the corona activity surrounding the stepped leader.

(a)

(b)
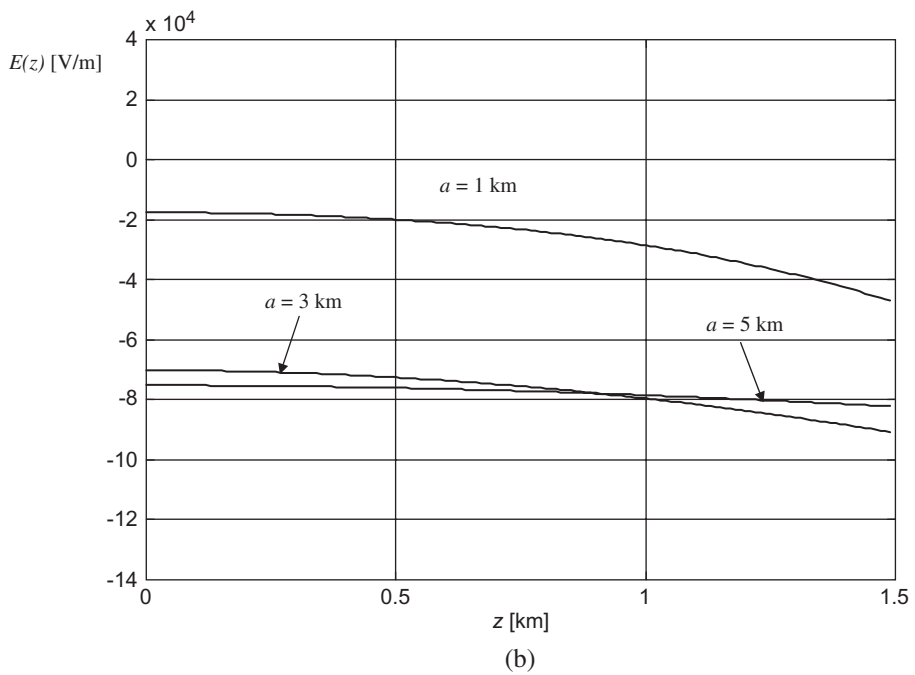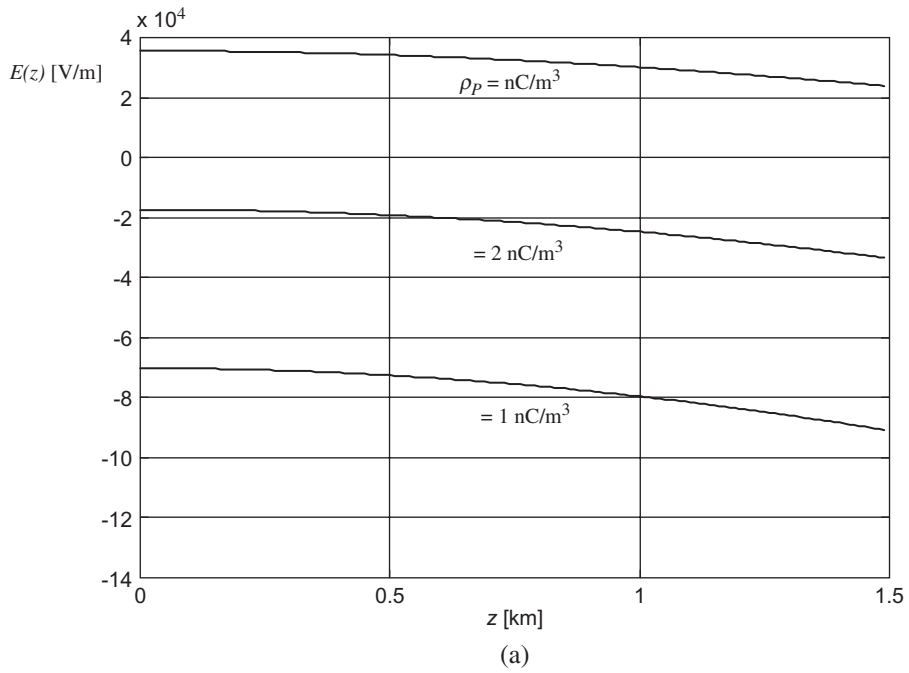
Fig. 1.7. (a)–(c) As Fig. 1.6 but with $h_B = 15$ km and $a = 3$ km in (a) and (c).
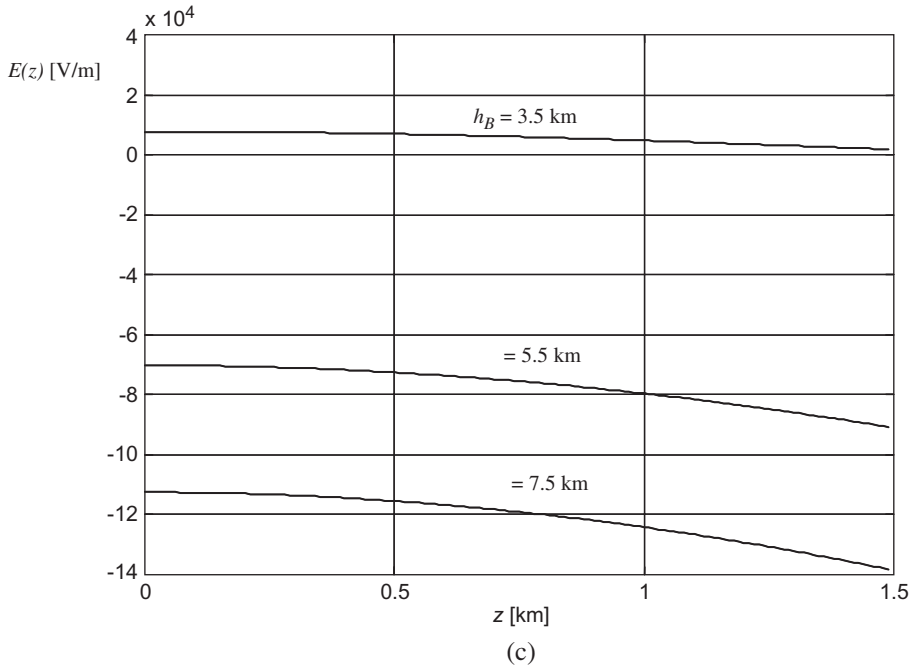
Fig. 1.7. continued.

Consider that substantial electrostatic field changes have been detected at the ground level only when the stepping leader emerges from the cloud base (such peripheral region includes the individual sources of VHF–UHF disturbances, see Le Boulch *et al.*, 1990; Rakov and Uman, 2003). Additionally, the relative magnitude of the B-process, given in tracing the so-called B, I, L (breakdown, intermediate and leader) sequence, is usually exaggerated to make the initiation point apparent (see Moreau and Rustan, 1990). Such an observation fully agrees with the simple theoretical prediction of the pre-stroke on-axis field E_1 at the ground plane. Assuming a linear charge density concentration λ leads to a vertical electric field

$$E_1 = \frac{\lambda}{2\pi\varepsilon_o h_1} \tag{1.1}$$

when the descending leader is vertical. Here, h_1 represents the tip elevation of the leader (the other end of the leader is safely assumed to be at infinity) and ε_0 stands realistically for free-space permittivity. Note that Eq. 1.1 can be easily derived from Eq. 1.6 (to be imaged) after considering that $\lambda = \pi r_f^2 \rho$, $dV = \pi r_f^2 dz$; r_f denotes leader radius, a quantity which could remain unspecified. With respect to the above example, it is easy to verify that the surface integral embodied in Eq. 1.6 becomes

$$\hat{\mathbf{u}} \int_S \frac{dS}{r} = \hat{\mathbf{u}}\frac{\pi r_f^2}{r}, \tag{1.2}$$

where $r = (R^2 + h^2)^{1/2}$ (observer on the plane is at a lateral distance R from the leader). The field orientation is dictated by $\hat{\mathbf{u}}$ which points vertically towards the ground over the leader tip (here, assumed to be the base of a thin cylinder). Consider that the overall surface implied in Eq. 1.2 is restricted to the quantity $S = \pi r_{\mathrm{f}}^2$. Therefore, imposing $R = 0$ and recalling that $\rho = \lambda/(\pi r_{\mathrm{f}}^2)$ immediately gives Eq. 1.1. Of course, E_1 points upwards from the ground if the ρ-polarity is realistically assumed to be negative.

Setting $\lambda = 1$ mC/m, a typical value for a linear charge concentration, gives a value of E_1 which is comparable with the quantity $E(z = 0)$, simultaneously contributed by the cloud charge (see, for example Fig. 1.6(b)), only when h_1 is reduced to the order of hundreds of metres or less (therefore, when h_1 is decreased to a quantity significantly less than h_{N}, see details below). This result is deemed as a further argument in favour of the self-consistent nature and reliability of the representation given in Fig. 1.1, a model substantially prone to neglect the outside electrostatic perturbations originated by additional sources from the inside.

Returning to the electrostatic influence of the above charge distribution $\lambda = 1$ mC/m along a vertical leader, Figs. 1.8 and 1.9 reproduce two examples of E-field changes at the ground when an on-axis leader advances downward below the isolated mature cells of radius $a = 1$ and 5 km, respectively (see Amoruso and Lattarulo, 2003). Also, the remaining cell quantities are assumed to be time invariant in both the examples (it is to bear in mind that the charge simultaneously lowered by the leader is at most one order of magnitude less than the overall charge stored in the main cloud regions). The large-radius case may also be representative of an extended cylindrical bank, the elemental cells of which merge in consequence to the same stage of maturation simultaneously reached by their own electrification processes. The charge density being invariant in both the examples makes the on-ground field in the large-radius case one order of magnitude greater than the field in the small-radius case. This observation accounts for the different background field perturbation exerted by the penetrating leader in the above cases. However, even at the late stages of the down-moving leader, the field at the plane remains almost unchanged or changes only moderately, irrespective of the radial extension of the cell. In fact, when the leader head has penetrated up to an elevation of 500 m, the background field is doubled only if $a = 1$ km, while it is practically uninfluenced if $a = 5$ km.

The above features, referred to a leader collinear with the cell, substantially apply if a significant lateral separation is assigned to a parallel leader from the cell axis (this occurs even if the leader is supposed to emerge from the circular periphery of the cell bottom and vertically propagates towards the plane). Now returning to the on-axis leader, the peak of the planar E-field considerably increases, say, of one order of magnitude beneath the small-radius cell only when the height of the leader head above the plane is restricted to 50 m. This is a height at which the ascending first return-stroke has typically attained the head of the descending stepped leader. It is worth noticing that under the above circumstances, the field peak is increased to 50% only beneath the large-radius cell.

On the basis of the above electrostatic considerations, it is possible to conclude that, with the exception of the perhaps unusual case of an isolated mature cell of rather modest radial extension, natural and man-made terrestrial systems are predicted to be practically
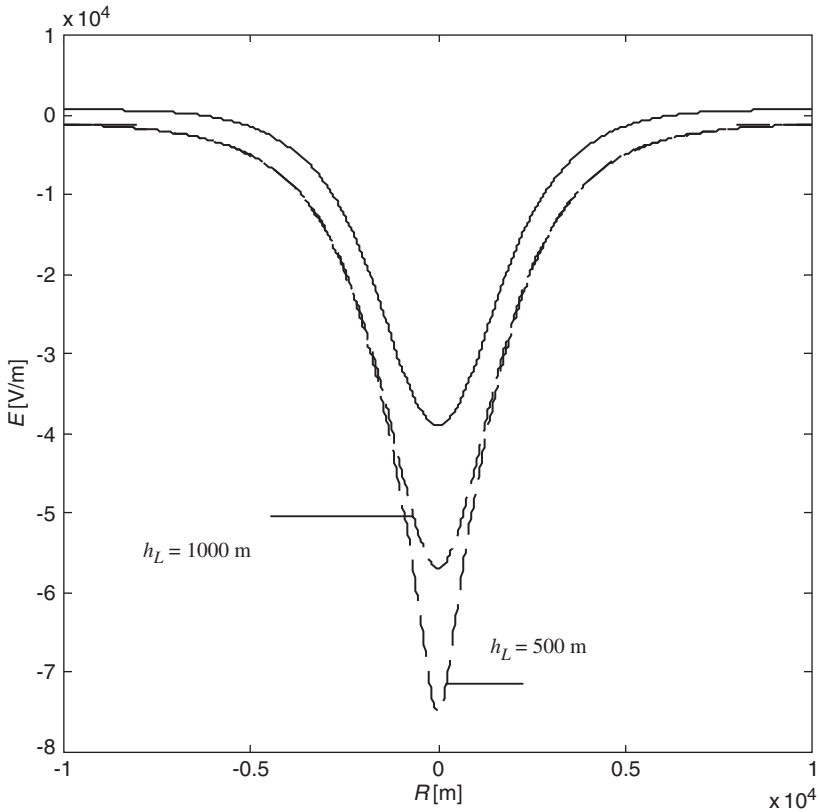
Fig. 1.8. Electric field at the ground level below a thundercloud cell of radius $a = 1000$ m, $|\rho_N| = |\rho_P| = 2 \times 10^{-9}$ C/m^3. Solid line: pre-leader phase. Dashed line: when the tip of an on-axis leader is at a height h_L above the ground.

ineffective in altering the maximum field, in magnitude and location, when the leader head has already reached a height of hundreds of metres. This is because the E-field profile at the plane is still dictated by the charged cloud, not by the leader. Specifically, the leader penetrating up to such a height moderately enforces the maximum background electric field in the worst case of a leader collinear to a small-radius cell and to slightly perturb the symmetric bell-shaped profile (in the sense that the lateral shift of the E-field peak results are unimportant) in the case of a vertical leader breaking up from the cell edge.

Up to now, the simple model adopted for a descending leader has deliberately neglected the surrounding ionisation region. Indeed, what is commonly referred to as a stepped leader channel is composed of a hot core sheath and a cold corona sheath. The core is carried by the current, lowering the negative charge originally stored somewhere in the N-region of the charged thundercloud, while the corona activity is essentially represented by the charge deposited by elongated streamers spreading at the leader head.
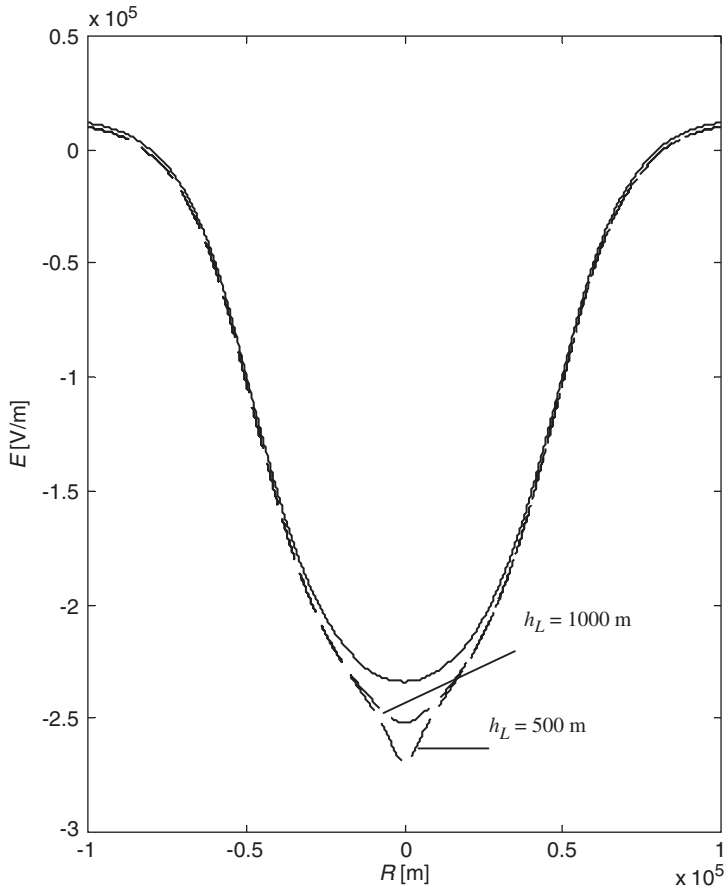
Fig. 1.9. As Fig. 1.8, $a = 5000$ m.

In fact, the simultaneous corona enveloping the lateral surface of the leader core substantially reduces, as discussed later, to a thin glow presenting a thickness comparable with the core radius. On the contrary, several investigators admit that such a lateral corona is in the same mode as the head, thus comprising radially extended streamers of the order of several metres at least (see the surveys by Cooray, 2003; Rakov and Uman, 2003). Laboratory experiments show that a key role in the formation of the leader channel is assumed by the electric field at the tip of the advancing core. Therefore, when this field is sufficient, namely if it attains a critical level holding the corona alive at the tip (the stability field), the leader channel approximately elongates showing a filamentary aspect. Even imposing realistically that the corona mode just applicable to the leader tip is that of long streamers, the corona mode surrounding the hot core is permitted to be a glow corona, the thickness of which is of the same order as core radius, thus only of 10^{-3}–10^{-2} m. Incidentally, consider that the leader core behaves as a pseudo-conductor, which implies that the corona onset voltage of the lateral corona is

higher than the tip one. The difference between such onset levels could increase since the radius of the hot channel expands according to the thermodynamic processes developed when the core is carried by the current needed for the leader elongation. However, the difference discussed seems too restricted to be responsible for the simultaneous existence of two different corona modes. Therefore, such a performance requires to be substantiated by more convincing theoretical and experimental arguments. To this end, an auxiliary experimental method, recommended for inferring that different ionisation modes can be simultaneously active on a conductor under unipolar corona, consists in detecting the impact of ion flow on a distanced collector introduced a priori in the drifting region. Irrespective of the actual negative corona mode under examination (Trichel pulse, glow or streamer, according to the order of appearance with increasing voltage) and related layer thickness, it is relatively easy to obtain the current fingerprints and current density profiles of the ion flow at a grounded planar electrode. Appendix B, concerned with such a subject, shows some experimental data when the electrode assembly is composed of a one-ended rectilinear thin-wire above, and inclined with respect to, a grounded horizontal collector. A negative potential is applied to the suspended wire so as to make the latter roughly representative of a slanting leader approaching the earth plane. The most attractive finding of the experiment (exhaustively discussed in the appendix) can only be explained by assuming that the ionisation surrounding the suspended wire is subdivided into two separate compartments, namely the endpoint corona and the lateral corona. Irrespective of the applied voltage, a streamer-mode corona concentrated at the conductor endpoint (from which, therefore, the single streamers elongate outwards), is inferred as being coexistent with a thin-sheath glow-mode corona distributed along the same conductor.

An unsophisticated theoretical model, applicable under saturation conditions in the drift region of the one-ended cylindrical wires, is also reported in the appendix and additional elements for further discussing the different dilation laws governing the termination and lateral ionisation regions, are provided. In general, assuming a saturation condition in the drift region when a theoretical model is used implies that the field divergence should be significantly smoothed in that region. Accordingly, the above simple model has been adopted only as a qualitative test to predict whether the ionisation region, interposed between a conductor of given geometry and the saturated drifting region, is permitted to significantly dilate or not. Specifically, irrespective of the applied voltage, an ionisation region constrained to occupy a thin sheath around a cylindrical conductor is given, as elsewhere verified (see Appendix C). In fact, the electric field in the outer drift region is independent of the radial distance r, thus constant even in the strong vicinity of the conductor surface. Instead, the electric field given for the simultaneous drifting region at the head of the conductor is inversely proportional to the radial distance from the emitting point. In contrast to the expected field-gradient smoothing imposed a priori for a saturated drift region, the given non-uniformity may only be interpreted, in a qualitative sense, by noting that the ionisation region in the gap dilates ahead hemispherically at the expense of the drift region. It is worth considering that the hyperbolic law describing the electric field decay becomes increasingly slow as the field point radially departs from the emitting termination.

Therefore, the streamer-mode corona of a lightning stepped leader is predicted to be active only ahead of the core tip with a spreading angle of 180°. Such an ionisation

region remains isotropic unless the tip, during the down-coming phase, approaches perturbing objects. This could be the case for aircraft or terrestrial locations. Under such circumstances, the discharge becomes non-isotropic, thus promoting a directional attachment process. Such a stepped leader's late phase is of paramount importance for both EMC and safety considerations and will be carefully re-examined in Section 1.6. Therefore, an electrodynamics-based treatment, in addition to, or even in substitution of, a usual electrostatic one, is introduced.

1.6 Pre-Stroke Electrodynamics

As will be appreciated later, distinctive of the present section is a so far overlooked electrodynamic interpretation of the stepped leader's advancement and attachment processes. To this end, the following pair of objections arise for an appropriate re-examination of the subject:

- The advancing leader is usually assumed as a stationary line-charge source (see Section 1.4). Therefore, the related field is a purely electrostatic one, the time-varying character of which is only ascribed to the leader elongation. Rather, the leader can be configured as a current-carrying conductor, thus behaving as a simultaneous source of electromagnetic field;

- The leader trajectory is tacitly understood as being guided by the pattern of a purely electrostatic field whose components are the self and background fields. Instead, the predominant contribution to the slanting and tortuous nature of a leader channel seems rather ascribed to underestimated electrodynamic forces obeying, after Pappas (1993), the so-called cardinal law of electrodynamics. The same law is also interpreted as being responsible for both the stepping character of the down coming leader and some unexpected details of the attachment process.

The basic theories related to the above two statements are skipped in Appendices C and D, respectively. Specifically, the subject treated in Appendix C proves that the prevailing source of the self E-field in the hemispherical space ahead and just beyond the ionisation region of the leader is the core-carrying current i_c which sustains the terminal-corona activity. In other words, a purely electrostatics-based treatment, so far extensively adopted elsewhere, fails in describing the down-coming phase of a leader, especially during the late instants of the attachment process. In fact, according to Eq. 1.20,

$$E_{d,\,r,\,\mathrm{av}} = \left(\frac{i_c}{4\pi\varepsilon_o r \mu}\right)^{1/2}$$

represents a rough estimation of the average field $E_{d,\,r,\,\mathrm{av}} = V/r$ in the saturated drifting region under extension (thus extended up to the radius r). Therefore, assigning a stepped-leader average current $i_c = 1$ kA gives a space-charge self-field $E_{d,\,r,\,\mathrm{av}}$ of the order of $10^5/r$ V/m (r expressed in metres) at the ionisation–drifting interface, namely on the hemispherical envelope of the radially elongating streamers comprising the glow (step under extension). Such a field often exceeds, of an order of magnitude at least, the thundercloud-originated background field if r does not exceed the order of few metres.

This simple prediction safely leads to the realisation that the leader penetration could have been influenced by the thundercloud-originated background field when r has attained, say, a value of 50 m, namely the average length of a step. However, the step extension typically reduces to 1/5 nearby earth, which implies that the background field can be ineffective in guiding the leader penetration. Meanwhile, the enforcement field of the down coming leader is increased enough to promote upwardly directed energetic leaders from earth objects (see later).

Let us now return to the advancing process of a stepped leader. The velocity v_s of the elongating streamers, radially diverging from the leader stem, approaches that (notation c) of light in vacuum. Namely, once the current i_c attains the leader channel termination, a moderate deceleration from c to an unspecified value $v_s < c$ is experienced by the moving charges at the leader's arc–streamer junction. According to Eq. 1.23 (which, in turn, is derived from general Eq. 1.22) and related notation, see Appendix D, it is quite admissible that v_s becomes less than $c/\sqrt{2}$, which implies that the injected streamers experience mutually repulsive Coulombian forces shaping a hemispherical glow ahead. In other words, owing to an abrupt current deceleration at the leader–streamer connecting point and consequent directional inversion of the transversal force, an arc-to-streamer transition, manifested in the form of a discharge spreading outwards, occurs. For the corona expansion to be sustained towards a steady state (see Appendix C), the current is required to increase progressively. This implies that v_s increases until the condition $c > v_s > c/\sqrt{2}$ is met and, therefore, previously prevailing repulsive forces between contiguous filamentary streamers become increasingly attractive now. As a consequence, the individual streamers forming the invisible hemispherical glow are forced to concentrate, i.e. to be subject to a conical compression giving rise ultimately to a new streamer-to-arc transition. When this optically faint phase is accomplished, the just formed hot-core segment abruptly becomes visible, thus causing the entire process to appear as a stepping one. Of course, unpredictable reasons could cause the velocity v_s from obeying a perfectly isotropic polar law in the hemispherical glow, a feature primarily responsible for stochastic directional changes of the conical glow compression with respect to the channel segment just lying behind. The described tortuous penetration of the stepped leader, due to non-zero angular shifts of the directional streamer-to-arc transition, can be sometimes complicated by the simultaneous formation of two or more diverging transitions, thus causing channel branching.

The leader channel is additionally subjected to minute tortuosity, which can again be accounted for by Eq. 1.22. Different from the case of a rigid current-carrying conductor, the inwardly directed forces transversal to the channel axis (see Eq. 1.23 applied to pairs of moving charges) essentially co-operate in holding it compressed. However, such forces are rather unstable, since the filamentary configuration assumed by the plasma constrains the charges to proceed rather than be aligned. According to Eq. 1.24, longitudinally repulsive forces significantly arise simultaneously and perturb the charge motion, thus causing a non-uniform distribution of the charge velocities over the cross section of the plasma. Unbalanced radial forces, invariably sensitive to v_s (see again Eq. 1.23), ultimately account for the second-order tortuosity. On the other hand, it is not difficult to expect that the above phenomenon vanishes if the parameter v_s happens to become invariant. This occurs only if v_s persistently remains as large as possible, i.e. if v_s tends to the limit quantity c for each moving charge and in any instant of the observation phase.

Such a condition should be substantially met when a descending leader approaches the ground, even though the surrounding halo can mask minute channel wanderings.

With special reference to a return stroke, the extensively detected decrease in the apparent velocity from a value close to c to around $c/3$ should be considered, even though the physical velocity is expected to remain unchanged. The discrepancy is explained by presuming that an invisible (owing to the discharge halo), minute tortuosity is disseminated along the channel, especially from a certain height above the ground (see additional considerations in Chapter 2). Therefore, the electrostatic influence of the plane somehow seems involved, but rather in the sense that the leader current increases in proximity to the ground. In fact, under such conditions, the significant current enhancement (also due to an increase in the travelling charge velocity) required to sustain the increasingly severe activity of the corona at the head of the channel, causes the minute tortuosity to reduce.

It is also worth considering that during the late instants of a down coming leader, inception of a blanket of upward penetrating energetic streamers is plausibly formed on the overstressed parts of an earth object. Such individual streamers, breaking up upright from a glow-mode corona activity over the exposed area, are also expected to be subjected to mutual attraction. This occurs if $v_s > c/\sqrt{2}$ (see Eq. 1.23 in Appendix D) and can be assigned to the moving charges forming the unidirectional currents associated with the streamers, in which case a number of streamer-to-leader transitions takes place. It is worth considering that apart from the electrostatic stress just below the down coming leader head, the displacement current associated with the stepping dynamics of the leader assumes a conduction mode when it serially traverses the multiple unconnected upward discharge. A prerequisite for a lightning flash to occur is that the nearby stepped leader successfully comes into contact with one of the described reacting upward leaders.

Even the intercepting properties of a terrestrial leader still require to be accurately investigated by introducing the electrodynamic mechanism. In fact, the total attraction between the two aligned leaders growing towards each other tends to vanish according to Eq. 1.26, since the ratio $v_s/c < 1$ substantially approaches unity. In other words, under the above conditions, the Coulombian attraction is counterbalanced by a simultaneous electrodynamic repulsion. However, two oblique leaders are permitted to join if the transversal components of the forces involved are predominant in guiding the attachment process. If the latter is destined to be accomplished successfully, the terminal segments of the pair of approaching leaders are therefore expected to go a little beyond each other before joining sidewards. The fact that the attachment is not expected to be exactly a frontal one accounts for the loop distinctive of the attachment process. The large electrodynamic repulsion experienced by the two aligned leaders which are about to join could also be responsible for the recorded channel split (Rakov and Uman, 2003).

Let us now return to the described proliferation of visible and invisible streamers, embryo-leaders and leaders, launched upward under the influence of a descending stepped leader. Such an energetic complex discharge, distributed on an electrostatically overstressed terrestrial area, can be effective in neutralising reiterated attacks of the downward approaching leader. Therefore, the formation of unconnected multiple upward streamers or leaders, causing simultaneous and mutually opposite electrodynamic

and electrostatic effects above the circumscribed locations (non-attraction areas) of the exposed object, can account for the pronounced horizontal deviation often affecting a channel before resolutely pointing towards the destination (striking) point over the terrestrial object. Accordingly, such a point is positioned inside one of the complementary attraction areas adjacent to the non-attraction ones.

Consider that if q_1 represents a stationary charge ($v_1 = 0$) on the plane just below a downward leader, the single moving counterpart q_2 distributed along the channel experiences an electrostatic force originated by q_1. The purely electrostatic nature of such a force is revealed by Eq. 1.22 when $v_1 = 0$. However, just before touching the ground, the described inception and propagation of an upward leader, capable of laterally hooking the downward-penetrating one, is promoted. On the other hand, a rather isolated or peripheral leader of a rather compact array of unconnected upward leaders can be effective in laterally hooking the causative counterpart. Even in the case of a tower or upright antenna-like structure, the probability for a stepped leader coming down in its neighbourhood to be laterally hooked by the uppermost attaching leader also increases as a function of the height of the structural protection system. In the light of the present description, a successful attachment is promoted if the tall system significantly overtops a rather extended non-attraction area surrounding it (so classified owing to the shorter and/or energetically faint unsuccessful competitors launched upwards there). In any case, the attaching point is expected to be rather positioned somewhere along the terminal segment of the upward leader than on its top.

1.7 Concluding Remarks

The above qualitative description involving electrodynamic effects allows an insight into the attachment process and gives a theoretical basis to improve the available predictive methods applied to protection systems and correlated EMC solutions. In general, more ad hoc air terminals or inadvertent man-made and natural objects have to meet the necessary conditions in order to successfully behave as intercepting systems. The necessary conditions promoting an attachment process can be summarised as follows:

(a) A certain amount of pre-stroke static charge, deposited in electrostatic equilibrium on the earth, has to be abruptly transferred upwards, thus pervading the structural lightning protection system, before sustaining the uppermost activity of vigorous streamers and consequent streamer-to-leader transitions;

(b) The currents carried by a successful pair of downward and upward leaders have to be intense enough to influence the direction of the stepped leader's late streamer-to-arc transition, namely the leader segment directly involved in the final jump;

(c) Among the upwardly directed competitors, the leader capable of attachment has to be launched in isolation.

The prerequisites for meeting conditions (a) and (b) are an effective earth termination or a large dimensional pre-charged terrestrial object. Condition (c) can either be referred to a terrestrial channel incidentally positioned at large lateral distance from an unconnected multiple leader formation of comparable height or to an overtopping channel surrounded

by unsuccessful competitors. In the first case, the down coming leader can be frequently repelled by a rather compact dissemination of upwardly going leaders (thus delimiting the non-attachment area) before performing the final jump where such leaders become thinned away (thus, in the attachment area). Therefore, the described repelling and attracting regions combine to make an isolated terrestrial leader (or even a current-carrying down conductor, see later) an effective interceptor. Instead, the down coming leader has to incidentally approach a tall terrestrial channel for promoting an attachment process. In both the cases, the down coming leader has to vertically penetrate enough somewhere around before being laterally hooked by the isolated channel (see Eq. 1.25).

Specifically, with respect to condition (b), the pair of charges q_i ($i = 1, 2$) in Eq. 1.22 can be replaced by the corresponding pair of quantities $I_i \, \mathrm{d}\vec{s}_i / \vec{v}_i$ (see Appendix D). Therefore, it is also admissible that the pre-stroke currents simultaneously carrying the pair of approaching downward and upward leaders be correlated, according to the so far unpredictable laws, to some electrical and geometrical parameters: such quantities could be represented by the striking distance d_s (namely, the distance between the striking point and the tip of the down coming leader just before the final step), height h of the intercepting structure and peak value of the return-stroke current. The above speculative considerations are supported by available empirical formulas, governing the interception efficiency of air terminals, according to the electrogeometrical models (see, for example, Chowdhuri, 1996). The formulas in question can be rearranged to assume the general structure

$$d_s = kI^a h^b, \tag{1.3}$$

where k, a and b are assigned quantities (specifically, a or b can also vanish).

It is worth pointing out that the dependence on the detectable current, expressed in Eq. 1.3, is the result of a convenient manipulation performed on an electrostatics-based formula, thus directly involving the undetectable charge deposited along the channel of the down coming leader. It appears clear by now, in the light of Eq. 1.22 or its optional current-dependent version, that the success or failure of Eq. 1.3 can be often ascribed to an overlooked enhancing or neutralising electrodynamic (Amperian) effect on the electrostatic (Coulombian) one during the attachment process. Probably, the fact that the formulas governing both the effects show a similar structure is responsible for the submerged character of the electrodynamic component during the previous empirical approaches, which led to the definition of Eq. 1.3.

Conditions (a)–(c) and related discussion represent substantial arguments for improving the available theories or methods, previously summarised in Section 1.1, and convention-ally accepted guidelines, all affected by a restricted, purely electrostatic interpretation of the attachment phenomenon. In other words, if the crucial role assumed by the currents involved is neglected, using a traditional electrostatic approach to explain the attachment becomes a rather hard exercise, invariably circumvented by an excess of empiricism. The electrodynamic approach can, as an example, account for the unexpected side attachments to down conductors or guy wires which are often less electrostatically stressed than, or even quite protected by, the air termination placed atop. In fact, a large number of upward leaders, disseminated over a horizontally extended air terminal as an inception effect

of a descending stepped leader, can give rise to a surprising repelling action, while an isolated leader, launched somewhere upwards, or, say, a vertically lying current-carrying metallic conductor can promote a successful side attachment (see Eqs. 1.25 and 1.27, respectively, in Appendix D). Even the interception efficiency of air terminations can be better appreciated by taking into consideration their own electrodynamic attraction in the interconnected protection system's current-carrying locations deprived of upward leaders.

The above considerations not only call in question the reliability of usually accepted theories which are applied to the primary lightning protection, but tacitly invite to re-examine the supplementary EMC problem of realising a secondary protection. In principle, unexpected attachments, thus involving regions outside the air-termination placement established by the methods summarised in Section 1.1, could give rise to unsafe situations. Fortunately, it is more probable that the lightning current directly strikes inappropriate conductors (for example, side wires) of the interconnected protecting system before discharging to earth without being prejudicial to the safety. However, such accidental circumstances imply that the current distributions (diversion modes) can significantly differ from those assumed in the design of the secondary protection. As a consequence, underestimated conductive, inductive and capacitive couplings could derive with consequent malfunctions or disruptions of sensitive electronics. Therefore, more than describing coupling models, which are extensively reported on basic EMC textbooks, the present chapter is rather aimed at recommending a careful revision of the subsidiary attachment mechanism by taking into account its so far underestimated electrodynamic character.

Appendix A

Let a generic volume V be filled by a continuous charge distribution of density ρ. If ε denotes a general medium permittivity (assumed to be a constant), then

$$\overline{E}(P) = \frac{1}{4\pi\varepsilon} \int_V \frac{\rho(M)\overline{r}}{r^3} \mathrm{d}V \tag{1.4}$$

represents the electric field on the observation point P. The above relationship, which includes the oriented distance $\overline{r}$ between a given location M of the elementary volume $\mathrm{d}V$ and P, holds irrespective of whether the latter point is inside, outside or on the surface S contouring V. A rigorous alternative to Eq. 1.4, given by Durand (1964), can be expressed as follows:

$$\overline{E}(P) = \frac{1}{4\pi\varepsilon} \left[\int_s \hat{\mathbf{u}} \frac{\rho}{r} \mathrm{d}S - \int_V \nabla\rho \frac{\mathrm{d}V}{r} \right] \tag{1.5}$$

whose distinctive feature involves only the volume charge density ρ to be deposited on the peripheral surface S and inner ρ-gradients as actual field sources. Such quantities are separately included in the integrands of specific surface and volume integrals, respectively. The unit vector $\hat{\mathbf{u}}$, associated with the elementary surface $\mathrm{d}S$, is outwardly directed while the vector differential operator ∇ in the volume integral is with respect

to the source point M, not the field point P. In general, no preference may be expressed for Eq. 1.5, in the place of Eq. 1.4, as per computational demands required. However, use of Eq. 1.5 becomes a convenient practice especially if the volume integral vanishes or is negligible, irrespective of local non-uniformity in the charge distribution. If ρ is perfectly constant in V, Eq. 1.5 reduces to

$$\overline{E}(P) = \frac{\rho}{4\pi\varepsilon} \int_s \hat{\mathbf{u}} \frac{\mathrm{d}S}{r} \tag{1.6}$$

Figure 1.10 represents the case in which ρ is constant but different in the three sub-regions of volume V_i ($i = 1$–3) delimited by the surfaces V_i. The sub-regions in question, comprising the overall volume V bounded by the surface S, are arranged in such a manner that V_2 is nested inside V_1 which, in turn, is contiguous to V_3. Therefore, ρ is subject to discontinuity at the two interfaces separating the sub-volumes V_1 and V_2 and the sub-volumes V_1 and V_3. It is a simple exercise to verify that if S_2 identifies the interface between V_1 and V_2, the interface between the adjoining regions V_1 and V_3 has the extension $(S_1 + S_3 - S)/2$. Accordingly, Eq. 1.6 becomes

$$\overline{E}(P) = \frac{\rho_1}{4\pi\varepsilon} \int_{s_1} \hat{\mathbf{u}}_1 \frac{\mathrm{d}S_1}{r_1} + \frac{\rho_2 - \rho_1}{4\pi\varepsilon} \int_{s_2} \hat{\mathbf{u}}_2 \frac{\mathrm{d}S_2}{r_2} + \frac{\rho_3}{4\pi\varepsilon} \int_{s_3} \hat{\mathbf{u}}_3 \frac{\mathrm{d}S_3}{r_3}, \tag{1.7}$$

where all the implied quantities occur consistently as subscripts.

Equation 1.7 is considerably attractive when the condition $\nabla\rho = 0$ is met, even if ρ abruptly changes between contiguous sub-regions. Furthermore, as will be appreciated later, the above formula is recommended even if the charge distribution occupying each sub-region is non-uniform, provided of course that the volume integral of $\nabla\rho$ in Eq. 1.5 tends to vanish in some field points. This is often the case when P is outside V, owing to the already proven second-order contribution of $\nabla\rho$ to the integral calculation of $\bar{E}(P)$ in the space-charge-free domain surrounding V. Such an approximate result is specially distinctive of expanded volumes of charge, since a charged cloud at a certain stage of dilation is subject to effective smoothing processes promoted by the local lack
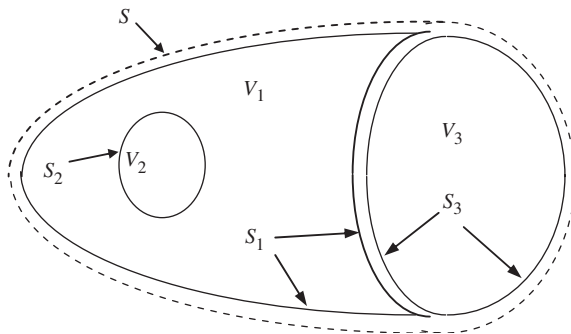
Fig. 1.10. Three sub-region charge distribution involved in Eq. 1.7.

of uniformity. Additionally, significant ρ-gradients could especially persist in the inner locations of expanded clouds, so that the decaying r^{-1} law invariably causes the distanced outer points to be slightly influenced. In any case, the error derived from using Eq. 1.6 instead of Eq. 1.5 (or Eq. 1.4), irrespective of severe ρ-gradients resulting somewhere in large volumes, could often be within the uncertainties affecting the process at work. The above considerations reasonably apply, in particular, beneath charged thunderclouds, so that a suitable version of Eq. 1.7 (second term is neglected) seems profitable to such a class of investigations.

For the sake of completeness, consider that restricted volumes of highly non-uniform charge density could cause significant charge dilution on the cloud contour, in which case the predominant contribution to $E(P)$ is inversely given by the integral of the ρ-gradient. Even in the latter case, adopting the simplified practice of neglecting the non-null ρ-gradient immediately gives zero-field in the outer domain. This is in apparent contrast to the Gauss's theorem, according to which a volume of net charge must produce a non-null external field. Indeed, a reasonable interpretation of the above approximate result is that the outer field is expected to abruptly decrease to zero. Substantially, this is the case if both ρ and $\nabla \rho$ vanish on the cloud boundary, irrespective of their own inner distributions. Such a field performance, not treated here, is typically reproduced outside, and longitudinally to, the elongated streamers.

Now returning to the description of the pre-stroke electric field scenario beneath a thundercloud, it is worth noticing that the field formulation expressed by Eq. 1.7 offers a rationale for appropriately arranging the source model and addressing the physical interpretation of the predictions. By taking account of the basic electrical properties of a cell described in Section 1.1, Eq. 1.7 ultimately leads to the three-level electrostatic representation of Fig. 1.1. The approximation substantially consists in

- neglecting possible charge density gradients in the volume occupied by the charge distribution;
- neglecting nested volumes of charge represented here by V_3; and
- considering only the charge density at the bounding surface.

For a concise but careful interpretation of the model features based on the proposed approach, the following reasonable compilation of statements has been arranged:

- A detailed description of indistinguishable and erratic $\nabla \rho$ patterns is deliberately avoided;
- Because of the upright cylindrical configuration usually adopted for a thunderstorm cell, the required computational effort reduces significantly, and an analytical calculation is made permissible by canonical functions (see Eqs. 1.8 and 1.9);
- The sources effectively involved are a pair of oppositely charged distributions over the inner sides of the upper and lower circles (cylinder bases) and both the sides of an interposed P–N interface (unchanged cross-sectional geometry);

- The field computation becomes finite and continuous even extending the field calculation across the charge layers implied in the modelling.

Therefore, the model is not compromised by an excess of arbitrary in-cloud assumption. Specifically, even horizontally displaced and spatially restricted negative-charge pockets, generally depleted during the return-stroke sequence, disappear in the model and average charge densities ρ_N and ρ_P, representative of the N- and P-region, respectively, are those actually involved. This simplifying assumption, which is especially appropriate to the present investigation (since it is restricted to the outer field facing ground) is supported by experimental observations. Indeed, the interface between the superimposed P and N regions is presumably fuzzy and unstable because of a number of uniformising processes (Coulombian/diffusional charge rearrangements, recombinations, corona activity, etc.) combined with dramatic wind perturbations. Such an expected detail is neglected in the model, according to which the charge abruptly reverses its polarity across the planar P–N interface. Finally, it is worth remembering that, in contrast to the dipole models involving point charges, the model is well behaved under conditions of source proximity in the rigorous sense discussed by van Bladel (1991).

Explicit formulas derived from Eq. 1.7 are reported below for two examples of special interest discussed in Section 1.5. The calculation is analytically amenable because of the vertical orientation of the electric field, thus parallel to the main axis of the axial-symmetric configuration assigned to the cylindrical cell, in both the treated cases. In fact, the outwardly directed unit vector $\hat{\mathbf{u}}$ is radial over the cylindrical surface and thus transverse to the one-dimensional field under examination. Therefore, only the array of single-layer charge distributions depicted in Fig. 1.1 and their images are the boundary sources involved in Eq. 1.7.

A.1 On-ground field

The mirroring action of the terrestrial plane, assumed to be a perfect conductor, is taken into account by the imaged version of Eq. 1.4, which only requires the electric field to be doubled. After removing $\hat{\mathbf{u}}$ from the integral sign of the basic Eq. 1.6 (in the treated case the $\hat{\mathbf{u}}$-orientation is an invariant), gives

$$\int_S \frac{dS}{r} = 2\left[-(1-\varepsilon')\frac{\pi}{2}h + r_d E(p) + \frac{a^2 - R^2}{r_d}K(p) + \frac{h^2}{r_d}\frac{a-R}{a+R}J_3(p,m)\right] \qquad (1.8)$$

in which $\varepsilon' = -1, 0, 1$ when R is less than, equal to, greater than a, respectively; $h = h_N, h_B$ or h_P; $r_d = [(a + R)^2 + h^2]^{1/2}$; $E(p)$, $K(p)$ and $J_3(p,m)$ are complete elliptic integrals of the first, second and third kind, respectively, where $p = 2\sqrt{(aR)/r_d}$ and $m = 2\sqrt{(aR)/(a + R)}$. An ancillary smoothing procedure has been adopted for making Eq. 1.8 regular when R is close to the radius a. In fact, m tends to unity in this case, which implies that $J_3(p, m = 1)$ is infinite. This analytical drawback accounts for an expected field singularity on the edge of a single layer (van Bladel, 1991). In fact, consider that the charge density is forced to remain finite even on the circular periphery

of the layer, which, by definition, is a geometrical entity of infinitesimal thickness. The theoretical difficulty is easily overcome by considering that the real contour of a cloud cell is deprived of sharp edges.

A.2 On-axis field (below the cell bottom)

When $z \leq h_N$, the on-axis electric field $E(z)$ along the z coordinate centred on the cell's vertical axis of Fig. 1.2 becomes (see again, Durand, 1964)

$$E(z) = \frac{\rho_N}{\varepsilon} \left(\frac{r_A + r_B}{2} - h_N \right) - \frac{\rho_P}{\varepsilon} \left(\frac{r_C + r_d}{2} - h_P \right) + \frac{|\rho_N| + |\rho_P|}{\varepsilon} \left(\frac{r_E + r_F}{2} - h_B \right), \quad (1.9)$$

where

$$r_A = \sqrt{a^2 + (h_N - z)^2}; \quad r_B = \sqrt{a^2 + (h_N + z)^2}; \quad r_C = \sqrt{a^2 + (h_P - z)^2}$$

$$r_d = \sqrt{a^2 + (h_P + z)^2}; \quad r_E = \sqrt{a^2 + (h_B - z)^2}; \quad r_F = \sqrt{a^2 + (h_B + z)^2}$$

Appendix B

As a meaningful example, Fig. 1.11 shows the normalised current density profile $j(d)$ (d denotes a longitudinal abscissa) detected just below a one-ended, horizontally stretched wire when the applied voltage is negative (see Amoruso and Lattarulo, 2005). The wire, whose radius $r = 0.5$ mm, is suspended at a height $h = 27$ cm and the applied voltage exceeds the corona onset levels at the tip and on the lateral surface of the conductor (some data are omitted owing to the strictly qualitative nature of the figure in such a context; second-order changes are detected when the polarity is reversed). The suspended conductor is discontinued by net truncation (a further second-order detail under corona), while the opposite end is connected to a high-voltage direct current (HVDC) supply by corona-free junctions. The profile collapse shown in the figure proves the existence of a net separation between the flows simultaneously emitted by the all-active wire's endpoint ($j(d)$ profile for negative d) and lateral surface ($j(d)$ profile for positive d). It is also worth noticing that the above two ion flows do not seem to be mutually influencing since the former profile substantially remains unchanged even if the latter one disappears, i.e. when the applied voltage is above and below the onset levels of the tip and lateral corona, respectively. In particular, the outer profile (when d is negative) results are surprisingly fitted by Warburg's cosine power law, with index close to 5. Subsidiary measurements prove that the profile changes along different radial directions, according to unspecified decaying laws.

The straight wire was progressively inclined and the planar current distribution methodically detected for several values of the angular deviation $0° \leq \alpha \leq 90°$ of the inclined rod from the vertical. All the on-ground projections of the slanting wire were assumed to be superimposed to the positive d axis, the origin of which represents the tip projection, irrespective of the inclination angle α. As the measuring system is a flush-mounted Wilson-plate-type current-sensing probe, the planar detection of the current
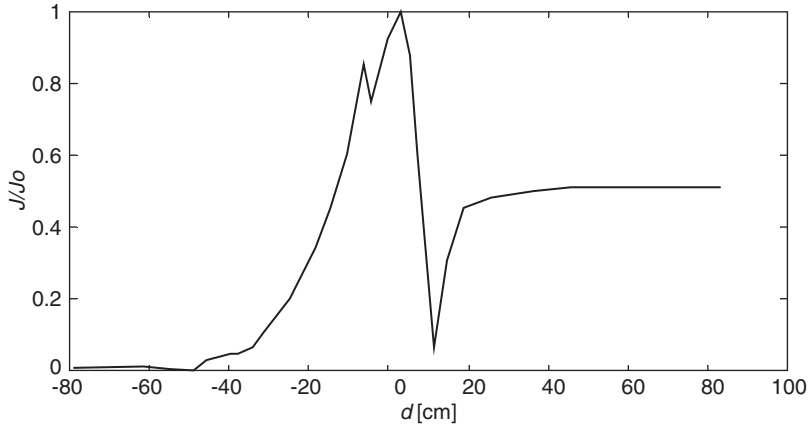
Fig. 1.11. A typical example of normalised current density distribution at the plane just below a horizontally stretched one-ended wire (on-ground projection positioned for $d \geq 0$; further data omitted owing to the strictly qualitative references in the text).

fingerprint was performed by a refined composition of a pair of rectilinear and mutually orthogonal motions connected to the wire's suspending system and probe-carrying collector. Grey-gradated current fingerprints, obtained at prescribed wire inclinations, is the graphical descriptor adopted in Fig. 1.12. For the sake of completeness, even the extreme cases of $\alpha = 90°$ (horizontal wire) and $\alpha = 0°$ (vertical wire; such a case, extensively reported elsewhere, is currently referred to as rod–plane or point–plane) have been included in the set of current fingerprints at the collector. All the figures but that representing the case $\alpha = 0°$ appear discontinued by a narrow zero-current band (corresponding to the collapse of the one-dimensional representation of Fig. 1.11) orthogonally crossing the d axis for d close to the origin. In addition, the excess of dilution affecting the ion flow before impacting the collector seems responsible for the fast-vanishing perception of the lateral wire activity at the plane level. A subsidiary observation is that the remote profile cessation distinctive of the usual case of $\alpha = 0°$, thus quite deprived of resurgence, substantially corresponds to the collapse detected for $\alpha > 0°$. In the latter case, the above-mentioned Warburg profile perfectly assumes an axially symmetric character.

Consider that the originally empirical Warburg law, applied to the canonical rod–plane corona, has been accounted for analytically by assuming that the actual charge injector in the drifting region simply reduces to a point source. In fact, the actual source behaves as being suspended in isolation above the plane and centred on the conductor end. A subsidiary detail is that a non-spherical discharging pattern is associated with the suspended point injector. More precisely, provided ideally that the plane is distanced at infinity, the ionisation is restricted to a hemispherical region ahead of the rod. The saturation condition applicable to the space charge in the outer drifting region is theoretically proved to be responsible for such a feature, while the upper wire seems by no means implied. When the plane approaches the rod, irrespective of the rod–plane orientation, the originally straight ion trajectories of the dilating hemispherical cloud bend to become substantially superimposed to the Laplacian fluxlines (Deutsch hypothesis). Consistently,

(a)

(b)
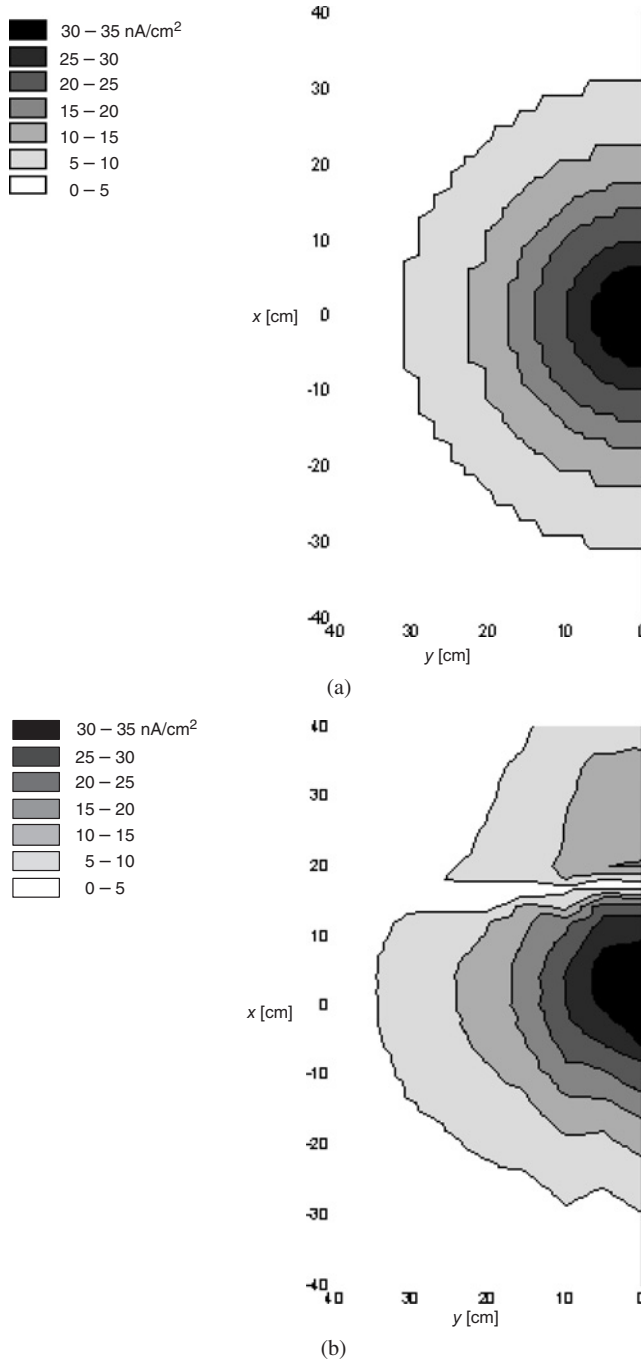
Fig. 1.12. Grey-gradated planar current fingerprints obtained at prescribed inclinations of the suspended conductor under corona (thin-wire conductor of radius $r = 1$ mm with net-truncated endpoint); inclination angle α referred to the vertical; applied voltage $V = +48$ kV. (a) $\alpha = 0°$ (vertical conductor), (b) $\alpha = 15°$ (inclined conductor) and (c) $\alpha = 90°$ (horizontal conductor).

(c)
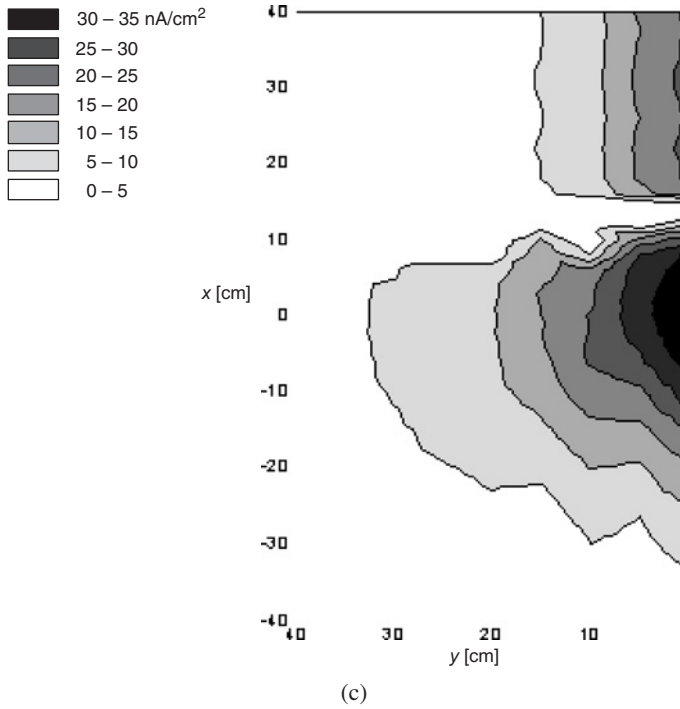
Fig. 1.12. continued.

the ionisation process and the consequent charge injection in the hemispherical region ahead of the rod are no longer isotropic, generally subject to an unspecified law. A remarkable observation is that the ionisation/injection law is prone to assume a distinctive polar law only in the rod/d axis lying plane, i.e. only for those injected charges which are destined to meet the collector along the $J(d)$ profiles (see, Fig. 1.11). Accordingly,

$$f(\xi) = \frac{j(\xi)}{j(\xi = 0)} = \cos^2 tg^{-1}\frac{|d|}{h}, \qquad (1.10)$$

where $j(\xi)$ represents the current density emitted with emission angle ξ and associated to an ion trajectory which meets the ground at the destination abscissa d ($\xi = 0°$ for $d = 0$). Therefore, even for the generic slanting-conductor case ($\alpha > 0°$) the referential direction for the injecting angle $\xi = 0°$ is vertical.

Equation 1.10 is consistent with the energy loss minimisation principle applied to the ion flow in a viscous medium. In fact, the number of ion–molecule collisions are minimised during the drifting time if $j(\xi)$ decreases as ξ increases, i.e. as the ion trajectory elongates. Amoruso and Lattarulo (2005), prove that Eq. 1.10 can be generalised and applied in conjunction with the Deutsch hypothesis to give successful reconstructions of the ionised field. In the canonical example of $\alpha = 0°$ (orthogonal rod–plane assembly), the predicted corona cessation for $\xi = 90°$ is analytically proved to be responsible

for the remote cut-off in the Warburg current density profile at the collector, a typical second-order anomaly.

In sum, the above data on the impacting ion flow's planar features offer the following substantial arguments, as far as a one-ended conductor is concerned,

- the enveloping corona activity is subdivided into two separate and easily discernible compartments, in the sense that the tip specifically behaves as a charge-injecting spot placed in isolation on the tip point, thus insensitive to the physical presence of the conductor, even if the latter is surrounded by a corona sheath;

- simple geometrical considerations, specifically involving ion trajectories impacting the ground on the periphery of the tip-originated ion flow fingerprint, lead to the discovery that their emission is orthogonal to the conductor axis, irrespective of its inclination; and

- the wire inclination makes the ion flow produced by the lateral corona activity dramatically diluted towards the ground. Such a feature is primarily indicative of a large inter-electrode drifting region at the expense of the ionisation region. In other words, the lateral corona is interpreted as being restricted to a thin glow around the cylindrical conductor.

The first observation contrasts with the predominant finding that the above two ionisation regions, one restricted to the termination of, and the other one propagated along, the thin conductor, merge or adjoin in a mutually indistinguishable manner. Rather, the latter picture is that of a one-ended conductor entirely enveloped in a questionable sole and uniform ionisation mode.

The second and third observations lead to the conclusion that the corona discharge spreads up at 180° ahead of the wire, while the corona activity along the leader can be restricted to a surrounding thin sheath. In fact, even if the voltage applied to an inclined (non-horizontal) rectilinear thin wire is large enough to promote a non-bridging strong streamer-mode corona at the endpoint (the more stressed location) the simultaneous lateral corona is essentially responsible for the second-order detection at the collector.

Appendix C

The space-charge-free electric fields surrounding a charge-supporting or current-carrying conductor, configured as a semi-infinite filament, obey a unique exact formulation which can also be applied realistically to thin conductors. The same formulation, subject to some specifications, also reported, can be adopted for corona-ionised E-fields.

C.1 Space-charge-free electrostatic solution

The geometrical notion of filamentary conductor evokes vanishing electrostatic influence and coupling. This simple and intuitive concept tacitly suggests that the charge residing

in electrostatic equilibrium along the conductor is uniformly distributed. If this is applied to an ideal conductor of zero cross section, the general procedure of imposing a zero tangential E-field for assessing the unknown charge deposition is complicated by a field singularity. Rather, recourse to the definition of partial electrostatic energy W, associated with an L long portion of an extended distribution λ_v of charge, turns out to be more fruitful. Accordingly,

$$W = \frac{1}{2} \int_L \lambda_v V \, dl \tag{1.11}$$

Bear in mind that W is subject to the minimisation principle, which ultimately makes W linearly proportional to L. Accordingly, the per unit charge λ_v is required to remain constant, throughout, since the applied voltage V also is independent of position. Therefore, assuming that a charged, corpulent electrode degenerates into a semi-infinite line with λ_v constant throughout, seems quite appropriate other than intuitively expected. Owing to the negligible coupling to nearby conductors, the discussed uniformity of the charge distribution remains undisturbed even inserting a conducting plane, regardless of the relative distance and orientation. With reference (for reasons which will be discussed in the next section) to a spherical coordinate system (r, θ, φ) centred on the filament endpoint, the electric field is only decomposed into the radial E_r and meridian E_θ field components as follows:

$$E_{s,r} = \frac{\lambda_v}{4\pi\varepsilon_o r} \tag{1.12}$$

$$E_{s,\theta} = \frac{\lambda_v}{4\pi\varepsilon_o r} \frac{1 + \cos\theta}{\sin\theta} \tag{1.13}$$

If the filament is placed above a conducting plane, Eqs. 1.12 and 1.13 require to be appropriately imaged.

C.2 Space-charge-free electrodynamic solution

If the filament is now carried by an applied step-function current $i_c(t)$, the front of which travels, say, with the velocity c of light in free space towards the endpoint (origin 0), then an expanding spherical wave is excited at the instant in which the current front attains the discontinuity point. In fact, provided that the filament is a good conductor embedded in a loss-free dielectric medium, no field is substantially detected before that instant. The optional notions of conduction-to-displacement current transition (Smyth and Smyth, 1976) and charge accumulation (Pappas, 1993), both applicable to the endpoint, can be adopted to account for the presence of an electromagnetic field (see below). An early treatment by Manneback (1923), gives an exact solution of Maxwell's partial differential equations in terms of radiating components $E_{d,\theta}$ and H_φ (the latter quantity representing the azimuthal magnetic field). Therefore, holding the spherical coordinate

system associated with Eqs. 1.12 and 1.13 unchanged, gives

$$E_{d,\theta} = -\frac{i_c(t-r/c)}{4\pi\varepsilon_o rc}\frac{1+\cos\theta}{\sin\theta} \tag{1.14}$$

$$H_\varphi = \frac{E_\theta}{\eta}, \tag{1.15}$$

where $\eta = \sqrt{(\mu_o/\varepsilon_o)}$ and μ_o stands for medium's intrinsic impedance and permeability. Consider that Eq. 1.14 is defined for angles $\theta > 0$, since setting $\theta = 0$ gives rise to a singularity. Later, the given wave description was accomplished by Schelkunoff (1952), which additionally introduced the radial quasi-static electric field

$$E_{d,r} = \frac{Q(t-r/c)}{4\pi\varepsilon_o r^2} \tag{1.16}$$

The quantity Q embodied in Eq. 1.16, equal to the time integral of $i_c(t)$ at the origin 0, substantially represents the charge which is accumulated, according to Pappas (1993) on that discontinuity up to the instant $t = r/c$. It is worth considering that the sets of Eqs. 1.14 and 1.15 and Eqs. 1.14–1.16, respectively describe a transverse electromagnetic field (TEM) and transverse magnetic field (TM) wave, both expanding with the same velocity c of the travelling step current. A TM wave substantially becomes a purely radiating TEM wave when the radial component, expressed by Eq. 1.16, reduces to a comparatively vanishing quantity (consider that Eq. 1.16 decreases faster than Eq. 1.14 as r increases).

Likewise the static case, restoring a plane causes Eq. 1.16 and the pair of formulas (Eqs. 1.14 and 1.15) to be appropriately imaged.

The linear density λ_i of the moving charge, positioned along the filament at a distance r from the endpoint, can be alternatively expressed as a function of the current or its time integral, namely by the ratios $i_c(t-r/c)/c$ or $Q(t-r/c)/r$, respectively. Accordingly, the pairs of formulas (Eqs. 1.16 and 1.14, and Eqs. 1.12 and 1.13) are proved to be similarly structured. Indeed, this is not a surprising discovery since, for a given source geometry, a static-field formula can be assumed as a basis for elaborating the corresponding – often more complex, even though this is not the case for a discontinued filament – radiative version.

C.3 E-field solution including corona

The step-function current $i_c(t)$ applied to the one-ended conducting filament could be interpreted as the current required to feed the corona activity at the terminal. Therefore, if $\vec{E}$ represents the total electric field in the drifting region (ionised field) and $\vec{E}(\lambda_v)$ the space-charge-free component, the source of which is a stationary charge distribution λ_v (superimposed to the moving quantity $\lambda_i = i_c/c$), then

$$\vec{E} = \vec{E}(\lambda_v) + \vec{E}(i_c) \tag{1.17}$$

As will be carefully proved later, the space-charge-dependent quantity $\vec{E}(i_c)$ in Eq. 1.17 can be expressed by a formula indistinguishable from Eq. 1.16, namely from the radial quasi-static component of a space-charge-free electric field. The latter can be regarded as a TM wave spherically propagating with a velocity c from the endpoint of a corona-free filament. This finding ultimately accounts for the formulation adopted in Eq. 1.17, where preference is expressed for the corona feeding current i_c carried by, instead of the space charge drifting outside, the conductor to represent the source of the space-charge field. Therefore, Eq. 1.17 evokes application of a superposition principle, according to which $\vec{E}(\lambda_v)$ and $\vec{E}(i_c)$ represent a purely electrostatic component ($i_c = 0$; applied voltage $V = V_o$, with V_o denoting endpoint-corona inception level) and a purely dynamic one ($V = 0$, applied current i_c), respectively. In sum, the above summation means that when $V > V_o$, the extra charge supplied by the current i_c to sustain the corona activity at the tip of a real wire is all injected into the drifting region, while a stationary charge, associated with V_o, is uniformly bound to the conductor with per-unit line distribution λ_v. The ionising layer (corona region), interposed between the conductor tip and the drifting space, is unimportant for the formalisation of the problem and, therefore, is deliberately neglected here. In spite of this, the geometry of the outer drifting region is assumed to continue into the ionisation one. This means that the pattern of filamentary streamers, occupying the ionisation region ahead of the conductor endpoint, is indistinguishable from that, extrapolated up to the active conductor, of the drifting ion trajectories. It is worth noticing that virtually removing the ionisation region interposed between the conductor and the drifting region and extending the latter up to the conductor surface is consistent with the superposition principle expressed by Eq. 1.17. In fact, if $\rho(t)$ and μ denote, according to the time-dependent drift equation (see, for example, Sigmond, 1978)

$$\rho(t) = \frac{\rho_o}{1 + \frac{\mu \rho_o}{\varepsilon_o} t}$$

the decreased volume charge density after the time interval t from the injection instant ($\rho(t = 0) = \rho_o$) and medium mobility, respectively, then

$$\rho(t) = \frac{\varepsilon_o}{\mu t} \tag{1.18}$$

if ρ_o tends to infinity and $t > 0$ (saturated, or space-charge dominated, condition). The above simplified formula is appropriate to the present treatment since the current density

$$j_o = \mu \rho_o E_o$$

at the surface of the active conductor must remain finite even imposing, in agreement with a current-impressed unphysical conditions ($V = 0$), $E(i_c) = E_o = 0$. Of course, simpler Eq. 1.18 could also be applied under physical conditions, provided that the strong inequality $\mu \rho_o t / \varepsilon_o \gg 1$ is verified. This condition is substantially verified in most of the drift regions of practical assemblies.

The set of corona-free Eqs. 1.14–1.16, in conjunction with Eq. 1.17, offers a rationale for predicting the drift pattern of the charge $Q(t)$ emitted at the conductor terminal.

$Q(t)$ invades the surrounding medium along the trajectories dictated by the radial quasi-static component $\vec{E}_{d,\,r}$, expressed in modulus by Eq. 1.16. Such a charge drift is insensitive to the remaining field components, namely to the purely static field $\vec{E}(\lambda_v)$ and the radiating one $\vec{E}_{d,\,\theta}$, respectively represented in modulus by the pair of Eqs. 1.12 and 1.13, and Eq. 1.14. In fact, the sources λ_v and i_c are separately assigned and the quantities involved in the exact superposition formula (Eq. 1.17) are decoupled field components. In particular, the above considerations lead to the conclusion that $\vec{E}(\lambda_v)$ is not responsible for any direct influence on the ion flow pattern. However, even overlooking such an explanation, it is easy to realise that $E_{d,\,r}$ largely exceeds $E_{d,\,\theta}$ in near-field conditions, hence in the domain close to the conductor where the space charge is concentrated. All conditions considered, $\vec{E}_{d,\,r}$ is identified with the sole field component to be associated with charge drift.

Distinctive of the saturation condition applied to a drift region is the application of Eq. 1.18 and the first-order assumption of a constant electric field equal to $E_{d,\,r}$. In fact, a physical prerequisite for a stable corona is the formation of an approximately uniform, or uniform electric field over the gap in the outer drifting region. Such a condition is promoted by the space charge injected into the drift region, where the so-called saturation condition is easily attained. Here, with special reference to the negative corona, previously injected free electrons are rapidly attached to the medium molecules to form a concentration of much more heavy, thus slow moving, negative ions. Simultaneously, the space charge causes the electric field at the surface of the emitter to remain stable, irrespective of the actual level of the applied voltage $V \geq V_0$, to a value just needed to sustain the corona activity. Such a value slightly exceeds the corona inception level E_0. A further effect, significantly contributed by the space charge in the drift region, consists in a contraction towards the emitter of the ionisation region while the field tends to become uniform along each ion trajectory. It is easy to verify that the former effect is strongly dependent on the structure assumed by the electric field in the drift region in consequence to the electrode geometry. Combining the above description to the approximate condition $\mu =$ constant assumed during the lifetime, accounts for the v invariance throughout the trajectory.

Accordingly, using Eq. 1.18 and assuming $v = \mu E_{d,\,r} =$ constant (which implies $t = r/v$) easily gives

$$\mathrm{d}Q = 4\pi r^2 \frac{\varepsilon_0 v}{\mu r}\mathrm{d}r = 4\pi r \frac{\varepsilon_0 v}{\mu}\mathrm{d}r$$

for an elementary spherical shell of radius r and thickness $\mathrm{d}r$. Therefore, the overall charge contained in the spherical cloud of radius r is

$$Q(r) = \int_0^r \mathrm{d}Q = \frac{2\pi r^2 \varepsilon_0 v}{\mu} = 2\pi r^2 \varepsilon_0 E_{d,\,r} \tag{1.19}$$

Additionally, recalling that $i_c = \mathrm{d}Q/\mathrm{d}t = v\,\mathrm{d}Q/\mathrm{d}r$ is the corona current also gives

$$E_{d,\,r}(r) = \frac{i_c}{4\pi\varepsilon_0 r v} \tag{1.20}$$

Equation 1.19, which is consistent with Gauss's theorem, persuades that the charge $Q(t)$ being emitted by the corona activity at the conductor endpoint can only spread out in the hemispherical space of radius r at the head of the conductor. It is worth considering that Eq. 1.20 is inconsistent with the postulated uniformity of $E_{d,r}$ under saturation conditions for the space charge. In fact, all the quantities embodied in Eq. 1.20 are constants but r. The fact that the non-uniform character of the field governed by Eq. 1.20 contradicts, especially for small values of r, the imposed saturation condition (for which $E_{d,r}$ is required to remain constant substantially along the ion drift trajectory), simply leads to infer that the drift region must have significantly receded from the head of the conductor, namely that the corona region, attached to the conductor, should rather expand outwards. To better appreciate such a rationale, reference could be made to the useful example of a cylindrical corona around a wire. Repeating the above approximate procedure easily gives

$$E_{d,r}(r) = \frac{i'_c}{2\pi\varepsilon_o v} = \left(\frac{i'_c}{2\pi\varepsilon_o\mu}\right)^{1/2}, \tag{1.21}$$

where i'_c represents the current loss per unit length, a constant quantity depending on the applied voltage. Therefore, in variance to Eq. 1.20, $E_{d,r}(r)$ is constant since the dependence on r disappears for a cylindrical field configuration. This implies that the ionisation region required to supply the ion flow in the outer drift region is expected to be confined to a thin sheath around the conductor. Such a qualitative prediction is consistent with experimental evidences, substantiated by more sophisticated models, showing how the low thickness under examination is restricted to a quantity independent of the applied voltage (and corona current) and rather dependent on the conductor radius (Takahashi *et al.*, 1982).

All conditions considered, it is possible to state conclusively,

- In general, a constant (or approximately) electric field in the saturated drift region can occur only farther and farther away from the emitting tip of a rod, namely where the streamer-filled glow region has been significantly dilated at the expense of the drift region; and

- In particular, an overall picture appropriate to an advancing leader is that of a cylindrical hot core, enveloped in a thin ionisation sheath, which preferentially projects elongated and vivid streamers only in a hemispherical region ahead of its endpoint. However, individual long streamers, breaking up from the glow-mode corona activity, can occur throughout the leader.

Appendix D

For individual charges, Pappas (1993) formulated a revised version of the law referred to as the cardinal law of electrodynamics by combining the original Ampere (electrodynamic) and Coulomb (electrostatic) forces. If two charges q_i ($i = 1, 2$), at a distance of r_{12} move with corresponding velocities $\vec{v}_i$, then the total force exerted, say, on q_2 obeys

the relationship

$$\vec{F}_{12} = \frac{q_1 q_2}{4\pi\varepsilon_{\mathrm{o}}} \frac{\vec{r}_{12}}{r_{12}^3} \left[1 + \frac{3}{r_{12}^2 c^2} (\vec{v}_1 \cdot \vec{r}_{12}) (\vec{v}_2 \cdot \vec{r}_{12}) - \frac{2}{c^2} \vec{v}_1 \cdot \vec{v}_2 \right] \qquad (1.22)$$

Unit in parentheses corresponds to the Coulomb force, while the remaining two terms correspond to the Ampere force. The value of the above formalisation can be appreciated if reference is made to the two pairs of simple case studies treated below. Equation 1.22 could also be expressed in terms of currents, instead of moving charges, by simply setting $q_i = I_i \, \mathrm{d}\vec{s}_i/\vec{v}_i$. The convenience of exploiting such an equality, which involves the oriented elementary length $\mathrm{d}\vec{s}_i$, will be appreciated later.

Case A (q_1 and q_2 move along parallel trajectories): $\vec{v}_1 = \vec{v}_2 = \vec{v}_s$; $\vec{v}_s \perp r_{12}$; $q_1 q_2 = |q_1 q_2|$ (charges of same sign). Accordingly, Eq. 1.22 reduces to

$$\vec{F}_{12} = \frac{|q_1 q_2|}{4\pi\varepsilon_{\mathrm{o}}} \frac{\vec{r}_{12}}{r_{12}^3} \left(1 - 2\frac{v_s^2}{c^2} \right) \qquad (1.23)$$

Case B (q_1 and q_2 move along collinear trajectories): $\vec{v}_1 = \vec{v}_2 = \vec{v}_s$; $\vec{v}_s /\!/ r_{12}$; $q_1 q_2 = |q_1 q_2|$. Now,

$$\vec{F}_{12} = \frac{|q_1 q_2|}{4\pi\varepsilon_{\mathrm{o}}} \frac{\vec{r}_{12}}{r_{12}^3} \left(1 + \frac{v_s^2}{c^2} \right) \qquad (1.24)$$

Equation 1.23 means that the two charges of the same sign at a distance, moving in parallel with same velocity and orientation, experience repulsive (positive) forces if $v_s < c\sqrt{2}$ and attractive (negative) forces if $v_s > c/\sqrt{2}$. Instead, Eq. 1.24 means that if the above charges move aligned, they always experience repulsive forces. The two simple cases described can be applied to a unipolar flow of charges in a discharging channel (for instance, a downward coming leader).

Consider now the example of a pair of oppositely directed moving charges which are also opposite in sign. Accordingly, setting now $\vec{v}_1 = -\vec{v}_2 = \vec{v}_s$ and $q_1 q_2 = -|q_1 q_2|$, gives

$$\vec{F}_{12} = -\frac{|q_1 q_2|}{4\pi\varepsilon_{\mathrm{o}}} \frac{\vec{r}_{12}}{r_{12}^3} \left(1 + 2\frac{v_s^2}{c^2} \right) \qquad (1.25)$$

$$\vec{F}_{12} = -\frac{|q_1 q_2|}{4\pi\varepsilon_{\mathrm{o}}} \frac{\vec{r}_{12}}{r_{12}^3} \left(1 - \frac{v_s^2}{c^2} \right) \qquad (1.26)$$

Equations 1.25 and 1.26 are easily obtained after imposing, likewise the above case studies A and B, $\vec{v}_s \perp r_{12}$ and $\vec{v}_s /\!/ r_{12}$, respectively. Even though similarly structured, the pairs of corresponding Eqs. 1.23 and 1.25, and Eqs. 1.24 and 1.26 differ, in particular, owing to the signs of the respective second members in parentheses. The signs under the result interchange, which implies that the forces represented by Eqs. 1.25 and 1.26

are always attractive (negative) since $v_s \leq c$. Specifically, if v_s approaches c then the transverse force represented by Eq. 1.25 triplicates with respect to the prediction made by involving the Coulombian component only, while the longitudinal one, represented by Eq. 1.26, vanishes. It is worth considering that Eqs. 1.25 and 1.26 are practically pertaining to the circumstance of a connecting leader launched from the striking point of an earthed object towards a down coming stepped leader. In fact, the currents I_1 and I_2 relative to two leaders involved in the attachment process are associated with charged counterparts which move with opposite velocities of comparable (here, assumed to be perfectly equal) values.

Specifically,

$$\vec{F}_{12} = -\frac{I_1 I_2}{4\pi\varepsilon_o} \frac{ds_1 ds_2}{v_1 v_2} \frac{\vec{r}_{12}}{r_{12}^3} \left(1 + 2\frac{v_1 v_2}{c^2}\right) \tag{1.27}$$

$$\vec{F}_{12} = -\frac{I_1 I_2}{4\pi\varepsilon_o -} \frac{ds_1 ds_2}{v_1 v_2} \frac{\vec{r}_{12}}{r_{12}^3} \left(1 - \frac{v_1 v_2}{c^2}\right) \tag{1.28}$$

represent the optional current-dependent formulation of Eqs. 1.25 and 1.26 in the more general case of $v_1 \neq v_2$. The above pair of formulas seem useful with reference to the case of a descending leader (the related quantities are subscripted with notation 1) in proximity to a current-carrying metallic conductor (notation 2). This could be the practical case in which element 2 is a down conductor or guy wire connected to an unspecified and unsuccessful upper air termination (at the opposite end, the connection to an earth termination system is tacitly understood). Accordingly, $v_1 = c$ and v_2 less than c of several orders of magnitudes are realistic assumptions now ($c/v_2 \gg 1$ derived from applying the current continuity principle to the serial connection between a leader behaving as a pseudo-conductor and a metallic wire). Therefore, Eqs. 1.27 and 1.28 become substantially identical since the second term (electrodynamic contribution) in parenthesis is negligible, in both the cases, in comparison to unity (Coulombian contribution). Therefore, irrespective of the reciprocal geometrical orientations, when one element of the pair directly involved in the attachment process is a metallic conductor, the force is always attractive (of Coulombian nature). With special application to the practical case of a down conductor parallel to a descending leader, such a force is largely greater than the composite (Coulombian–Amperian) force experienced in the two-leader case. In fact, distinctive of the former and latter cases are the assumptions $v_1/v_2 = c/v_2 \gg 1$ and $v_1/v_2 = 1$, respectively, while the order of magnitude of the product $I_1 I_2$ remains practically unchanged in both the cases discussed (the set of down conductors are carried by comparable currents which altogether feed the leader(s) launched upward from the upper air terminal).

electrostatics and a critique to some protection systems", IEEE Power Tech. 2003, Bologna, Copyright 2003, with permission from IEEE.

References

Amoruso V., Lattarulo F., "Thundercloud pre-stroke electrostatic modeling", J. Electrostatics, **56** (2002) 255.

Amoruso V., Lattarulo F., "Lightning precursory electrostatics and a critique to some protection systems", IEEE Power Tech., Bologna, 2003.

Amoruso V., Lattarulo F., "Deutsch hypothesis revisited", J. Electrostatics, **63** (2005) 717.

Berta I., "Static control", J. Electrostatics, **63** (2005) 679.

Carpenter B.R., Drabkin M.M., "Protection against direct lightning strokes by charge transfer systems", IEEE 1999 Int. Symp. on Electromagnetic Compatibility, Seattle, 1999.

Chowdhuri P., *Electromagnetic transients in power systems*, John Wiley, New York, 1996.

Cooray V., "The mechanism of the lightning flash", in *The lightning flash*, V. Cooray Ed., IEE Power & Energy Series 34, London, 2003.

D'Alessandro P., Gumley J.R., "A 'Collection volume method' for the placement of air terminals for the protection of structures against lightning", J. Electrostatics, **50** (2000) 279.

Durand E., *Electrostatique* (Les distributions – Vol. 1), Masson, Paris, 1964.

Ette A.I.I., Aina J.I., Utah E.V., "Point discharge characteristics and charge configuration in thunderclouds", in *Electrical processes in atmospheres*, H. Dolezalek and R. Reiter Eds., Steinkopff, Darmstadt, 1977.

Horvát T., "Standardization of lightning protection based on the physics or on the tradition"? J. Electrostatics, **60** (2004) 265.

Ianoz M., "Lightning and EMC", in *The lightning flash*, V. Cooray Ed., IEE Power & Energy Series 34, London, 2003.

Le Boulch M., Hamelin, J., Weidman C., "UHV-VHF radiation from lightning", in *Lightning electromagnetics*, G. Gardner Ed., Hemisphere, New York, 1990.

Manneback C., "Radiation from transmission lines", AIEE J., **42** (1923) 95.

Mazzetti C., "Principles of protection of structures against lightning", V. Cooray Ed., IEE Power & Energy Series 34, London, 2003.

Moreau J.P, Rustan P.L., "A study of lightning initiation based on VHF radiation, in *Lightning electromagnetics*, G. Gardner Ed., Hemisphere, New York, 1990.

Pappas P.T., "Electrodynamics from Ampere to now: future perspective", in *Essays on the formal aspects of electromagnetic theory*, A. Lakhtakia Ed., World Scientific, Singapore, 1993.

Rakov V.A., Uman M., *Lightning. Physics and effects*, Cambridge University Press, Cambridge, 2003.

Rust W.D., Moore C.B., "Electrical conditions near the bases of thunderclouds in the Southwestern United States", in *Electrical processes in atmospheres*, H. Dolezalek and R. Reiter Eds., Steinkopff, Darmstadt, 1977.

Schelkunoff S.A., *Advanced antenna theory*, John Wiley, New York, 1952.

Sigmond R.S., "Corona discharges", in *Electrical breakdown of gases*, J.M. Meek and J.D. Craggs Eds., John Wiley, New York, 1978.

Smyth J.B., Smyth D.C., "Lightning and its radio emission", Radio Sci., **11** (1976) 977.

Takahashi Y., Yoshida M., Anma Y., Kobayashi S., Endo M., "Thickness and luminosity distribution of positive corona sheath in air", J. Phys. D: Appl. Phys., **21** (1982) 639.

van Bladel J., *Singular electromagnetic fields and sources*, IEEE Press, New York, 1991.

Williams E., "Charge structure and geographical variation of thunderclouds", in *The lightning flash*, V. Cooray Ed., IEE Power & Energy Series 34, London, 2003.

This page intentionally left blank

CHAPTER 2

A Reasoned Approach to Lightning Electromagnetics and Coupling to Nearby Power Transmission Lines

V. Amoruso and F. Lattarulo

Abstract

The prerequisite for a reliable evaluation of the induced effects on transmission and distribution lines exposed to lightning originated electromagnetic fields substantially consists in reconstructing the source from available LEMP databases. The current difficulty in finding a discharge model by proper methods to inverse source problems of electromagnetics should prudently invite to rather make use of reasonably simple but rigorous formulations in substitution of over sophisticated arbitrary models. As will be appreciated with application to the present difficult subject, often overlooked basic properties of rigorous basic models can successfully promote subsequent improvements and interpretation of the simulated physical mechanisms. In fact, the method adopted has permitted the subsidiary roles actually played by the earth and thundercloud in the overall discharge to be better understood. The approach recommended in this chapter also gives coupling results affected by errors comparable to and, paradoxically, less than those derived from currently available more complex models.

2.1 Introduction

A variety of present-day reasons (a selection of which are summarised below) could explain the renewed interest on the lightning phenomenon and its related effects:

- Even though the physics of lightning has never changed, a large debate on the progressive tropicalisation of the climate in some regions is currently underway (for example, this seems to occur in the European nations facing the Mediterranean

basin), a phenomenon which is showing significant changes in the currently available thunderstorm maps and lightning statistics from earlier studies;

- The growing number of exposed structures and systems and their non-uniform territorial distribution is making the application of security criteria increasingly pressing and a diversified problem;

- With special reference to household and office appliances connected to distribution and communication lines, there is an increasing social need for a careful outlining of the notions of risk perception and safety; and

- The miniaturisation of electronic components and optimisation of the insulating compartment of power systems concur in significantly increasing the sensitivity and vulnerability to the lightning originated electromagnetic impact.

The large amount of up-to-date experimental data and models (see, for example, the review books or selected collections of articles (Gardner, 1990; Cooray *et al.*, 2004; Cooray, 2003; Rakov and Uman, 2003) to which the present chapter will refer extensively) allows an insight into such an attractive and important subject. On the other hand, the required "balance of evidences" prior to standardisation (especially addressed here to protection/mitigation criteria and devices), seems still in progress (see, for example, Plumer, 1995; Horvát, 2004). Lightning can be substantially considered as an unstable product of little understood electrification processes, which develops inside a thundercloud or banks of thunderclouds. Therefore, the incidental, capricious and unreproducible nature of such a phenomenon makes the interpretation more speculative, and thus the currently available models are questionable. Typically, available referential data are sets of recorded oscillograms arranged in the form of excitation-field components whose detection at a distance from the discharging channel is approximately known. This is the usual representation of a lightning electromagnetic pulse (LEMP) which, unfortunately, can no longer be considered as a proper benchmark to substantiate the reliability of electromagnetic models of lightning. As will be proved later, impressive reproductions of experimental oscillograms can be derived from different, and sometimes conflicting, models owing to the large number of variables and assumptions invariably introduced and combined successfully. Such an unreliable practice applied to the fitting process seems to be responsible for

- the significant degree of uncertainty in applying some notions of plasma physics to lightning; and

- the lack of rigorous correlation between experimental databases, generally available in the form of field oscillograms, recorder–source distance, channel-base currents and optical observations.

Even though the excitation field and related coupling still require to be exhaustively described by a definite treatment, recourse to unsophisticated but exact source formulations, which can discourage the introduction of arbitrary assumptions, still turns out to be a recommended practice. This chapter is concerned with the evaluation of the lightning phenomenon by an engineering approach (in which the discharge current at the channel base is assigned), the induced effects on an overhead line positioned in critical proximity to a return-stroke channel. The method adopted is based on an elsewhere

underestimated but reliable analysis which, in conjunction with sustainable physical assumptions, assists in recognising those field components of the electromagnetic environment actually behaving as a threat (Amoruso and Lattarulo, 2003). Such field components are expressed by simple time-dependent relationships which also contribute in making the evaluation of the induced effects analytically amenable. The reduced computational effort required and the intelligible character of the formulas involved turn out to be important prerequisites for technical applications. In general, the design of devices and systems directly or indirectly involved in lightning effects can be successfully developed if the limitations of the model at hand are taken into consideration, especially those posed by a restricted knowledge of the physical mechanisms responsible for the genesis and performance of the interfering field. The proposed analysis is thus recommended for disregarding substantially the unproved assumptions and conjectures which could seriously compromise its reliability.

The additional difficulty in using uncorrelated experimental data for validation of the theory seems only partially overcome using artificially triggered lightning. In fact, the given response, in terms of LEMP and induced effects on victims, could depart from the lightning produced during natural events. As will be appreciated at the end of this chapter, the model under examination gives additional arguments for discussing the similarities claimed between natural and triggered flashes. All conditions considered, preference is expressed here for a validation criterion rather based on average quantities and essential waveshape features as referential data. The canonical example of coupling to a nearby line will be considered even for further sustaining the value of the preliminary LEMP model. Incidentally, the restricted spectral components associated with a lightning event, combined with the condition of channel–victim proximity, could at once explain the significant amount of quasi-static component typically detected in the surrounding LEMP. Indeed, contrary to the dominant opinion, the quasi-static source will be substantially identified in the discharging thundercloud, in the sense that the ground channel is proved to contribute slightly to the quasi-static field. The suspended large source represented by the N region of a thundercloud becomes electrodynamically active only when the ascending return stroke attains and neutralises some of the variously distributed or concentrated charge locations, generally of those which form peripheral layers or inner clusters of pockets. Additionally, the quasi-static field vanishes faster with distance than that of the simultaneous radiation from the ground channel and usually presents a reduced electric-field component tangential to the line. Overall, the quasi-static electric field results appear comparatively little involved in the coupling mechanism throughout the nearby line (the latter is so much extended as being only partially lying just below the discharging cloud cell). Therefore, the excitation field strictly connected to the interfering mechanism seems to be the only radiating component, even in close proximity to the channel. In other words, provided that the victim is along a horizontal line, there are no reasons that lead to accomplish the coupling model by introducing an uninfluential quasi-static component, regardless of its important role in shaping a nearby LEMP. However, the cloud-originated quasi-static field will be taken into account for showing how a fairly good LEMP reproduction can be obtained. Unfortunately, involving the cloud source results in the introduction of some arbitrary parameters which makes the given LEMP reproduction as questionable as that of the ones provided by previous models.

2.2 Remarks on the Pre-Stroke and Stroke-in-Progress Phases

2.2.1 Corona activity

In general, under unipolar corona, the ionisation sheath of the outside radius r_c, surrounding a conductor of radius r_o presents a thickness $r_c - r_o$ which is of the same order of magnitude as r_o (Takahashi *et al.*, 1982; Jones *et al.*, 1988). The sheath in question is interposed between the conductor and the large drifting region filling the inter-electrode space. The above property has been proved irrespective of the applied voltage and rather proportional to a restricted power of r_o. After Takahashi *et al.* (1982), the empirical formula

$$r_c - r_o = kr_o^n \tag{2.1}$$

can be applied to the glow corona. Here, the radii are expressed in millimetres, while k and n are dimensionless coefficients, respectively close to 1.6 and 0.7 (as confirmed by different investigators). Owing to the restricted values given by Eq. 2.1, a usual assumption adopted for space-charge field computations is that of neglecting the thin ionisation region and interpreting the active conductor as an injector of charge directly into the drifting domain (Maruvada, 2000). Equation 2.1 provides a radius r_c larger than but of the same order as r_o, so that a filamentary representation of the whole discharging channel under corona is appropriate, irrespective of the current intensity. In fact, the hot core of a stepped leader can be considered as a pseudo-conductor having a radius of a few millimetres. In a qualitative sense, Eq. 2.1 could be explained by considering that the electric field of the space charges injected into the drifting region reduces the mean electric field in the ionisation region and tend to stabilise the corona current for a given gap voltage. As the latter increases, the current increases according to the quadratic law, in such a way that the increased space charge in the drift region makes the average electric field and radial extension of the ionisation region substantially unchanged. This implies that the ionising activity, which assumed a narrow filament glow-type character just above the inception conditions, tends to remain unaltered even if the applied voltage increases. In the latter case, however, broad filaments may break out somewhere from the compact corona glow. The only detectable phenomenon almost in direct proportion to the corona current consists of a diffuse brightness which envelopes the thin ionised region (Takahashi *et al.*, 1982).

Instead, the magnitude usually proposed in the treatment of the ionised channel co-axial to the hot core of a stepped leader is of the order of several metres at least. The stable narrow filament glow-corona mode is assumed to be replaced by a compact streamer-corona mode, which is in contrast to Eq. 2.1. The questionable corona structure is assumed to be subject to a radial expansion until the electric field boundary is equal to that of the electric field breakdown in air. This equality may be attained at distances of several metres from the core axis only in the unrealistic condition of neglecting the explained stabilising function, which is especially exerted by the concentrated heavy space charges in the outer drift region. Unfortunately, the dispute on the corona structure cannot be resolved by reliable optical records owing to the confounding presence of the radially extended halo mentioned earlier. Even the broad filament structure recorded in laboratory during the voltage-chopping technique (Waters, 1978) cannot be claimed as

an evidence of the radial extension of the corona activity prior to the sudden removal of voltage. In fact, the highly luminous, fast time-varying neutralisation process is assumed to cross the ionisation sheath and significantly penetrate the large drift region, thus also involving the space charge accumulated in the gap during the leader growth. Additionally, laboratory tests on long spark gaps sustain the postulated short cross-sectional dimensions of lightning-precursory leader channels, i.e. their slender and tortuous aspect owing to the lateral narrow-filament glow corona. Even the simultaneous broad filament structure of the streamers, substantially concentrated at the head of the hot core, is methodically reproduced throughout the pre-stroke phase.

Even though unstable and vivid long streamers can incidentally break up from the stable thin glow along the hot core (under further favourable conditions, streamer-to-arc transitions can occur where the leader branches), responsible for a compact production of penetrating streamers only at the leader head seems to be the conductor geometry, irrespective of the corona current. In fact, during the filamentary elongation of the elemental streamers (hence, before the corona stabilisation), the field distribution law in the space domain at the head of the leader differs from that around the lateral surface. Substantiating such a geometrical property by simple theoretical models turns out to be an impracticable exercise. However, such a difficulty has been circumvented by adopting the qualitative approach as explained in Chapter 1, Appendix C, Subsection C.3 "E-field solution including corona".

Therefore, there are convincing arguments to support the filamentary nature of a leader channel and related return stroke. As will be appreciated later, such a model is important for appropriately explaining the apparent velocity assumed by the head of a return stroke, generally advancing upwards along the leader channel.

Returning now to the pre-stroke phase, it is worth bearing in mind that the electrostatic performances of a leader, realistically intended as a linear distribution of charge, is substantially indistinguishable from that of a filamentary conductor. Distinctive of a conductor of negligible surface is the as much negligible electrostatic influence with nearby conductors or between different parts of the same filament if it assumes a non-rectilinear configuration. This property accounts for the undisturbed uniformity permitted for the linear charge distribution throughout. Therefore, even the descending leader can be approximately represented by a constant line distribution having λ_v charge per unit length, irrespective of its actual distance from the earth plane. If the charge-bearing filament is however assumed upright and just above a conducting plane, and if reference is made (for reasons which will be appreciated later) to a spherical coordinate system (r, θ, φ) linked up with the filament endpoint, see Fig. 2.1, the resulting electric field $E_{s,\theta}$ becomes

$$E_{s,\theta} = \frac{\lambda_v}{2\pi\varepsilon_o r} \frac{1+\cos\theta}{\sin\theta}, \tag{2.2}$$

where ε_o denotes the free space permittivity applied to the filling medium. It is worth considering that Eq. 2.2 represents the imaged version of a pair of formulas describing the electrostatic field surrounding a one-ended straight distribution of charge in isolation (Durand, 1964). Equation 2.2 clearly shows that the field pattern is
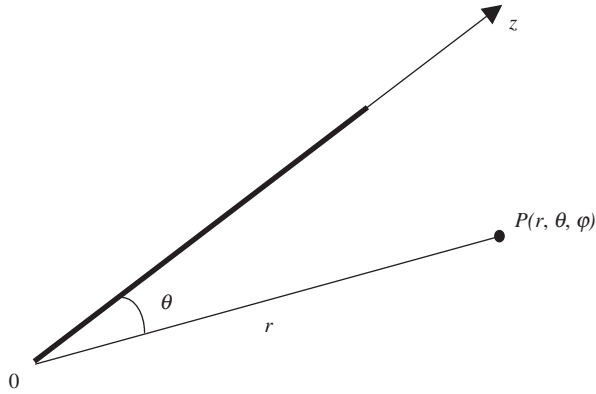
Fig. 2.1. Filamentary representation of a one-ended conductor.

circular – a degenerated case of a general elliptic pattern – since the gap of the orthogonal line-plane geometry vanishes. The above formula will be taken into account later as a subsidiary element of discussion on the electrodynamic field produced when a return-stroke rises upwards.

2.2.2 Surge current velocity

Let us assume that during a return-stroke phase, the discharging current especially carries the central arc of radius r_o along a pre-ionised upright channel of overall radius r_c. If the linear variable z runs along a reference axis centred on the channel, having origin on its foot-end, then

$$L_a(z) = \frac{\mu_o}{2\pi} \ln \frac{2z}{r_o}$$
$$C_a(z) = \frac{\lambda(z)}{V} = \frac{2\pi\varepsilon_o}{\ln(2z/r_c)} \quad (2.3)$$

According to the transmission line representation, L_a and C_a express the per unit length inductance and capacitance, respectively, of the discharging channel; μ_o is the permeability of the same medium; V and $\lambda(z)$ denote initial charge voltage of and linear charge distribution lowered by the leader.

Therefore, rearranging the set of Eq. 2.3 invariably gives

$$v = \frac{1}{\sqrt{L_a C_a}} \cong c \quad (2.4)$$

In fact, the radii r_c and r_a, mutually not too different according to Eq. 2.1, enter logarithmically in Eq. 2.3. It is clear that allowing the surge current velocity v to decrease

from the velocity c of light in free space at the return-stroke onset to, say, $c/3$ as z increases, i.e. as the front of the discharging current propagates along the lower visible segment of the pre-ionised channel, means that r_c is required to become unrealistically large. Therefore, the only reasonable effect seemingly responsible for a substantial reduction of v is the minute tortuosity, superimposed to the ostensive meandering path of a ground channel (Cvetić *et al.*, 1999a), often masked by the surrounding halo. A common high-voltage technique which makes the described second-order serpentine perceivable by suitable optical devices consists in inserting in the discharge circuit a large serial resistance which reduces the arc current. By keeping the applied voltage unchanged, the jagged arc again becomes submerged by a surrounding corpulent halo if the resistance is removed and, therefore, the arc current increases. Such a laboratory artifice accounts for the expected zig-zag movement of a return-stroke in its halo, so that correlating the actual propagation time, practically related to the velocity c in agreement with Eq. 2.4, to the apparently shortened longitudinal extension of the visible discharge, causes v to be significantly, but only apparently, reduced. Of course, v should virtually be decreased further if the visible tortuosity and slanting disposition of the channel is similarly taken into account when an upright model is adopted. The propagation velocity detected needs a supplementary correction, as recommended by Cvetić *et al.* (1999b) owing to the observer's retardation in estimating the actual height attained by the upper end of the ascending return-stroke.

2.2.3 Earth performances

With special reference to nearby victims, it is assumed that a significant increase of soil conductivity, with respect to standard conditions (Keller and Frischknecht, 1966), can accompany a lightning event. This is merely because lightning-struck regions are exposed to heavy rainfalls. Therefore, the ground portion surrounding the striking point requires to be appropriately examined by taking into account the influence of meteoric water. In general, basic electric and dielectric models of aqueous mixtures (Keller and Frischknecht, 1966; Fuller and Ward, 1970), in conjunction with ad hoc empirical Archie's law, turn out to be valid references to appreciate the key role that the water content plays with respect to fractional amount, salinity acquired and permeation pattern. Abundant meteoric water can provisionally cause conductivity enhancement on the earth's surface and at shallow depths. In spite of this restriction, simultaneous electrostatic conditions, involving the influence of the charged thundercloud, allow the investigation to be appropriately concentrated only to the wet thin layer (instead of being extended throughout the lower half-space). In fact, the N region of a thundercloud cell is generally charged up to several tens of coulombs, a quantity far exceeding (of at least one order of magnitude) the amount of charge actually neutralised by a return stroke. Therefore, the electrostatic attraction exerted by the upper N region on the terrestrial counterpart, distributed over the ground surface, can only be subject to moderate decrease during the dynamic phase. This implies that the flow of positive charge, initially deposited in static equilibrium on the outer wet surface of the soil, and partially transferred by contact to the outermost free-water layer, holds rather flush with the plane even during the dynamic phase. In other words, the terrestrial charges, previously surrounding the striking point are then abruptly drained and concentrated towards the channel base at the return-stroke onset, are forced to flow along radial trajectories confined to the soil surface, exactly

where the conducting properties are provisionally enhanced by rainfall. Just below the striking point, a globular ionisation, often accomplished by vivid streamers, takes place under normal soil conditions. Instead, direct inspections on struck earthings, the upper soil–air interface which was simultaneously exposed to rainfall, often permit clear recognition of tracking, as if the buried electrode were bridged by the more conducting upper layer. The substantial result of the above description, involving the electrostatic influence of the cloud is that irrespective of the minute differences in the standard bulk properties of the soil region surrounding a striking point, the provisionally enhanced conductivity of the outer layer is crucial in determining the actual conducting route. Under the circumstances described, the conductivity in question is estimated to be of the order of 10^{-2} S/m and above, a quantity accounting for the practical replacement, in the model, of the lossy lower half-space by a perfectly conducting surface. For an exhaustive appreciation of the above approximation, see, for example, Nucci *et al.* (1988), where the influence of the finite conductivity assigned to the soil on the voltage induced on a line is compared with the case of a perfectly conducting plane.

For the reader's convenience, we can now arrange a reasonable compilation of assumptions, drawn from the present and previous sub-sections, especially useful for engineering applications. In sum, we can safely state that:

(a) the complex meandering geometry of the channel may be neglected, for an approximate calculation, provided that the true propagation velocity of the discharge current, close to that of light in free space, is virtually replaced with a reduced equivalent quantity. Using a certain amount of expertise in examining optical and LEMP databases leads to ascertain that the average velocity, indicative of the physical one, should be approximately reduced to 1/3 if preference is expressed for the canonically straight model of channel;

(b) the return-stroke arc and the surrounding corona sheath present comparable, hence both negligible, cross-sectional dimensions. Such a physical condition is suggestive of a corona-free current-carrying filamentary antenna as an appropriate electromagnetic descriptor;

(c) owing to the electrostatic attraction exerted by the thundercloud, the ground portion involved in the dynamic phase is restricted to the outer wet layer which, therefore, substantially behaves as a perfect conductor.

2.3 Antenna Model

For an approximate calculation of the excitation field, assigning a priori the space–time current distribution law, which is an unknown one, represents a typical antenna-theory problem. Let us assume that an inherently approximate integral formulation, involving non-homogeneous Maxwell's equations, somehow allows the current distribution to be correctly evaluated and then assigned for the supplementary field calculation. The latter can be performed by the usual partitioning-based approach involving elementary current dipoles. Let us also assume that analytically tractable boundary conditions exist for a direct and inherently exact solution of homogeneous Maxwell's equations by the method of variable separation. Both approaches must, in principle, give identical results, which

imply that an integral formulation turns out to be a legitimate numerical method for general applications (see Appendix A). Indeed, two prudent considerations need to be mentioned here, the first of which merely states the fact that the above identity is, rigorously speaking, never attained, even by adopting an advanced integral formulation-based technique (see, for example, the prominent critique by Schelkunoff, 1952). In fact, a certain degree of uncertainty, accompanying the introduction of required arbitrary assumptions, is distinctive of the numerical method in question. Such a drawback is, in practice, circumvented by a favourable property manifested by integral formulation-based techniques when application is made to thin-wire antennas: the field calculation performed by a line integral gives a radiation pattern invariably affected by second-order errors, along with the current distributions affected by first-order errors (Schelkunoff and Friis, 1952; Uman and Krider, 1982).

Instead, a second underestimated consideration urges to claim that the given current to be ideally impressed to a long conductor is a transient one. As will be appreciated later, one can run the risk of inappropriately performing the line integral for the field calculation when current dipoles representing elemental field sources are typically used. Such a drawback is distinctive of LEMP investigations, in which case the field is excited by a surge of current travelling down a tall channel (the top of which is positioned at a height of the order of a few kilometres). The computational failure mentioned can be avoided by using an exact analytical solution which is devoid of source decomposition and, hence, is expressed by simpler time-dependent formulas. The additional merit ascribed to such an alternative model is that of promoting a correct interpretation of the physical mechanisms under investigation.

Therefore, bearing in mind the above-listed observations (a) and (b) and provisionally

- neglecting the finite length of the channel;
- removing the plane; and
- adopting an engineering approach based on impressing an assigned current to a one-ended straight filament representing the conducting channel,

lead to an oversimplified but surprisingly useful filamentary model of a return stroke, shown in Fig. 2.1. Location of the observation point P, at a distance is determined by a spherical coordinate system (r, θ, φ) centred on the terminal O of the one-ended conductor. Here, a surge current of unspecified waveshape $i(t, z = 0)$ is produced. According to the transmission line model, the positive current which travels with velocity v along the z axis represents the progressive neutralisation of the pre-charged negative channel.

Before introducing the resolving formulas, the associated boundary-value problem posed by the geometry of filament needs to be discussed. The notion of conducting filament can be derived from the degeneration of a conical conductor with apex on O, in which case $\theta = 0$ denotes the bounding surface of such an entity. However, the latter also evokes a degenerated cylinder since the above notion indifferently applies to originally conical or originally cylindrical configurations when both degenerate into a line. If preference is expressed for interpreting the filament as a degenerated cone, an exact solution of

Maxwell's partial differential equations is rigorously permissible. Specifically, they are separable into a set of ordinary differential equations which can be arranged as follows:

$$\frac{\partial}{\partial \theta}\left(\sin\theta\, H_\varphi\right) = s\varepsilon r\, E_r \sin\theta$$

$$\frac{\partial}{\partial r}\left(r H_\varphi\right) = -s\varepsilon r\, E_\theta \tag{2.5}$$

$$\frac{\partial}{\partial r}\left(r E_\theta\right) = -s\mu r\, H_\varphi,$$

where Laplace-transform representation of variable s is used. The field components involved E_r, E_θ and H_φ, respectively denote radial electric field, meridian electric field and azimuthal magnetic field. Note that the prerequisite for the model velocity v to be less than c can be attained by replacing the pair of physical parameters μ_o and ε_o with unspecified corresponding virtual quantities μ and ε satisfying the condition $v = (\varepsilon\mu)^{-1/2} < c$. The set of equations (Eq. 2.5) represents a homogeneous formulation for a spherical TM wave which permits the following exact solution for E_r, E_θ and E_φ when the field point is positioned outside the filament (Schelkunoff, 1952; Smyth and Smyth, 1976).

$$E_r = \frac{I(s, z = 0)}{4\pi\varepsilon s r^2}\mathrm{e}^{-sr/v} \tag{2.6}$$

$$E_\theta = -\eta\frac{I(s, z = 0)}{4\pi r}\frac{1 + \cos\theta}{\sin\theta}\mathrm{e}^{-sr/v} \tag{2.7}$$

$$H_\varphi = \frac{E_\theta}{\eta} \tag{2.8}$$

Here, $I(s, z = 0)$ and $\eta = (\mu/\varepsilon)^{1/2}$ denote Laplace transform of the current applied and intrinsic impedance of the medium surrounding the channel model, respectively. According to the earlier discussion on the pair of degeneration cases leading to a common ideal line, application of Eqs. 2.6–2.8 can be extended to the practical example of a cylindrical thin-wire, especially if P is somewhat distanced from the wire surface.

The solution for the radiation component, represented by the pair of quantities E_θ and H_φ (see above Eqs. 2.7 and 2.8, respectively), was initially given by Manneback (1923). Later, Schelkunoff (1952) reconsidered the subject with the intention of introducing the quasi-static component E_r, see Eq. 2.6, which provides the solution. As a whole, the structures of the above equations, applied to a one-ended current-carrying rectilinear filament (provisionally considered as a perfect conductor), lead to the finding that

    (d) the surrounding electromagnetic field is a TM spherical wave that originates at the filament end where the current is impressed;

    (e) the fronts of the surge current (source) and spherical wave (excitation field) propagate simultaneously with the same velocity v in contiguous and complementary compartments of the total domain, respectively occupied by the filamentary source (formally bounded by the surface $\theta = 0$) and the outer medium (where $\theta > 0$).

In a realistic thin-wire representation, the former front travels along (thus inside) a straight conductor, the latter one expands outwards already assuming a definitive spherical configuration at some unspecified short distance from the conductor surface.

Let us assume now, according to observation (c), that the rectilinear filament is connected to a perfectly conducting orthogonal plane. The current-carrying filament is now fed by a planar and radial conduction flow concentrating at the plane–filament junction (in the previous isolation case, the feeding current was a displacement one which, from infinity, flowed in a spherical pattern towards the terminal O). The surrounding field can be evaluated by using the mirror image of the current-fed filament in substitution of the plane. The final result is that Eq. 2.6 vanishes and Eq. 2.7 is doubled, i.e. the inherently quasi-static radial component E_r disappears and the inherently radiating components E_θ and H_φ form a twice as intense TEM spherical wave. Therefore, Eqs. 2.7–2.8 are to be replaced with

$$E_\theta = -\eta \frac{I(s, z = 0)}{2\pi r} \frac{1 + \cos\theta}{\sin\theta} \mathrm{e}^{-sr/v} \tag{2.9}$$

$$H_\varphi = \frac{E_\theta}{\eta} \tag{2.10}$$

Accordingly, the above compilation of observations could be accomplished by the following:

(f) After neglecting the finite conducting properties of the current route and the finite height of the channel, the surrounding LEMP component contributed by an upright channel is completely described by a TEM spherical wave centred on its base; the wavefront propagates outwards or inwards, if the current is positive or negative, respectively, with the same velocity v of the upwardly directed return-stroke elongation.

2.4 Discussion

With respect to observation (d), the displacement-to-conduction current transition at the feeding point of an isolated and rectilinear filament causes the generation and propagation of a spherical TM wave on that end location. No supplementary electromagnetic energy can escape outwards from the travelled segment of the entire filament if the latter is a perfect conductor. The above considerations slightly change if the ideal conductor, having negligible cross section and infinite conductivity, is replaced, say, by a resistive thin wire embedded in a gaseous medium having good insulating properties. It has also been proved that the above performances also apply to bent conductors, provided that the curvature radii are significantly larger than the cross-sectional one. Restoring the plane causes the original TM wave to become a TEM one which means that the quasi-static component of the former field, represented by the radial electric field disappears. It is worth considering that the TEM spherical wave generated at the point of junction of the filament with the orthogonal plane exactly represents the excitation mode associated with the sharp plane-to-filament transition of the discharging current. Additional point

radiators can be disseminated along a tortuous filament with respect to sharp directional changes. However, applying Eqs. 2.6–2.8 to such cases appropriately (see Smyth and Smyth, 1976 for details) leads to the finding that the electromagnetic energy actually escaped at each directional transition is deprived of the quasi-static component. In addition, the resulting radiation energy significantly reduces if the single V-shaped elements composing the zig-zag arrangement are short and the V-apex angles are rather obtuse. The former geometrical condition is especially applicable to the invisible (owing to the enveloping luminous sheath of the channel) second-order tortuosity. However, using an equivalent, perfectly vertical channel model, in which case even the visible first-order tortuosity is omitted, only accounts for the disappearance of minor fine structures in the true LEMP oscillograms. Rather, important structures evoke channel branching, a circumstance which is distinctive of first return-strokes.

A simplified model with an equivalent velocity v (see observation (a)) and upright channel of infinite length will be adopted for describing nearby couplings. The channel will be realistically assumed to have a finite length only for reproducing a typical LEMP. Incidentally consider that a discontinuous current-carrying conductor becomes the source of a further spherical TM wave originated at the truncation point. Specifically, the travelling current is supposed to be suppressed at the upper end of the channel, which requires that an equal counter-current is applied on time. Therefore, excitation of an additional wave, also obeying Eqs. 2.6–2.8, is promoted and the overall surrounding field is composed of a pair of mutually retarded spherical TEM and TM waves, the point sources of which are respectively positioned at the channel's foot-end and top. The lower radiating spot becomes active at the return-stroke onset, whilst the upper one becomes active when the return-stroke extinction process begins, thus with a retardation related to the finite values assigned to v and channel length. As stated earlier, the TM wave originated in the top will reasonably be neglected when the investigation is rather aimed at evaluating the induction effects on nearby terrestrial victims, so that the crucial parameter associated with the channel only reduces to v.

As stated earlier, the unusual and apparently improper terminology "point radiator" evokes, in general, excitation of spherical waves centred on sharp geometrical transitions along the filamentary conductor. Therefore, if the latter is represented by a two-ended rectilinear filament in isolation, each endpoint radiates in consequence to a displacement-to-conduction transition to which a pair of impressed currents is submitted. One of them represents the original feeding current, the other one represents the counter-current applied with a certain retardation at the opposite terminal. In principle, a suitable application of the multiple-dipole model should achieve the same result and, therefore, is ultimately expected to strengthen the two-radiator model described earlier. Unfortunately, with respect to a return-stroke LEMP,

- introducing the notion of cylindrical wave axially expanding around the channel segment under discharge, which is in contrast with that of spherical wave expanding around its base;

- predicting a supplementary electromagnetic energy spreading at the head of an upwardly moving return-stroke, which is in contrast with the presence of a serial resistive segment representative of the remaining leader channel; and

- assuming mutually different propagation velocities for the current source and excitation field, which is in contrast with the basic in-tandem propagation rigorously admissible for the source and its field,

are meaningful examples of misinterpretations and deep-rooted persuasions which could be ascribed to questionable handling of partitioning methods.

In the light of Eqs. 2.6–2.8, the first invalid argument seems to derive from an inappropriate generalisation of the indefinite-line case, where the points O and P are positioned at infinity and at a finite distance $d = r \sin \theta$ from the line, respectively. Accordingly, θ vanishes and r tends to infinity, which implies that the quasi-static component E_r disappears and $(1 + \cos \theta)/(r \sin \theta)$ becomes $2/d$ in both the formulas of E_θ and H_φ. In other words, the originally spherical TEM radiation expressed by the components E_θ and H_φ alone, i.e. those components propagated up to P from the infinitely distant endpoint O, assume, as a matter of fact, an axial-symmetrical character, rather evocative of a cylindrical propagation. Incidentally, consider that the radial-field retardation is implicitly included in the overall retardation involving r instead of z. For the reconstruction of LEMP, P can be close to O (near-field case) or, conversely, so remotely positioned that both channel endpoints are almost at equal distance from the observer (far-field case), two limitations which make the discussed notion of cylindrical wave propagation inapplicable anyway.

The second question requires to be exhaustively discussed now. The advancing return-stroke and the upper complementary portion of the channel occupied by the charge previously lowered by the leader can be considered as connected and collinear segments of a unique ground channel. According to the engineering approach involving a transmission line model, a prerequisite for impressing a surge current at the foot-end of the pre-ionised channel is that it is considered as a discharged (zero net-charge) fairly good conductor. In fact, the progressive upward neutralisation of the negatively pre-ionised channel is replaced with an equivalent positive current travelling upwards along the same channel behaving as a zero-charge-bearing conductor. Owing to the progressive leader-to-arc transition, the enhanced conductivity acquired by the channel portion travelled by the surge current, with respect to the upper one about to be travelled, is not a valid reason for neglecting the conducting character of the latter serial segment. Considerations of plasma physics lead to the conclusion that the internal behaviour of a leader depends on ohmic heating and gas dynamic expansion which evokes the properties of a resistive electrode. In any case, the transition to local thermodynamic equilibrium, distinctive of the return-stroke formation, is accompanied by abrupt enhancement of the electrical conductivity. During such a fast phase, recombination of particles along with energy transfer are the dominant processes, confined in the channel, taking place across the mobile leader–arc junction.

Conversely, an advancing return-stroke is usually modelled as an elongating filament, a practice which tacitly leads to the removal of the upper leader channel and, therefore, to the conclusion that a certain amount of electromagnetic energy can continuously spread out at the return-stroke head. Instead, a vanishing field is excited by a travelling surge current along a conductor deprived of large and abrupt geometrical transitions, as theoretically predicted here and elsewhere, methodically supported by both optical and field

detection during the ascending phase of a return stroke. According to such experiments, first and subsequent return strokes are guided by a common pre-ionised leader channel and no significant UHV–VHV disturbance has been detected during the return-stroke ascending phase (Uman and Krider, 1982; Gardner, 1990). Both observations represent a total transfer into the upper leader channel of a certain amount of electric energy propagating along with the current wavefront throughout the cloud-to-ground channel extension. Rather, according to the present treatment, the outside electromagnetic energy is that of a spherical TEM wave originated at the channel base and propagating simultaneously to the current front with the same velocity. On the other hand, the emission-free condition for $z > 0$ can, under special conditions, be violated when integral methods applied to an elongating linear distribution of current are used, generally associated with partitioning criteria involving columnar arrays of current dipoles. A basic agreement between the results of the multiple-dipole model and Eqs. 2.9 and 2.10 is also found by Thottappillil *et al.* (2004), under specified conditions. Therefore, decomposing a channel into a cascade of elementary current dipoles, and then invoking superposition for field reconstruction, is a safe practice only if the current wave has traveled along the channel, i.e. during the extinction phase.

As mentioned earlier, the commonly adopted arbitrary assumption of two different velocities for the surrounding wave and its travelling source along the channel is in contrast with observation (e). The channel tortuosity is proved to substantially influence the distanced excitation field only through an apparent decrease of the common propagation velocity for the current and its field. As a consequence, replacing a tortuous ground channel by an upright one bridging the same cloud-to-ground gap, and consistently reducing according to observation (a), c to $v < c$ implies that $\eta = (\mu/\varepsilon)^{1/2} = v/c(\mu_0/\varepsilon_0)^{1/2} = v/c\,\eta_0$. In other words, the intrinsic resistance η_0, representative of the physical medium, requires to be virtually replaced by the unphysical quantity η if an equivalent rectilinear channel is used. Consistent with such an assumption is the supplementary retardation $r(1/v - 1/c)$ actually affecting the expansion of the spherical wave originated at the foot of a zig-zag channel. The value of such a simple representation is corroborated by Le Vine and Meneghini (1978), with special reference to the influence of the non-rectilinear channel geometry at distances exceeding the maximum departure between the most influencing segment of a real channel and its straightened representation.

It is worth considering that observation (f) is substantially in contrast with those predictions including a non-zero quasi-static electric field. The described planar current flow, radially directed towards the striking point, is quite consistent with the imaged formulation expressed by the pair of Eqs. 2.9 and 2.10, where the quasi-static component E_r disappears. This is particularly true on the plane, where imposing the tangential electric field $E_r = 0$ is consistent with the condition of perfect conduction practically assumed in observation (c) for a wet soil.

On the other hand, typical ramps and humps, recorded under near-field conditions ($|sr/v| \ll 1$) for the simultaneous on-ground ($\theta = \pi/2$) components E_θ and H_φ, respectively, cannot be accounted for by Eqs. 2.9 and 2.10. In fact, such formulas are deprived of quasi-static components and give excitation field components whose time-dependent features rather reproduce that of the current at the channel base. Note that even the physical far-field waveshapes significantly differ from that of the above current,

an observation which could discourage recourse to Eqs. 2.9 and 2.10. Instead, the disagreement mentioned helps in better exploiting the hidden properties of the formulation under examination. However, as will be better appreciated later, an enhanced sophistication degree, required for a suitable LEMP reconstruction based on Eqs. 2.6–2.8, is superfluous for most EMC applications in power systems, where, often, only the case of nearby-victim is important. In other words, contrary to different treatments, some convincing arguments will be raised (see Section 2.2.5, with special reference to observations (g) and (h)) which prove how only the simple TEM spherical wave described by Eqs. 2.9 and 2.10 is sufficient for the coupling calculation, which is irrespective of the complete LEMP reproduction in that field point. However, the LEMP reconstruction will also be accomplished only for giving more convincing arguments on the value of the present approach.

Rather, it seems worth considering that the structure of Eq. 2.2, governing the pre-stroke electrostatics when the head of the penetrating leader is about to arrive at the plane, is similar to that of the electrodynamic field, during the return-stroke phase, expressed by Eq. 2.9. It is a simple exercise to verify that Eq. 2.2 exactly becomes Eq. 2.9 if the equality $\lambda_v = i(t - z/c, z = 0)c$ is assumed, where λ_v represents a distribution of negative charge which will be neutralised by a positive step current i travelling upwards with a velocity c. The substantial similarities of the above formulas is not surprising, also with reference to a further general consideration after Schelkunoff and Friis (1952). They suggest a tentative strategy for arriving at the solution of a radiation field based on starting from a static formulation. Accordingly, the pair of Eqs. 2.9 and 2.10 are only apparently structured as quasi-static fields, in the sense that the strong inequality $|s\rho/v| \gg 1$, distinctive of radiation, applies to the above field formulation regardless of ρ. In other words, a TEM wave, which depends by definition on the propagation coordinate r, also presents a transversal dependence whose formulation is, as a matter of fact, not dissimilar to a Laplacian field. This is also discussed in Appendix A where an integral formulation is adopted to especially prove, in a different manner, the fully radiating nature of the excitation field even in the region surrounding an indefinite channel. As will be appreciated later in Section 2.6.2, such a feature deserves to be carefully examined owing to its crucial role in simplifying the coupling analysis, hence, in throwing light on the actual influence of the quasi-static field.

2.5 Return-Stroke Current

Let us consider a charged electrode assembly with a conductor suspended just above the plane. When an arc bridges the gap, the previously stored electrostatic energy is exchanged, during the dynamic phase, into a number of components which includes the electromagnetic energy. With special reference to lightning, several attempts can be made to obtain the impulsive return-stroke current starting from assigned electrostatic conditions. However, the implied models could be oversimplified as compared to the complexity of the real subject under study. The commonly referred engineering approach, based on impressing a channel-base current and generally making use of a transmission line model for describing the propagation along the channel, is largely adopted and substantially recommended for LEMP and field coupling studies. This is especially because the channel-base return-stroke current and its propagation upwards have been extensively

investigated by experimental methods. As shown in Appendix B, the surrounding LEMP can be reconstructed successfully if a certain amount of current propagated up to, or just beyond, the thundercloud bottom is subtracted with the intention of taking into account a partial depletion of the surrounding charge. Here, h_b represents the height at which such charge neutralisation occurs. The remaining current goes on carrying the upper channel segment until charged high-altitude pockets, where a definitive return-stroke extinction takes place, are attained. Such an uppermost height, which is of the order of several kilometres, is set here to infinity without affecting the model accuracy significantly. In fact, a large attenuation (other than an increasing delay) is reasonably expected to affect the residual current crossing the N region. According to our model, the abrupt current decrease at the lower height $z = h_b$ can be simulated by injecting an oppositely directed current.

The space–time current distribution assigned along the channel is of the type

$$i(t, z) = i_f(t, z) + i_s(t, z) \tag{2.11}$$

In fact, experimental data tacitly help to decompose $i(t, z)$ into the above two partial currents i_f and i_s, respectively representing a fast time-varying discharge neutralising the channel and a slow one involved in the partial neutralisation of the thundercloud N region. The above current components, simultaneously injected at the channel foot-end ($z = 0$), can be described by an exponential formulation. Therefore,

$$i_f(t, z) = i_f \left(t - \frac{z}{v}, z = 0 \right) e^{-kz} \tag{2.12}$$

with k close to $2 \times 10^{-4} \mathrm{m}^{-1}$, while

$$i_f(t, z = 0) = I_{of} \sum_{j=1}^{3} A_i e^{-\alpha_i t} \tag{2.13}$$

and

$$i_s(t, z) = i_s \left(t - \frac{z}{v}, z = 0 \right) \tag{2.14}$$

with

$$i_s(t, z = 0) = I_{os} (e^{-\alpha_4 t} - e^{-\alpha_5 t})$$

The empirical Eq. 2.11 substantially agrees with optical observations, even though the attenuation factor k can be subject to several interpretations. The fast triple-exponential law (Eq. 2.13) and the slow two-exponential law (Eq. 2.14) are crucial for shaping the current peak and tail, respectively, of the overall channel-base current $i(t, z = 0)$. The latter is reproduced in normalised form in Fig. 2.2 (curve (a)) and the values arbitrarily assigned to the set of variables I_{of}, I_{os}, α_i ($i = 1$–5) involved in Eq. 2.11 are indicated in the legend of Fig. 2.2. With special reference to Eq. 2.13, care has been taken to meet
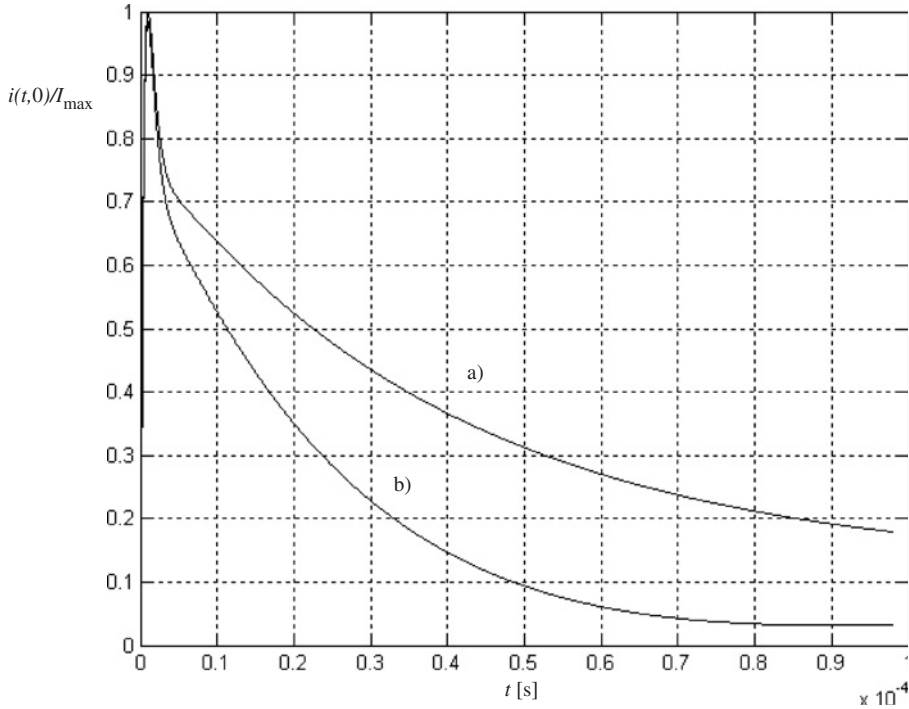
Fig. 2.2. Normalised channel-base currents: (a) and (b) according to Eqs. 2.13 and 2.14, respectively. $A_i = -0.64, 0.48, 0.16$ ($i = 1$–3). $I_{of} = 10^5$ A; $I_{os} = 3 \times 10^3$A; $\alpha_i = 2.2 \times 10^6, 1.2 \times 10^6, 2.5 \times 10^4, 1.438 \times 10^2$ and $5.12 \times 10^5 s^{-1}$. As a result, $I_{max} = 23\,906$ A.

the condition $\sum_{j=1}^{3} A_j = 0$ which ensures i_f, likewise i_s, vanish at the instant $t = 0$ of the current onset. Incidentally, it is worth considering that the additive condition

$$\sum_{j=1}^{5} A_j \alpha_j = 0$$

with $A_4 = 1$ and $A_5 = -1$ (see Eq. 2.14) preserving the time-derivative of Eq. 2.11 from discontinuity at the onset time is violated because it is in contrast with a multi-exponential formulation. The above subsidiary condition needs to be met when the time derivative of the current is involved in the LEMP or coupling calculation. This is often the case in several treatments, so that a different current fitting which gives, at the expense of the analytical amenability, a vanishing time-derivative for $t = 0$ (extensively used elsewhere, Heidler *et al.*, 1999). Incidentally, the method adopted here is, as a matter of fact, devoid of the above analytical difficulty, so that preference has been expressed for the simpler exponential formulation.

Rather, detrimental for an immediate calculation of the excitation field by Eqs. 2.9 and 2.10 is the decay law affecting i_f (see Eq. 2.12). In fact, the LEMP treatment by the above

formulation requires that the current travels without attenuation and distortion throughout the filamentary channel. Infringing such a condition introduces more complexity into the model but nothing is changed with regard to the vanishing quantity of the outwardly directed energy. Energy exchanges are invariably confined in the channel, while the outer radiation only needs to be more carefully formulated. The theoretical difficulty of taking into account a decaying current in a model inherently expressed by an ideal transmission line has been resolved by Amoruso and Lattarulo (2003) in a manner suitable to engineering applications. Adopting conveniently Laplace transforms, the input current $I(s, z = 0)$ has virtually been replaced with

$$I'(s, z = 0) = \frac{s}{v} \int_0^\infty I(s, z) dz \qquad (2.15)$$

Recalling Eq. 2.11 and back-transforming gives

$$i'(t, z = 0) = I_{\text{of}} \sum_{i=1}^{3} \frac{A_i}{\alpha_i - \beta} \left(\alpha_i e^{-\alpha_i t} - \beta e^{-\beta t} \right) + i_{\text{s}}(t, z = 0), \qquad (2.16)$$

where $\beta = kv$. A normalised version of the above current is also included in Fig. 2.2 (curve (b)) for the purpose of comparison. Consider that $i'(t, z = 0)$ approaches $i(t, z = 0)$ if k vanishes, so that such an equivalent current, travelling with no attenuation along the channel, can represent a possible generalisation of the theory of Schelkunoff (1952), which is only applicable to one-ended ideal filaments. Of course, the upper limit of the integral in Eq. 2.15 needs to be replaced with any finite quantity if the conductor is a segment of finite length (see above the explanation for approximately setting the upper limit equal to infinity in the case of a ground lightning). The time-dependent formulation of the counter-current injected at an intermediate height h_{b} is similar to Eq. 2.11, by appropriately including the retardation h_{b}/v. Such an upper feeding current causes an additional point source of a TM spherical wave, obeying equations similar to Eqs. 2.6–2.8 (to be imaged), to appear for $z = h_{\text{b}}$. As discussed earlier, such a source is crucial for the successful on-ground reproduction of the overall LEMP since a non-zero radial electric field is also generated at the suspended opposite feeding point. However, as will be observed in Section 2.6, the latter source can be practically neglected if the investigation is rather aimed at evaluating the indirect effects on nearby victims, a restriction of substantial interest for EMC applications to power systems. Therefore, the following section will deliberately ignore the above complication, while a separate mention is reserved for the total LEMP reconstruction in Appendix B.

2.6 Induced Voltage on a Nearby Line

2.6.1 Actual excitation field

With reference to the location of a lightning flash, let us consider nearby field points placed on or just above the ground, i.e. those points whose polar coordinates r and θ are, respectively smaller than h_{b} and equal to or less than $\pi/2$. In the restricted field domain where the above conditions hold, in those terrestrial locations where the interference is

severe even for power system components, the above model gives convincing arguments to safely state that

(g) owing to the comparatively large distance of the upper point source, the horizontal quasi-static electric field changes slightly;

(h) owing to the relatively short distance of the striking point, intended as a source of a radiating TEM wave, the upper source at a distance can be neglected.

With reference to observation (g), consider that the depleting N region, embedded in the lower region of a thundercloud, is expected to be substantially responsible for the quasi-static contribution to the LEMP. When the return-stroke current front attains the height h_b, an intra-cloud globular zone, essentially pervaded by corona streamers, surrounds the channel. The discharge spreading is promoted by water vapour and pre-ionised conditions which cause abatement, respectively, of the statistical time lag and corona inception level. The sphere-like depleting region, which behaves as a resistance internally and as a perfect conductor externally (for electrokinetic and electrostatic considerations, respectively), is assumed to be connected to the channel for $z = h_b$. Consider that the spherical dilation in the N region is representative of the inwardly directed streamer penetration departing from the peripheral point placed at a height h_b. Accordingly, the dilation is assumed to hold tangential to the cloud bottom at the point of channel–sphere junction mentioned earlier. Therefore, the vertical channel and the upper inflating sphere (the latter corresponding to a partial extinction of the return-stroke current) are interpreted as connected portions of a composite source model. The surrounding overall field is obtained by ideally tearing the filament–sphere junction and restoring the current continuity by applying two equal and oppositely directed currents at the terminals of the torn junction. As discussed earlier, the formulation for such currents is substantially similar to Eq. 2.11 and takes into account the retardation, with respect to the return-stroke onset instant, affecting the upper partial extinction. When the in-cloud sphere is fed by the corresponding terminal current, a quasi-static electric field is produced in the sphere-to-plane gap, in the sense that such a field is the result of a conduction-to-displacement transition taking place at the surface of the sphere. The vertical electric field and azimuthal magnetic field calculated at the plane for some significant lateral ranges are reported in Appendix B. A radiating spherical field is simultaneously excited at a height h_b when one terminal current is injected into the channel at the junction point. When the front of the excited wave is at or just above the plane, the field components arrive reduced to about r/h_b and retarded to about $2h_b/c$. Consider that the case under study becomes important when the above dimensionless ratio decreases up to the order of 10^{-2} and the time-dimensioned one increases up to the order of tens of microseconds. The above quantities concur to predict a computational inaccuracy within the uncertainty affecting the problem under examination if the upper source is, for the sake of simplicity, ignored.

Therefore, recalling Eq. 2.9 and taking into account observations (g) and (h) gives

$$E_z = E_\theta \sin\theta = -\frac{\eta_o}{2\pi r}\frac{v}{c}\left(1+\frac{z}{r}\right)i'\left(t-\frac{\rho}{v}, z=0\right) \tag{2.17}$$

$$E_\rho = E_\theta \cos\theta = \eta_o \frac{1}{2\pi r}\frac{v}{c}\frac{z}{\rho}\left(1+\frac{z}{r}\right)i'\left(t-\frac{r}{v}, z=0\right) \tag{2.18}$$

The above pair of approximate formulas represent the vertical and horizontal E_θ components for $\rho \ll h_b$, where $r = \sqrt{(z^2 + \rho^2)}$, $\rho = r \sin \theta$ and $z = r \cos \theta$. Owing to the axial-symmetry of the field under examination, the pair (ρ, z) denotes, under orthogonal coordinate form and irrespective of the azimuthal variable, the observer's location.

Equations 2.17 and 2.18 simplify further if the realistic condition $z \ll \rho$ is met. Therefore, they become

$$E_z = -\frac{\eta_o}{2\pi\rho}\frac{v}{c}i'\left(t - \frac{\rho}{v}, z = 0\right) \tag{2.19}$$

$$E_\rho = \eta_o\frac{v}{2\pi c}\frac{z}{\rho^2}i'\left(t - \frac{\rho}{v}, z = 0\right) \tag{2.20}$$

It is worth considering that the above simple description of the nearby electric field on or just above the ground can significantly depart from that given in general by more sophisticated multiple-dipole models. In the latter case, a supplementary spherical wave, centred atop and linked up with the elongating dipole chain can appear and significantly contribute to shaping the near field. This occurs especially when the rising current front is at the same height as the observation point. The enhanced sophistication of such a model tacitly helps the investigator, ultimately involved in reproducing canonical near-field features, to manage a considerable number of variables at his disposal.

2.6.2 Coupling to a nearby line

Densely populated areas are generally supplied by a complex system of transmission and distribution cables often interconnected by indoor gas-insulated substations. Such installations are effectively protected by direct and indirect effects of lightning. Conversely, large extension of the power system, generally comprising overhead transmission lines interconnected by outdoor substations, is exposed to the above effects. When a lightning strikes the ground at a short distance from a suspended line, the interfering LEMP is responsible, in particular, for the appearance of a significant surge voltage along the conductor. The magnitude and spectral content of the induced effects are of interest even for a power facility owing to its connection to vulnerable equipments. The canonical case of a horizontally stretched (sag neglected) loss-less single-wire line raised at a height $h_L \ll h_b$ and terminated in its characteristic impedance Z_L is examined, see Fig. 2.3. In such a manner, a detailed comparison with experimental data and available theories is made possible; in addition, the discernible character of the analysis promotes a more efficient selection of unambiguous results and their physical interpretation. Extending the analysis to a multi-conductor line turns out to be a straightforward exercise with the assistance from extensively available general commentaries (see, for example, Paul, 1995; Tesche *et al.*, 1997). The typical case of a flash striking a point S at a distance not exceeding the order of 100 m from one of the on-ground projections O and L (for $z = 0$ or L, respectively) of the two opposite line terminals, are considered.

With reference to the coordinate system shown Fig. 2.3, whose x axis is superimposed to the line projection at the plane, the transient response is represented by the induced
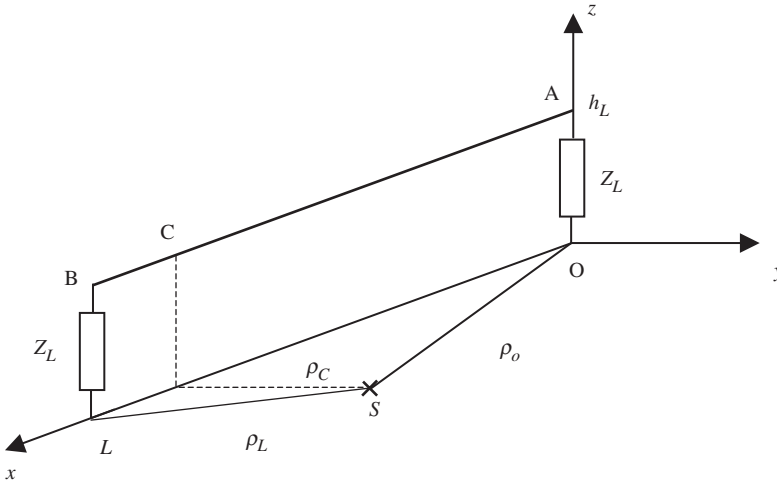
Fig. 2.3. Aerial line subject to an interfering flash which strikes the ground on the point S. Point C on the line is at a minimal distance ρ_c from S.

voltage $u(x, t)$ and current $i(x, t)$. Such parameters are embodied in the pair of equations (Nucci *et al.*, 1993; Barker and Short, 1996; see also the equivalent representation given by Tesche *et al.*, 1997).

$$\frac{\partial u(x, t)}{\partial x} + L_1 \frac{\partial i(x, t)}{\partial t} = -\frac{\partial}{\partial t} \int_0^{h_L} B_y(x, z, t) dz$$

$$\frac{\partial i(x, t)}{\partial x} + C_1 \frac{\partial u(x, t)}{\partial t} = -C_1 \frac{\partial}{\partial t} \int_0^{h_L} E_z(x, z, t) dz. \tag{2.21}$$

In this expression, L_1 and C_1 are inductance and capacitance per unit length of line; $B_y = \mu_o H_y$, with H_y denoting the magnetic field component along the y axis. Consider further that the first part of Eq. 2.21 could also be differently arranged after involving specific field components. Briefly,

$$-\frac{\partial}{\partial t} \int_0^{h_L} B_y(x, z, t) dz = E_x(x, z = h_L, t) - E_x(x, z = 0, t) - \frac{\partial}{\partial x} \int_0^{h_L} E_z(x, z, t) dz$$

$$\tag{2.22}$$

is also derived (Barker and Short, 1996) if E_x denotes the E_ρ component along the x axis. The complexity of the above equation reduces significantly after considering that

- $\int_0^{h_L} E_z(x, z, t) dz \cong h_L E_z(x, z, t)$ since E_z slightly changes if $z = h_L \ll \rho$ (see above the second formula in the pair of Eqs. 2.21 and Eq. 2.22);

- the tangential electric field $E_x(x, z = 0, t)$ at the plane vanishes according to observation (c); and

- the tangential electric field $E_x(x, z = h_L, t)$ at a height h_L also vanishes according to observations (f) and (h).

The latter simplifying assumption requires to be exhaustively proved. To this end, it is not difficult to verify that

$$\frac{\partial}{\partial \rho} \int_0^{h_L} E_z(z)dz \cong h_L \frac{\partial E_z}{\partial \rho} \cong E_\rho(\rho, z = h_L, t) - \mu_o \frac{h_L}{2\pi\rho} \frac{\partial i'}{\partial t} \qquad (2.23)$$

The above solution for the integral has been obtained by involving Eq. 2.20 and recalling that $\eta = \mu_o c$ and $v = d\rho/dt$. Consider further that the discussed radiating character of the TEM wave surrounding the channel-foot source leads to the conclusion that the typical far-field condition $|s\rho/v| \gg 1$ can also be extended to the case in which ρ vanishes. This implies that the negative term on the right-hand side of Eq. 2.23 largely exceeds E_ρ, as the Laplace-transform representation easily manifests. In fact, setting $z = h_L$ in Eq. 2.20 and recalling the equality $\eta = \mu_o c$ gives the ratio

$$\frac{E_\rho(s, z = h_L)}{\mu_o(h_L/2\pi\rho)I'(s, z = 0)e^{s\rho/v}} = \frac{v}{s\rho} \ll 1$$

since the radiation condition $|s\rho/v| \gg 1$ legitimately holds. Equation 2.23 is better verified along any x axis diverging from the radial ρ axes originating on S (see Fig. 2.3), an observation which ultimately implies

$$\frac{\partial}{\partial t} \int_0^{h_L} B_y(x, z, t)dz \cong h_L \frac{\partial E_z}{\partial x} \qquad (2.24)$$

by substitution into Eq. 2.22. Such a result, in conjunction with the definition of scattered voltage u_s, is crucial in simplifying the pair of Eq. 2.21 remarkably. In fact, for the line under examination, using the relationship

$$u = u_s - h_L E_z \qquad (2.25)$$

correlating the induced and scattered voltages, and recalling Eq. 2.24, easily allows Eq. 2.21 to be converted into the traditional and amenable pair of Telegrapher's travelling wave equations

$$\frac{\partial u_s(x, t)}{\partial x} + L_1 \frac{\partial i(x, t)}{\partial t} = 0$$

$$\frac{\partial i(x, t)}{\partial x} + C_1 \frac{\partial u_s(x, t)}{\partial t} = 0 \qquad (2.26)$$

Accordingly, the analysis reduces to solving the above set of equations for u_s, by taking into account Eq. 2.25 for ultimately obtaining u. The required boundary conditions are

$$- R_L i(x = 0, t) = u_s(x = 0, t) - h_L E_z(x = 0, t)$$

$$- R_L i(x = L, t) = u_s(x = L, t) - h_L E_z(x = L, t)$$

The variable z has been omitted in the notation of E_z since reference is tacitly made here in the case of $z = 0$. The above simplified formalism leads to the realisation that the coupling mechanism can be exhaustively described by a simple line model driven at both terminals by oppositely driving source generators of voltages $h_L E_z(x = 0, t)$ and $h_L E_z(x = L, t)$ and same internal impedance Z_L.

Accordingly,

$$u(x, t) = u_s(x, t) - \frac{u_i(x = 0, t - x/v_L)}{2} - \frac{u_i[x = L, t - (L - x/v_L)]}{2} \qquad (2.27)$$

represents the solution for the induced voltage, where the currently referred to as incident voltage $u_i = -h_L E_z$ is used. Here, $v_L = \sqrt{L_1 C_1} \cong c$ denotes the velocity of the travelling wave along the line. The adopted space-time notation incorporates the delays affecting the vertical E-field when it attains the line endpoints placed at $z = 0$ and L and the pair of delays x/v_L, $(L - x)/v_L$ affecting the surge voltages travelling down the line after being produced at both terminal risers. It is worth mentioning that the field component involved in the line excitation is reduced to the vertically polarised E-field originated in S. Therefore, Eq. 2.27 can be conveniently reformulated as follows:

$$u(t - \rho/c) = u_i(t - \rho/c) - \frac{u_i(t - \rho_o/c - x/v_L)}{2} - \frac{u_i[t - \rho_L/c - (L - x)/v_L]}{2}$$
$$(2.28)$$

according to Fig. 2.3. In Eq. 2.28, the line sections of generic coordinate x is expressed in terms of distance $\rho(x)$ from S; specifically, ρ becomes $\rho_o = \rho(x = 0)$ or $\rho_L(x = L)$ with reference to the line terminals.

Therefore, the simple analytical structure of Eq. 2.28 governing the induced voltage on the line is accounted for owing to

- the realistic condition $\rho \ll h_b$ applied along the more excited segment of a long line or throughout a short line;

- the slight influence of the LEMP components, but the radiating vertical E-field, on the coupling mechanism involving the line.

All conditions considered, an important finding is that the calculation of the near-source interference can be restricted to the use of an amenable pair of Telegrapher's equations since a simpler end-driven transmission line is the substantial involvement of the network model. In fact, the physical prerequisite for carefully introducing a sequence of distributed generators is the substantial influence of the horizontal electric field. Several investigators are convinced that such a questionable field component can be effectively implied in the coupling mechanism, an assumption which contrasts with the realistic character of observations (c), (f), (g) and (h).

2.6.3 Example of application and discussion

In the case of natural events, a careful validation of theoretical predictions is thwarted by the lack of exhaustive and correlated databases. Even neglecting the quasi-static component of a LEMP, the number of parameters and assumptions arbitrarily assigned are still too large. The experimental data, some of which are supplied with a significant degree of uncertainty, include the current's peak and waveshape, channel-base location, electromagnetic field components simultaneously recorded in several environmental points and actual soil impedance. As mentioned earlier, impressive but rather unreliable LEMP reproductions can be obtained as a result of successful combinations of manifold adjustables involved in the fitting process. Therefore, a tentative approach to the model validation could be that of renouncing a detailed comparison with specific experimental data and rather using a reasonable selection of general performances and observations as a first-order but more reliable test mark. The above-mentioned selection, with respect to service or test lines, is summarised below:

(i) When natural lightning strikes at an unspecified distance from a long line, the overvoltage exhibits positive polarity when the field front reaches the measuring endpoint before propagating along the line, and negative polarity if the field front has passed over the line before it reaches the measuring endpoint (Tesche *et al.*, 1997);

(ii) Under the same circumstances, a pronounced peak followed by a rather lasting tail is distinctive of the overvoltage waveshape (de la Rosa *et al.*, 1988);

(iii) When rocket-triggered lightning is used for testing a nearby short line, the induced voltages detected at the opposite ends are much smaller than those detected midway, where the distance from the flash is shorter (see, for example, Figs. 9 and 10 in Barker *et al.*, 1996, and related debate involving Barker and Short, 1996); and

(iv) The peak voltage U_M obeys the empirical law.

$$U_M = 63 I_o \frac{h_L}{\rho_{min}}, \qquad (2.29)$$

where I_o and ρ_{min} denote current peak and distance of the stroke from the line (Barker *et al.*, 1996).
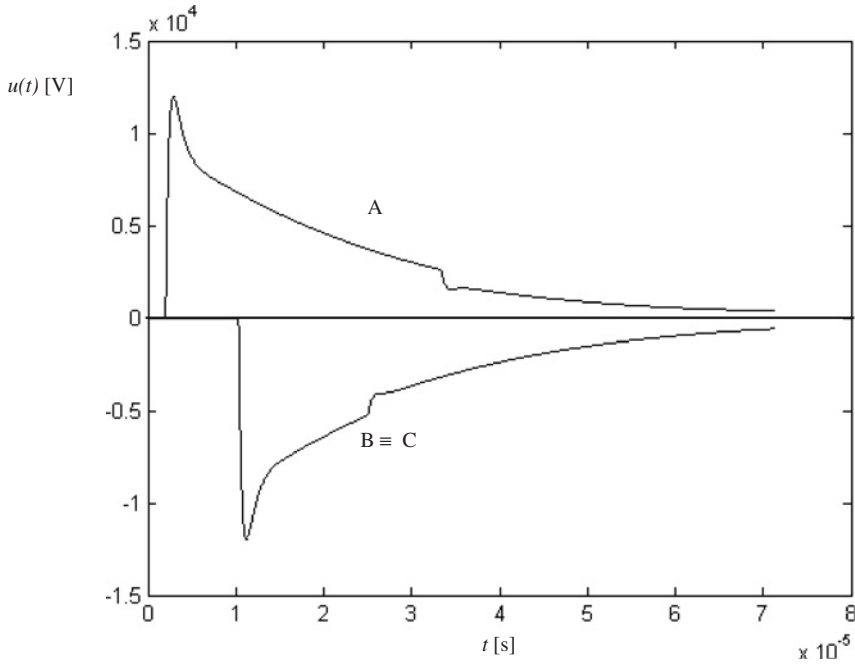
Fig. 2.4. Induced voltage u at both ends A and B of a line (L $= 2500$ m; $\rho_o = 200$ m, $\rho_L = 2508$ m). S is at a minimal distance $\rho_c \equiv \rho_o$ from endpoint A (see Fig. 2.3).

Setting $\rho = \rho_o$, ρ_L in Eq. 2.28 gives

$$u(t - \rho_o/c) = \frac{u_i(t - \rho_o/c)}{2} - \frac{u_i(t - \rho_L/c - L/v_L)}{2} \tag{2.30}$$

$$u(t - \rho_L/c) = \frac{u_i(t - \rho_L/c)}{2} - \frac{u_i(t - \rho_o/c - L/v_L)}{2} \tag{2.31}$$

Figure 2.4 shows the overvoltages at both line terminals given by the above formulas when the condition $\rho_o \ll \rho_L$ involving the striking point S is met. According to Fig. 2.3, the above condition means that S is close to one terminal of the long line. The discernible structures of Eqs. 2.30 and 2.35 allow the resulting two curves to be easily explained: u_i calculated by setting $\rho = \rho_o$ largely exceeds the voltage response at the opposite end owing to the decaying $1/\rho$ law embodied in Eq. 2.17. Therefore, such a law is responsible for the unimportant perturbations superimposed on the regular tails for later times, which implies that the two surge voltages substantially differ only in polarity and delay, the latter being related to the finite velocity $v_L \cong c$ permitted for the travelling surge.

It is worth discovering that

- in accordance with statement (i), the overvoltage u reverses its polarity at the opposite terminal placed at a larger distance from the striking point;
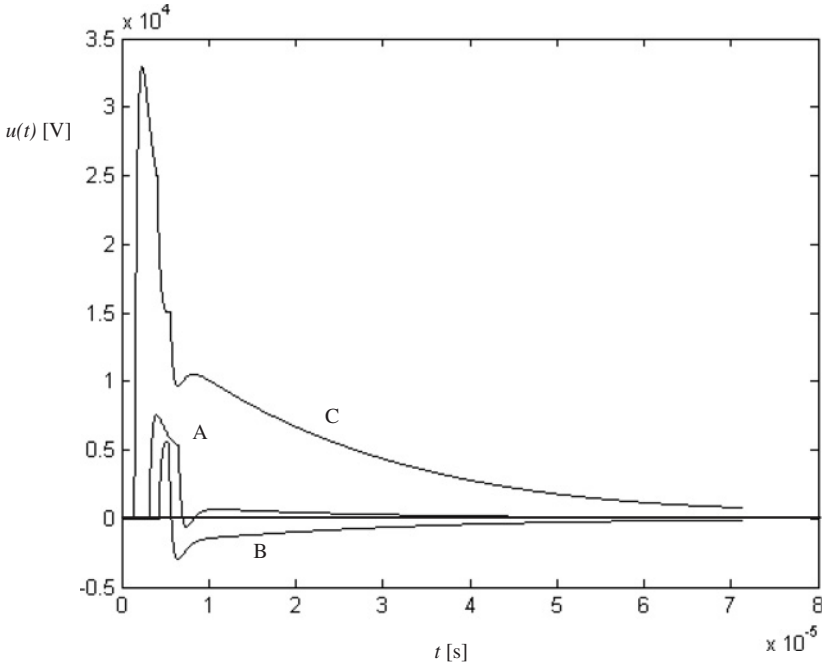
Fig. 2.5. Induced voltages u at the points A, B and C of a line (L $=$ 680 m; ρ_o $=$ 315 m, $\rho_L = 425.5$ m); S is at the minimal distance $\rho_c = 145$ m from the line.

- in accordance with statement (ii), predominant features of the surge waveshapes are a pronounced peak and a subsequent prolonged tail.

Also deserving attention are the curves shown in Fig. 2.5, which have been obtained by applying Eq. 2.28 twice to a generic section C and to both terminals A and B (see Fig. 2.3 again). The theoretical tracings resemble fairly well the experimental records in the sense that

- according to statement (iii), the peak value in C is several times larger than those in A and B.

If the simplifying observations (c), (f), (g) and (h) are ignored, the resulting line model requires the additional contribution of voltage generators, disseminated along the line, in substitution of the non-negligible effect due to the tangential E-field. In this case, the oversophisticated circuit driven by additional serial generators can lead to unverified voltages at both terminals, in the sense that the relevant peaks are only slightly smaller than those calculated midway (the only quantity close to the experimental data; Barker *et al.*, 1996).

The critical value of the above result requires that the coupling to a short line is more closely examined. Accordingly, imposing a restricted voltage rise-time t_r so that the

conditions $\rho_o - \rho_m + X_m/c > t_r$ and $\rho_o - \rho_L + L/c > t_r$ are simultaneously met, leads to

$$\frac{U_M(x = L)}{U_M(x_m)} \cong \frac{2\rho_L}{\rho_m} = 2\sqrt{1 + \left(\frac{L - x_m}{\rho_m}\right)^2} \tag{2.32}$$

Such a formula substantially holds if the peaks obeying Eq. 2.28 are reached before the reflected surge voltages are arrived at. This occurs when larger t_r or shorter L is assumed, in which case the voltage peaks are subjected to minor changes throughout the line. The circumstances described do not seem to be experimentally reproduced by Barker *et al.* (1996), an argument ultimately supporting further the present simpler procedure based on observations (c), (f), (g) and (h).

A further argument for discussion derives from the definition of maximum voltage peak U_M (at the minimal distance ρ_{min} from the striking point), as derived from Eq. 2.19. Accordingly

$$U_M = h_L E_{M, z} = 60 I_o \frac{h_L}{\rho_{min}} \frac{v}{c} \tag{2.33}$$

Setting, say, ρ_{min} of the order of 100 m causes U_M to appear when the current front has travelled the channel a few hundred metres upward, as expected in the case of test lines under the influence of rocket-triggered flashes. Therefore, an excellent reproduction of Eq. 2.29 is given by imposing $v \cong c$ in Eq. 2.33, by assuming the lower segment of the return-stroke substantially as vertical and straight. Such a physical assumption presumably applies because of the guiding function exerted by the metallic wire before melting. The important role played by the ratio v/c embodied in Eq. 2.33 can be appreciated additionally by considering that Eq. 2.29 exceeds the early predictions made with reference to natural events.

2.7 Concluding Remarks

Probably, the most striking finding connected to the engineering approach recommended here in the treatment of lightning-induced effects on nearby lines, consists in the purely radiating nature of the electromagnetic field implied in the coupling mechanism. The exact source formulation adopted has also permitted the verification that only the vertical E-field component is actually responsible for the induced overvoltage. In fact, the critical distances of interest between the striking point, intended as a source of a TEM spherical wave, and the line is at least one order of magnitude smaller than that between the first extinction point, somewhere positioned on the thundercloud periphery, and the line itself. Therefore, a significant charge depletion, simulated by current absorption, is permitted irrespective of the complete extinction which the return-stroke generally experiences later when it attains higher altitude pockets of charges. A detailed description of the relevant quasi-static field accomplishing the LEMP is estimated to be unimportant for the coupling, even though the latter develops under conditions of channel–victim proximity. Previous treatments seem to depart from the above description in that significant amounts of both vertical and horizontal quasi-static E-field components, produced by the channel, are simultaneously involved in the interaction model. This is due to the

substantial electromagnetic energy spreading up from the upper end of an elongating return-stroke. A consequent effect is the appearance of a significant tangential E-field, in addition to the increased finite conductivity assumed for the soil. Instead, the considerably simpler coupling model proposed here, involving only the terminal forcing elements in the final network representation of the victim, is governed by the traditional Telegrapher's equations. This pleasant finding is derived by applying some realistic conditions to an exact, even though underestimated, field formulation which, as a matter of fact, deduct the tangential E-field and the quasi-static spectral components from any significant role in the nearby interfering mechanism. The exact field formulation adopted calls in question the line integral of the current dipole field, a common computational practice which, unfortunately, can result in the introduction of arbitrary assumptions. A paradigmatic example in which a high degree of speculation is attained in modelling a phenomenon of uncertain nature, whose experimental data are even deprived of correlation, is represented by the rising phase of a return stroke. Therefore, the discussion on the given results has been performed deliberately by circumventing somewhere unfruitful or misleading quantitative comparisons. The purpose of this chapter is to show how selecting an exact, even though oversimplified, model is always a recommendable practice – according to the basic "Occam's razor" principle – when a large degree of uncertainty affects the phenomenon under examination. Furthermore, this simple approach turns out to be a favourable starting condition for proceeding safely in more sophisticated methods and, possibly, in finding out unexpected physical properties.

For instance, the model recommended here indicates that the quasi-static LEMP source is substantially represented by the depleting thundercloud. Specifically, the reconstruction of a large hump on the tail of the magnetic field – a crucial LEMP signature on near-field records – is interpreted as phenomenologically distinct from the shorter hump exhibited by far-field records (see discussion on Fig. 2.6(d) in Appendix B). However, such considerations are, as a matter of fact, unimportant for an engineering approach to EMC problems involving nearby victims, in which case the vertical component of a spherical wave, originated at the striking point, has been recognised as the very threat deserving attention.

In the light of the above analysis, the often vindicated good reproducibility of natural lightning and its effects by means of an artificially triggered lightning for full-scale (Barker *et al.*, 1996) or reduced-scale tests (Ishii *et al.*, 1999) needs to be carefully reconsidered. It is worth bearing in mind that

- owing to significant differences in the channel tortuosity and inclination, v is expected to better approach c in the case of an artificially triggered lightning. Therefore, the correlation between real channel configuration and overvoltage peak, ultimately expressed by the ratio v/c in Eq. 2.34, can lead to conservative prediction (larger overvoltages);

- the actual conducting properties of soil during the test could differ from those under natural circumstances. In fact, provided realistically that there is a lack of rainfall before and during the test, a significant tangential E-field, ultimately producing additional interference with the line, will appear. Therefore, replicating overvoltages, in waveshape and magnitude, could result in partial failures;

(a)

(b)
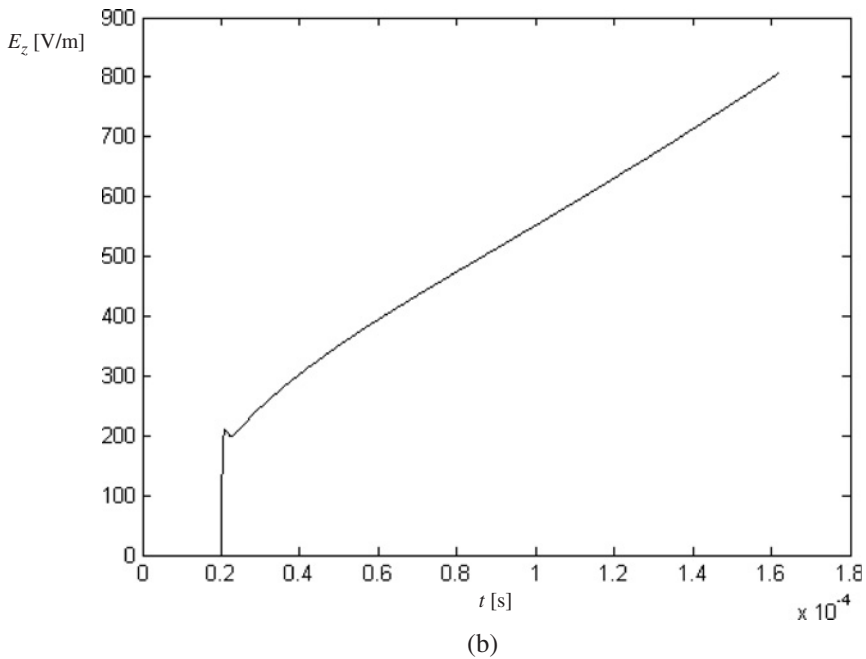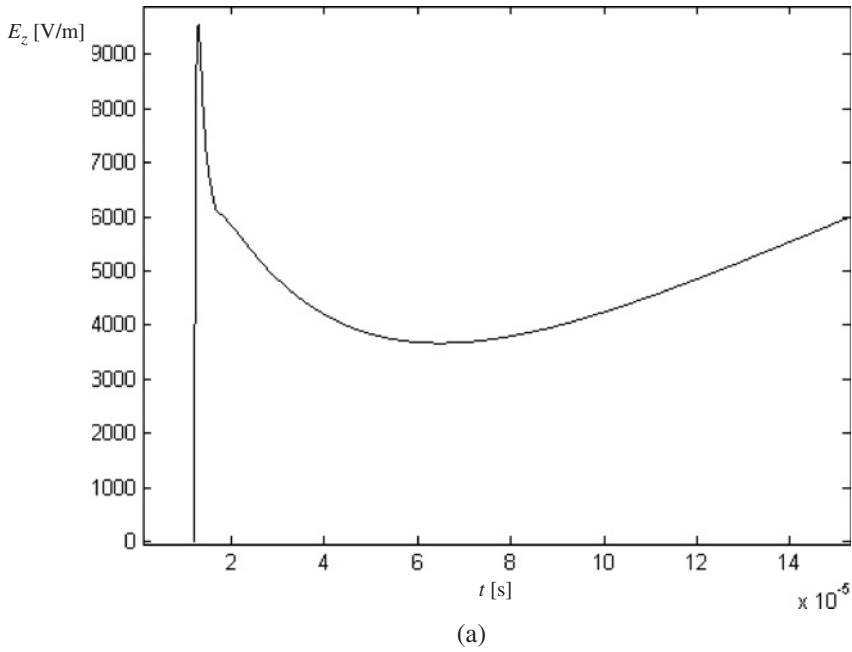
Fig. 2.6. Theoretical oscillograms (a), (b), (c) and (d) of the vertical electric field for $\rho = 50$, 2000, 10 000 and 200 000 m, respectively (see Fig. 2.2 for the current data and the legend of Fig. 2.7 for additional features regarding Fig. 2.6(d)).

E_z [V/m]

(c)

t [s]

E_z [V/m]

(d)

t [s]
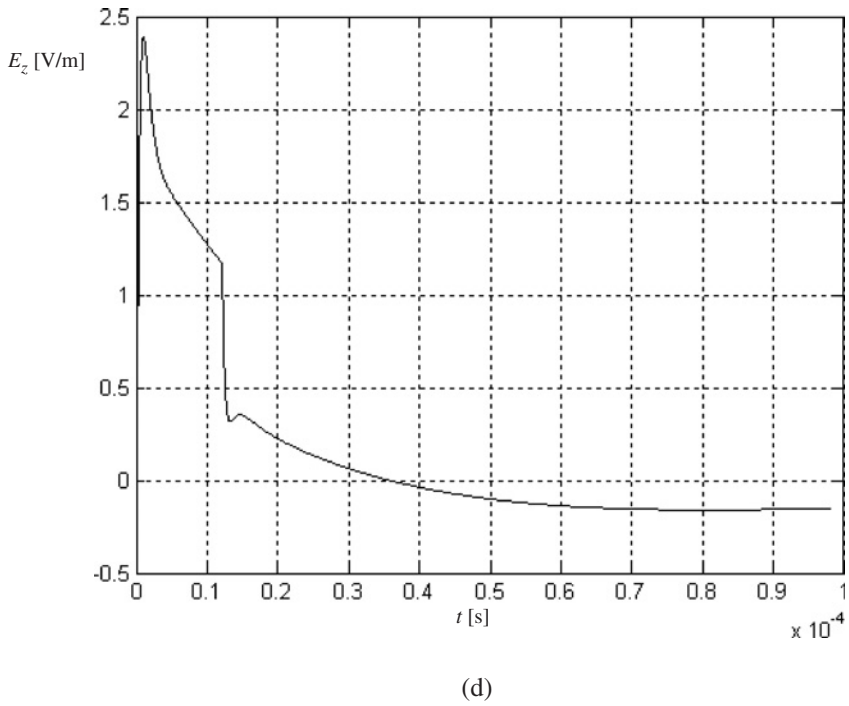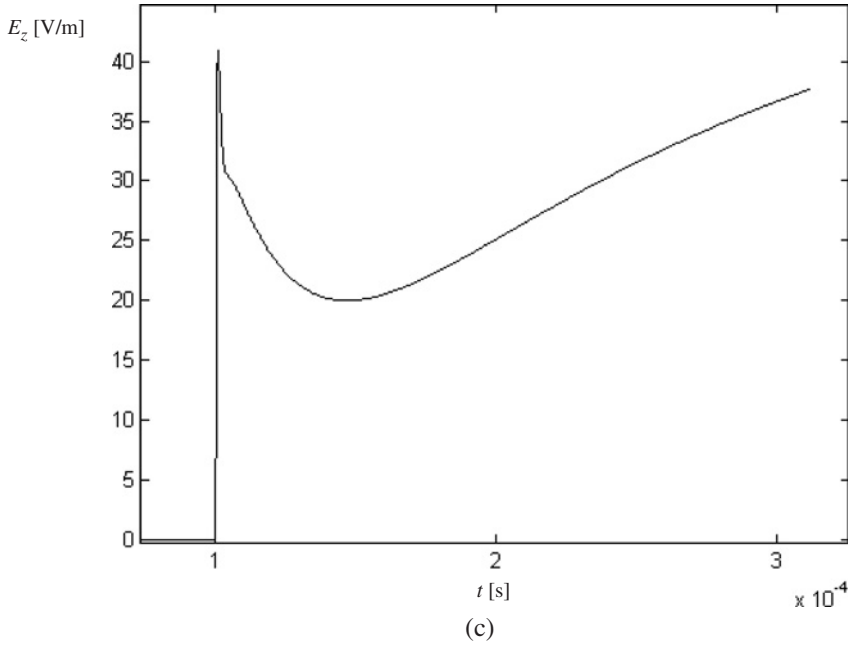
Fig. 2.6. continued

- a good reproduction of a standard natural flash is strongly dependent on the onset instant of an artificial flash. In fact, the latter could be successfully triggered even when the stage of maturation of the thundercloud cell, precursor to a natural event, has not been accomplished.

On the other hand, replacing a natural upper leader by a metallic wire however ensures a good cloud-to-plane bridging while the artificially triggered return-stroke elongates upwards. Such a conducting continuity is the prerequisite for preventing unphysical appearance of a large radiator on the channel discontinuity. Therefore, no significant electromagnetic energy is allowed to spread up at the upwardly directed return-stroke head until it is guided by the unspooled wire.

Appendix A

An electric dipole of current moment $I(s, h)ds$, located at a height h on the z axis of the vertical channel produces an elementary vertical potential vector (Wait, 1982)

$$dA_z(s) = \frac{I(s, h)dh}{4\pi}F(s) \tag{1.34}$$

Here, $F(s)$ is the integral function

$$F(s) = \int_0^\infty \frac{\lambda}{u_o}\left[e^{-u_o|z-h|} + e^{-u_o(z+h)}\right]J_o(\lambda\rho)d\lambda$$

since a perfectly reflecting plane is tacitly assumed; $J_o(\lambda\rho)$ and $u_o = \sqrt{(\gamma_o^2 + \lambda^2)}$ denote Bessel function of the first type of zero order with integral variable λ and propagation constant of the upper half-space, respectively ($\gamma_o = s/c$ because $v = c$ has been set for the sake of simplicity). Accordingly,

$$A_z(s) = \frac{I(s, h = 0)}{4\pi}\int_0^\infty e^{\gamma_o h/c}F(s)dh \tag{1.35}$$

expresses the line integration of Eq. 2.34 when the channel is indefinitely long. The excitation field can be completely represented in the function of $A_z(s)$ as follows:

$$E_\rho = \frac{1}{s\varepsilon_o}\frac{\partial^2 A_z}{\partial\rho\partial z} \tag{1.36}$$

$$E_z = \frac{1}{s\varepsilon_o}\left(-\gamma_o^2\frac{\partial^2}{\partial z^2}\right)A_z \tag{1.37}$$

$$H_\varphi = -\frac{\partial A_z}{\partial\rho} \tag{1.38}$$

When the radiation condition $|\gamma_o\rho| \gg 1$ is adopted, then $u_o \cong \gamma_o$ since $|\gamma_o^2| \gg \lambda^2$. Such an approximation, in conjunction with tabulated Bessel function integrals, makes the above field equations analytically tractable. As expected, the final result exactly

reproduces, in particular, Eqs. 2.19 and 2.20. However, it is worth bearing in mind that the given results agree by imposing the radiation condition. In other words, Eqs. 2.19 and 2.20 can also be derived from the present treatment if the integrand of Eq. 2.35 has its major contribution in the range in which $|\gamma_o^2| \gg \lambda^2$. The all-radiating nature of the field in question is confirmed by formally imposing now the quasistatic condition $|\gamma_o \rho| \ll 1$, which conversely implies $|\gamma_o^2 \lambda| \ll \lambda^2$. Accordingly, setting $u_o \cong \lambda$ in Eq. 2.35 and performing similar analytical manipulations leads to the discovery that Eq. 2.35 and, in turn, Eqs. 2.36 and 2.37 vanish.

Appendix B

As described earlier, the N region located in the lower portion of a thundercloud cell assumes an important role in determining the quasi-static features of a LEMP during the depletion phase. The latter develops simultaneously in the form of expanding globular region to the return-stroke partial extinction at an intermediate height h_b. The return-stroke current portion involved in such a spherical depletion assumes, in the outer space, the character of displacement current flowing along the Laplacian fluxlines of the sphere-to-plane electrostatic configuration. Figures 2.6 and 2.7 show, respectively, the simultaneous vertical electric field and azimuthal magnetic field calculated at the plane for some significant lateral ranges. Such theoretical tracings replicate fairly well the canonical features of LEMP oscillograms. Specifically, both the typical E-field ramps and B-field humps, are especially detectable at short distance from the flash, are reproduced in Figs. 2.6 and 2.7, respectively. The quasi-static effect of the upper cloud depletion practically disappears at a remote distance considered in Fig. 2.6(d). Here, the far-field waveshape depicted has been reconstructed by introducing i' (see Eq. 2.15) into the pair of Eqs. 2.9 and 2.10 and the opposite current i'_b, injected at a height h_b, in the corresponding field formulas similar to Eqs. 2.6–2.8. The latter field formulation requires to be imaged and referred to a spherical coordinate system centred at a height h_b. Even the effect of the slow time-varying current component i_s, incorporated into Eq. 2.15, becomes progressively unimportant at later times, since the mutual retardation between the excited opposite fields tends to vanish if r largely exceeds h_b. Conversely, such a retardation affects the waveshape during the first instant, i.e. when the contributions of the opposite fast time-varying field components, dependent on the currents i' and i'_b, are dominant. A refined composition of such field components are responsible, with reference to the graphical details of Fig. 2.6(d), for the modest hump, often followed by polarity inversion, positioned behind the initial peak. The LEMP model described could require further improvements, invariably introducing a number of arbitrary parameters. Consider that available good-quality LEMP reproductions (see, for example, Amoruso and Lattarulo, 1993; Cooray, 1998) have been obtained by using different working hypotheses and basic models, even though a certain degree of speculation is distinctive of such a class of investigations.

In general, starting from LEMP databases for reconstructing the discharging source means that the investigator has been involved in an inverse source problem which, consequently, requires a good knowledge of questions on uniqueness and stability of the solution. In fact, a typical feature of inverse problems is that of being ill-posed, in the sense that small changes in the available data can produce arbitrarily large errors in the estimation

(a)

(b)
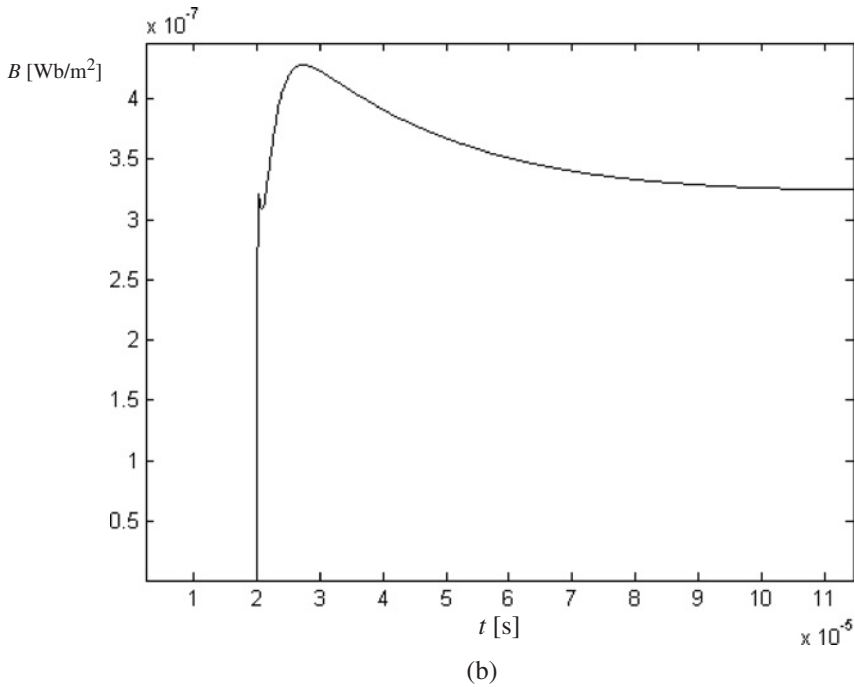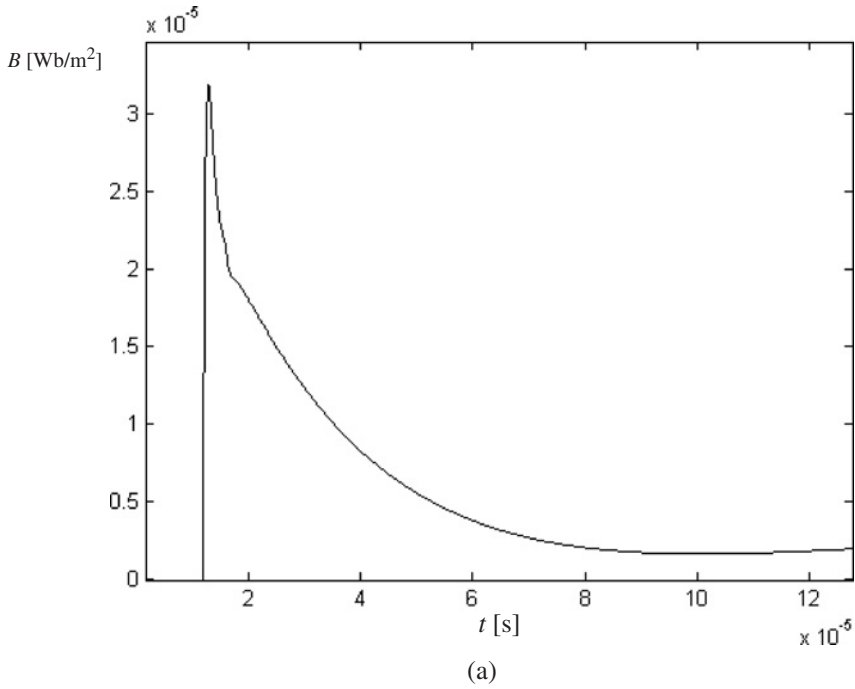
Fig. A.1. Theoretical oscillograms (a), (b) and (c) of the azimuthal magnetic flux density $B = \mu_o H_\varphi$ for $\rho = 50$, 2000, 10 000 m, respectively (see Fig. 2.2 for the current data). By replacing the ordinate E_z with $B = E_z/c$, Fig. 2.6(d) is also representative of B for $\rho = 200\,000$ m.

B [Wb/m^2]

(c)
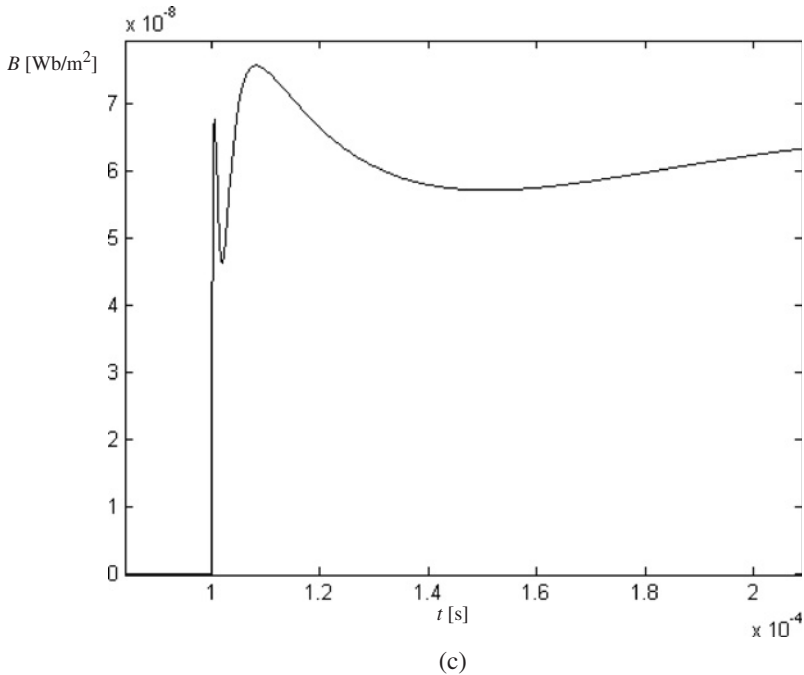
Fig. A.7. continued

of the parameters of interest and, in turn, large effects in the reconstruction of source (see for example, Bleistein and Cohen, 1977; Bertero, 1989). Preliminary to the development of the forward problem applied to the LEMP evaluation (and related coupling to the line), the expedient adopted here for circumventing the difficulties inherent in the definition of an unquestionable source has been that of selecting it on the basis of its generality (Traub and Werschulz, 1994). Therefore, the practical rationale adopted has been to keep as simple a source as possible, capable of offering an exact solution of the associate forward problem (Barrow, 1998).

Acknowledgement

References

Amoruso V., Lattarulo F., "The electromagnetic field of an improved lightning return-stroke representation", IEEE Trans. Electromag. Compat., **35** (1993) 317.

Amoruso V., Lattarulo F., "Remarks on lightning electromagnetics", EABE, **27** (2003) 375.

Barker P.P., Short T.A., "Response to comments", IEEE Trans. Power Delivery, **11** (1996) 994.

Barker P.P., Short T.A., Eybert-Berard A.R., Berlandis J.P., "Induced voltage measurements on an experimental distribution line during nearby rocket triggered flashes", IEEE Trans. Power Delivery, **11** (1996) 980.

Barrow J.D., Impossibility. *The limits of science and the science of limits*, Oxford University Press, Oxford, 1998.

Bertero M., "Linear inverse and ill-posed problems", Adv. Electron. Electron Phys., **75** (1989) 1.

Bleistein N., Cohen J.K., "Nonuniqueness in the inverse source problem in acoustic and electromagnetics", J. Math. Phys., **18** (1977) 194.

Cooray V., "Predicting the spatial and temporal variation of the electromagnetic fields, currents, and speeds of subsequent return strokes", IEEE Trans. Electromag. Compat., **40** (1998) 427.

Cooray V., Ed., *The lightning flash*, IEE Power & Energy Series 34, London, 2003.

Cooray V., Nucci C.A., Rachidi F., Eds., "Selected papers from the 26th international conference on lightning protection", J. Electrostatics, **60** (2004).

Cvetić J.M., Stanić B.V., Heidler F., "Properties of the channel discharge function in the generalised lightning travelling current source return stroke model", Proc. 13th Zurich Symp. Electromagnet. Compatib., Zurich, Feb 16–18, 1999a.

Cvetić J.M., Heidler F., Schwab A., "Light intensity emitted from the lightning channel: comparison of different return-stroke models" J. Phys. D: Appl. Phys., **32** (1999b) 273.

de la Rosa F., Valdivia R., Péres H., Loza J., "Discussion about the inducing effects of lightning in an experimental power distribution line in Mexico", IEEE Trans. Power Delivery, **3** (1988) 1080.

Durand E., *Électrostatique*, Tome I, Masson, Paris, 1964.

Fuller B.D., Ward S.H., "Linear system description of the electrical properties of rocks", IEEE Trans., **GE-8** (1970) 7.

Gardner R.L., Ed., *Lightning electromagnetics*, Hemisphere, New York, 1990.

Heidler F., Cvetić J.M., Stanić B.V., "Calculation of lightning current parameters", IEEE Trans. Power Delivery, **14** (1999) 399.

Horvát T., "Standardization of lightning protection based on the physics or on the tradition?" J. Electrostatics, **60** (2004) 265.

Ishii M., Michishita K., Hongo Y., "Experimental study of lightning induced voltage on an overhead wire over lossy ground", IEEE Trans. Electromag. Compat., **40** (1999) 39.

Jones J.E., "On the drift of gaseous ions", J. Electrostatics, **27** (1992) 283.

Jones J.E., Dupuy J., Schreiber G.O.S., Water R.T., "Boundary conditions for the positive direct-current corona in a coaxial system", J. Phys. D: Appl. Phys., **21** (1988) 322.

Keller G.V., Frischknecht F.C., *Electrical methods in geophysical prospecting*, Pergamon Press, Oxford, 1966.

Le Vine D.M., Meneghini R., "Electromagnetic fields radiated from a lightning return-stroke: application of an exact solution to Maxwell's equation", J. Geophys. Res., **83** (1978) 2377.

Manneback C., "Radiation from emission lines", J. AIEE, **42** (1923) 95.

Nucci C.A., Mazzetti C., Rachidi F., Ianoz M., "On lightning return-stroke models for LEMP calculations", Proc. 19th Int. Graz. Conf. on Lightning Protection, 1988.

Nucci C.A., Rachidi F., Ianoz M.V., Mazzetti C., "Lightning-induced voltages on overhead lines", IEEE Trans. Electromag. Compat., **35** (1993) 75.

Paul C.R., "Crosstalk", in *Handbook of electromagnetic compatibility*, R. Perez Ed., Academic Press, New York, 1995.

Plumer J.A., "Lightning", in *Handbook of electromagnetic compatibility*, R. Perez Ed., Academic Press, New York, 1995.

Rakov V.A., Uman M., *Lightning. Physics and effects*, Cambridge University Press, Cambridge, 2003.

Maruvada P.S., *Corona performance of high-voltage transmission lines*, RSP, Baldock, England, 2000.

Schelkunoff S.A., *Advanced antenna theory*, John Wiley, New York, 1952.

Schelkunoff S.A., Friis H.J., *Antennas*: *theory and practice*, John Wiley, New York, 1952.

Smyth J.B., Smyth D.C., "Lightning and its radio emission", Radio Sci., **14** (1976) 977.

Takahashi Y., Yoshida M., Anma Y., Kobayashi S., Endo M., "Thickness and luminosity distribution of positive corona sheath in air", J. Phys. D: Appl. Phys., **21** (1982) 639.

Tesche F.M., Ianoz M.V., Karlsson T., *EMC analysis methods and computational models*, John Wiley, New York, 1997.

Thottappillil R., Uman M.A., Theethayi N., "Electric and magnetic fields from a semi-infinite antenna above a conducting plane", J. Electrostat., **62** (2004) 209.

Traub J.F., Werschulz A.G., "Linear ill-posed problems are all solvable on the average for all gaussian measures", The Math. Intelligencer, **16(2)** (1994) 42.

Uman M.A., Krider E.P., "A review of natural lightning: experimental data and modeling", IEEE Trans. Electromag. Compat., **24** (1982) 79.

Wait J.R., *Geo-electromagnetism*, Academic Press, New York, 1982.

Waters R.T., "Spark breakdown in non-uniform fields", in *Electrical breakdown of gases*, J.M. Meek and J.D. Craggs Eds., John Wiley, New York, 1978.

CHAPTER 3

Effects of Geomagnetic Storms on Long Distance AC Transmission Systems

E. De Tuglie and M. La Scala

Abstract

Solar Induced Currents (SICs) are the cause of many detrimental effects on power systems. It is worth to note that the scientific interest for this topic is cyclical and follows the relevant periods of the solar activity. The large blackout of North East USA and Canada of 1989 linked to a large solar activity definitively marks a milestone in the scientific research and activity in this field. It is also worth noting that sometimes this issue becomes a sort of scapegoat to explain inexplicable phenomena or coincidences as in the case of the numerous blackouts that occurred worldwide in the Summer of 2003, which were improperly related to a particularly high solar activity. In this chapter, we limit our analysis to their effect on long transmission line and the beneficial effect that some new equipment, such as Static Var Compensators (SVCs), can play in preventing malfunction when an appropriate coordinate compensation strategy is applied.

3.1 Introduction

The ejection of particles with particular trajectories caused by solar flares could interact with the earth's magnetic field. A little later than the occurrence of the solar flare (about twenty to forty hours), these particles can cause relatively rapid transient variations in the earth's magnetic field, well-known as geomagnetic disturbances or geomagnetic storms. This magnetic interaction can cause problems on electric power system and on the communications system. This is primarily due to the fact that the geomagnetic disturbances produce an induced Earth-Surface Potential (ESP). The induced potential, of course, increases as the size of the system increases. Consequently, the induced ESP gives rise to spurious currents in long transmission lines and equipment that are in some way grounded at points geographically remote from each other. In the case of

electric power systems the trend is to build longer lines which are able to cover large geographical areas. For this reason some of the problems caused by geomagnetic storms can become more pronounced. Several studies on the occurrence of relevant ejection of particles by solar flares have been conducted in the past and it has been observed that this phenomenon has a cyclic characteristic with an estimated period of about eleven years.

In power systems, the spurious currents due to the geomagnetic disturbances are called Solar Induced Currents (SICs). Some measurements of SICs on actual power systems are reported in the literature (Albertson *et al*., 1973, Boteler *et al*., 1982, Pijola, 1985). As far as the effects on equipment and anomalous operations of power systems is the main concern, it was shown in the literature that they all can nearly be traced to the presence of the SIC in the windings of transformers (Bolduc and Aubin 1977 a; Albertson *et al*., 1981; Aspnes and Akasofu 1981; Aspnes *et al*., 1981; Boteler *et al*., 1989; Ringlee and Stewart 1989). Since the SICs have a fundamental period of several minutes (from 6 to 15 minutes), they can be considered quasi-DC and their main effect is the simultaneous AC and DC excitation of energised transformers. SICs have been measured in excess of 100 A in transformer neutral leads in extreme cases (Albertson *et al*., 1974).

The magnitude of the SIC depends on the geology of the material through which it is passing (Wrubel, 1992). In fact, large deviations of subsurface resistances are encountered on land. In particular, igneous rock presents a high resistance to the SICs. When a high resistance is encountered, the current is diverted to any parallel path that presents a lower resistance to the current. If power lines cross the igneous rock formation and connections are available for the current to gain access to the power lines, the currents will appear on the power lines (Pijola, 1985).

The magnitude of the SIC can be many times greater than the AC excitation current, and thus causes half-cycle saturation of the core. This situation gives rise to an anomalous increase in the magnetising current and it will display a pulse of short duration and high magnitude. This fact can cause fluctuations in system voltage unusual VAR flow, generation of harmonics, relaying problems, internal localised heating in transformers and, in general, a reduction of transfer capability of the power system. In this chapter, we show how the capability of AC transmission lines decreases significantly when the magnitude of SICs increases. We also compare these results with the ones relative to the presence of Static Var Compensator (SVC). It is also shown how the presence of SVC mitigates the effect of SIC if an appropriate coordinated compensation strategy is adopted. The control law is derived from optimal control theory and a decentralisation technique.

3.2 System Representation

In order to study the detrimental effect of SICs in terms of capability reduction of long AC transmission lines, in this work, we consider a linearised model, which represents an equivalent generating unit connected to an infinite bus by a double circuit overhead transmission line as shown in Fig. 3.1.
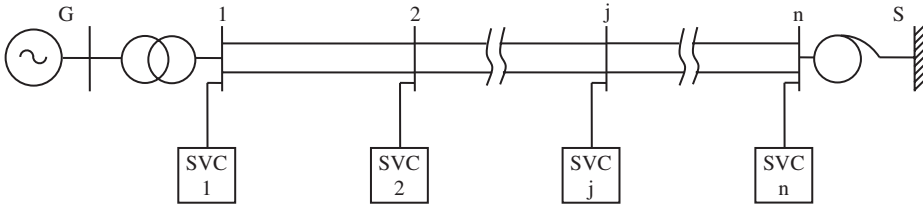
Fig. 3.1. Single-line diagram of a long distance AC transmission system.

The transmission line comprises L sections of equal length. The line is connected at one of its extremity by a transformer and at the other by an autotransformer. The controlled reactive compensation is provided by the n SVC located in Fig. 3.1. To derive the overall system representation, the voltage at bus S (infinite bus) is taken as reference. Each consecutive section of the transmission line is represented by an equivalent π configuration and the whole transmission network, including the transformers at both the sending and receiving end, is described, by neglecting network dynamics, by a proper set of algebraic equations in terms of nodal voltages and currents. The equivalent generating unit is assumed to be equipped with a static excitation system and is represented by a third-order model based on Parks equations.

In order to understand how the effects and remedial actions of the SIC have been represented, the modelling of the following components requires a more detailed description.

3.2.1 Power transformer and autotransformer representation

The effect of SIC can be modelled like a DC source acting simultaneously with AC source on the equivalent circuit of a transformer.

Straight lines without introducing significant error can represent the magnetising curve (Bolduc *et al.*, 1977 a). This assumption is particularly applicable to grain-oriented silicon steel because the saturation knee is sharp. As denoted in Fig. 3.2 we assume that ωL_1 and ωL_2 are the slopes for the unsaturated and saturated part of the magnetisation curve, respectively.

The amplitude of direct current must be regarded as the average value of the magnetising current. The occurrence of direct current, like a geomagnetic current, can move the normal operating conditions in a saturated part of the magnetising curve. For this reason, the magnetising current displays a pulse of short duration and high magnitude at each cycle.

In our study, we refer to ωt_1 and ωt_2 as the saturation and desaturation angle (Bolduc and Aubin, 1977 b). A parameter A can be defined such that $\omega t_1 = \pi - \alpha$ and $\omega t_1 = \pi + \alpha$ for a large power transformer. Under the realistic hypothesis that the resistance
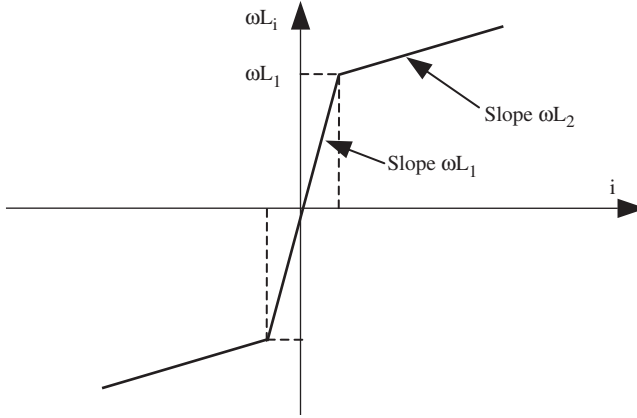
Fig. 3.2. Representation of the magnetising curve.

of the primary winding can be neglected, a parameter A can be defined as follows:

$$A = \frac{V_0}{\omega L_2 + \omega L_\mathrm{p}} \tag{3.1}$$

where:

V_0 represents the normal crest voltage of the primary winding of the transformer, ωL_2 is the slope of the saturated part of the magnetising curve and ωL_p is the primary leakage reactance added to the primary network inductance. Equation 3.1 represents the magnetising current component in saturated conditions. If we denote $\bar{i}$ as the average magnetising current due to the DC equivalent generator of ESP applied to the overall circuit resistance, it is possible to obtain

$$\frac{\bar{i}}{A} = \frac{1}{\pi} \left(\sin \alpha - \alpha \cos \alpha \right) \tag{3.2}$$

As proposed in (Bolduc *et al.*, 1977 b), converting the expression for magnetising current into Fourier series, the fundamental (I_1) and harmonics of higher order can be readily available:

$$\frac{I_1}{A} = \frac{1}{\pi} \left(\alpha - \sin \alpha \cos \alpha \right) \tag{3.3}$$

$$\frac{I_n}{A} = \frac{2}{\pi \left(n^2 - 1 \right)} \left(\frac{\cos \alpha \sin n\alpha}{n} - \sin \alpha \cos n\alpha \right) \quad n = 2, 3, \ldots \tag{3.4}$$
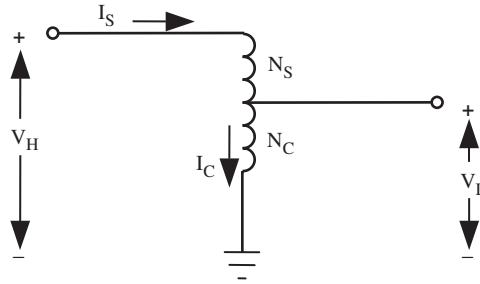
Fig. 3.3. Definitions for Eq. 3.6.

These harmonic components are used to calculate the increase of the reactive power due to SIC using the relationship (Albertson *et al*., 1981):

$$Q = \sqrt{3}V \left(\sum_{i=1}^{n} I_i^2 \right)^{1/2} \tag{3.5}$$

where:

Q = reactive power;
V = RMS value of applied sinusoidal phase to phase voltage;
I_i = RMS value of the i-th harmonic component of exciting current;
n = highest order harmonic studied.

In order to derive an analogous formulation of the problem when an autotransformer is used, an effective value of $\bar{i}$ is calculated to account for unequal SIC flows in the series and common winding (Albertson *et al*., 1981). By examining the Magnetomotive forces (MMF's) due to each winding, the following relationship can be derived.

$$\bar{i} = \left| \frac{NI_S + I_C}{N + 1} \right| \tag{3.6}$$

as defined in Fig. 3.3, where $N = \frac{N_S}{N_C}$.

In both cases (transformer and autotransformer) the excess of reactive power due to saturation of the core evaluated as in Eq. 3.5 is taken into account by introducing an equivalent magnetising reactance x_{meq} in the usual model of the transformer. This representation is in accordance with some SIC monitoring system such as the one reported in Bolduc *et al*., (1977 b).

3.2.2 Static VAR compensator representation

Each SVC consists of a thyristor-controlled reactor with fixed capacitor (TCR/FC), as shown in Fig. 3.4.
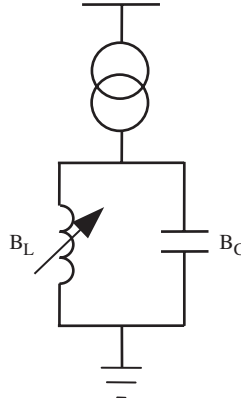
Fig. 3.4. Single-phase equivalent circuit of a Static VAR Compensator (TCR/FC type).
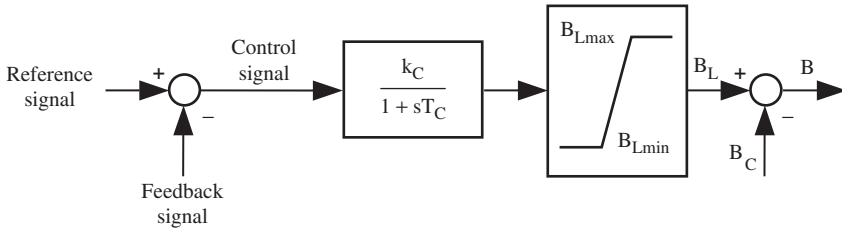
Fig. 3.5. Block diagram of a static VAR system with automatic voltage regulator.

Each SVC with its firing control system is represented, for simplicity, by a first-order model characterised by a gain and a time constant; time delays in the SVCs are neglected (Happ *et al.*, 1978, Newell *et al.*, 1980, Brucoli *et al.*, 1985).

Figure 3.5 shows the control block diagram of the generic SVC.

3.3 Coordinated Compensation Strategy

After linearisation of the system equations about a given operating point, the overall system can be represented by the following equations in the state space form as:

$$\dot{\mathbf{x}} = \mathbf{A}\mathbf{x} + \mathbf{B}\mathbf{u} \tag{3.7}$$

$$\mathbf{y} = \mathbf{F}\mathbf{x} + \mathbf{M}\mathbf{u} \tag{3.8}$$

where:

$\mathbf{x} = \begin{bmatrix} \mathbf{x}_G^T & \mathbf{x}_c^T \end{bmatrix}^T$ is a $(3 + n)$-dimensional state vector, $\mathbf{u} = \begin{bmatrix} \mathbf{u}_G^T & \mathbf{u}_c^T \end{bmatrix}^T$ a $(l + n)$-dimensional control-input vector and $\mathbf{y} = \begin{bmatrix} \mathbf{y}_G^T & \mathbf{y}_c^T \end{bmatrix}^T$ a $(3 + n)$-dimensional output

vector. The vectors $\mathbf{x}_G = [\boldsymbol{\Delta\delta}, \mathbf{p}\boldsymbol{\Delta\delta}, \boldsymbol{\Delta\psi_f}]^T$ and $\mathbf{y}_G = [\boldsymbol{\Delta P_G}, \mathbf{p}\boldsymbol{\Delta\delta}, \boldsymbol{\Delta V_G}]^T$ include the state and output variables, respectively, of the equivalent machine. Note that P_G and V_G denote generated active power and voltage at terminals of the generating unit and δ is the rotor angle.

The vectors $\mathbf{x}_c = [\boldsymbol{\Delta B_1}, \boldsymbol{\Delta B_2}, \ldots, \boldsymbol{\Delta B_n}]^T$, $\mathbf{u}_c = [\boldsymbol{\Delta u_{c1}}, \boldsymbol{\Delta u_{c2}}, \ldots, \boldsymbol{\Delta u_{cn}}]^T$ and $\mathbf{y}_c = [\boldsymbol{\Delta V_{c1}}, \boldsymbol{\Delta V_{c2}}, \ldots, \boldsymbol{\Delta V_{cn}}]^T$ include the states. The inputs and the outputs relative to the n SVCs which have been located on the transmission line: B_i represents the susceptance of the i-th SVC and ΔV_{ci} is the deviation of voltage at the SVC busbars. $\mathbf{A}$, $\mathbf{B}$, $\mathbf{F}$ and $\mathbf{M}$ are matrices whose dimensions are determined by the dimensions of the vectors.

A way to systematically derive a robust control such that the system results insensitive to DC current disturbance is, to apply the theory of optimal control and then to develop a decentralisation procedure. For this purpose, we assume that the system is controllable and observable, and that the behaviour of the system outputs can be assessed by the quadratic index:

$$J = \int_0^\infty \left(\mathbf{y}^T \mathbf{Q} \mathbf{y} + \mathbf{u}^T \mathbf{R} \mathbf{u} \right) dt \tag{3.9}$$

where, $\mathbf{Q}$ is a $(3 + n) \times (3 + n)$ positive semi-definite constant matrix and $\mathbf{R}$ is a $(l + n) \times (l + n)$ positive definite constant matrix. The elements of $\mathbf{Q}$ and $\mathbf{R}$ have to be chosen to reflect the allowable ranges of both the output and control variables (De Sarkar and Dharma Rao, 1973). As is well-known, the optimal control law which minimises the index J subject to Eqs. 3.7 and 3.8 is unique and is given by a solution of a problem that involve the Riccati equations as reported in (Athans *et al.*, 1974):

$$\mathbf{u} = -\mathbf{K}\mathbf{x} \tag{3.10}$$

With this assumption the $\mathbf{y}$ vector can be expressed as:

$$\mathbf{y} = -\mathbf{H}\mathbf{x} \tag{3.11}$$

where $\mathbf{H} = \mathbf{F} - \mathbf{M}\mathbf{K}$.

It is important to note that the matrix $\mathbf{K}$ appearing in Eq. (3.10) is a full matrix and, consequently, the optimal control signal for the excitation system of the equivalent machine and for each SVC requires the feedback of all the states of the system. To circumvent the technical and economic difficulties imposed by the implementation of such an optimal control scheme of the centralised type, a decentralised control strategy can be developed. This control scheme should require local variables to be fed back for each dynamic component of the system. This objective can be reached by adopting a new control law, which presents the following structure:

$$\bar{\mathbf{u}} = -\mathbf{K}_d \mathbf{y} \tag{3.12}$$

where $\bar{\mathbf{u}} = \begin{bmatrix} \bar{\mathbf{u}}_G^T & \bar{\mathbf{u}}_c^T \end{bmatrix}^T$ is a $(1+n)$-dimensional vector and

$$\mathbf{K}_d = \text{block diag} \begin{bmatrix} \mathbf{k}_{dG}, k_{d1}, k_{d2}, \ldots, k_{dj}, \ldots, k_{dn} \end{bmatrix}^T \qquad (3.13)$$

The elements of 1×3 submatrix $\mathbf{k}_{dG}$ are the feedback gains of the excitation system control signal, whereas the elements of the 1×1 generic sub-block k_{dj} are the feedback parameters of the control signal relative to the j-th SVC.

The new control law $\bar{\mathbf{u}}$ should be strictly related to the previously derived optimal control law $\mathbf{u}$ in order to assure for the system, a performance as "near" as possible to the performance assured by $\mathbf{u}$. Noting that, by Eq. 3.11, $\bar{\mathbf{u}}$ can be expressed as:

$$\bar{\mathbf{u}} = -\mathbf{K}_d \mathbf{H} \mathbf{y} \qquad (3.14)$$

the most obvious approach for determining $\mathbf{K}_d$ is to relate $\mathbf{u}$ with $\bar{\mathbf{u}}$ in some norm and to derive $\mathbf{K}_d$ as the solution of a minimum norm problem (De Sarkar and Dharma Rao, 1973, Athans and Falb, 1974, Ben-Israel and Greville, 1974, Happ and Wirgau, 1978, Newell *et al.*, 1980, Brucoli *et al.*, 1985). Following this strategy, from Eqs (3.4) and (3.14) the following residual vector can be defined:

$$\mathbf{q} = \bar{\mathbf{u}} - \mathbf{u} = (\mathbf{K} - \mathbf{K}_d \mathbf{H}) \, \mathbf{x} \qquad (3.15)$$

where $\mathbf{q} = \begin{bmatrix} q_G, q_1, q_2, \ldots, q_n \end{bmatrix}^T$ is a $(1+n)$-dimensional vector.

For a given $\mathbf{x}$, the $\mathbf{K}_d$ matrix can be found by minimising the Euclidean norm of the residual vector (Ben-Israel and Greville, 1974), namely:

$$\min_{\mathbf{K}_d} \|\mathbf{q}\|^2 \qquad (3.16)$$

To determine the matrix $\mathbf{K}_d$, let matrices $\mathbf{K}$ and $\mathbf{H}$ be decomposed into:

$$\mathbf{K} = \begin{bmatrix} \mathbf{k}_G \\ \mathbf{k}_1 \\ \mathbf{k}_2 \\ \vdots \\ \mathbf{k}_j \\ \vdots \\ \mathbf{k}_n \end{bmatrix} \quad \begin{bmatrix} \mathbf{h}_G \\ \mathbf{h}_1 \\ \mathbf{h}_2 \\ \vdots \\ \mathbf{h}_j \\ \vdots \\ \mathbf{h}_n \end{bmatrix} \qquad (3.17)$$

where the matrices $\mathbf{k}_G$ and $\mathbf{k}_j$ $(j = 1, 2, \ldots, n)$ have dimensions $l \times (3+n)$; the matrices $\mathbf{h}_G$ and $\mathbf{h}_j$ $(i = 1, 2, \ldots, n)$ have dimensions $3 \times (3+n)$ and $l \times (3+n)$, respectively.

Then, from Eq. 3.15 we obtain:

$$\mathbf{q}_G = \left(\mathbf{k}_G - \mathbf{k}_{dG}\mathbf{h}_G\right)\mathbf{x} \tag{3.18}$$

$$\mathbf{q}_j = \left(\mathbf{k}_j - \mathbf{k}_{dj}\mathbf{h}_j\right)\mathbf{x} \quad j = 1, 2, \ldots, n \tag{3.19}$$

Now, considering that Eq. 3.16 can be separated into

$$\min_{\mathbf{k}_{dG}} \left\| \mathbf{q}_G \right\|^2 \tag{3.20}$$

$$\min_{\mathbf{k}_{dj}} \left\| \mathbf{q}_j \right\|^2 \quad j = 1, 2, \ldots, n \tag{3.21}$$

the submatrices $\mathbf{k_{dG}}$ $\mathbf{h_G}$ and $\mathbf{k_{dj}}$ $(j = 1, 2, \ldots, n)$ can be derived as minimum norm least-square solutions of Eqs. 3.20 and 3.21, respectively (Ben-Israel and Greville, 1974):

$$\mathbf{k}_{dG} = \mathbf{k}_G \mathbf{k}_G^+ \tag{3.22}$$

$$\mathbf{k}_{dj} = \mathbf{k}_j \mathbf{k}_j^+ \tag{3.23}$$

where the superscript $+$ denotes the pseudoinverse.

Once the matrix $\mathbf{K}_d$ has been determined, the control signals for the equivalent generator and for each SVC are expressed as

$$\bar{\mathbf{u}}_G = -\mathbf{k}_{dG}\mathbf{y}_G \tag{3.24}$$

$$\bar{\mathbf{u}}_{cj} = -\mathbf{k}_{dj}\mathbf{y}_j \quad j = 1, 2, \ldots, n \tag{3.25}$$

where $\mathbf{y}_{cj} = \Delta \mathbf{V}_{cj}$.

3.4 Test Results

The procedure illustrated in the previous section has been applied to the double-circuit 765 kV, 2000 km AC transmission line. The system data used in the simulation studies are the following:

- *Individual generator of the equivalent generating unit*
  rating = 615 MVA, 15 kV, 60 Hz, $x_d = 1.45$ p.u., $x_q = 1.00$ p.u.

  $x_{md} = 1.00$ p.u., $x_d' = 0.5$ p.u., $H = 4$ S, $D = 0.011$ p.u. MW s rad^{-1}, $T_{d0}' = 9.5$ s;

- *Excitation system of individual generator*
  $k = 200$, $E_{fdmax} = 4.6$ p.u., $E_{fdmin} = -4.6$ p.u.;

- *Single-circuit transmission line*
  positive-sequence inductance $l_d = 0.827 \times 10^{-3}$ H km^{-1}, positive-sequence capacitance $c_d = 0.0141 \times 10^{-6}$ F km^{-1}, zero-sequence inductance $l_0 = 3\,l_d$, zero-sequence capacitance $c_0 = c_d/1.50$;

– *Sending-end transformer*
   14×615 MVA, 15/765 kV, 60 Hz, ΔY secondary grounded,

   $x_T = 0.15$ p.u., $\omega L_2 = 0.22$ p.u., $\omega L_p = 0.05$ p.u. on high voltage side,

   all banks consist of three single-phase units;

– *Receiving-end autotransformer*
   9×1050 MVA, 765/500 kV, 60 Hz, Y neutral grounded,

   $x_T = 0.10$ p.u., $\omega L_2 = 0.38$ p.u., $\omega L_p = 0.04$ p.u. on high voltage side,

   all banks consist of three single-phase units;

– *SVCs at sending and receiving-end substations*
   $K_c = 50$, $T_c = 0.15$ s, $x_T = 0.2114$ p.u. (on 2643 MVA base), linear control
   range: 200 MVAR (ind.), 1500 MVAR (cap.);

– *SVCs at intermediate Substations*
   $K_c = 50$, $T_c = 0.15$ s, $x_T = 0.1586$ p.u. (on 2643 MVA base), linear control
   range: 800 MVAR (ind.), 1500 MVAR (cap.);

– *SVC transformers*
   1500 MVA, 765/15 kV, 60 Hz, $Y\Delta$ primary grounded,

   $x_T = 0.15$ p.u., $\omega L_2 = 0.54$ p.u., $\omega L_p = 0.05$ p.u. on high voltage side,

   all banks consist of three single-phase units;

The Surge Impedance Loading (SIL) of one circuit is 2643 MVA and this is taken as the MVA base. There are 14 hydrogenerating units with identical characteristics operating at the sending end and the total rated power available at bus G is 8610 MVA. The transmission line comprises five sections of equal length (400 km). Six SVCs of the TCR/FC type were placed in the system. The amount of fixed shunt compensation and the linear control range of the SVCs were determined by performing accurate stability studies. In practice, under normal conditions, the line operates with the controlled reactors partially inserted. When the transmitted power is null, the controlled reactors are inserted completely.

After deriving the system representation, we applied the design procedure described in the preceding section. Thus, by considering $P = 0.9$ p.u. as operating point for the system with a flat voltage profile of 1.0 p.u. and by assuming $\mathbf{Q} = \text{diag}[0.2, 0.01, 0.6, 0.1, 0.15, 0.4, 0.5, 0.6, 0.6]$ and $\mathbf{R}$ as a unit matrix, $\mathbf{K_d}$ was evaluated and the following feedback control signals for the excitation system of the equivalent generating unit and for the six SVCs were found:

$$\bar{u}_G = -0.2268 \Delta P_G + 0.0097 \Delta \dot{\delta} - 0.1124 \Delta V_G$$
$$\bar{u}_{c1} = -0.8926 \Delta V_{c1}$$
$$\bar{u}_{c2} = -0.6042 \Delta V_{c2}$$
$$\bar{u}_{c3} = -0.5151 \Delta V_{c3}$$
$$\bar{u}_{c4} = -0.5077 \Delta V_{c4}$$
$$\bar{u}_{c5} = -0.5530 \Delta V_{c5}$$
$$\bar{u}_{c6} = -0.4825 \Delta V_{c6}$$

Table 3.1. Comparison of system dominant eigenvalues for different control configurations and different values of SIC's magnitude.

Control configuration	Eigenvalues	
	$i = 0$ [A]	$i = 100$ [A]
Without SVCs	-0.03	-0.01
	$-0.28 \pm \text{j}3.58$	$-0.37 \pm \text{j}2.86$
With SVCs	-0.73	-0.69
	$-1.51 \pm \text{j}4.54$	$-1.63 \pm \text{j}4.54$

To test the system small system disturbance stability and to make comparisons, the dominant eigenvalues of the system are listed in Table 3.1 for the above-mentioned control configuration and under two SICs magnitude conditions. This table shows how the presence of the SVCs improves the stability. In addition, with a fixed system loading condition near the SIL ($P = 0.9$) and SIC magnitude of 100 A, the dominant eigenvalues relative to the proposed control have a negative real part and are almost insensitive to geomagnetic currents.

It is interesting to investigate how the presence of SVCs mitigates the effects of SIC with regard to the maximum transmissible power. In order to derive the capability of the transmission system, we gradually increased the load at the receiving end of the line. Through load-flow-analysis and successive linearisations, it was possible to carry on eigenvalues analysis. The maximum capability was obtained corresponding to the first operating point characterised by an unstable eigenvalue. Figures 3.6 and 3.7 show how a significant
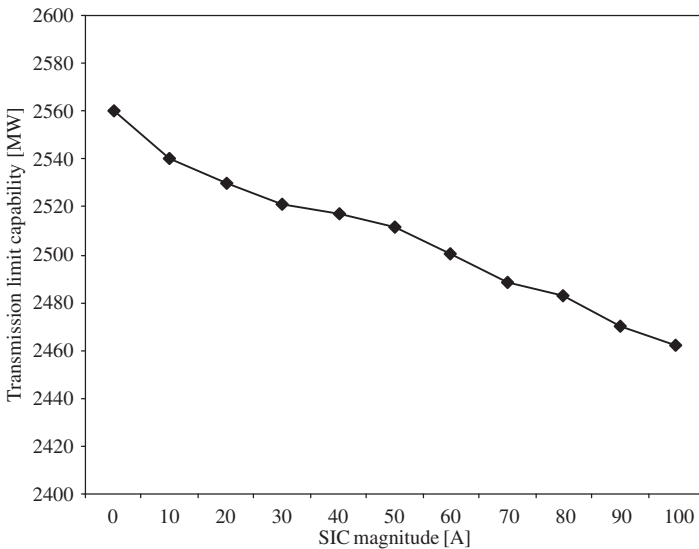
Fig. 3.6. Transmission limit capability without SVCs.
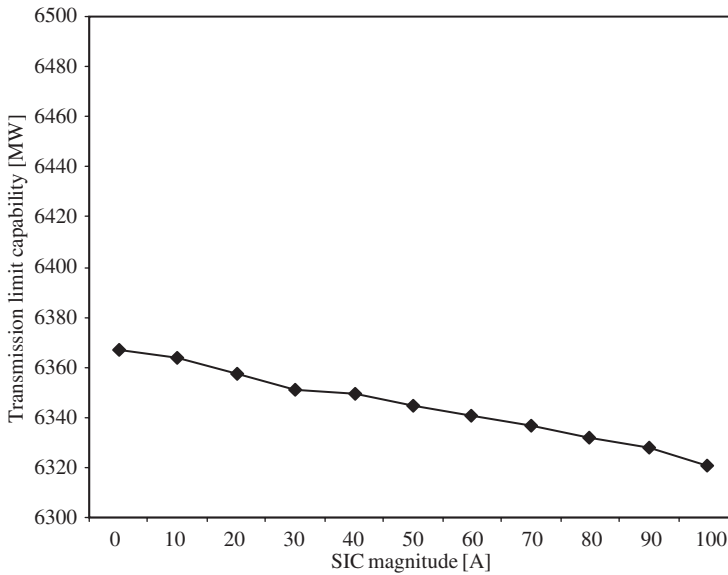
Fig. 3.7. Transmission limit capability with SVCs.

decrease of the maximum transmitted power can be observed when no control is applied. In addition, the presence of the coordinated control makes the system almost insensitive to SIC. Of course the line capability is significantly higher when SVCs are adopted.

3.5 Conclusions

In this chapter, a methodology for improving load capability of a long AC transmission lines has been investigated. In the work, it was shown how the maximum-transferred power on the transmission system is seriously affected by the presence of SICs. A coordinated control of SVCs at intermediate stations of the transmission system seems to be very effective in increasing transmission limits and makes the system almost insensitive to SICs. It should be considered, however, that in the past, experts reported a coincidence between the magnetic storms and tripping of SVCs likely due to protection malfunction of these components. This aspect should be considered in the design of SVCs protection systems in order to ensure the results reported in this work.

References

Albertson V.D., Kappenman J.G., Mohan N., Skarbakka G.A., "Load-flow studies in the presence of geomagnetically-induced currents", IEEE Trans. on Power Apparatus and Systems, **PAS-100(2)** Feb. (1981).

Albertson V.D., Miske S.A., Thorson Jr. J.M., "The effects of geomagnetic storms on electrical power systems", IEEE Trans. on Power Apparatus and Systems, **PAS-93(4)** July/August (1974).

Albertson V.D., Thorson Jr. J.M., Clayton R.E., Tripathy S.C., "Solar induced currents in power systems: cause and effects", IEEE Trans. on Power Apparatus and Systems, **PAS-92(2)**, Mar./Apr. (1973).

Aspnes J.D., Akasofu S.I., "Effect of solar induced current on autotransformer tertiary windings", IEEE Trans. on Power Apparatus and Systems, **PAS-101(3)** Mar. (1981).

Aspnes J.D., Merritt R.P., Akasofu S.I., "Harmonic generation in transformers related to DC excitation and system loading", IEEE Trans. on Power Apparatus and Systems, **PAS-100(4)**, Apr. (1981).

Athans M., Falb P.L., *Optimal control*, McGraw-Hill, New York, (1974).

Ben-Israel A., Greville T.M.E., *Generalized inverses: theory and applications*", John Wiley and Sons, New York, 1974.

Bolduc L., Aubin J., "Effects of direct currents in power transformers – Part I – A general theoretical approach", Electr. Pow. Sys. Res., (1), (1977a).

Bolduc L., Aubin J., "Effects of direct currents in power transformers – Part. II – Simplified calculations for large transformer", Electr. Pow. Sys. Res., **1** (1977b).

Boteler D.H., Shier R.M., Watanabe T., Horita R.E., "Effects of geomagnetically induced currents in the B.C. Hydro 500 kV system", IEEE Trans. on Power Delivery, **4(1)** Jan. (1989).

Boteler D.H., Watanabe T., Shier R.M., Horita R.E., "Characteristic of geomagnetically induced currents in the B.C. Hydro 500 kV system", IEEE Trans. on Power Apparatus and Systems, **PAS-101(6)** Jun. (1982).

Brucoli M., Torelli F., Trovato M., "A decentralized control strategy for dynamic shunt VAR compensation in interconnected power system", Proc. Inst. Electr. Eng., Part C, **132** (1985).

De Sarkar A.K., Dharma Rao M., "Stabilization of a synchronous machine through output feedback control", IEEE Trans. on Power Apparatus and Systems, **PAS-92** (1973).

Happ H.H., Wirgau K.A., "Static and dynamic VAR compensation in system planning", IEEE Trans. on Power Apparatus and Systems, **PAS-97**, (1978).

Newell R.J., Risan M.D., Raatz D.D., Haut R.L., "Staged field testing of the Victory Hill static VAR control", IEEE Trans. on Power Apparatus and Systems, **PAS-99** (1980).

Pijola R., "On currents induced in power transmission systems during geomagnetic variations", IEEE Trans. on Power Apparatus and Systems, **PAS-104(10)**, Oct. (1985).

Ringlee R.J., Stewart J.R., "Geomagnetic effects on power systems", IEEE Power Eng. Rev., July (1989).

Wrubel J.N., "Monitoring program protects transformers from geomagnetic effects", IEEE Comp. Appl. in Power., **5(1)** Jan. (1992).

This page intentionally left blank

CHAPTER 4

Evaluation of the AC Interferences between Transmission Lines and Metallic Underground Structures

S. Bruno, E. De Tuglie, and M. La Scala

Abstract

In this chapter, the influence of AC currents on metallic structures and pipelines is addressed. An approach for evaluating currents due to High Voltage (HV) AC overhead transmission line is developed. The basic contribution of this chapter is given by a comparison between analytical calculations and on-the-field measurements in order to give to the reader the exact flavour of basic assumptions and their effect in real-life systems. Measurements were conducted on one of the most crowded corridors in Puglia (Italy), where six overhead HV power transmission lines and one natural gas pipeline coexist on the same passageway.

4.1 Introduction

The necessity to develop mathematical tools and representations for the computation of electromagnetic interference with underground metallic structures has originated from the general trend in the last few decades, of concentrating most utility infrastructures (overhead AC transmission lines, traction lines, telecommunication lines, pipelines for fluid transportation, etc.) in the same corridors. The interest towards the influence of AC on metallic structures is related to the possible resulting hazards regarding the safety of people coming into contact with the pipeline, the risks of damage to the pipeline coating and metal and the risks of damage to the equipment connected to the pipeline (cathodic protection systems) (CIGRÉ 36.02, 1995).

The influence of a power system on an adjacent metallic structure is usually studied as the sum of three complementary coupling effects: capacitive, inductive and conductive. The capacitive coupling effects usually appear when the pipeline is insulated from the earth and in the presence of aerial pipelines and aerial transmission lines.

Inductive coupling is generally experienced when a pipeline (aerial or underground) is in the proximity of High Voltage (HV) power transmission lines. The electric field produced by the power system, magnetically coupled with the metallic structure, gives rise to induced voltages whose magnitude depends on several factors and in dangerous cases, can reach values of few thousand volts.

The conductive interference is experienced when currents are flowing through the grounding of a power system (a transmission line, a power plant, an electrical installation) and a metallic victim infrastructure in the proximity is grounded. In this case, the insulating coating might be exposed to the potential difference between the local earth and the pipeline potential (arc discharges can occur on the surface of bitumen-coated pipelines for voltages of just 1000–1200 V).

Recently, there has been a growing interest towards the phenomenon of corrosion due to alternating currents, since up to some years ago, corrosion specialists considered DC currents to be the major cause of corrosion of metallic structures whereas AC effects were considered negligible. The study of physical motivations for AC corrosion is still under investigation (DIN EN 12954-2001, 2001) and is beyond the scope of this chapter, which is basically devoted to the computation of the influence on metallic underground structures. Nevertheless, a brief discussion of this phenomenon is worthy of consideration.

Electrolysis in AC is quite different from DC, in fact the corrosive effects are not symmetrical with reference to the positive and negative half-wave since a lot of secondary effects act in such a way that the final balance is a loss of material.

In earlier times, the corrosive effect of AC currents was considered negligible since it was perceived that the positive (anodic) 50 Hz half-wave lasted for a time (10 ms) which was too short to give rise to any significant change in the polarisation of the metallic structure due to the traditional cathode protection. At this stage of the research investigation, there is no doubt on the existence of corrosion due to AC currents, although the mechanisms are still not completely known. A ratio of 1/100 or 1/1000 is observed between the effects of corrosion due to AC with respect to DC; however, the phenomenon is still significant when compared to chemical corrosion. Nevertheless, the AC currents can still be dangerous when crater cracks are experienced or the integrity of the structure relies on thin materials or small-diameter pipes. It can be misleading to measure the danger caused by corrosion in these cases in terms of gram per year square centimetre, but it is better to evaluate the depth of the corrosive effects.

Current density influences the corrosion strongly; in fact, if density is high enough to create an increase in temperature locally, the corrosion can increase super-linearly.

Another important issue is the observation that, recently, the improvements in pipeline coating have increased the electrical insulation to earth. In fact, the specific resistance

increased from 5–50 kΩm^2 for bitumen coating to 100–1000 kΩm^2 for polyethylene. This constructive practice results in two harmful effects:

- Larger induced voltages on pipes; and
- A larger current density to the ground through small and unlikely imperfections of the coating.

In Europe, the attention towards AC corrosion effects started to grow in the 1980s, when few cases were deeply investigated, since no explanation in terms of DC effects was possible and cathodic protections requirements were met. It was realised, on the basis of this experience, that many AC corrosion cases were not recognised in the past. Only recently, it has been possible to have a unique framework of the basic parameters that should be jointly evaluated in order to prove that a particular corrosive activity is linked to AC.

The basic elements which should be taken into consideration before affirming the presence of AC corrosion are:

- Presence of an AC voltage on the pipeline or on the underground metallic structure;
- Presence of an imperfection or a defect in the coating;
- Presence of corrosion;
- pH > 10 in the soil around the structure;
- Shape of the corrosion, usually rounded;
- Corrosion of the metal larger than the defect of the coating;
- Voluminous corrosion products;
- After removing the corrosion products it is possible to observe a black, resistant, compact film made of magnetite;
- AC and DC current density is high;
- Ground resistance is low;
- Presence of calcium carbonate on the metallic surface;
- Presence of magnetite; and
- Presence of a type of stalactite in the ground close to the corrosion.

As far as we know on the basis of the experience accumulated up to now, it is possible to identify basic factors which increase the risk of corrosion due to AC currents:

- Voltages between pipes and the ground although characterised by a negative potential higher than the usual DC protection criterion, do not provide a sufficient level of protection if simultaneously, a AC current density higher than 20–30 A/m^2 is observed;
- Chemical composition and resistivity of the soil close to the coating imperfections play an important role on the corrosion speed;

- Soils rich in $CaCO_3$ and CO_2 increase the corrosion speed;

- An increase in the cathode protection currents can have a negative effect on AC corrosion by increasing the speed of the phenomenon; and

- The risk is higher for pipes having a higher insulation resistance to ground (for example, polyethylene coating) in the presence of small imperfections or defects (few square centimetres).

Finally, gas distribution companies and, in general, the community of civil engineers directly involved in building underground structures showed great interest towards these phenomena whose importance was not completely perceived in the past. This is due to the observation that AC currents in the ground are in general more frequent than DC currents, which can be observed basically close to the railway tracks. Furthermore, there is a general worry about the possibility of corrosion of iron in concrete buildings.

Another important motivation for evaluating voltages on pipelines or underground metallic structures is to avoid touch voltages exceeding safety limits. Usually different standards apply in different countries. In general, Italian standards consider 50 V a dangerous voltage. The same limit value (50 V) is proposed by ANSI/IEEE Std. 776-1987 (1987) for the systems at 60 Hz.

However, some Italian standards (CEI 103-10 and CEI 9-34) adopt the safety threshold of 60 V, a criterion derived by the CCITT Directives (1989). The ANSI/IEEE Std. 776-1987 (1987) also indicates 60 V as the safety threshold, historically adopted by electric power and railway companies.

We believe that more conservative limits should be assumed such as the one proposed by the NACE Standard RP-0177-95 (1995) or the Canadian standard (CAN/CSA C22.3 No. 6-M91, 1991), i.e. 15 V which takes into account the particular conditions and the extension of the contact which can occur for operators on this kind of installations.

The voltage thresholds of 50 and 60 V can be adopted for a continuous voltage exposure. When over-voltage is instantaneous due to, for example, the insurgence of a fault, the limit value is higher. Also in this case, different thresholds can be found in the international standards and recommendations. In CIGRÉ 36.02 (1995), the limit value of exposure for humans is 1000 V for 0.15–0.2 s. The CCITT Directives (1989) propose different values, depending on the duration of exposure: a limit of 2000 V can be considered for avoiding damage to people (for less than 0.1 s) and damage to the pipeline or connected equipment (less than 1 s).

Another aspect that should be considered is the effect of induced voltages on cathode protection and the apparatus connected to this important function. The superimposition of AC voltage on DC voltage can change the protection level ensured by the cathode protection system and introduce measurement errors which can reduce the effectiveness of the apparatus. The effects of AC components can be negligible only when characterised by current density lower than 30 A/m^2 (DIN EN 12954-2001, 2001). For higher values of current density, the usual levels of cathodic protection might

be inadequate. Since the phenomenon of AC corrosion is still under investigation, the normatives do not quantify the effects of interaction between AC induction and cathodic protection.

4.2 System Representation

Several computational methods have been developed for studying the effects of a power transmission line on nearby grounded metallic systems. In general, the methods can be divided into two categories: "long conductor" and "short conductor" approach (Dawalibi and Southey, 1989).

The "long conductor" approach, also defined as "circuit theory" approach, is a very well-known analytical method whose fundamentals have been developed in the 1920s by Carson (1926) and Pollaczek (1926). Most of these methods are aimed at evaluating the quasi-static self- and mutual impedances and admittances, which can be considered as the *trait d'union* between the field and circuit theory. "Long conductor" approaches cannot be used in the presence of short conductors, typically found in cathodic protection installations, in grounding systems and more generally, in mitigation and compensation systems.

These limitations are not encountered by the "short conductor" approaches that are based on the field theory and Maxwell equations, and which can be adopted differently in the presence of long and short conductors. Long conductors can always be considered as composed by small segments that are represented as short conductors. The "short conductor" approaches are very elegant but might require very strong computation efforts.

In this chapter, a universal method for the evaluation of the influence of a power transmission line on a metallic grounded system has been adopted. This method, proposed by Haubrich *et al*. (1994), has the advantages of being applicable to any system, having a simple formulation and requiring a reduced computation effort. A very important feature, regarding calculations and computational effort, is that its formulation allows taking advantage of the common practice in solving electrical power systems. A similar approach has also been described in CIGRÉ 36.02 (1995).

This approach has been chosen by us for its simplicity in the evaluation of induced voltages in metallic underground structures. In this chapter, through real-life examples, its effectiveness and degree of accuracy when compared to the on-the-field measurements are shown.

The first step is to consider three different systems: a power system responsible for the influence on other systems (denoted by the letter P), a long metallic victim system (denoted by V) and a shielding system (denoted by S).

The main idea is to transform the electromagnetic field generated by the power system into a current generator injecting the quantity $\boldsymbol{I}_{QPV}$ in a section of the system V. The victim system V (a pipeline, a telecommunication cable or any long grounded metallic system)

is represented by means of a nodal admittance matrix $\boldsymbol{Y}_V$. Each node of the victim system represents a section of the entire system V. The system has been divided into sections in order to represent the changes of the coupling with the system P due to sudden changes in the direction of the tracks, intersections, diameter variations, changes of the coating and of the thickness of the coating. For each node, the value $\boldsymbol{I}_{QPV}$ is calculated by means of the coupling matrix.

If in the zone of influence, there is also a grounded shielding system aimed at reducing the effects of influence on the victim system, the shield can be represented analogously to system V, separating the system into nodes and considering the induced current $\boldsymbol{I}_{QPS}$ injected at each node. In general, the relationship between the power system and the shield system can be represented by means of a coupling matrix.

Also, the mutual interference between the victim system and the shield cannot be neglected and is represented by means of a coupling matrix and a current induced by V on S ($\boldsymbol{I}_{QVS}$) and current induced by S on V ($\boldsymbol{I}_{QSV}$). Note that no currents are induced in the power system since the effects of other systems on P can be reasonably neglected. Figure 4.1 gives a schematic description of the approach.

An important feature of the proposed method is that it allows one to take into account the effects of inductive and conductive interference, which can simultaneously develop during faults in transmission line structures close to the metallic grounded system.
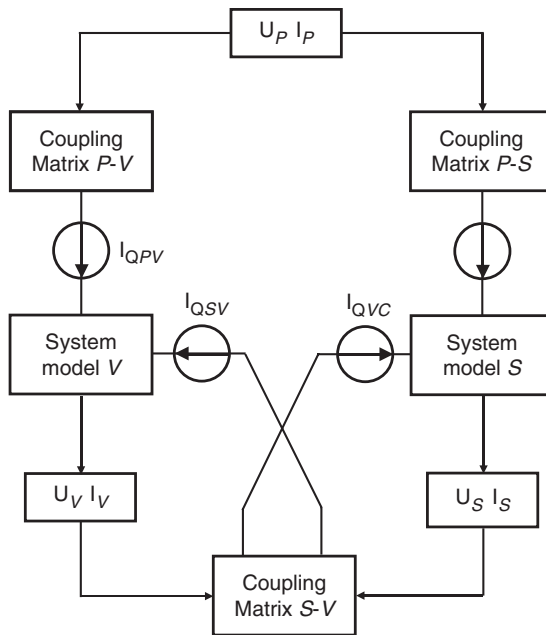
Fig. 4.1. Schematic description of the adopted method.
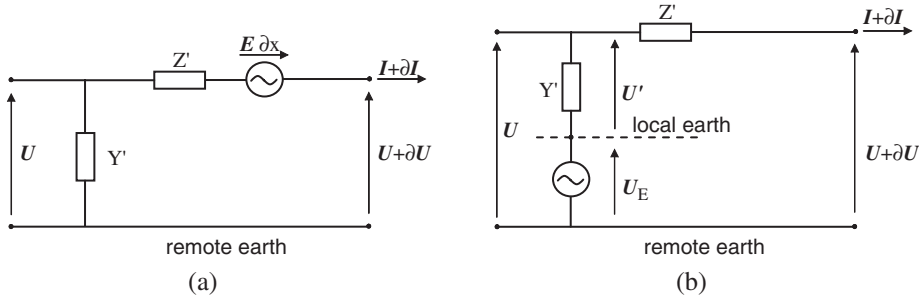
Fig. 4.2. Electric model representing the influence of the electric field E on an infinitesimal section ∂x of the influenced system for inductive interference (a) and conductive interference (b).

The inductive interference, due to the geometric and electric imbalance of the power system, can be evaluated for both normal and faulty conditions considering a small section ∂x of the system and a constant electric field E.

According to the scheme in Fig. 4.2(a), and considering that γ is the propagation coefficient and Z_W is the characteristic impedance, $Z' = \gamma \times Z_W$ and $Y' = \gamma / Z_W$, the following expressions can be derived:

$$\frac{\partial U}{\partial x} = E - \gamma \times Z_W \times I \tag{4.1}$$

$$\frac{\partial I}{\partial x} = -\frac{\gamma}{Z_W} U \tag{4.2}$$

Considering that the electric field is constant, Eqs. (4.1) and (4.2) can lead to:

$$\frac{\partial^2 U}{\partial x^2} = \gamma^2 \times U \tag{4.3}$$

$$\frac{\partial^2 I}{\partial x^2} = \gamma^2 \left(\frac{E}{\gamma \times Z_W} \right) \tag{4.4}$$

The conductive interference is characterised by the presence of an alternated electric field in the ground, due to the currents that are flowing in the grounding system of an electrical installation. The interference on the victim system can be modelled as described in Fig. 4.2(b), where E is a constant electric field and $\partial U_E / \partial x = E$. The equations that represent this model are:

$$\frac{\partial U}{\partial x} = -\gamma \times Z_W \times I \tag{4.5}$$

$$\frac{\partial I}{\partial x} = -\frac{\gamma}{Z_W} (U - U_E) \tag{4.6}$$

$$\frac{\partial^2 \boldsymbol{U}'}{\partial x^2} = \gamma^2 \times \boldsymbol{U}' \tag{4.7}$$

$$\frac{\partial^2 \boldsymbol{I}}{\partial x^2} = \gamma^2 \left(\boldsymbol{I} + \frac{\boldsymbol{E}}{\gamma \times Z_W} \right) \tag{4.8}$$

Considering a section of the victim system characterised by a homogeneous Z' and Y' all along its length l, Eqs. (4.1) and (4.2) for inductive interference can be solved by applying the Laplace transform, obtaining:

$$\begin{bmatrix} \boldsymbol{U}_1 \\ \boldsymbol{I}_1 + \boldsymbol{I}_Q \end{bmatrix} = \begin{bmatrix} \cosh(\gamma l) & Z_W \times \sinh(\gamma l) \\ 1/Z_W \times \sinh(\gamma l) & \cosh(\gamma l) \end{bmatrix} \begin{bmatrix} \boldsymbol{U}_2 \\ \boldsymbol{I}_2 + \boldsymbol{I}_Q \end{bmatrix} \tag{4.9}$$

Analogously, Eqs. (4.5) and (4.6) representing the conductive interference can be solved obtaining:

$$\begin{bmatrix} \boldsymbol{U}_1 - \boldsymbol{U}_{E1} \\ \boldsymbol{I}_1 + \boldsymbol{I}_Q \end{bmatrix} = \begin{bmatrix} \cosh(\gamma l) & Z_W \times \sinh(\gamma l) \\ 1/Z_W \times \sinh(\gamma l) & \cosh(\gamma l) \end{bmatrix} \begin{bmatrix} \boldsymbol{U}_2 - \boldsymbol{U}_{E2} \\ \boldsymbol{I}_2 + \boldsymbol{I}_Q \end{bmatrix} \tag{4.10}$$

Equations (4.9) and (4.10) can be represented by a π-equivalent model, shown respectively in Figs. 4.3(a) and (b), by assuming:

$$Z = \sinh(\gamma l)$$

$$Y = \tanh(\gamma l/2)/Z_W$$

$$I_Q = \frac{E}{\gamma \times Z_W}$$

If the exposure along the victim system is not constant, it is necessary to divide the system into n sections characterised by uniform exposure and separated by nodes. Each section can be represented with a quadripole like the one represented in Fig. 4.3. The network
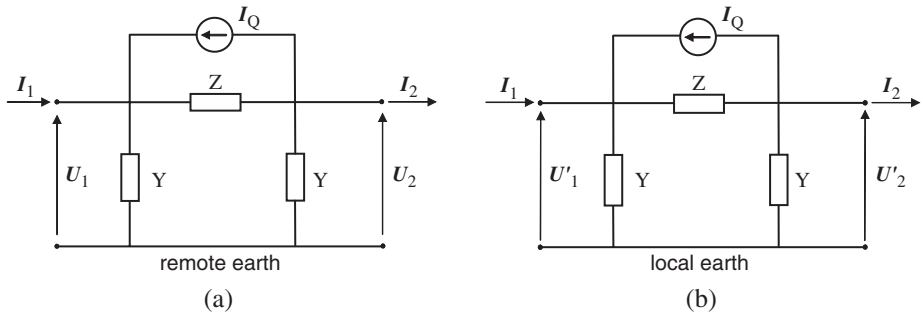
Fig. 4.3. π-equivalent model for inductive interference (a) and conductive interference (b) on a section of the victim system with homogeneous characteristics all along its length l.

obtained by connecting the n quadripoles can be solved through the nodal approach, obtaining the relation:

$$U_n = [Y_n]^{-1} I_{Qn} \tag{4.11}$$

where U_n is the nodal voltage vector (U'_n in the case of conductive interference), and I_{Qn} is the equivalent current generator vector that takes into account the influence of the electric field E for each section.

Whenever in the proximity of the system V there is a shielding system S, it is necessary to take into account the mutual influence between these two systems. If the two circuits have good isolation from the ground, the coupling can be considered as purely inductive. In Fig. 4.4, the model adopted for representing the systems V and S is shown.

In Fig. 4.4(a), E_V and E_S represent the inductive interference with the system P. The coupling between V and S is represented through two series voltage generators: Z_{VS} is the mutual impedance. The system shown in Fig. 4.4(b) is an equivalent model constituted by a passive element (Y) taking into account the self and mutual admittances and two current generators representing the external influence due to the coupling.

The system in Fig. 4.4(a) can be represented by the equation:

$$\begin{bmatrix} Z_V & Z_{VS} \\ Z_{VS} & Z_S \end{bmatrix} \begin{bmatrix} I_V \\ I_S \end{bmatrix} + \begin{bmatrix} E_V \\ E_S \end{bmatrix} = \begin{bmatrix} \Delta U_V \\ \Delta U_S \end{bmatrix} \tag{4.12}$$

that can easily be written as:

$$\begin{bmatrix} I_V \\ I_S \end{bmatrix} + \begin{bmatrix} Z_V & Z_{VS} \\ Z_{VS} & Z_S \end{bmatrix}^{-1} \begin{bmatrix} E_V \\ E_S \end{bmatrix} = \begin{bmatrix} Z_V & Z_{VS} \\ Z_{VS} & Z_S \end{bmatrix}^{-1} \begin{bmatrix} \Delta U_V \\ \Delta U_S \end{bmatrix} \tag{4.13}$$
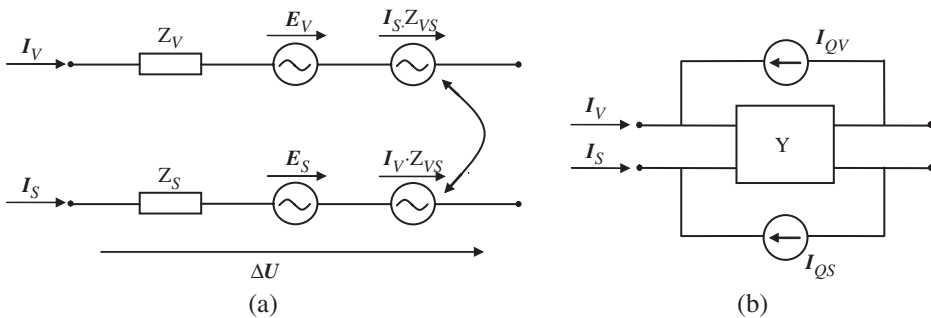
Fig. 4.4. Inductive coupling between V and S, scheme (a) and equivalent model (b).

$$I_{QV} = E_V Y_{VV} + E_S Y_{VS}$$
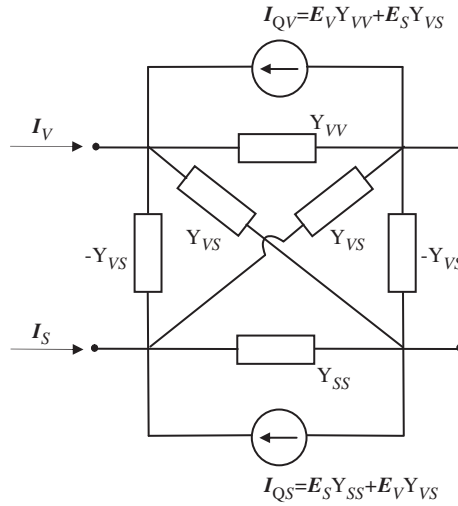
Fig. 4.5. Pictorial representation of the model that takes into account the influence of P on V and S, and the mutual influence between V and S.

The model in Fig. 4.4(b) is represented by the equation:

$$\begin{bmatrix} I_V \\ I_S \end{bmatrix} + \begin{bmatrix} I_{QV} \\ I_{QS} \end{bmatrix} = Y \begin{bmatrix} \Delta U_V \\ \Delta U_S \end{bmatrix} \tag{4.14}$$

Equations (4.13) and (4.14) coincide if:

$$Y = \begin{bmatrix} Y_{VV} & Y_{VS} \\ Y_{VS} & Y_{SS} \end{bmatrix} = \begin{bmatrix} Z_V & Z_{VS} \\ Z_{VS} & Z_S \end{bmatrix}^{-1} = \frac{1}{Z_V Z_S - Z_{VS}^2} \begin{bmatrix} Z_S & -Z_{VS} \\ -Z_{VS} & Z_V \end{bmatrix}$$

and

$$\begin{bmatrix} I_{QV} \\ I_{QS} \end{bmatrix} = \begin{bmatrix} Z_V & Z_{VS} \\ Z_{VS} & Z_S \end{bmatrix}^{-1} \begin{bmatrix} E_V \\ E_S \end{bmatrix}$$

Figure 4.5 gives a schematic representation of the model represented by Eq. (4.14).

4.3 Test Results

The feasibility of the approach described in the previous chapter has been proved by implementing it on the representation of a real system and by comparing test results with actual measurements.

The system that has been investigated is a methane pipeline, which extends to about 77 km across the south of Italy. Along its trajectory, the pipeline is very often in the
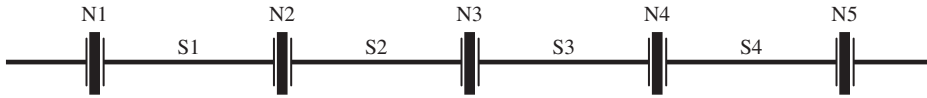
Fig. 4.6. Sections and nodes for the representation of the system under investigation.

zone of influence of several HV overhead transmission lines, running parallel or having crossing points with them.

For the sake of simplicity, the interference analysis has been conducted on a portion of the pipeline where the induction phenomena are most severe. In particular, this portion is 55-km long and can be divided into four sections, named S1, S2, S3 and S4, connected to each other by insulated flanges as shown in Fig. 4.6. The characteristics and parameters for each section are reported in Table 4.1.

Along the chosen portion, there are six overhead transmission lines interfering with the chosen system, five 380 kV transmission lines and one 220 kV. In Table 4.2, the main characteristics and parameters of the overhead HV lines are listed.

The evaluation of voltage profiles has been performed referring to normal operating conditions experienced at 9.30 a.m. on a Wednesday in the month of December. The simulated values have been compared to actual measurements carried out in specific locations suitable for inspection and measurement. The measured and simulated voltages are reported in Table 4.3, showing that estimations are very close to the reality.

The values reported in Table 4.3 are related to some specific locations, whereas in Fig. 4.7, the simulated voltage trajectory along the entire length of the natural gas

Table 4.1. Parameters of the pipeline.

		Section S1	Section S2	Section S3	Section S4
Diameter	(m)	0.90	0.90	0.90	0.90
Insulating material		Bitumen	Bitumen	Bitumen	Bitumen
Insulating thickness	(mm)	4.5	4.5	4.5	4.5
Specific coating resistance	(Ωm^2)	40 000 (assumed)	40 000 (assumed)	442 624 (measured)	40 000 (assumed)
Impedance	$(m\Omega/m)$	$0.120 + j0.616$	$0.120 + j0.616$	$0.120 + j0.616$	$0.120 + j0.616$
Admittance	$(\mu S/m)$	$35.3 + j4.37$	$35.3 + j4.37$	$3.20 + j4.37$	$35.3 + j4.37$
Characteristic impedance	(Ω)	$3.4 + j2.46$	$3.4 + j2.46$	$10.5 + j2.34$	$3.34 + j2.41$
Propagation coefficient	(m^{-1})	$(1.09 + j1.02)$ 10^{-4}	$(1.09 + j1.02)$ 10^{-4}	$(2.34 + j5.34)$ 10^{-5}	$(10.8 + j9.98)$ 10^{-5}
Soil electrical resistivity	(Ωm)	200	200	200	100

Table 4.2. Parameters of the overhead HV lines.

Line (number)	Voltage (kV)	Configuration	Line current (A)	Line ampacity (A)	Overhead ground wires (number)	Construction	Area (mm^2)	Circuits (number)
1	380	Horizontal	314.5	1671	2	Al–steel	125	Single
2	380	Horizontal	206	1671	2	Al–steel	125	Single
3	220	Triangular	131	417	1	Al–steel	125	Single
4	380	Horizontal	143	1671	2	Al–steel	160	Single
5	380	Horizontal	76	1671	2	Al–steel	160	Single
6	380	Horizontal	150	1671	2	Al–steel	160	Single

Table 4.3. Results of pipeline's induced (emf).

Section (number)	Measurement point (number)	Estimated (emf) (V)	Measured (emf) (V)
S1	1	13.42	11.85
	2	9.18	8.41
	3	8.68	7.81
	4	6.91	6.12
S2	1	38.22	35.15
	2	41.61	44.85
	3	42.42	45.28
S3	1	13.49	9.18
	2	12.66	10.73
	3	68.02	65.53
S4	1	48.09	50.20
	2	3.81	2.35
	3	2.32	1.96
	4	1.07	1.43
	5	1.18	1.89

pipeline has been represented. Measured data have also been presented in order to give a pictorial comparison with the simulated data. Figure 4.7 shows very clearly that the voltage profiles are characterised by discontinuities, corresponding to the insulated flanges.

A further investigation regarding the maximum levels of voltages that can be induced on the natural gas pipeline has been carried out by stressing the system and hypothesising that the HV transmission lines have reached their steady-state maximum capacity (i.e. the current flowing in each line equals its ampacity). Figure 4.8 shows voltage profiles on the overall pipeline obtained during this simulation. As it can be noted, in this condition, voltage values can exceed 300 V giving rise to potential hazards regarding safety and human health as well as the security of the devices connected to the pipeline.
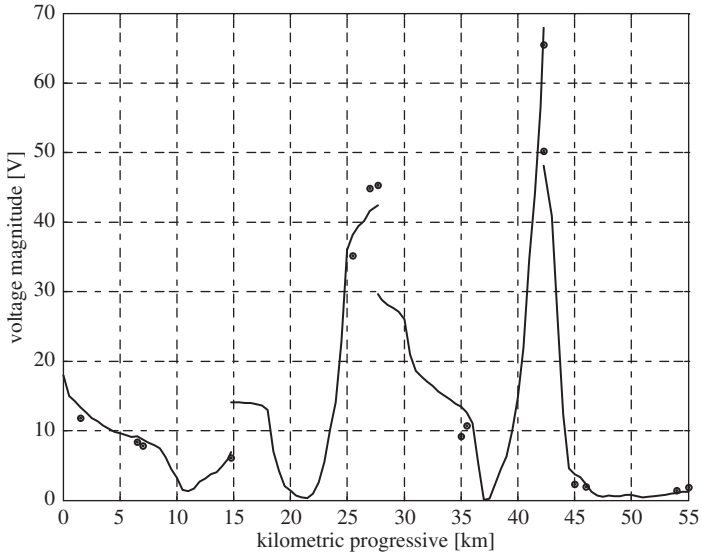
Fig. 4.7. Voltage profile on the overall pipeline under normal operating conditions: estimated values (solid line) and measured values (circles).
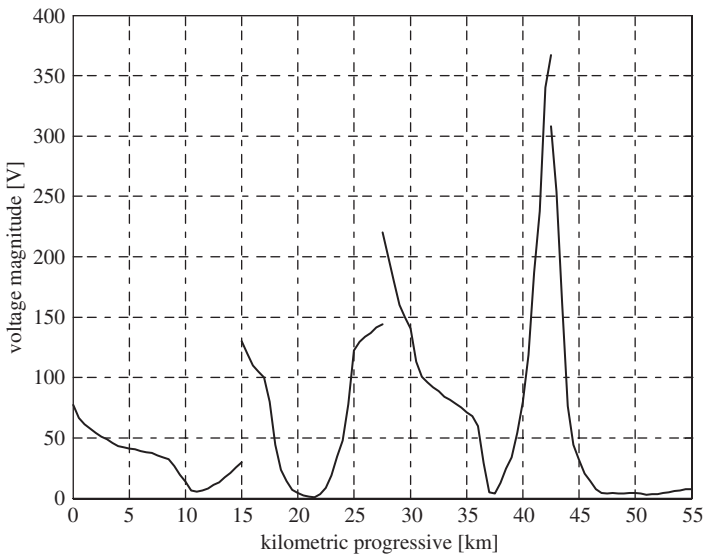
Fig. 4.8. Voltage profile on the overall pipeline under critical operating conditions.

The last simulations deal with the study of voltages induced on the pipeline as a consequence of a fault on the power transmission lines. It was assumed that a single phase-to-ground fault was occurring at a 380 kV transmission line at the eleventh kilometre of the pipeline track. It was also assumed that the other HV transmission lines were operating under normal conditions.

For the fault selected, a fault current of 5.74 kA and a clearing time of about 0.07 s has been calculated. The simulations showed that, as a consequence of the fault, the voltage magnitude profile would follow a behaviour like the one reported in Fig. 4.9, trajectory (a). The figure clearly shows how, in this case, it would be possible to experience on the pipeline dangerously high voltages that exceed the security and safety limits defined in the CCITT Directives (1989).

In order to reduce the magnitude of induced voltages at acceptable levels, it has been supposed that a shielding system has been built along the pipeline. In the simulation performed, a shielding system, consisting of an underground wire following the same track of the pipeline, was supposed to be installed (160 mm^2 wire size, 1.5 m of interring depth).

Results of this simulation, reported in Fig. 4.9, trajectory (b), clearly show how the presence of the shield was able to reduce the effects of the influence of AC and keep voltages on the pipeline beneath safety and security limits.
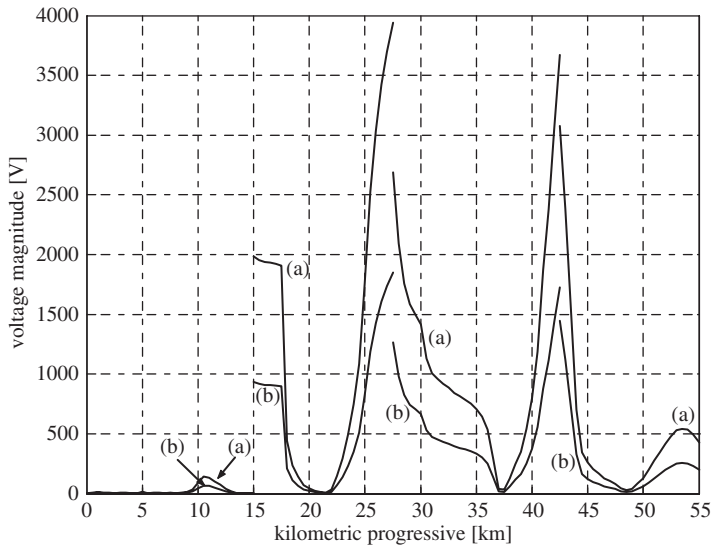
Fig. 4.9. Voltage profile on the overall pipeline with one phase-to-ground fault occurring at a 380 kV line at 11 km (a) without shielding system and (b) with shielding system.

4.4 Conclusions

Mathematical tools and representations for the computation of electromagnetic interference with underground metallic structures have been motivated by the general trend of concentrating most utility infrastructures (overhead AC transmission lines, traction lines, telecommunication lines, pipelines for fluid transportation, etc.) in the same corridors. It has been shown that the influence of AC on metallic structures can give rise to possible hazards regarding the safety of people who may come in contact with the pipeline, the risks of damage to the pipeline coating and metal, and the risks of damage to the equipment connected to the pipeline (cathodic protection systems).

The influence of a power system on an adjacent metallic structure has been studied in this chapter through the so-called "universal approach" characterised by its extreme simplicity in its application to a real-life example. The effectiveness of the method is proved on the basis of a comparison with measurements obtained on one of the most crowded corridors in Italy, where six overhead HV power transmission lines and one natural gas pipeline coexist on the same passageway.

References

ANSI/IEEE Standard 776-1987, *IEEE guide for inductive coordination of electric supply and communication lines*, IEEE Publishing, New York, 1987.

CAN/CSA-C22.3 No. 6-M91, Principles and Practices of Electrical Coordination between Pipelines and Electric Supply Lines, 1991.

Carson J.R., "Wave propagation in overhead wires with ground return", Bell Syst. Tech. J., **5**, 1926, pp. 539–554.

CIGRÉ Working Group 36.02, Report on "Electromagnetic Compatibility with Telecommunication Circuits, Low Voltage Networks and Metallic Structures", Guide on the Influence of High Voltage AC Power Systems on Metallic Pipelines, 1995.

Comité Consultativ International Télégraphique et Téléphonique (CCITT), Directives Concerning the Protection of Telecommunication Lines against Effects from Electric Power and Electrified Railway Lines, Vol. II, III, IV, Geneva, 1989.

Dawalibi F.P., Southey R. Da., "Analysis of electrical interference from power lines to gas pipelines. I. Computation methods", IEEE Transactions on Power Delivery, **4(3)**, (1989), 1840–1846.

DIN EN 12954-2001 European Standard, Cathodic Protection of Buried or Immersed Metallic Structures – General Principles and Application for Pipelines, 2001.

Haubrich H.-J., Flechner B.A., Machczynski W., "A universal model for the computation of the electromagnetic interference on earth return circuits", IEEE Trans. Pow. Del., **9(3)**, (1994), 1593–1599.

NACE Standard RP-0177-95, Recommended Practice: Mitigation of Alternating Current and Lightning Effects on Metallic Structures and Corrosion Control Systems, 1995.

Pollaczek F., "Über das Feld einer unendlich langen wechsel stromdurchflossenen Einfachleitung", Elektr. Nachr. Tech., **3**, 1926, pp. 339–360.

This page intentionally left blank

CHAPTER 5

The Crucial Case of Quasistatic Magnetic Field Penetration into Metallic Enclosures: An Unexplored Model

Francesco Lattarulo

Abstract

A useful compilation of practical formulas, governing the shielding impairment of non-magnetic metallic enclosures against quasistatic magnetic fields, is provided. To this end, the adopted theoretical procedure makes up for a detailed knowledge of the field pattern with an exhaustive set of field surrogates expressed by unsophisticated formulation. The shield degradation is intended to be caused by apertures, often hardened by continuous or discontinuous materials. The given formulas are especially recommended whenever currently available approximate methods prove to be inadequate, namely when assumption is made of noncircular holes in close proximity to interior receivers. Specifically, the aperture shape is taken into account by using an elliptic model and the given results are carefully commented upon. The practical value of the proposed method consists in having circumvented direct evaluation of purely 3D fields. Instead, the adopted strategy can simply make use of a 2D field calculation, restricted to the sheet surface surrounding the hole, after exploiting the homological affinity claimed in projective geometry between circular and elliptic figures.

5.1 Introduction

One of the most appealing EMC problems consists in predicting the shielding degradation of discontinued metallic enclosures exposed to quasi-static fields. In this chapter, special attention will be paid to the impairment represented by the magnetic field for the following two main reasons:

- Irrespective of the presence of apertures, ordinary non-magnetic conducting panels, often arranged in such a way as to form an enclosure, invariably make the interior

vulnerable system less effectively impervious to the magnetic than to the electric field. The unfavourable performance against magnetic fields is due to the negligible reflective and absorptive behaviours of the enclosure wall at low frequencies; the favourable performance against electric fields is due to the large conductivity of the adopted materials which causes the displacement current collected by the hollow body to convoy into the low-resistance wall, where it flows in the form of conduction current;

- With reference to the concentrated field penetration, the coupling to an interior wire crossing an aperture represents a paradigmatic case study. Therefore, the fields of interest often reduce to the components of the net electric field tangential to and the simultaneous magnetic field linking the exposed segment of the wire. Owing to the structures assumed by the above fields passing through the hole and actually coupled to the interior conductor, it is verified that the former field often approaches zero, while the latter is important.

The above observations especially apply to high-current source cases, namely when use is for example made of the "bulk current injection" (BCI) for laboratory tests (Williams, 1996). Typically, such simulations in which the current spreads up over the conducting portions of the enclosure and takes the path of least impedance, have long been adopted to investigate the induced effects of a lightning discharge directly striking an aircraft. Specifically, reproducing the scenario of the residual field in the shielding volume is the prerequisite for a careful knowledge of induced effects on the complex wiring laid, say, onboard aircraft and running nearby the apertures. In this case, a large amount of the produced magnetic field may be assumed to be of quasi-static nature owing to the restricted spectral components of the return-stroke current and the short geometrical quantities often involved (hole dimensions and observer's distance, both small in comparison to the free-space wavelength).

The magnetic field penetrates an enclosure in a variety of ways, involving concentrated and distributed mechanisms, strictly depending on the enclosure's physical and geometrical parameters. The shield material is usually made of electrically thin sheets whose conducting properties are:

- somewhere interrupted by the presence of largely spaced, unfilled holes of varying dimensions (reciprocal electromagnetic influence neglected);

- somehow restored in correspondence to delimited areas of the shield by loading the apertures there positioned with continuous sheets of different conducting properties or with grids or meshes of same or different conducting properties; and

- regularly interrupted by shortly spaced apertures substantially forming a grid distributed throughout the enclosure surface.

The above solutions are adopted since light, air and cable passages are made permissible, even though low weight and cost, as well as unsophisticated manufacture, are the most important advantages. The first and second categories respectively include unloaded and loaded apertures in isolation. As regards the second class, a large original hole results in being completely blocked by a plate or substantially is reduced to a regular array

of short-dimensioned holes. More precisely, the perforation may directly be made on a restricted area of the shield or on a separate plate adopted for hardening a large aperture. Especially in avionics technology, the aperture loading is often made by copper mesh protected carbon fibre reinforced composite panels. Shielding mesh cages for medical diagnostics and even cables with braided-wire shields are typical examples falling within the third category. Unfortunately, apart from being costly and time-consuming, available computational methods only based on purely numerical methods make interpretation of the physical mechanisms under examination a rather difficult exercise. Such a drawback is especially critical in EMC design where progressive solutions, assumed at prototype level in conjunction with pre-compliance tests, are often needed before arriving at the product conformity certification. Additionally, large structures with short apertures can require a domain discretisation to be unachievable even with the powerful features of currently available computers. Therefore, semi-analytical models, in that suitable to effectively provide guidelines for an optimal configuration of the system, are still recommended as subsidiary computational resources. In fact, in most EMC problems, a detailed knowledge of the field pattern in the protected region is not needed, while some analytically tractable field surrogates can fruitfully be involved in the coupling mechanism with interior victims.

As previously mentioned, distinctive of an electrically short aperture in an electrically thin panel (the latter additional low-frequency condition means that the thickness is less than skin depth) is the promotion of field penetration by concentrated and distributed mechanisms which can approximately be described by separate procedures before combining the relevant results. Instead of the field pattern itself, knowledge of a set of specific integral quantities strictly involved in the former mechanism (i.e. polarisability and penetrant flux), as well as circuit parameters (i.e. resistance and inductance) of the perforated enclosure subject to the latter mechanism (thus including the resistance-dependent diffusion), is of paramount importance for the subsequent coupling problem. Direct penetration through a hole is extensively treated elsewhere by adopting the magnetic dipole theory applied to electrically short apertures (see, for example, Taylor, 1973; Méndez, 1978; Casey, 1981). According to this theory, a small aperture is in general considered as being equivalent to a combination of radiating electric and magnetic dipoles whose dipole moments are respectively proportional to the normal electric field and the tangential magnetic field of the incident wave. The polarisability of small apertures of different shapes has been investigated by numerical (De Meulenaere and Van Bladel, 1977) and approximate, but more manageable, techniques (McDonald, 1985; Jaggard, 1981). An unwanted, distributed field penetration (non-zero net field in the shielding volume) depends on the fact that the eddy currents, induced in the thin-walled shield by the applied time-varying magnetic field, are inadequate to generate in the protected volume an exactly opposing field, namely to buck out the imposed field. Responsible for such a reduced response are the finite conductivity of the employed material and dissemination of discontinuities over the conducting route. The eddy-current dependent shielding effectiveness will conveniently be evaluated by a circuit formulation after Bridges, 1988 (see later sub-Section 5.2.3).

However, at lower frequencies, some important limitations, summarised below, arise when the problem of a sheet with holes is dealt with by analytical approach.

In synthesis,

- The quasi-static approximation performed by the magnetic dipole theory (small aperture approximation) is invalid in close vicinity to the hole, as claimed or verified elsewhere (see, for example, Taylor, 1973; the survey by Vance, 1995);

- Converse to the calculation of polarisability, the effect of the aperture shape on both the directly penetrating (concentrated nearby each aperture) and distributed (throughout the enclosed volume) fields is hard to be estimated, irrespective of being the small aperture unloaded or loaded. In fact, the boundary value problem posed for the calculation of the penetrating magnetic flux has so far been proved to be analytically intractable for noncircular holes (Casey, 1981);

- Overwhelming theoretical difficulties arise in the case of mutually interacting nearby holes, even when assuming them to be of circular shape (Sten, 1999).

The first drawback cannot be underestimated since the interior wires often run at ranges down to one radius of, or even directly across, the aperture. The second drawback, which at first appears to be a second-order one, requires, as will be appreciated later, to be carefully examined. In fact, the earlier proved slight dependence of polarisability on the opening shape does not seem to be a convincing argument to postulate that the shielding degradation is unaffected by the hole geometry. The third limitation is circumvented by adopting purely numerical simulations, even though the physical understanding of the controlled phenomenon results rather frustrated.

In the present chapter, a novel analytical generalisation, based on using an isolated elliptic aperture, is proposed. Incidentally, it is worth bearing in mind that the ellipse is largely recognised to be an accurate substitute, for several applications, of a variety of shapes presenting the same aspect parameter (aperture width to length ratio). The analytical difficulty posed by the discussed boundary value problem has been overcome, thus permitting the effect of the aperture shape to be successfully quantified. Since aimed at giving a complete evaluation of useful field surrogates for EMC problems, the present approach is based on

- (a) the planar electrokinetic field pattern surrounding an isolated elliptic hole on an infinitely extended current-carrying sheet (the conservative assumption of a uniformly distributed current in the cross-section of an electrically thin sheet is tacitly adopted);

- (b) the homological affinity between circumference and ellipse; and

- (c) correcting factors for an approximate extension of formulas, deriving from an exact single-hole treatment, to that of shortly spaced holes.

The above-mentioned surrogates are the magnetic flux linking an aperture related average penetration, and the shielding effectiveness of the entire enclosure, respectively pertaining to concentrated and distributed field penetrations. Concerning this, see the conclusion of Section 5.3 and the quoted Appendix D for a detailed discussion on the notion of flux linkage; see sub-Section 5.2.2 and related Appendix A for the definition of average flux penetration introduced here. Specifically, the resistance and inductance

of an enclosure with largely spaced holes, both involved in the definition of shielding effectiveness, are evaluated by the 2D Laplacian field mentioned in (a). The supplementary notion expressed in (b), which descends from a similarity property applied to projective geometry, is needed for accomplishing the calculation of the concentrated field penetration. The dimensionless quantities expressed in (c) derive from a numerical calculation methodically applied to the above 2D Laplacian field when the sides of a rectangular sheet are comparable to the main semi-axes of the central elliptic aperture. It is worth considering that the value of the present approach consists in reducing the complexity of the original problem, generally requiring a 3D field calculation, by adopting a simpler 2D numerical method.

As will be clear in sub-Section 5.2.3, an interior victim positioned at a substantial distance from a discontinued thin wall or forming a large loop can however be linked by the flux of a background field. Such a residual field, which is rather uniformly distributed throughout the bulk of the shield, primarily derives from a diffusional mechanism through the resistive wall. However, even a concentrated mechanism, through single holes, can result in the formation of a rather intermingled global flux additionally permeating the interior space. When a victim is brought, say, close to only one of a number of mutually isolated apertures, it is permissible, in evaluating the interference, to superimpose the total distributed flux to the concentrated one which penetrates through the hole under examination. In some cases, however, the bulk of an efficient shield is so highly impervious to exogenous fields and/or the surface area of the loop representing the linked victim is so restricted and close to the aperture that the distributed field can be disregarded in the coupling model. Such an approximation especially applies when the victim happens to be positioned nearby the sole aperture of a highly conducting shield.

5.2 Unloaded Short Aperture

5.2.1 Preliminary remarks

The concentrated and distributed magnetic flux penetrations will be calculated analytically in the case of isolated openings. The investigation will be continued by considering a perforated conducting structure intended as a regular lattice of hole-centred short cells. Such a minutely composed structure will be assumed either to form an entire enclosure or to occupy a restricted area delimited by the contour of a large aperture. The theoretical treatment of each cell will be performed by a supplementary field calculation, only involving a 2D approach, in order to extend the previous analysis to the case of mutually influencing apertures.

Let a low-frequency current be uniformly applied on an infinitely extended conducting sheet of conductivity σ and thickness δ. An elliptic hole, of main semi-axes a and $b \leqslant a$, is cut on the sheet and a coordinate system (x, y) is centred on the hole and oriented with the x- and y-axes along a and b, respectively. If J is the vector of the surface current density, then the generated tangential magnetic field H results fully identified. In fact, $J = n \times H$, with n denoting an outwardly pointing unit vector applied to the sheet face exposed to H (consider that $J = H$ in magnitude). However, the assigned uniformity of the J- and H-fields result perturbed by the presence of the hole. Of course, the above

description holds unchanged if the roles of source and induced effect are reversed, namely if $\boldsymbol{H}$ and $\boldsymbol{J}$ are assumed being the applied and induced vector quantities, respectively.

5.2.2 Concentrated magnetic flux penetration

The perturbed H-field surrounding an isolated hole substantially manifests itself as an inwardly directed flux ϕ which passes through a fractional amount of the hole and reverses its orientation in the interior region before passing through the complementary surface of the hole with outward direction. Detailed features of such a field leakage can only be described by a 3D field calculation which simplifies if the field pattern is symmetrical with respect to a plane transverse to the sheet. This occurs if the hole presents a symmetry axis, specifically, if its intersection with the sheet plane lies along the directions of the main semi-axes a or b of an elliptic hole and the externally impressed field $\boldsymbol{H}$, tangential to the sheet plane, is oriented along b or a, respectively. With these properties in mind, irrespective of the $\boldsymbol{H}$ orientation (see Appendix A),

$$\phi = \mu_{\mathrm{o}} H a b \tag{5.1}$$

where μ_{o} stands for free-space permeability. According to previous claims (Casey, 1981), the total penetrating flux ϕ linking the aperture is independent of the $\boldsymbol{H}$ orientation and only dependent on the elliptic area (through the product ab). However, the former feature turns out to be of restricted practical interest since the average penetration of the field is equal to $p = a/2$ or $b/2$ if $\boldsymbol{H}$ is oriented along a or b, respectively. The notion of average penetration introduced here is useful for an approximate evaluation (here omitted) of the fractional amount of the total flux ϕ linking, say, interior wiring. In such a case, the relevant induced effect is significantly dependent, through p, on the aperture geometry.

5.2.3 Distributed magnetic field penetration

The subject treated here is strictly connected to the bulk shielding properties of an enclosure and, therefore, especially regards

- innermost victims, generally preserved from the influence of concentrated H-field penetrations;

- interior victims, under the influence of concentrated fluxes passing through nearby holes, also resulting partially or totally linked by a distributed flux of comparable magnitude.

The lumped-parameter circuit representation of Fig. 5.1 gives exhaustive arguments to understand how the bulk shielding properties of a resistive and leaky shield are compromised by diffusional mechanism through the material of the thin wall and penetration through its discontinuities. The external inductance L_{ext} of a shield is a material-independent global quantity which increases as a function of the number and geometry of discontinuities in the thin wall; instead, the internal resistance R_{int} depends on the
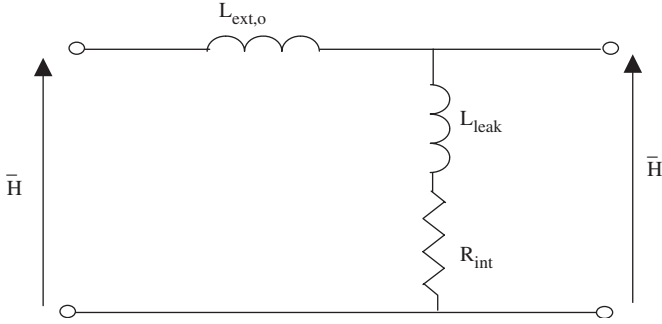
Fig. 5.1. Analog lumped-parameter circuit for representing the interior magnetic field of magnitude H_i.

shield's finite conductivity other than, in a way similar to the inductance L_{ext}, on the discontinuities. An important figure of merit, here applied to a non-magnetic metallic enclosure presenting a transfer function $T(j\omega)$, is the shielding effectiveness S. If expressed in decibels,

$$S = -20 \log_{10} |T(j\omega)|$$

where

$$T(j\omega) = \frac{H_i}{H} = \frac{R_{int} + j\omega L_{leak}}{R_{int} + j\omega L_{ext}} \tag{5.2}$$

According to the above definition, if H denotes a uniform magnetic field restored in the protected space after removing the enclosure, the internal magnetic field H_i results likewise uniform and equal to the product $T(j\omega)H$. Consider that the pair of parameters R_{int} and L_{ext}, embodied in Eq. 5.2, characterises the physical single-turn loop to which the current-carrying portion of the closed shield can be assimilated. In fact, if L_{leak} represents the total leakage inductance due to the holes, the difference $L_{ext} - L_{leak} = L_{ext,o}$ becomes the inductance of the same loop deprived of discontinuities (holes filled). Therefore, the notion of shielding degradation can substantially be expressed by setting R_{int} and L_{leak} both > 0, in which case S, otherwise approaching infinity, happens to assume any finite value. In other words, an ideal enclosure on which induced effects are allowed to take place behaves as a perfectly conducting, continuous and wide one-turn coil carrying eddy currents. According to Eq. 5.2, $H_i = 0$ since R_{int} and L_{leak} both vanish while $L_{ext} = L_{ext,o} > 0$. On the other hand, assuming non-zero R_{int} and L_{leak} means that some defective qualities, typically affecting a physical thin-walled coil, are taken into account. The lumped-parameter circuit model adopted here is responsive to the uniform nature of H_i (if the exogenous far field H is uniform), in spite of local field perturbations due to discontinuities. In fact, the inwardly propagated short-range perturbation of H_i is quite disregarded (bear in mind the definition of p given in sub-Section 5.2.2), even though an average increase of H_i in the inner uniform-field space is somehow taken

into account via L_{leak}. A simple physical explanation of the raised correlation between sheet discontinuity and increase of the unperturbed background field H_i can be attempted by preliminary setting, for the sake of simplicity, $R_{\text{int}} = 0$ and discussing in terms of reactive flux permeating a magnetic circuit. If the shield is a perfect conductor, the circulating current required to buck out H from the interior space is irrespective of the presence of discontinuities in the wall. In spite of this, a residual internal field H_i is however experienced owing to the reduced reluctance encountered by the flux of the reaction field, which, therefore, becomes $H - H_i < H$. In fact, if the applied field H is suppressed and the eddy currents are virtually preserved, leakage of the internal induced field in correspondence of a hole results in a pronounced, outwardly protruding fluxtube which, otherwise, has to cross the internal side of the hole-free surface. This implies that the local reluctance decreases since the fluxtube involved in the leakage experiences substantial enlargement while protruding through the hole. According to the adopted model, the global reaction field is expected to decrease from the upper-bound value H to $H - H_i$. This tacitly means that the circulating current required to perfectly shield out the applied field is a necessary but not sufficient condition. The purpose of reducing H_i to zero throughout the shielding volume is fully attained only if such a current is distributed over the shield surface according to a specific law dictated by the shape and orientation of the hole-free shield. Instead, the real current distribution can even significantly depart from the above law owing to the influence of the holes. Of course, the reaction field decreases (H_i increases) further if the simultaneous diffusional mechanism, represented by the finite resistance R_{int} of the thin-walled, discontinued shield, is restored.

Everything considered, the current distribution ideally needed for abating the net field H_i to zero is unattainable owing to

- the material resistivity and current perturbation surrounding each discontinuity in the thin-walled sheet (J-field disturbance); such impairments are responsible for appearance of a non-zero R_{int} (in the case of a continuous shield, finite resistivity gives rise to a lesser value of R_{int}); and

- the mutually correlated and simultaneous J- and H-field disturbances caused by the apertures. Such field disturbances are ultimately responsible for a non-zero L_{leak} (so that $L_{\text{ext}} = L_{\text{ext,o}} + L_{\text{leak}} > L_{\text{ext,o}}$).

The total impedance $\dot{Z} = R_{\text{int}} + j\omega L_{\text{ext}}$ of the eddy-current route contouring the protected volume could be assumed as being composed of a series/parallel arrangement of partial impedances whose i-th element is denoted by $\dot{Z}_{\text{i}} = R_{\text{int,i}} + j\omega L_{\text{ext,i}}$. Provided that the holes are so dispersed that applying a low degree of discretisation to the route of the surface current is a permissible practice, then a restricted set of $\dot{Z}_{\text{i}}$ is associated with the large-dimensional elemental sheets, some of which present as central holes. As will be clear later, the adopted surface partialisation is quite irrespective of the physical pattern assumed by the joined metal sheets from which the enclosure is fabricated.

Before evaluating the impedance $\dot{Z}_{\text{i}}$ associated with a generic surface element of the current loop around the enclosure, it is profitable to discover that if V_{e} and S_{e} are the shielding volume and total surface of the loop, respectively, then $L_{\text{ext,o}} = \mu_{\text{o}} h$, with $h = V_{\text{e}}/S_{\text{e}}$. Such a simple formula has first been rigorously found by Casey (1988) for

some canonical shapes and later extended by Tesche *et al.* (1997) for an approximate application to arbitrary volumetric shields. Consider how $L_{ext,o}$ results substantially irrespective of the enclosure's orientation (with respect to incident magnetic field $\boldsymbol{H}$) and shape (provided that the ratio h is an invariant). Responsive for such a performance are the non-uniform distributions of the simultaneous J- and H-fields over and inside, respectively, a wide one-turn coil subject to the current-impressed condition. The turn in question is assumed showing generic cross-sectional configuration of area V_e/W and finite width W. Instead, if reference is virtually made to a parallel-plate line with indefinitely extended plates kept at distance h apart, the results of both the surface J-field and volumetric H-field are uniform. Therefore, the external inductance $L_{ext,o} = \mu_0 h$ of a generic shield can be interpreted as that of a squared-base equivalent cell, of side $(S_e/2)^{1/2}$ and height h, if the holes are filled and reference is made to the above parallel-plate model. It is simple to verify that if δ is the thickness of the thin-walled enclosure, the resistance associated to $L_{ext,o}$ is $R_{int,o} = 1/(\delta\sigma)$. After having arbitrarily partitioned the above model by cells of rectangular bases, simple formulas derive for the calculation of the partial resistance $R_{int,i}$ and inductance $L_{ext,i}$ associated to the i-th element. However, in spite of assuming uniform distributions for the above-mentioned fields, a demanding theoretical effort is required to attain explicit forms for $R_{int,i}$ and $L_{ext,i}$ when a hole is centred on an elemental sheet. If not otherwise specified, the treatment will from now on be restricted to the generic i-th element, so that the subscripts int, ext and i on the symbols for the various quantities involved will deliberately be dropped since there is no chance to mistake them for any other quantity.

The electrokinetic field on a planar sheet can be described by a pair of conjugate potential and flux functions (Morse and Feshbach, 1953; Babister, 1966) which permits the electrical resistance and inductance of a delimited sheet portion surrounding a hole to be made explicit in a rigorous way. Specifically, if the current flows along the x-axis uniformly, the contour of the region in question is determined by two pairs of orthogonal and symmetric potential and flux lines. These are identified, in the context of the Laplacian pattern, by the intersections $\pm x_l$ and $\pm y_w$ with the coordinate axes, respectively. Using the analysis skipped in Appendix B, gives

$$R_x = R_{ox}\xi_x \tag{5.3}$$

in which

$$\xi_x = \frac{n_y + \dfrac{ab}{2}T_x}{n_y - \dfrac{ab}{2}T_y};$$

$R_{ox} = |x_l|/(|y_w|\delta\sigma) = l/(\omega\delta\sigma)$ represents the resistance of a solid rectangular sheet of sides $l = 2|x_L|$ and $w = 2|y_W|$;

$T_\tau = \int_{\lambda_\tau}^{\infty} d\lambda/\left[(\lambda + q^2)\sqrt{(\lambda + a^2)(\lambda + b^2)}\right]$, with $q = a, b$ and $\lambda_\tau = x_l^2 - a^2$ or $y_w^2 - b^2$ for τ denoting x or y, respectively; $n_y = a/(a+b)$ is one of the two depolarising factors

$n_x, n_y (n_x = 1 - n_y)$ associated, after Osborn (1945), to a planar ellipse. Consider that $n_\tau = abT_\tau/2$ if $\lambda_\tau = 0$ ($x_l = a$ or $y_w = b$).

When the current flows along the y-axis, the structure of Eq. 5.3 holds also for R_y provided that the formulas representing R_{oy} and ξ_y are expressed with n_x, T_y and $|y_w|$ interchanged with n_y, T_x and $|x_l|$, respectively. Assuming simultaneously $|y_l| \gg a$ and $|y_w| \gg b$ implies that the four orthogonal curves delimiting the sub-domain under consideration tend to straighten, thus making Eq. 5.3 substantially appropriate for the case of a rectangular plate of sides l and w. After some manageable manipulations, it is possible to verify that if the hole becomes a circle of radius $r = a = b \ll l, w$, Eq. 5.3 reduces to

$$R_x = R_{ox}\xi_x' \tag{5.4}$$

in which

$$\xi_x' = \frac{1 + \left(\dfrac{2r}{l}\right)^2}{1 - \left(\dfrac{2r}{w}\right)^2}$$

Similar to the above elliptic-hole case, the quantities l and w require to be interchanged for the calculation of the quantities R_{oy} and ξ_y' pertaining to the case of a current flowing along the y-axis.

The structure of the formula $R_x = l\xi_x/(w\delta\sigma)$, given by rearranging Eq. 5.3, applied to a holed rectangular sheet of length l, tacitly allows to find out a hole-filled equivalent sheet. The equivalence results in replacing the original length l with $l\xi_x > l$. This simple reasoning leads to a similar increase in the external partial inductance L_x of the hole-filled equivalent sheet, so that $L_x = \mu_o(l\xi x)\,h/w$ can be written ultimately. Incidentally, consider that the J-field (namely, the planar current distribution) is simultaneously involved in the definitions of R_x and L_x and that the surface J- and H-fields are orthogonal Laplacian fields. The claimed structural similarity between the formulas of R_x and L_x has rigorously been verified in Appendix B, where the non-magnetic nature of both holed metallic sheet and environmental medium is additionally assumed. Accordingly,

$$L_x = L_{ox}\xi_x \tag{5.5}$$

in which $L_{ox} = \mu_o lh/w$. Equation 5.5 reduces to

$$L_x = L_{ox}\xi_x' \tag{5.6}$$

in the case of a circular hole of radius $r = a = b$. The structures of Eqs. 5.5 and 5.6 are also now preserved if the current flows along the y-axis; of course, careful interchanges between involved corresponding quantities are likewise needed.

Last, consider that the described two canonical alternatives allowed for the current to flow along the x- or y-axis of the i-th sheet's reference frame, leads to ultimately interpret
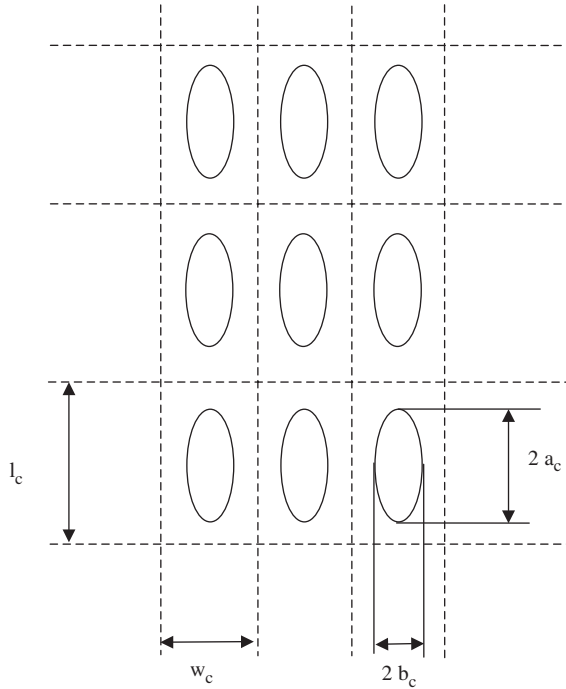
Fig. 5.2. Surface array for regularly spaced elliptic holes.

$l = b_i,\ w = d_i$ and $l = d_i,\ w = b_i$, respectively. Therefore,

$$\dot{Z}_i = R_{\mathrm{int},i} + j\omega L_{\mathrm{ext},i} = \xi_i \frac{b_i}{d_i}\left(\frac{1}{\delta\sigma} + j\omega\mu_{\mathrm{o}}h\right) \qquad (5.7)$$

can unambiguously be written for the generic i-th element after rearranging Eqs. 5.3 and 5.5. It is now clear that the prerequisites for a careful calculation of the enclosure's total parameters R_{int} and L_{ext} are that all the holes of the real structure are arbitrarily spread out on the twin surfaces S_{e} of the parallel-plate and their arbitrary discretisation into some rectangular elements is made in such a way that the holes result centred on and distant from the sides of the relevant elements.

Last, as regards the distributed complex mechanism of the field penetration, Eq. 5.7 permits the appreciation of

- the significant dependence on geometry of isolated and variously oriented apertures cut on the enclosure sheet; and

- the negligible contribution of $L_{\mathrm{ext},i}$, expressed by the second term in parentheses, if the frequency $f \ll (2\pi\delta\mu_0 h)^{-1}$.

5.3 Loaded Short Aperture and Perforated Sheet

The subject of sub-Section 5.2.3 gives arguments to somehow expect that a simple 2D field solver can be adopted, instead than a purely 3D one, when the dimensions $2a_c$ and $2b_c$ of a central hole become comparable with the lengths l_c and w_c of a rectangular boundary. The latter linear quantities can realistically represent the sides of a large number of equal cells composing a regular lattice in which the multiple-hole surface of a sheet can be discretised (see Fig. 5.2, where subscript c has been adopted with reference to the cell there represented). In fact, the electrokinetic field trapped in the conducting interstices among the holes ensures existence of the field map's special equipotential and flux lines superimposed upon the orthogonal straight lines of the lattice. According to the categorisation previously adopted in Section 5.1, the structure under consideration could be restricted to the surface of a loaded aperture surrounded by a continuous material or extended throughout the surface of a regularly perforated sheet. The reduction to a 2D numerical approach has promoted generalisation of Eqs. 5.3 and 5.5 in order to accommodate the cases in which the hole dimensions are not negligible in comparison to those of the sheet contour.

Accordingly, after a certain amount of computational efforts, the resistance R_c and inductance L_c of the cell are verified to obey the common semi-empirical formula

$$G_c = v G_c' \tag{5.8}$$

where the generic notation G has been adopted in substitution of R or L. Here, G_c' specifically represents Eqs. 5.3 or 5.5 with all the geometrical quantities subscribed by c; $v = k \exp[(l_c/w_c)/(b_c/l_c + w_c)]$ is a correcting factor whose embodied parameter $k = k(2b_c/w_c)$ is given by the curves of Fig. 3(a) and (b).

Indeed, when the contour of the hole approaches that of the rectangular cell, using an elliptic representation of such a hole becomes impractical and gives rise to significant errors. Such a drawback has been circumvented by rather interpreting each holed cell as a minute combination of contiguous rectangular conductors forming a series/parallel arrangement with respect to the flow of an impressed current (along l_c or w_c). Even now, the simple structure of Eq. 5.8 can be exploited provided that $v = v(2b_c/w_c)$ is directly given by using the curves of Fig. 5.4(a) and (b). Incidentally, consider that formalisation of G_c' results in an easy exercise since reference should be made to a simplified straight line field pattern.

The pair of parameters composed by the resistance R_L and inductance L_L of the entire lattice is indistinguishable from that of a single cell, see Eq. 5.8, if the rectangular lattice is composed by a same number of cells per row and column. In the general case of v cells per row and u cells per column (the current is assumed flowing along the columns), $G_L = G_c u/v$. For a non-rectangular lattice, G_L can be calculated by using a suitable arrangement of cells. For the calculation of the shielding effectiveness, use of Eq. 5.7 is once again recommended where $\dot{Z}_i$ is also representative of the impedance $\dot{Z}_L = R_L + j\omega L_L$ of a regularly perforated i-th sheet. The total impedance $R_{int} + j\omega L_{ext}$ embodied in Eq. 5.2 identifies with $\dot{Z}_L$ when the enclosure is represented by a regularly perforated cage.
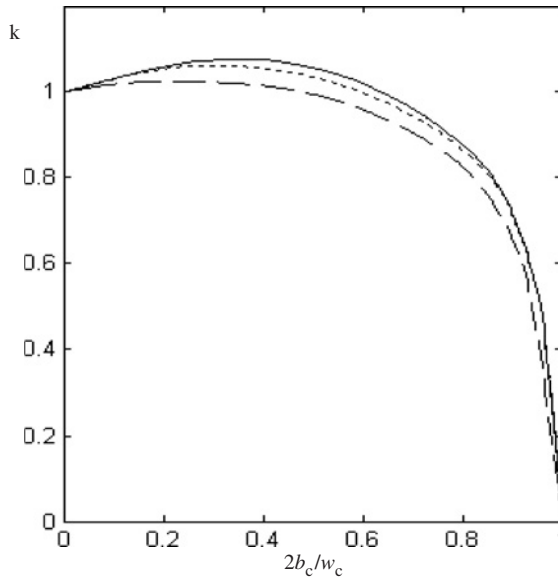
(a)
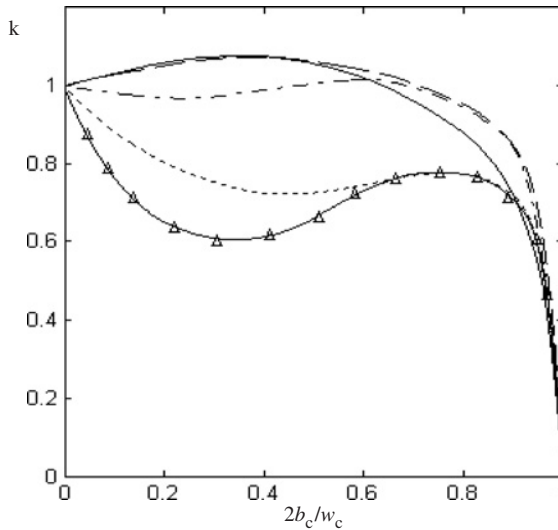
(b)

Fig. 5.3. Curves of the correcting factor k for circular and elliptic holes; (a) and (b): elliptic holes with major axis a_c longitudinal and transversal to the current flow. (a) (————) circle; (- - - -) ellipse with $a_c/b_c = 2$; (- - - -) ellipse with $a_c/b_c = 4 \div 10$. (b) (————) circle; (- - - -) ellipse with $a_c/b_c = 2$; ($\cdot - \cdot - \cdot$) ellipse with $a_c/b_c = 4$; (- - - -) ellipse with $a_c/b_c = 6$; (—△—) ellipse with $a_c/b_c = 8$.

(a)

(b)
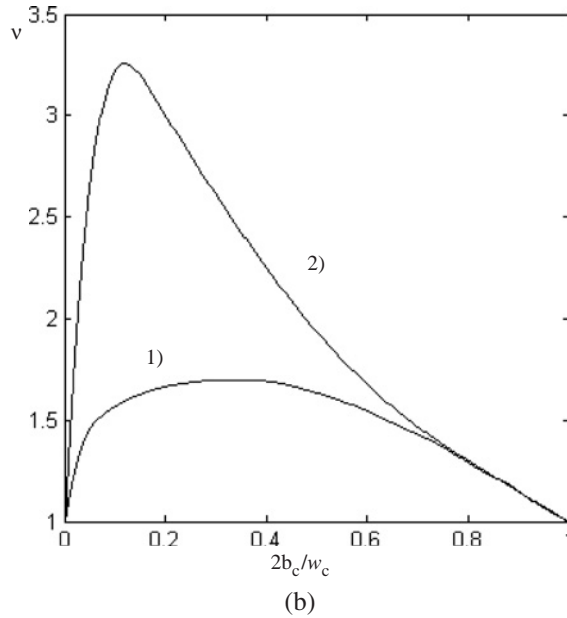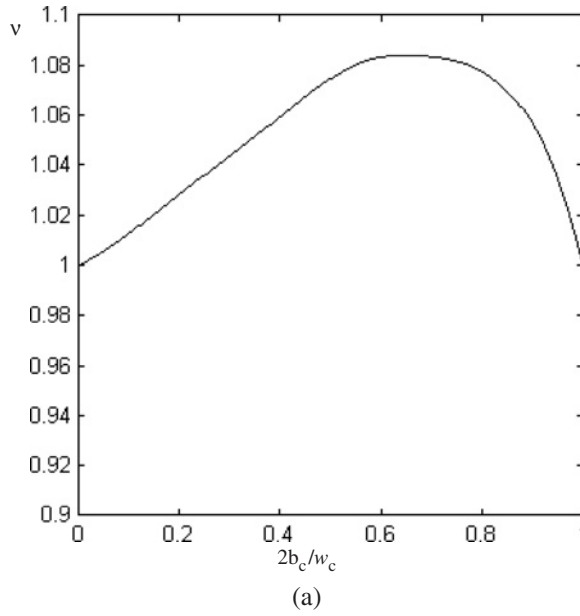
Fig. 5.4. (a), (b) – Curves of the correcting factor ν for square and rectangular holes; (a) square and longitudinal rectangles; (b) transversal rectangles with width-to-length ratio = 2 and 4 for the curves (1) and (2), respectively.

Even in the case of shortly spaced holes, the penetration p into the interior region is expected as being restricted to quantities equal to $a_c/2$ and $b_c/2$, thus considerably lesser than the distance assigned to a potential receiver from the inner surface of the loaded aperture. Similar considerations should be applied when the loading is made by a continuous filler. In the latter case, if the aperture is hardened by a resistive sheet of conductivity σ_h (contact resistance between loading material and rim of the aperture neglected), Eq. 5.1 becomes

$$\phi_x = \mu_o H_x a' b \tag{5.9}$$

or

$$\phi_y = \mu_o H_y a b' \tag{5.10}$$

where subscript x or y unambiguously refers to the orientation a priori assumed for $\boldsymbol{H}$; $m = (\sigma - \sigma_h)/\sigma_h$ and $m' = (\sigma_h - \sigma)/\sigma$; $a' = a(mb/a + b(1+m)) \leqslant a$; $b' = b(ma/b + a(1 + m)) \leqslant b$, so that the average penetration of the field is equal to $p = a'/2$ or $b'/2$ if $\boldsymbol{H}$ is oriented along x or y, respectively (see Appendix C).

Contrary to the example of unloaded hole (see above Eq. 5.1), Eqs. 5.9 and 5.10 prove that ϕ depends on the relative orientation of the hole when it is shorted by a sheet with different conducting properties. Under such circumstances,

$$\xi_x = \frac{1 + m'\left(n_x - \dfrac{ab}{2}T_x\right)}{1 + m\left(n_y - \dfrac{ab}{2}T_y\right)} r_x \tag{5.11}$$

with

$$r_x = \frac{1 + mn_y}{1 + m'n_x} \tag{5.12}$$

is the formula to be introduced into Eqs. 5.3 and 5.5 for evaluating R and L, respectively (see also Appendix B). The considerations already made in sub-Section 5.2.3 for ξ_y may likewise be repeated here.

It is simple to verify that setting $\sigma_h = 0$ in Eqs. 5.9–5.11 (unloaded hole) implies that ϕ_x and ϕ_y both approach ϕ expressed by Eq. 5.1, while ξ_x reduces to the corresponding quantity embodied in Eq. 5.3. Equations 5.9–5.11 apply in the following cases:

- conductively filled plastic composites as a special hardening material (typically, this is the case in avionics technology);

- transparent conducting material which fill viewing windows (typically, this is the case for measuring instruments).

It is worth considering that $0 < \sigma_h < \sigma$ is a realistic assumption which invariably causes field penetration even if the holes are completely blocked. Of course, if σ_h approaches σ, then a' and b' both vanish, which in turn implies that the penetrant flux ϕ_x or ϕ_y (see Eq. 5.9 or 5.10) and its inward penetration $p = a'/2$ or $b'/2$ tend to vanish.

Everything considered, the above description proves that both crucial parameters R_{int} and L_{leak} affecting the shielding quality of a discontinued enclosure are fully determined by the on-plane orthogonal J- and H-field patterns subject to disturbance. If the latter disappears (hole-free condition), $R_{int} = R_{int,o} > 0$ and $L_{leak} = 0$.

The present theory has also been successfully used in Appendix D to show that only a theoretical component of the magnetic flux passing through an unloaded or loaded hole can, rigorously speaking and in agreement with a familiar terminology, link the cavity as well as an interior receptor which happens to cross it. Accordingly, some theoretical difficulties arise in defining the inductance of a hole, while the corresponding resistance is appropriate and, as expected indeed, tends to infinity if the hole is unloaded.

Appendix A

Flux linking a short elliptic aperture

With reference to Fig. 5.5 and irrespective of the applied H-field orientation, the component $H_{z,c}$ (along the z-axis) penetrating or emerging from a circular hole of radius b obeys the law (Casey, 1981)

$$H_{z,c} = \frac{2H}{\pi} \frac{\rho}{\sqrt{(b^2 + \rho^2)}} \cos \alpha \qquad (5.13)$$
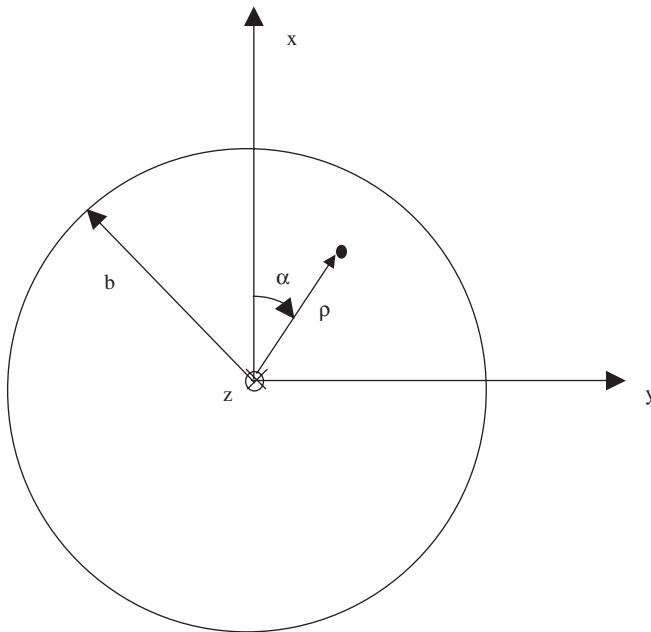
Fig. 5.5. Polar representation centred on a circular hole of radius b cut on a sheet which lies on the (x,y)-plane.

Here, $\rho = \sqrt{x^2 + y^2} \leqslant b$ and $\alpha = tg^{-1} y/x$. The field averaged on the semi-surface $A_c/2 = \pi b^2/2$ of the circle of area A_c, into which the flux ϕ_c of the field $H_{z,c}$ penetrates (or from which it comes out), is $H_{z,m} = 2H/\pi$. Therefore,

$$\phi_c = \mu_o H_{z,m} \frac{A_c}{2} = \mu_o H(2b) \left(\frac{b}{2}\right) = \mu_o H b^2 \tag{5.14}$$

represents the magnetic flux linking the circular aperture. The interior flux ϕ_c becomes tangential to the hole and flows with the same orientation of the applied exterior field H only in correspondence of a specific cross-section. If H is, say, oriented along the y-axis, the planar surface area $A_{y,c}$ results equal to $2b \cdot b/2 = b^2$ and positioned across and transverse to the linked circular hole. It is worth considering that

- the averaged (over $A_{y,c}$) magnetic field $H_{y,c}$ of the linking flux ϕ_c is exactly equal to the undisturbed exterior field H. Accordingly, $H_{z,m}(A_c/2) = H A_{y,c}$ easily derives from Eq. 5.14;

- $p = b/2$ represents the average penetration depth of ϕ_c; and

- the equalities $\phi_c/(\mu_o A_c/2) = \phi_e/(\mu_o A_e/2) = 2H/\pi = H_{z,m}$ have been found (see later) with reference to the flux ϕ_e linking an elliptic hole of semi axes a and $b < a$ and area $A_e = \pi ab$ (see, in Fig. 5.6, the ellipse in which the circumference of radius b is inscribed).

Therefore, in the case of an elliptic hole oriented with the minor axis b along H, Eq. 5.14 becomes

$$\phi_e = \mu_o H_{z,m} \frac{A_e}{2} = \mu_o H(2a) \left(\frac{b}{2}\right) = \mu_o H ab \tag{5.15}$$

After the circular aperture, $A_{y,e} = 2a \cdot p$ with $p = b/2$ are established now for the elliptic one.

The circumscribing referential circumference of radius a, see again Fig. 5.6, is the geometrical prerequisite for repeating the above procedure when H becomes x directed. Thereby, $A_{x,c} = \pi a^2$ replaces $A_{y,c}$ while interchanging methodically a and b, as required, gives $A_{y,e} = 2b \cdot p$ with $p = a/2$. An interesting observation is that p changes with the relative orientation of the elliptic aperture with H, while $H_{z,m}$ and H, intended as the fields averaged over $A_c/2$ (or $A_e/2$) and $A_{x,c}$ (or $A_{y,e}$), respectively, both remain unchanged. Therefore, the orientation in question is quite uninfluential and, on the other hand, substantively influential for the linking flux ϕ_e and the penetration depth p, respectively. Such a finding is especially important for elongated holes, in which case the semi-axis a of the elliptical model results significantly departed from b.

Equation 5.15 and relevant considerations, based on the equivalence between a circumference and an inscribed or circumscribed ellipse as depicted in Fig. 5.6, descend from an attractive property of projective geometry involving the notion of homological affinity. According to such a theory, the contours and surfaces of a pair of geometrical figures correspond mutually along a common direction, generally referred to as affinity direction,
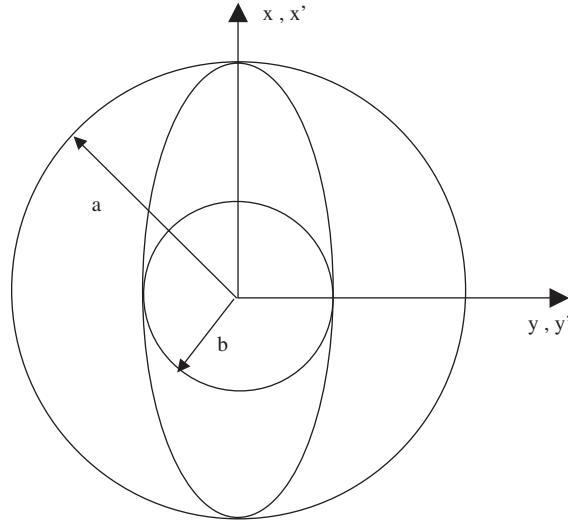
Fig. 5.6. Representation of ellipses homologically affine to a circle.

if the latter is superimposed on a specific main axis of each figure. In order to appreciate the notion under examination, special attention could, for example, be paid to the ellipse of semi-axes a, b and the inscribed circumference of radius b reproduced in the above figure. Let the main axes of the ellipse be taken as a frame of reference (x,y) differing from (x',y'), assuming the latter for the circumference. If the coordinate axes x' and y' are superimposed on x and y, respectively, the canonical figures under examination result homologically affine along the common direction of the y- and y'-axes if the equalities

$$x = \frac{a}{b}x'; \quad y = y' \tag{5.16}$$

are a priori established. By virtue of the above expressed affinity, the ellipse of equation

$$\frac{x^2}{a^2} + \frac{y^2}{b^2} = 1 \tag{5.17}$$

corresponds to the circumference of equation

$$x'^2 + y'^2 = b^2 \tag{5.18}$$

In fact, rearranging Eqs. 5.16 and 5.17 immediately gives Eq. 5.18. A similar procedure can be performed to prove the homological affinity between the above ellipse and its circumscribed circumference of radius a, thereby along the common direction of the respective x- and x'-axes.

Appendix B

Resistance and inductance of an elliptic aperture when resulting unfilled, or filled by a continuous sheet

Let a generic function $f = f(x, y)$ of the variables x and y be the general integral of the 2D form of Laplace's equation

$$\frac{\partial^2 f}{\partial x^2} + \frac{\partial^2 f}{\partial y^2} = 0 \qquad (5.19)$$

Consider that there is a pair of functions $\varphi = \varphi(x, y)$ and $\psi = \psi(x, y)$, real and continuous with their derivatives, satisfying the equality $f = \varphi + j\psi$. Therefore, the functions φ and ψ, which are also solutions of Laplace's equations, are called conjugate functions. Setting $\varphi = $ const. and $\psi = $ const. means that two families of orthogonal curves, respectively playing the roles of potential and flux functions of a physical planar field, are represented. If $\boldsymbol{J}$ denotes the surface current density oriented in the negative direction of the x-axis,

$$I(y) = [\psi(+|y|) - \psi(-|y|)]\,\delta = -2Jy \frac{1 + m\left(n_y - \dfrac{ab}{2}T_y\right)}{1 + mn_y} \qquad (5.20)$$

represents the exact solution, referred to the boundary-value problem posed in sub-Section 5.2.3, for the partial current delimited by the sheet thickness δ and the curves $\psi = \psi(\pm|y|)$. The notation adopted for such curves tacitly means that they are symmetrical with respect to the x-axis and cut orthogonally the y-axis at the points of ordinate $y = \pm|y|$. The total current

$$I = I(y = y_w) = [\psi(+|y_w|) - \psi(-|y_w|)]\,\delta = -2Jy_w \frac{1 + m\left(n_y - \dfrac{ab}{2}T_y\right)}{1 + mn_y} \qquad (5.21)$$

is assumed as being uniformly applied to a rectangular sheet, with centred elliptic hole, at the thin base of area $w \cdot \delta$. The hole is filled by a material of conductivity σ_h and surrounded by a material of conductivity σ, so that the dimensionless quantity $m = (\sigma - \sigma_h)/\sigma_h$ embodied in the above formulas takes into account the material properties pertaining to the nature of the field under examination, which is an electrokinetic (or ohmic-current) one. The contour sides of the holed rectangular sheet are distanced (hence, large) enough to be practically preserved from field perturbations surrounding the hole. In particular, $I = -2Jy_w = -Jw$ if the hole is completely blocked by a homogeneous material (of course, such a circumstance can alternatively be formalised by setting $\sigma = \sigma_h$ or $a = b = 0$). By the way, consider that the negative sign in Eqs. 5.20 and 5.21 means that the current has been applied against the y-axis orientation.

Let the pair of curves $\varphi(x = \pm|x|)$ denote two field equipotentials, symmetrical with respect to the y-axis, cutting orthogonally the x-axis at the points of abscissa $x = \pm|x|$.

Accordingly,

$$V' = \varphi(+|x|) - \varphi(-|x|) = -2\frac{J}{\sigma}x \frac{1 + m'\left(n_x - \dfrac{ab}{2}T_x\right)}{1 + m'n_x} \tag{5.22}$$

represents the difference between the potentials of the curves $\varphi = \varphi(\pm|x|)$ provided that the previous material factor m is replaced by $m' = (\sigma_h - \sigma)/\sigma$. Such a notation means that the above pair of curves are symmetrical with respect to the y-axis and cut the x-axis orthogonally at the points of ordinate $x = \pm|x|$. See sub-Section 5.2.3 for the significance of further variables and functions involved. The total voltage appearing between the pair of l-distanced $(l = 2x_l)w$-wide sides of the rectangular sheet obeys the law

$$V = \varphi(+|x_l|) - \varphi(-|x_l|) = -2\frac{J}{\sigma}x_l \frac{1 + m'\left(n_x - \dfrac{ab}{2}T_x\right)}{1 + m'n_x} \tag{5.23}$$

where the ratio J/σ represents the uniform electrokinetic field for a homogeneous sheet. In particular, $V = -2Jx_l/\sigma = -Jl/\sigma$ if the hole is completely blocked by a homogeneous material ($\sigma_h = \sigma$). Dividing Eq. 5.23 by 5.22 and setting $\sigma_h = 0$ gives Eq. 5.3 which represents the resistance of a rectangular sheet on which a hole is cut.

The tangential flow of the current I also causes superposition on one surface of the sheet of a simultaneous and orthogonal magnetic field $\boldsymbol{H}$. Such a vector is in modulus equal to J and directed in opposition to the x-axis (the latter feature accounts for the negative sign in the formulas reported below). Likewise the previous treatment,

$$\phi' = \varphi(+|x|) - \varphi(-|x|) = -2\mu_o Hx \frac{1 + m'\left(n_x - \dfrac{ab}{2}T_x\right)}{1 + m'n_x} \tag{5.24}$$

represents now a partial amount of surface magnetic flux delimited by the curves $\varphi = \varphi(\pm|x|)$, while the total flux obeys the law

$$\phi = \varphi(+|x_l|) - \varphi(-|x_l|) = -2\mu_o Hx_l \frac{1 + m'\left(n_x - \dfrac{ab}{2}T_x\right)}{1 + m'n_x} \tag{5.25}$$

In particular, $\phi = -2\mu_0 Hx_l = -\mu_0 Hl$ if the hole is completely blocked by a homogeneous plate. See again sub-Section 5.2.3 for the significance of further variables and functions involved. Consider how responsible for the similar structures of Eqs. 5.22–5.25 is the current density J which represents the fundamental electrokinetic-field function and, simultaneously, the source of the magnetic field (of course, the roles of source and induced effect between J and H can be interchanged). Dividing Eq. 5.25 by 5.21, setting $\sigma_h = 0$ and introducing the height h delimiting the partial area $h \cdot x_l$ linked by a portion of the interior flux AH_i, gives Eq. 5.5 which represents the external inductance associated

with the holed elemental sheet under examination. Instead, rearranging Eqs. 5.21 and 5.23 (or 5.25), and realistically assuming $0 < \sigma_h < \sigma$, again gives Eqs. 5.3 and 5.5, provided that ξ_x obeys Eq. 5.11, for it is distinctive of an aperture loaded by a continuous plate.

Appendix C

Flux penetration into an aperture blocked by a sheet of different material

Rearranging Eq. 5.24 and imposing $x = a$, which implies $abT_x/2 = n_x$, gives

$$\phi' = \varphi(+|a|) - \varphi(-|a|) = -2\mu_o Ha \left(1 + \frac{|m'| \, n_x}{1 + m'n_x} \right) \tag{5.26}$$

The above surface flux is collected by the elliptic contour of main semi-axes a and b. Let the loaded hole be now disclosed and b virtually changed in order for the hole to catch the same flux. Accordingly, $m' = -1$ and Eq. 5.26 becomes

$$\phi' = -2\mu_o Ha \left(1 + \frac{b'}{a} \right) \tag{5.27}$$

where

$$b' = b \frac{|m'| \, a}{a + b(1 + m')}$$

is given by equalising Eqs. 5.26 and 5.27. By remembering Eq. 5.15,

$$\phi_e = \mu_o H_{z,m} \frac{A_e}{2} = \mu_o H(2a) \left(\frac{b'}{2} \right) = \mu_o Hab' \tag{5.28}$$

which implies, according to Eq. 5.26, that

$$p = \frac{b'}{2} = \frac{b}{2} \frac{|m'| \, a}{a + b(1 + m')} \leqslant \frac{b}{2} \tag{5.29}$$

It is worth considering that ϕ_e and p can profitably be assumed as surrogates of the concentrated penetrating field when the aperture is elliptic, oriented with the minor axis along $\boldsymbol{H}$ and blocked by a sheet of conductivity $\sigma_c < \sigma$. In alternative to Eq. 5.29,

$$p = \frac{b'}{2} = \frac{b}{2} \frac{ma}{b + a(1 + m)} \leqslant \frac{b}{2} \tag{5.30}$$

can also be written. In fact, Eq. 5.30 derives from repeating the above procedure for the current, namely by involving Eq. 5.20 instead of 5.24. Of course, consistent with such a substitution is imposing $y = b$, which implies $abT_y/2 = n_y$. If care is taken of replacing

a with b and b' with a', then Eqs. 5.28 and 5.29 (or 5.30, indifferently) can be adopted even in the case of $\boldsymbol{H}$ pointing along the major axis of the elliptic hole.

Appendix D

Some remarks on the notion of flux linkage applied to a hole

Using Eq. 5.20 and rearranging gives

$$I(y) = -2Jy\left(1 - \frac{m\frac{ab}{2}T_y}{1 + mn_y}\right) = I_{\mathrm{o}}(y) + I_p(y) \tag{5.31}$$

Here, $I(y)$ represents the net current, surrounding an isolated elliptic hole, when the far current density $\boldsymbol{J}$ is oriented in opposition to the x-axis. Such a current can be decomposed into the unperturbed term $I_{\mathrm{o}}(y) = -2Jy$ and the oppositely directed perturbation component

$$I_p(y) = 2Jy\frac{m\frac{ab}{2}T_y}{1 + mn_y} < 2Jy \tag{5.32}$$

The above formula reduces to

$$I_p(y) = 2Jy\frac{ab}{2n_y}T_y \leqslant 2Jy \tag{5.33}$$

for an unloaded aperture ($m = \infty$).

The structures of formulas 5.32 and 5.33 suggest that the perturbation current I_p can be pictured as being split into a pair of symmetrically circulating (with respect, in this example, to the x-axis) planar flows. The latter progressively dilute while mutually departing outside the hole contour and conversely convoy, symmetrical to the y-axis, into the hole contour, where they proceed to be joined and concentrated uniformly. The circulating nature of such twin flows of current accounts for the approximation to zero of the net function $I_p(y)$ for $y \gg b$. In fact, the quantity T_y embodied in both Eqs. 5.32 and 5.33 vanishes under the above conditions. It is worth considering that it is exactly I_p the source of the distributed magnetic flux able to partially or fully enclose the hole surface, therefore, to fully linking a wire laid across the hole, on the interior side of a thin-walled shield, along the x-axis. The magnetic flux component correlated to $I_o(y)$ cannot participate the linkage with the flux component correlated to $I_p(y)$, thus making the linking features of the $I(y)$-originated overall flux hard to interpret without hesitation.

Everything considered, the above treatment and related discussion give supplementary arguments to state that

- the current crossing and the resistance of an unloaded hole are equal to zero and infinity, respectively, as expected indeed. In fact, rearranging Eqs. 5.31 and 5.33 and setting $m = \infty$ and $y = b$, gives $I(y = b) = 0$ since $I_p = -I_{\mathrm{o}} = 2Jb$;

- differently from the resistance, the notion of inductance does not seem rigorously applicable to a hole since the net flux passing through (hence, actually linking) a hole is invariably null. In addition, such a notion should suffer from an indeterminate form if applied to an unloaded hole since also $I(y = b)$ vanishes ($I(y = b) > 0$ only if m differs from infinity; on the concern, compare Eqs. 5.32 and 5.33);

- adopting the usual terminology "flux linking a hole", or similar ones, is permissible if the above clarifying considerations can tacitly be understood, a rather severe condition which could not exactly be met.

References

Babister A.W., "The mathematical theory of fields", in *Field analysis*: *experimental and computational methods*, D. Vitkovitcht Ed., Van Nostrand, London, 1966.

Bridges J.E., "An update on the circuit approach to calculate shielding effectiveness", IEEE Trans. Electromag. Compat., **EMC-30** (1988) 211.

Casey K.F., "Low frequency electromagnetic penetration of loaded apertures", IEEE Trans. Electromag. Compat., **EMC-23** (1981) 367.

Casey K.F., "Electromagnetic shielding behavior of wire-mesh screens", IEEE Trans. Electrom. Compat., **30** (1988) 298.

de Meulenaere F., van Bladel J., "Polarizability of some small apertures", IEEE Trans. Antennas and Propag., **AP-25** (1977) 198.

Jaggard D.L., "On using isoperimetric inequalities and isoperimetric quotients in electromagnetic theory and applied physics", in *Theoretical methods for determining the interaction of electromagnetic waves with structures*, J.K. Skwirzynski Ed., Sijthoff & Noordhoff, Alphen aan den Rijn, 1981.

McDonald N.A., "Polynomial approximations for the electric polarizabilities of some small apertures", IEEE Trans. Microwave Theory Tech., **MTT-33** (1985) 1146.

Méndez H.A., "Shielding theory of enclosures with apertures", IEEE Trans. Electromag. Compat., **EMC-20** (1978) 296.

Morse P.M., Feshbach H., *Methods of theoretical physics* (Part II), McGraw-Hill, New York, 1953.

Osborn J.A., "Demagnetizing factors of the general ellipsoid", Phys. Rev., **67** (1945) 351.

Sten J.C.-E., "Magnetic moment and surface dipole distributions of circular holes in a conducting screen", IEEE Trans. Electromag. Compat., **41** (1999) 290.

Taylor C.D., "Electromagnetic pulse penetration through small apertures", IEEE Trans. Electromag. Compat., **1** (1973) 17.

Tesche F.M., Ianoz M.V., Karlsson T., *EMC analysis methods and computational models*, John Wiley, New York, 1997.

Vance E.F., "The nuclear electromagnetic pulse", in *Handbook of electromagnetic compatibility*, R. Perez Ed., Academic Press, New York, 1995.

Williams T., *EMC for product designers*, Newnes, 1996.

This page intentionally left blank

CHAPTER 6

Diakoptic Approach to EMC Problems Involving the Human Body

V. Amoruso and F. Lattarulo

Abstract

A lumped-parameter circuit model of a variously postured human body (HB), useful for studying the current response to both extremely low frequency (ELF) electric field exposure and electrostatic discharge (ESD), is described here. Therefore, the current distribution calculated inside a variously postured HB is the one induced by the quasi-static coupling with an applied electric field or abruptly appearing during an ESD event. The HB has previously been partitioned into 11 blocks, corresponding to as many anatomically discernible parts, each represented by a tern of resistive, inductive and capacitive parameters. Specifically, the set of block capacitances has been determined by a procedure based on the diakoptic theory, for which the HB has been assumed as being a perfectly conducting multi-spheroidal structure composed of 11 elements. The circuital resistive and inductive parameters are calculated by a subsidiary electromagnetic approach to biological tissue modelling. The reasons leading to recommend the diakoptic method for the above EMC applications are extensively discussed.

6.1 Introduction

Tribo-electrification and exposure to extremely low frequency (ELF) electric fields cause the induction of electric charges in the human body (HB). In the case of alternating fields, the human body experiences an internal transfer of opposite polarity charges every half-cycle, whereas in the case of tribo-electrification phenomena, a non-repetitive rapid transfer of charge (electrostatic discharge, ESD) can occur between the HB and an object having a different electric potential and positioned very close to or even brought into contact with it. However, both phenomena are strongly influenced by the capacitive coupling of the body with the earth and with near metallic objects (earthed or floating).

133

The human body's biological tissue properties, shape, posture and distances from nearby objects are some of the parameters determining the electric fields induced inside and current densities. These *in situ* electrical quantities are directly related to several interaction mechanisms, at cell level, which are established and recognised by Standards (see IEEE Std. C95.6-2002, ICNIRP 1998). For an exhaustive review on the interaction of ELF fields with living systems, see Repacholi (1999).

Experimental investigations conducted on cell cultures (*in vitro* studies) and animals (*in vivo* studies), or directly involving human subjects (volunteer groups monitored in laboratory or forming a numerous population for an epidemiological approach), in conjunction with theoretical models of the HB for simulating the exposure conditions have led to improve the understanding of the interaction of the HB with the electromagnetic fields, even if there are many open questions relative to the possible association between exposure to ELF fields and the onset of serious diseases. A pertinent review about the effects of electric and magnetic fields and potential health hazards is reported in NRC (1997).

The evaluation of the electrical quantities especially induced in an HB interacting with an ELF electric field has been the subject of considerable research over the last four decades. After the first measurements carried out under actual working conditions (Barnes *et al.*, 1967), for example, the use of a hollow full-size metallic mannequin of a man disposed under a high-voltage transmission line (Deno, 1977), the pioneering research of experimental macro-dosimetry later extended to animal models (Kaune and Phillips, 1980; Kaune and Forsythe, 1983 and 1985; Miller, 1991). The measured average current distribution and their densities are still an important reference for the theoretical macro-dosimetry.

A considerable amount of theoretical research work was developed by adopting both analytical and numerical methods. The choice of the analytical method has led to model living systems using simple geometrical shapes, such as a sphere (Spiegel, 1976), prolate spheroid (Barnes, 1967), hemi-ellipsoid (Bayer *et al.*, 1977; Lattarulo and Mastronardi, 1981; Hart and Marino, 1982) and vertical cylinder (King, 1998). Using these geometrical shapes, the boundary problem is simplified and a first approximation of the electrical quantities (electric fields and current densities) induced inside the biological tissues is provided.

Different numerical methods (such as the Method of Moments (MOM) by Spiegel, 1977, Surface Charge Integral Equation Method (SCIEM) by Chen *et al.*, 1986, Monte-Carlo random-walk technique by Pickles, 1987, Charge Simulation Method (CSM) by Mahdi and Anis, 1987, Finite Element Method (FEM) by Chiba *et al.*, 1984) have been used to take into account the complexity of the HB shape and heterogeneity of the inner biological tissues (such as SCIEM by Chuang and Chen, 1989, Finite Difference Time Domain method (FDTD) by Gandhi and Chen, 1992; Stuchly and Dawson, 2000, Boundary Element Method (BEM) by Poljak *et al.*, 2005; Gonzales *et al.*, 2005).

The accuracy of the results obtained by these numerical techniques is likely to be higher as the discretisation degree of the domain under study becomes greater. Singularities could arise along the boundary of two different adjacent domains

and suitable post-processing of results could be required for reducing the errors. Moreover, data preparation, computation time and memory become very expensive when the partitioning degree increases or when a "dynamic" dosimetry has to be simulated. For example, for a fixed posture of the HB, the calculation carried out by adopting the finite difference method could involve millions of unknowns and a computation time of tens of hours using a workstation of hundreds of megabytes of physical memory for a high-resolution (3.6 mm voxels) modelling (Dawson and Stuchly, 1998).

A HB numerical model characterised by a good accuracy, in spite of adopting a low body-partitioning degree, has been implemented by Amoruso and Lattarulo (1989), for studying ELF uniform electric-field exposure problems. This model is based on the diakoptic theory previously vindicated by Goubau *et al*. (1982) and Schwering *et al*. (1986), for analysing the low-frequency performances of multi-element antennas. The interaction of the HB with the external electric field is represented by a circuit of 11 capacitances to earth (stray capacitances) corresponding to as many main parts (head, chest, abdomen, limbs) in which the HB has ideally been partitioned. A careful experimental investigation (Amoruso and Lattarulo, 1994) has allowed the verification that manipulating large-dimensional elements by the diakoptic approach gives rise to no significant loss of computational accuracy. The results are estimated as being affected by an error lower than 5%, which is compatible with the wide class of engineering applications permitted by this technique.

Later, the above HB model has been improved by introducing serial resistive and inductive parameters, for each block of the body, to simulate a discharging HB subject to ESD (Amoruso *et al*., 2000). The obtained lumped parameter circuit (implemented by PSPICE) is able to evaluate the (total) ESD current, in waveform and peak value, as well as the contributions of each block. Moreover, the accurate computation of the capacitive coupling involving each block allows the HB's posture and proximity to variously dimensioned and earthed/floating victims to be taken into account (Amoruso *et al*., 2001, 2002). The results of the analysis carried out by this model (in terms of transient current distribution inside the HB) are in good agreement with those obtained by the FDTD method, recently applied to the HB interaction with ESD (Okoniewska *et al*., 2004).

By virtue of the good accuracy of the results, restricted computation time and memory and ease of application, the diakoptic approach is strongly recommended for improving the cost/benefit ratio when posed with capacitive coupling problems.

6.2 Diakoptic Approach Applied to ELF Electric Field Exposure of HB

6.2.1 Evaluation of equivalent capacitances to earth

A well-known mechanism of interaction of HB biological tissues with ELF electric fields is the induction of time-varying electric currents and fields. The displacement current, collected by several surface portions of the body exposed to the electric field, penetrates into the body completely (because of the high penetration depth as compared to the dimensions of the HB), thereby assuming an essentially ohmic nature. Cardiovascular system,

as well as the brain and central nervous systems, are considered likely sites of interaction with ELF fields, since the involved tissues are sensitive to electrical signals. Therefore, the current density is the main parameter proposed by the ICNIRP (1998) for protection against adverse health effects under the exposure circumstances described here. Because of the body non-homogeneity, current densities are suggested as being averaged over a cross section of 1 cm^2 perpendicular to the current direction, thus implying the use of high-resolution numerical models to analyse the electric field exposure effects. However, these numerical techniques (see, for example, FDTD adopted by Okoniewski *et al*., 2001), recommended for evaluating the specific absorption rate (SAR) distribution in single portions of the HB at higher frequencies, are very expensive in terms of memory requirement, time consumption and data implementation as far as quasistatic exposure simulations are concerned (in which case the structural sizes are negligible fractions of shorter wavelength). Moreover, FDTD requires the introduction of ELF excitation models taking into account the electric field distortion produced by the HB itself. Conversely, the diakoptic technique gives average current densities comparable with the average values computed by high-resolution numerical methods and, by virtue of its features, can solve quasistatic 3D problems quickly and accurately, even when body animation is introduced into the simulation.

The very advantage of the diakoptic approach lies in the fact that using large-dimensioned block simulators of canonical shape is a permissible practice. As a result, the low body-partitioning degree ensures even shorter processing time and computer memory. Therefore, $N = 11$ basic anatomical parts of an HB (head, chest, arms, forearms, abdomen, thighs, legs) have been replaced by as many conducting prolate and oblate spheroids which can be so arranged as to simulate any human posture. Figure 6.1 shows an interconnected assembly of spheroidal conductors for simulating a man standing on the earth's plane. The latter is taken into account by introducing the mirror image of the man's model. The multi-spheroidal arrangement has been chosen to mimic the various postures rather than for fitting the geometry of the single human blocks. In fact, Chow and Yovanovich (1982) (see also Greason, 1992) extensively prove that an electrostatic simulator of a variously shaped body is a sphere of appropriate radius.

Table 6.1 reports the semi-axes a_i, b_i, c_i of each spheroid, which are derived from basic anatomical ratios and empirically obey the condition that the sum of the spheroidal surfaces is equal to the overall surface ($\approx$1.8 m^2) of a 1.70 m tall man ($\approx$70 kg). The interconnections between each pair of contiguous spheroids is ensured by a set of ideal wire segments bridging pairs of terminals. The exact location of the terminals on each spheroid is unimportant, as the electrostatic equivalence imposed on the spheroidal assembly requires only a capacitive representation. When this structure is exposed to the vertical uniform electric field E_{o}, the displacement currents collected by the spheroids flow through conducting routes to the plane. The contacts with the earth are generally represented by concentrated impedances which can be preliminarily short-circuited (Lin *et al*., 1990). Moreover, to avoid calculation complexity, the person is considered as standing on one foot while the other one is a little suspended so that the reciprocal positions of the spheroids remain (and therefore their mutual capacitive couplings) substantially unchanged. Accordingly, the junction current distribution is that depicted in Fig. 6.1. The junction currents, including the short-circuit total current I_1, are the unknowns of the problem.
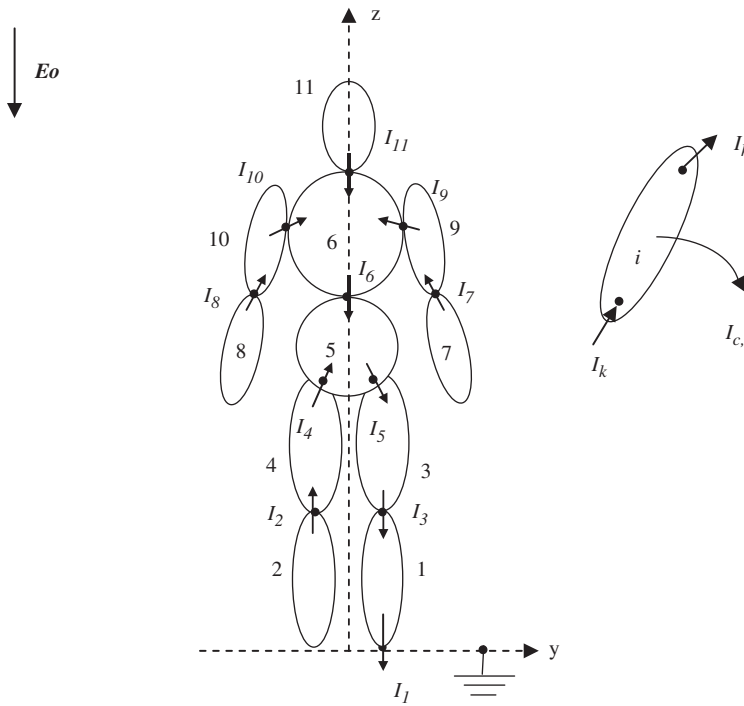
Fig. 6.1. Multi-spheroid model of an HB for studying the ELF electric field exposure by the diakoptic method.

Table 6.1. Spheroid semiaxes a_i, b_i, c_i adopted for the HB model of Fig. 6.1 and relative centre coordinates for an upright 1.70 m tall man.

Spheroid numbering	Prolate $a_i > b_i = c_i$		Oblate $a_i = b_i > c_i$		Centre coordinates			C_{eq_i} [pF]
	a_i [m]	b_i [m]	a_i [m]	c_i [m]	x_i [m]	y_i [m]	z_i [m]	
1, 2	0.21	0.06			0	±0.13	0.21	10.63
3, 4	0.22	0.09			0	±0.13	0.65	4.26
5			0.14	0.09	0	0	0.95	2.17
6			0.17	0.09	0	0	1.26	4.33
7, 8	0.18	0.05			0	±0.29	0.79	3.67
9, 10	0.19	0.06			0	±0.25	1.16	4.27
11	0.14	0.09			0	0	1.56	7.17

By adopting the antenna reciprocity theorem, the induced currents can be driven by a voltage source V_o applied between the body and the earthed plane after removing the incident field.

With reference to the case study at hand, the diakoptic technique consists in breaking up the man-like antenna into single spheroids and applying a suitable current at each

terminal of the torn junction. The relationship between the scalar potentials produced by the dominant current distribution at the terminals of the diakopted structure and the current applied at the same terminals, as well as at the terminal of the other elements, is formulated in terms of impedance matrix of the diakopted structure

$$[V^*] = [Z^*][I^*] \tag{6.1}$$

where $[V^*]$ is the scalar potential vector, $[I^*]$ is the unknown applied-current vector, and $[Z^*]$ is the diakopted structure's impedance matrix. Denoting m and n as two generic terminals of the diakopted structure, the relevant element of matrix $[Z^*]$ is

$$Z_{mn}^* = \frac{1}{j\omega C_{mn}} \tag{6.2}$$

where

- C_{mn} is set equal to the intrinsic capacitance C_i if the m-th and n-th terminals lie on the same ith spheroid, as reported in Table 6.2;

- C_{mn} is calculated by averaging C_{ij} and C_{ji} as defined in Table 6.2 if the m-th and n-th terminals lie on ith and j-th spheroids, respectively. The parameter ξ_j inserted in the formula of C_{ji} is distinctive of the surface, confocal to the ith spheroid of centre O_i, on which the centre O_j of the j-th spheroid lies (Durand, 1964; Li *et al.*, 2002). Similarly, C_{ij} assumes the same expression of C_{ji} provided that the subscript i is replaced with j.

- ω is the angular frequency of the electric field.

In order for the diakopted and assembled structures to be functionally indistinguishable, an interconnection matrix $[M]$ is used to enforce the current continuity and the equality

Table 6.2. Approximate expressions of the spheroid intrinsic C_i and mutual C_{ij} capacitances.

		Oblate ($a_i = b_i > c_i$)	Prolate ($a_i > b_i = c_i$)
C_i		$\dfrac{4\pi\varepsilon_o\sqrt{a_i^2 - c_i^2}}{\tan^{-1}\sqrt{\left(\frac{a_i}{c_i}\right)^2 - 1}}$	$\dfrac{8\pi\varepsilon_o\sqrt{a_i^2 - b_i^2}}{\ln\frac{a_i+\sqrt{a_i^2-b_i^2}}{a_i-\sqrt{a_i^2-b_i^2}}}$
C_{ji}		$\dfrac{4\pi\varepsilon_o\sqrt{a_i^2 - c_i^2}}{\tan^{-1}\sqrt{\frac{a_i^2-c_i^2}{\xi_j+c_i^2}}}$	$\dfrac{8\pi\varepsilon_o\sqrt{a_i^2 - b_i^2}}{\ln\frac{\sqrt{\xi_j+a_i^2}+\sqrt{a_i^2-b_i^2}}{\sqrt{\xi_j+a_i^2}-\sqrt{a_i^2-b_i^2}}}$
C_{ij}	As before, after replacing i with j		

of potentials on all the junction sections. Therefore,

$$[I^*] = [M][I] \tag{6.3}$$

$$[V] = [M]^T[V^*], \tag{6.4}$$

where $[M]^T$ is the transpose of $[M]$, $[I]$ and $[V]$ denote the vectors of the unknown junction currents and of the junction voltages, respectively. The generic element of $[M]$ is 1 (or -1) if the current enters (or leaves) the terminal, otherwise it is zero.

Rearranging Eqs. 6.1, 6.3 and 6.4 gives

$$[V] = [M]^T[Z^*][I^*] = [M]^T[Z^*][M][I] \tag{6.5}$$

Finally,

$$[V] = [Z][I] \tag{6.6}$$

represents the assembled structure, where

$$[Z] = [M]^T[Z^*][M] \tag{6.7}$$

is the assembled structure matrix. According to the stationary property of the matrix representation (Goubau, 1982), the elements Z_{ij} of the matrix $[Z]$ are affected by second-order errors, even after assuming first-order current distribution for their calculations. This implies that the input capacitances C_{mn} could even be roughly formulated (see also Appendix A).

Therefore, the junction currents are determined by

$$[I] = [Z]^{-1}[V] = [Y][V] \tag{6.8}$$

where $[Y] = [Z]^{-1}$ and $[V] = [V_0\,0\,0\,\ldots\,0\,0]^T$ is the junction voltage vector. The elements $Y_{i,1}(i = 1/11)$ of the first column of matrix $[Y]$ represent the junction currents I_i if V_0 is set equal to 1 V. Accordingly

$$Y_{i,1} = I_i|_{V_0=1} \tag{6.9}$$

The interaction of the HB with the ELF electric field can be represented by 11 equivalent earth capacitances C_{eq_i} connected in parallel. As it will be explained later, each capacitance C_{eq_i} is correlated to the displacement current

$$I_{c,i} = \omega C_{eq_i} V_0\big|_{V_0=1} \tag{6.10}$$

collected by the surface of the ith spheroid as if it were isolated. By applying Kirchhoff's law to the ith spheroid (see the inset of Fig. 6.1), $I_{c,i}$ is expressed as a function of the junction currents involving the same spheroid. Last, the equivalent capacitances C_{eq_i} can be calculated by the expressions reported in Table 6.3.

Table 6.3. Formulas for determining the equivalent capacitances relative to the example of Fig. 6.1.

Element number	C_{eq_i}	Element number	C_{eq_i}
1	$\dfrac{Y_{1,1} - Y_{3,1}}{\omega}$	7	$\dfrac{Y_{7,1}}{\omega}$
2	$\dfrac{Y_{2,1}}{\omega}$	8	$\dfrac{Y_{8,1}}{\omega}$
3	$\dfrac{Y_{3,1} - Y_{5,1}}{\omega}$	9	$\dfrac{Y_{9,1} - Y_{7,1}}{\omega}$
4	$\dfrac{Y_{4,1} - Y_{2,1}}{\omega}$	10	$\dfrac{Y_{10,1} - Y_{8,1}}{\omega}$
5	$\dfrac{Y_{5,1} - Y_{4,1} - Y_{6,1}}{\omega}$	11	$\dfrac{Y_{11,1}}{\omega}$
6	$\dfrac{Y_{6,1} - Y_{9,1} - Y_{10,1}}{\omega}$	C_o	$\dfrac{Y_{1,1}}{\omega}$

The overall capacitance C_o of the structure (calculated as reported in Table 6.3) is equivalent to the 11 earth capacitances C_{eq_i} connected in parallel. Accordingly

$$C_o = \frac{Y_{1,1}}{\omega} = \sum_{i=1}^{11} C_{eq_i} \qquad (6.11)$$

Table 6.1 reports the values of C_{eq_i} for a 1.70 m tall man standing on the earth with his arms down.

6.2.2 Effective electrostatic heights and evaluation of the junction currents

The short-circuit current I_1 flowing to the earth, when the structure having capacitance C_o is exposed to a uniform vertical field E_o, can be evaluated by an analogic application of Thevenin's theorem to the quasistatic induction. Once the assembled multi-spheroid structure has been disconnected from the earth, it acquires the potential $h_o E_o$, where h_o denotes the electrostatic effective height of the assembled structure (Maruvada and Hylten-Cavallius, 1975). If the electric field E_o is removed and the spheroid structure is driven by a voltage source, then

$$V_o = h_o E_o \qquad (6.12)$$

and the feeding current becomes the total current

$$I_1 = \omega C_o E_o h_o \qquad (6.13)$$

If h_i is the electrostatic height of the ith spheroid, then C_{eq_i} is such that the following weighted-mean law should be satisfied

$$h_o = \frac{\sum_{i=1}^{11} h_i C_{eq_i}}{C_o} \tag{6.14}$$

The electrostatic heights h_i can be evaluated as reported by Maruvada and Hylten-Cavallius (1975) for different geometrical shapes. In practice, when the spheroid is substantially above earth, h_i can safely be set equal to the height of its geometric centre, while h_i becomes zero when the spheroid touches the earth. With reference to most usual postures, establishing h_i for intermediate cases and generic ellipsoid inclinations often results in an unimportant exercise.

Rearranging Eqs. 6.13 and 6.14 gives

$$I_1 = \omega E_o \sum_{i=1}^{11} C_{eq_i} h_i = \sum_{i=1}^{11} I_{c,i} \tag{6.15}$$

where

$$I_{c,i} = \omega E_o C_{eq_i} h_i \tag{6.16}$$

is the partial current collected by the ith spheroid. Additionally, the junction currents I_i can be calculated according to Kirchhoff's law applied to the ith spheroid (see inset of Fig. 6.1).

For a better interpretation of Eq. 6.16, it should be stressed that C_{eq_i} takes into account all the nearby mutual influences experienced by the ith spheroid in the context of the assembled structure. Therefore, C_{eq_i} can represent the capacitance of an equivalent ith element virtually assumed in isolation. Therefore, the partial current $I_{c,i}$ collected by the ith spheroid in the context of the assembled structure can be calculated quite ignoring the presence of the remaining $N-1$ spheroids.

6.2.3 Earthed person on the plane

The results obtained by the diakoptic procedure with application to the standard case of an upright man with his arms down are especially useful for comparison purpose. Table 6.4 reports the currents I_b induced inside some of the HB cross sections by a vertically impinging, uniform electric field $E_o = 10$ kV/m at $f = 60$ Hz. Such quantities are in agreement with the experimental and theoretical data provided elsewhere (Deno, 1977; Chiba *et al.*, 1984). The error is lower than 5 and 8% with respect to Deno's data and most of Chiba's data, respectively. The larger errors methodically found with respect to Chiba's data (the error increases to 25% only for the abdomen) are due to the fact that an oversimplified axial-symmetric mannequin is the model adopted by these authors.

Table 6.4. ELF dosimetry at $E_o = 10$ kV/m, $f = 60$ Hz. The standing human body (1.70 m; arms down) is considered on an earthed plane.

Body section	Diakoptic procedure I_b [μA]	Experimental data	
		(Deno, 1977) I_b [μA]	(Chiba et al., 1984) I_b [μA]
Feet	150.1	156.0	150.0
Pelvis	129.6	137.2	126.8
Chest (heart)	111.2	114.3	−
Abdomen	122.1	125.8	101.0
Knee	74.8	74.2	70.7
Neck	42.3	40.4	43.7
Arm	24.4	21.8	−

Moreover, Fig. 6.2(a) shows the comparison between the axial current distributions obtained by the diakoptic and both FDTD (Gandhi and Chen, 1992) and Deno's experimental data related to a 1.75 m tall man with same E_o and f. The axial current density distribution obtained by the diakoptic technique is compared with the experimental data (reported by Kaune and Phillips, 1980 and Chiba *et al.*, 1984) in Fig. 6.2(b) and with the

(a)   (b)   (c)
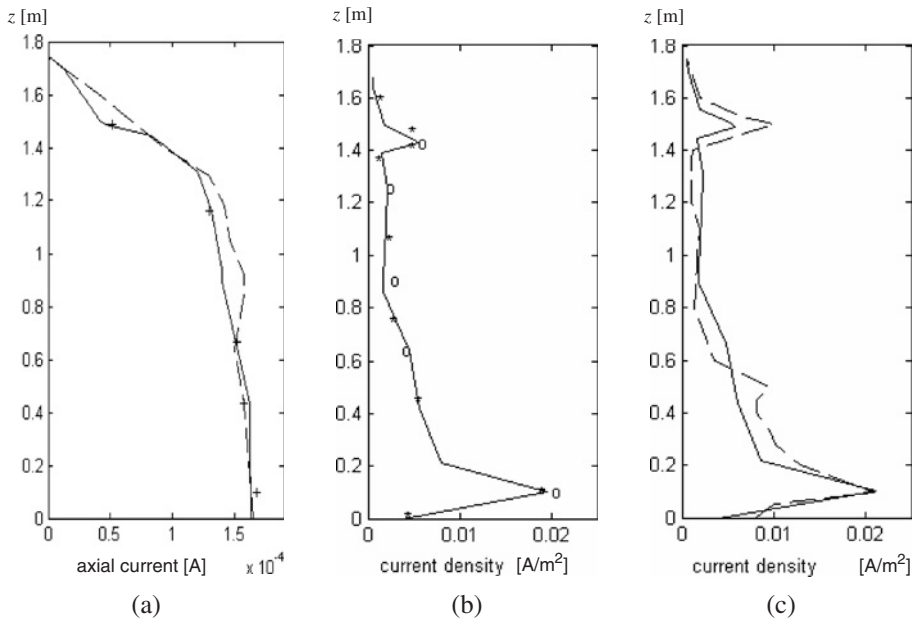
Fig. 6.2. ELF dosimetry at $E_o = 10$ kV/m and $f = 60$ Hz for an earthed standing man (on the plane): (a) Comparison between the theoretical average axial current distributions [(—) diakoptic method; (- - -) FDTD method (Gandhi and Chen, 1992)] and experimental data [(+ + +) Deno, 1977] for a 1.75 m tall man. (b) Comparison between the axial current density distribution obtained by the diakoptic method (—) and experimental data [(o o o) Kaune and Phillips, 1980; (∗ ∗ ∗) Chiba *et al.*, 1984] for a 1.70 m tall man. (c) Comparison between two theoretical axial current density distributions [(—) diakoptic method; (- - -) BEM (Gonzales *et al.*, 2005)] for a 1.75 m tall man.

axial current density distribution computed by BEM (Gonzales *et al.*, 2005) in Fig. 6.2(c), respectively (see the caption of Fig. 6.2 for details). In spite of the low partitioning degree of the domain under study, the most striking result is that the good accuracy attained by the diakoptic procedure is corroborated by the given experimental and theoretical data using more sophisticated methods. It is worth considering that the reported examples require less than 100 kB of memory for each dosimetric estimation and a computing time of 0.3 s if a Pentium 4 processor is used. Incidentally, note that the current density values in the head and trunk are lower than 10 mA/m^2 by one order of magnitude, which is the basic restriction provided by ICNIRP (1998) for occupational exposures.

As previously stated, owing to its own special features, the diakoptic procedure is recommended for exposure studies applied to animated systems. A pair of examples are reported to better appreciate the above statement. A preliminary evaluation of the geometrical quantities describing the movement of the kinematic chain has been implemented for both the examples. The case of a man whose arms are put into a side rotation, is considered first. Notation α denotes the angle between the main upright-man axis and straight-arm axis, therefore, $\alpha = 0°$ corresponds to the arm down. Figure 6.3 shows the currents I_b simultaneously flowing in different cross sections of the body as a function of α. Note how the more the arms rise, the more the inner currents increase, except for the current flowing through the neck, which decreases as expected. Maximum values
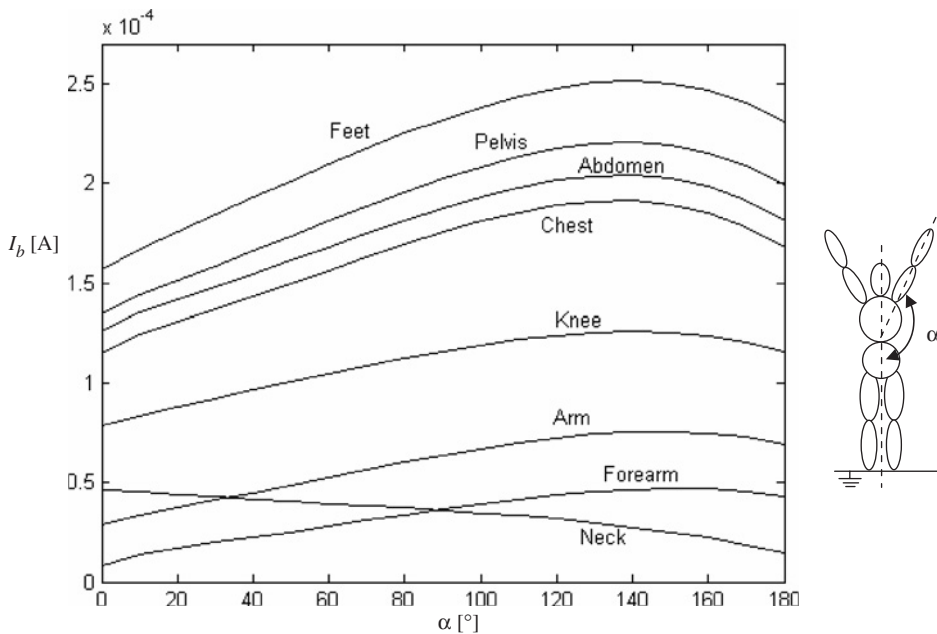
Fig. 6.3. ELF "dynamic" dosimetry for $E_o = 10$ kV/m and $f = 60$ Hz; earthed standing man on the plane): currents I_b induced in some sections of a 1.75 m tall man as a function of the arm inclination angle α (see inset); both arms are assumed being symmetrically rotated ($\alpha = 0°$: arms down; $\alpha = 180°$: arms up).

are obtained in the range $\alpha = 140°/160°$. The maximum relative changes are 165, 467 and -67% for the currents in the arm, forearm and neck, respectively, if referred to the corresponding magnitudes for $\alpha = 0°$ (changes relative to the remaining currents are about 60%; see caption to Fig. 6.3 for details).

The second example is relative to the simulation of a standard walk of the man. The currents I_b given in some sections of the body are shown in Fig. 6.4. It is worth mentioning that the total current flowing to earth (namely the current I_1 of Fig. 6.1) changes slightly during the movement; however, the current flowing into each foot changes from I_1 to about $I_1/2$, depending on if one-foot or both-feet are earthed, respectively. However, such alternating distribution does not affect the body sections placed above the pelvis.
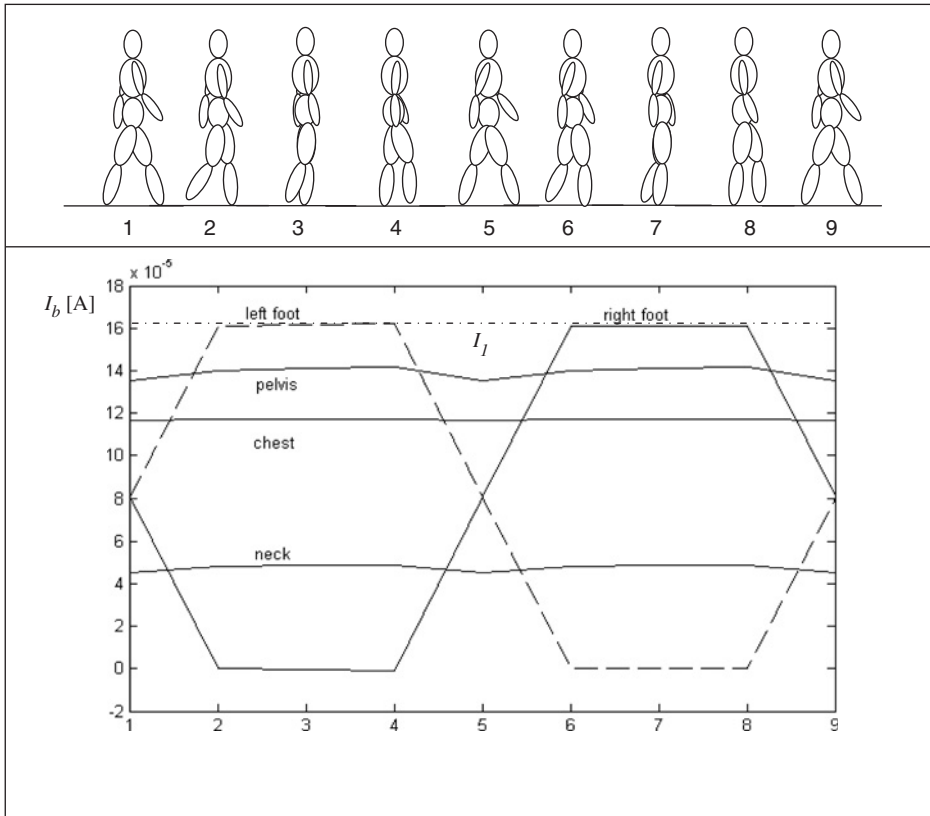
Fig. 6.4. Currents I_b induced in some sections of a 1.75 m tall man walking in a uniform electric field $E_o = 10\,\text{kV/m}$, $f = 60$ Hz. The x-axis reports the numeric sequence of the postures assumed by the human body during the walking.

6.2.4 Person suspended above the earth

The diakoptic approach is appropriate for modelling the case of a person (earthed or floating) suspended above the earth. In fact, rearranging Eq. 6.14 gives

$$h_o \sum_{i=1}^{N} C_{eq_i} = \sum_{i=1}^{N} h_i C_{eq_i} \tag{6.17}$$

Let n_1 (with $1 \leq n_1 < N$) and $N - n_1$ be two sets of spheroids such that $(h_i - h_o) > 0$ and <0, respectively. Accordingly, Eq. 6.17 becomes

$$h_o \sum_{j=1}^{n_1} C_{eq_j} + h_o \sum_{k=n_1+1}^{N} C_{eq_k} = \sum_{j=1}^{n_1} h_j C_{eq_j} + \sum_{k=n_1+1}^{N} h_k C_{eq_k} \tag{6.18}$$

Rearranging Eqs. 6.17 and 6.18 gives

$$\sum_{j=1}^{n_1} C_{eq_j}(h_j - h_o) = \sum_{k=n_1+1}^{N} C_{eq_k}(h_o - h_k) \tag{6.19}$$

After multiplying by ωE_o, both sides of Eq. 6.19 represent the displacement current collected by the suspended body disconnected from the earth. The two specified sets of blocks are distinguished by the overall electrostatic height h_o. It is noteworthy that the single equivalent capacitance C_{eq_i} calculated for a pre-established configuration may be arranged indifferently according to Eq. 6.13 or 6.19 to give a dosimetric assessment for an earthed or a floating body. Table 6.5 reports different current distributions for a man suspended at 1 m above the earth (relative to the same geometrical data of Table 6.1). In this case, h_o becomes 1.83 m, namely the electrostatic centre h_o rises from the thigh to the pelvis level. This change of h_o influences the current distribution in both earthed and floating cases. In the earthed case, the suspended HB

Table 6.5. ELF dosimetry at $E_o = 10$ kV/m, $f = 60$ Hz obtained by diakoptic approach when the standing HB (1.70 m; arms down) is considered 1 m suspended above the plane.

Body section	Earthed I_b [µA]	Floating I_b [µA]
Feet	319.04	0
Pelvis	219.69	33.95
Chest (heart)	158.28	35.37
Abdomen	205.37	34.97
Knee	134.31	14.30
Neck	61.50	18.63
Arm	42.34	5.26

experiences an increase in current throughout the body with respect to the standard case (earthed person). Specifically, the currents permeating the abdomen, pelvis and chest experience an increase of about 69%, whereas the arm, of about 100%. In spite of this increase, the current densities in the head and trunk are still in compliance with the basic restriction of 10 mA/m^2 (ICNIRP, 1998).

Conversely, all the current decreases in the floating case: the maximum value of the current is located in the heart section and corresponds to 27% of the induced current in the standard case. Moreover, the inner current decreases departing from this section towards the head or the feet.

6.3 Improved HB Model for ESD Applications

6.3.1 Preliminary remarks

The diakoptic procedure involving the HB proves to be especially predictive of typical figures of merit for ESD applications as discharge probability and severity (Amoruso *et al*., 2000). In fact, instead of the usual procedure based on manipulating Maxwell's coefficients (see the exhaustive survey by Greason, 1992), the diakoptic method directly involves stray and mutual capacitances. Hence, a not negligible argument in favour of the method vindicated here just consists in the fact that the more familiar (especially for practising engineers) notion of capacitance is basically exploited.

Here, the interconnected multi-spheroid system described in Section 6.2 is used to reproduce a generically postured man as a floating charge source in proximity of a charge sink. The latter object is represented by an additional 12th spheroid. As previously considered, the choice of the spheroids, instead of the spheres used early by Amoruso *et al*. (2000) for representing each HB portion, is prone to give more accurate results since an aggregate of ellipsoids better approximates a given posture without causing accidental interpenetrations between contiguous elements. Even the physical partial capacitances C_{eq_i} of the new man-victim model, which are functions of the HB posture, take into account the mutual electrostatic influence of the nearby object. The presence of earthed planar surfaces, representing floor and vertical wall, is considered by the imaged versions of the capacitances C_{eq_i}. These result as connected in parallel for representing the charging phase preliminary to the discharge (ESD event proper).

By assuming that the HB is charged as a function of an assigned voltage V_o and that an ESD event occurs, the all-pervading currents, as well as the total one applied to the victim, can be calculated after accomplishing the above capacitive circuit by a pair of serial lumped parameters $R_i, L_i (i = 1/11)$ for each ith element involved in the discharging phase. The serial parameters are rather evaluated by simple frequency-dependent notions (see later) and then by a more general diakoptic approach (which is possible in principle) in order not to compromise it with an excess of computational complexity. The layout of a lumped-parameter network evoking a standing man is shown in Fig. 6.5. The capacitance and resistance for each shoe-wearing foot have been set equal to $C_s = 50$ pF and $R_s = 100$ MΩ, respectively. The network of Fig. 6.5 has been implemented by PSPICE and the given transient responses for different simulations of ESD events are discussed later.

The spectrum corresponding to the total ESD current waveform is characterised by a bandwidth extending up to 1 GHz. Thus, the implied shortest wavelength (≈ 0.30 m) approaches the order of magnitude of the larger semi-axes of the used spheroids (see Table 6.1). At first, this comparison could lead to refine further the HB model discretisation for preserving the method accuracy. Indeed, the diakoptic method holds an acceptable accuracy even in the critical conditions described above. In fact, an optimum degree of partialisation as a function of the body's fatness parameter (the fatness parameter is currently defined as 2ln [(body length)/(body radius)], according to a currently adopted antenna theory terminology) was found by Goubau *et al.* (1982). Such a discretisation degree decreases significantly as the fatness parameter decreases. This is just the case for the present application, since most anthropometric ratios of the selected elemental parts are not exceeding the order of some unities.

Contrary to an optional transmission-line model, the capacitances C_{eq_i} of the terns (R_i, L_i, C_{eq_i}) of lumped parameters composing the network of Fig. 6.5 discharge simultaneously when T is switched on and the given currents are not subject to delay. However, the differences between the approximate current distributions obtained by the circuit of Fig. 6.5 and the corresponding delayed-curve family of a transmission-line model are negligible, as it will be appreciated later in Fig. 6.8.

The overall current is assumed as being discharged directly to the earth by an undisturbing filamentary conductor (earth junction), if the victim is removed. When this is restored, perceivable differences in the current's waveshape and magnitude are to be ascribed to the electrostatic influence of the victim on each element composing the HB (if the latter holds a rigid posture).

6.3.2 Evaluation of the serial parameters R_i and L_i

For each elemental block, the representative serial parameters are evaluated by adopting the following simplifying conditions:

- Each biological element is assumed to be a homogeneous and isotropic cylinder; the penetration depth does not exceed the order of some centimetres for a 0.05/1 GHz frequency spectrum. Therefore, skin and inner fat, muscle and bone layers will, for the sake of simplicity, be considered by an overall equivalent medium. Hence the high-frequency resistance can be expressed as $R_i \approx R_{oi} r_{oi}/(2\delta_i)$, where $R_{oi} = l_i/(\sigma_i \pi r_{oi}^2)$ is the DC resistance; l_i and r_{oi} are length and radius of a cylinder representing the ith anatomical element; $\delta_i = [1/(\pi f \sigma_i \mu_0)]^{1/2}$ is the penetration coefficient, f is the frequency, and σ_i and μ_0 are the equivalent conductivity and permeability, respectively. Rearranging the above assumptions gives:

$$R_i = k_{pi} \frac{l_i}{2r_{oi}} \sqrt{\frac{f\mu_0}{\pi\sigma_i}} \tag{6.20}$$

  (k_{pi} is defined later)

- The inductance L_i for $i = 5/11$ is associated only with the inner magnetic field (internal inductance, see Ramo *et al.*, 1984). In fact, the fatness parameter associated with the elemental blocks and their reciprocal positions are responsive for
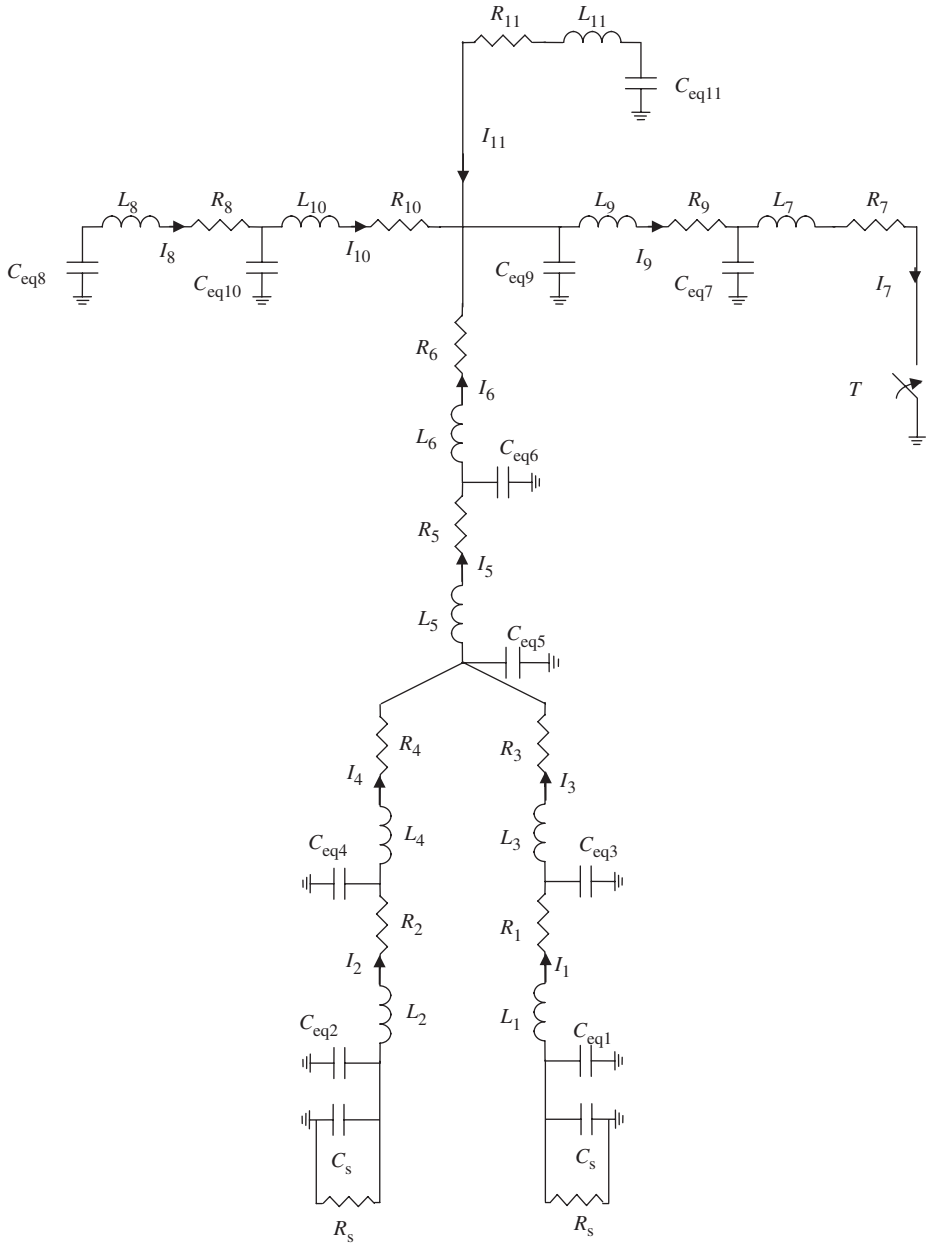
Fig. 6.5. Lumped-parameter network representation of the HB for ESD current reconstruction.

neglecting the external magnetic couplings. Therefore, L_i is correlated to the block resistance by

$$L_i \approx \frac{R_i}{2\pi f} = \frac{l_i}{4\pi r_{oi}} \sqrt{\frac{\mu_o}{\pi \sigma_i f}} \tag{6.21}$$

- On the contrary, the inductance term L_i for the pair of lower limbs ($i = 1/4$) is evaluated as an outside inductance, since such anatomically twin parts are always close and parallel in most postures. In this case, the proximity effect results in a circumferential variation of the current density (Henry, 1970). In other words, the current flow is expected to concentrate on external narrow bands along the thighs and legs. A thin-wire representation, leading to

$$L_i = \frac{k_{pi} l_i^2}{c^2} \frac{2}{C_{eq_i}} \tag{6.22}$$

can be adopted for the lower limbs; $k_{pi} \geq 1$ is a dimensionless factor introduced to take into account the proximity effect on the current density distribution approximately (setting $k_{pi} = 1$ in Eq. 6.22 means that the current flows uniformly along the surface of the ith element of capacitance C_{eq_i}). Such an effect, which is almost frequency independent in the high-frequency regime (Henry, 1970), is introduced by assigning simply $k_{pi} = 3$, irrespective of most body postures of practical interest and implied lower members.

- Both resistance R_i (for any body element) and inductance L_i (only for the upper elements) are functions of the penetration depth. This means that the above mentioned quantities become non-linear functions. In order to preserve an overall computational agility, the calculation is carried out in the assumption that the serial parameters are frequency independent and calculated for $f = 400$ MHz.

6.3.3 Transient analysis

The parametric terns (R_i, L_i, C_{eq_i}), correlated to each ith element, are inserted in the circuital model of the assembly (in general, victim included). Figure 6.6 is an example of ESD oscillogram (current I_7 of Fig. 6.5) obtained when the HB assumes a typical upright posture on an earthed plane and the ESD current is directly convoyed to the earth by a non-disturbing short-circuit. The disturbing effects of nearby electrostatic entities (wall, earthed or floating large victims) will be considered in further examples. The parameters R_i, L_i and C_{eq_i}, relevant to the case of Fig. 6.6, are summarised in Table 6.6. It is worth noticing that L_i-values relative to the lower limbs are about two orders of magnitude higher than those relative to the remaining body parts. In fact, the former are calculated by Eq. 6.22 and the latter by Eq. 6.21.

Let us now pay attention to the leg and the forearm as representative examples. In the first case, $l_i / r_{oi} = 10$ with $l_i = 0.53$ m, $\sigma_i = 1$ S/m (bone layer not involved), $k_{pi} = 3$ and $C_{eq_i} = 10.63$ pF are the values which, once introduced into Eqs. 6.20 and 6.22, give $R_i = 189\,\Omega$ and $L_i = 1.76\,\mu$H, respectively. In the second case, $l_i / r_{oi} = 5$,
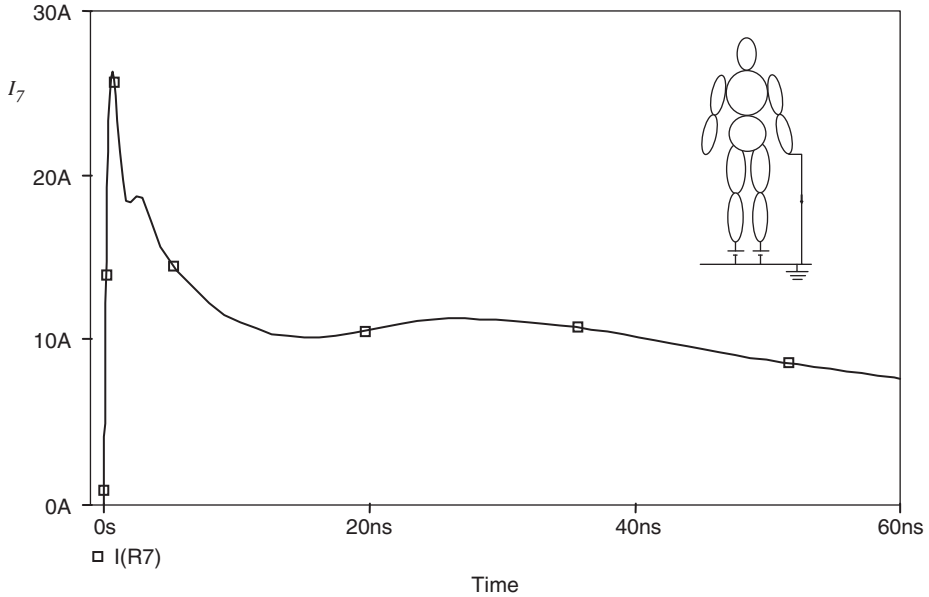
Fig. 6.6. Standard postured, one-arm earthed HB and related current oscillogram for contact ESD; charging voltage $V_0 = 8$ kV.

Table 6.6. HB-model electrical parameters (foot capacitance not included) for an upright 1.70 m tall man.

Element	C_{eq_i} [pF]	L_i [μH]	R_i [Ω]
Legs (1–2)	10.63	1.76	189
Thighs (3–4)	4.26	4.39	127
Abdomen (5)	2.17	0.02	46
Chest (6)	4.33	0.022	55
Forearms (7–8)	3.67	0.078	196.5
Arms (9–10)	4.27	0.064	159
Head (11)	7.17	0.023	58

$\sigma_i = 0.025$ S/m (bone layer involved) and $k_{pi} = 1$ is the set of data leading, by Eqs. 6.20 and 6.21, respectively, to $R_i = 196.5\,\Omega$ and $L_i = 0.078\,\mu$H.

Setting a charge voltage $V_o = 8$ kV (which corresponds to level 4 of the IEC Standard 61000-4-2 1995) gives quite expected waveform parameters (specifically, $I_o \approx 26$ A; rise time $t_s = 0.6$ ns). This leads to argue, contrary to previous conjectures, that the typical sharp peak followed by a secondary lower peak is not at all specific of the geometrical details connected to the man-handled intruder facing, or in contact with, a larger victim surface.
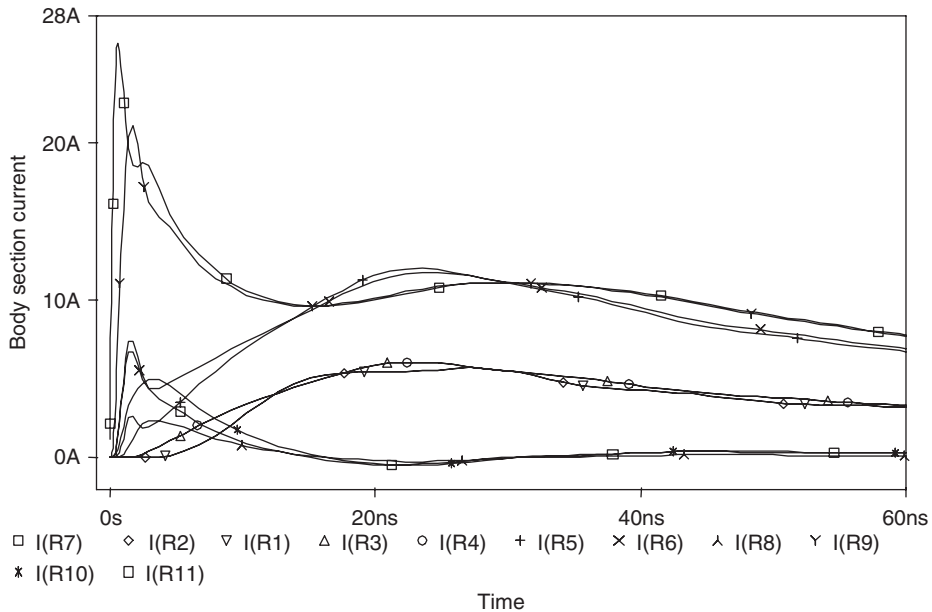
Fig. 6.7. Current distribution through each member of the HB postured as in the example of Fig. 6.6.

Figure 6.7 reports the current distribution through each part of the HB relative to the posture of Fig. 6.6. The calculation evidences that all the body parts above the thighs are important for the edge formation in the current waveform. The lower limbs, conversely, are especially responsible for the tail formation because of the larger inductances involved. Figures 6.8(a) and (b) show the first instants of these current oscillograms (fast-rising front currents in Fig. 6.8(a); slowly rising front current in Fig. 6.8(b) for some body sections. Note how the fine structure of the terminal current I_7, during the first 5 ns including the edge, is interpretable as the combined result of the discharging arms, head, chest and abdomen. In fact, all the reported currents are convoyed into the earthed arm. Each body part contributes differently to the overall discharge as a function of the values of L_i, C_{eq_i} and R_i and of the network topology. The HB acts as a low-pass filter by virtue of the stray capacitances and serial inductances adopted to model the odd-shaped body. The spectral contents of the pulses relative to most body parts are limited to about 100 MHz. Only the discharging forearm retains the high frequency content of the ESD waveform. The simplifying hypotheses adopted here are indirectly sustained by the observations made later by Okoniewska *et al.* (2004) since these are quite consistent with the behaviour described above.

The enlarged timescale adopted in Fig. 6.8 allows better appreciation of the lumped-parameter circuit model adopted here. For a given body section, during the first instants preceding the fast rising fronts, the slowly time-varying portion included in the fine structure of the current waveform turns out to be practically substitutive
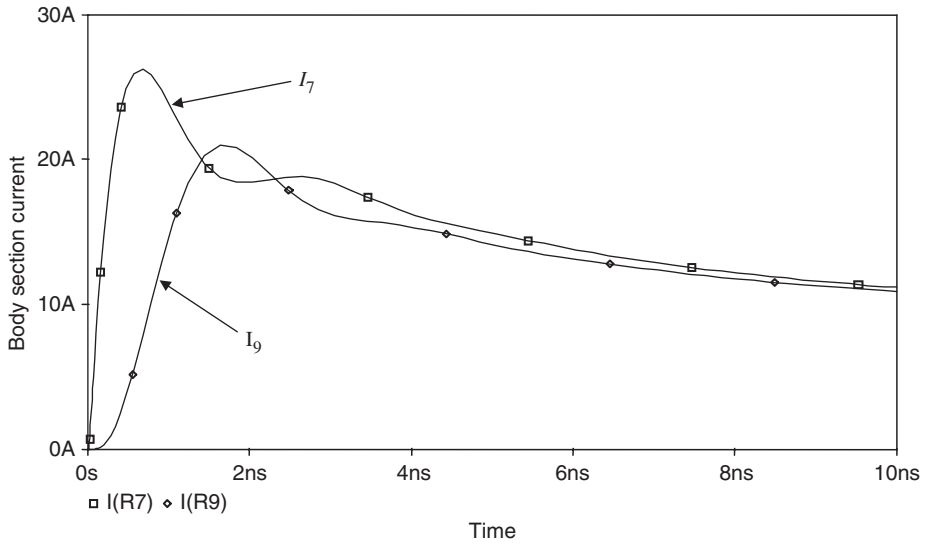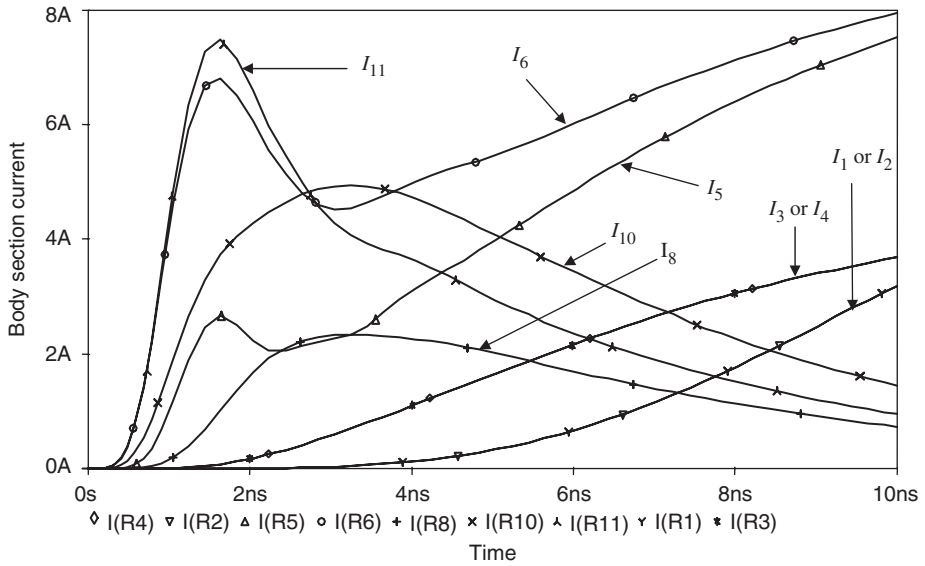
Fig. 6.8. Enlarged timescale view of the current distribution shown in Fig. 6.6; (a) fast-varying currents; and (b) slowly varying currents.

of pure delays distinctive of an optional transmission-line model. In fact, the described slowly varying portion is more and more elongated towards growing times as the relevant body section is receded from the hand-victim terminal. This performance is ensured by the serial inductances distributed in the lumped-parameter network of Fig. 6.5.

A selection of examples, implemented by PSPICE routine, will be reported in the following sub-section to carefully investigate the contact and air-discharge performances. Specifically, the arc is replaced by an ideal switch or modelled by a non-linear resistance in the contact and air discharge modes, respectively.

6.3.4 Contact discharge mode

Table 6.7 summarises sets of C_{eq_i} relative to the examples treated here. The same table also reports the current parameters (peak value I_o, risetime t_s and current amplitudes I_{30} and I_{60} at 30 and 60 ns, respectively), all calculated in contact discharge mode as a function of the described postures and environmental conditions.

Figures 6.9–6.13 are relative to different human postures with one hand earthed: hands-down man (with a side wall), hands-up man (side wall included and removed), seated man on insulating seat and bent man. It is worth noticing how the basic features of the ESD current remain almost unchanged. However, comparing the curve of Figs. 6.6 and 6.12 with those of Figs. 6.9 and 6.13, respectively, shows that the influence of the side wall results in an increase of the first peak (the other waveform parameters are not likely to be influenced; see Table 6.7 for details).

Table 6.7. Equivalent capacitance set and waveform parameters calculated in contact discharge mode for the several treated examples.

Element				
	C_{eq_i} [pF]	C_{eq_i} [pF]	C_{eq_i} [pF]	C_{eq_i} [pF]
Leg (1–2)	10.63	10.06	10.60	10.05
Thigh (3–4)	4.26	3.62	6.08	5.29
Abdomen (5)	2.17	6.48	4.41	4.06
Chest (6)	4.33	2.98	5.47	5.19
Forearm (7–8)	3.67	3.72	5.59	9.25
Arm (9–10)	4.27	4.24	4.21	4.89
Head (11)	7.17	7.19	2.27	5.70
Waveform parameters relative to $V_o = 8$ kV				
I_{peak} [A]	25.95	26.31	28.84	30.92
t_r [ns]	0.59	0.73	0.733	0.85
I_{30} [A]	11.1	11.1	11.33	11.18
I_{60} [A]	6.62	7.68	7.93	8.25

continued

Table 6.7. —Cont'd

	C_{eq_i} [pF]	C_{eq_i} [pF]	C_{eq_i} [pF]	C_{eq_i} [pF]
Leg 1	12.26	12.51	12.72	11.30
Leg 2	10.65	10.89	10.94	10.75
Thigh 3	4.80	7.03	6.64	8.60
Thigh 4	6.85	4.82	5.05	6.38
Abdomen 5	2.31	3.04	3.06	5.72
Chest 6	3.94	5.19	5.91	7.01
Forearm 7	5.16	13.83	16.99	17.14
Forearm 8	3.25	3.91	4.01	7.07
Arm 9	4.68	10.47	13.62	9.15
Arm 10	4.44	4.64	4.85	5.13
Head 11	7.40	8.58	9.87	4.60
Victim	15.94	53.53	—	—
Waveform parameters relative to $V_o = 8$ kV				
I_{peak} [A]	27.06	31.6	33.22	33.52
t_r [ns]	0.87	1.06	0.9	1.02
I_{30} [A]	11.17	11.01	11.36	11.42
I_{60} [A]	7.83	8.5	8.77	8.72
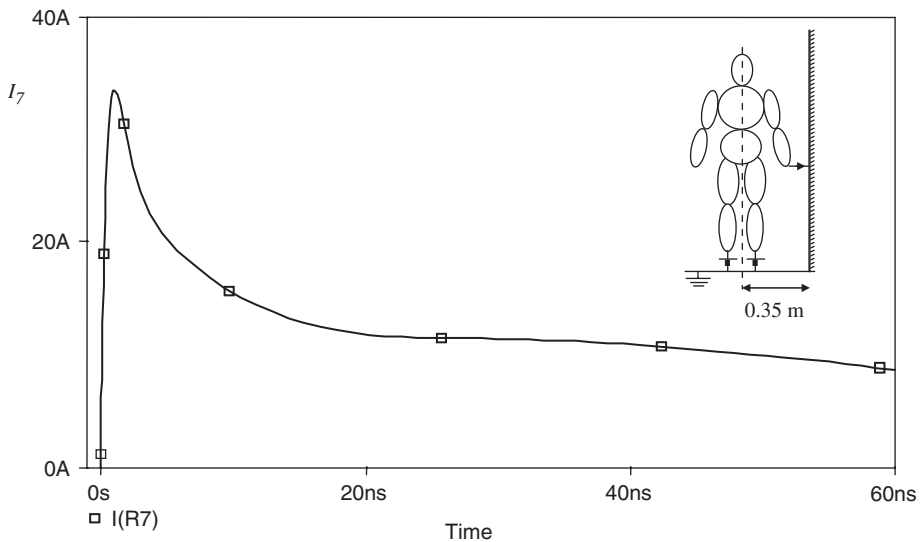
Fig. 6.9. As Fig. 6.6, vertical side-wall included.
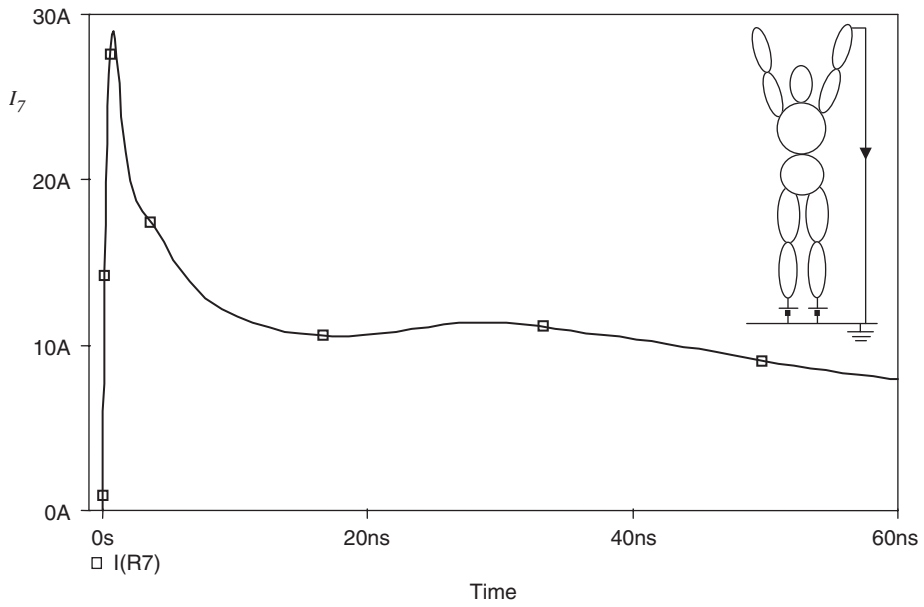
Fig. 6.10. Arms-up postured, one arm earthed HB. Additional data as Fig. 6.6.
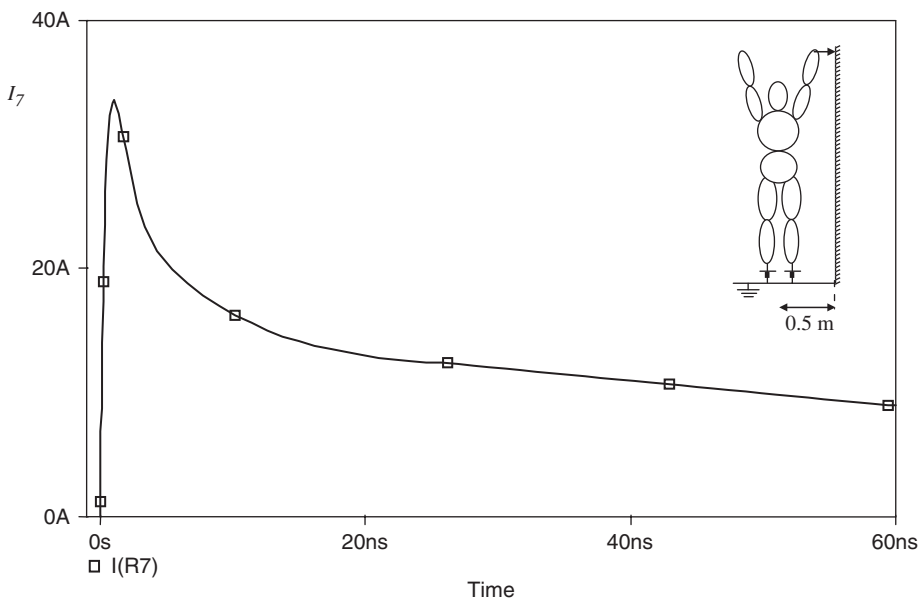
Fig. 6.11. As Fig. 6.10, side wall included.
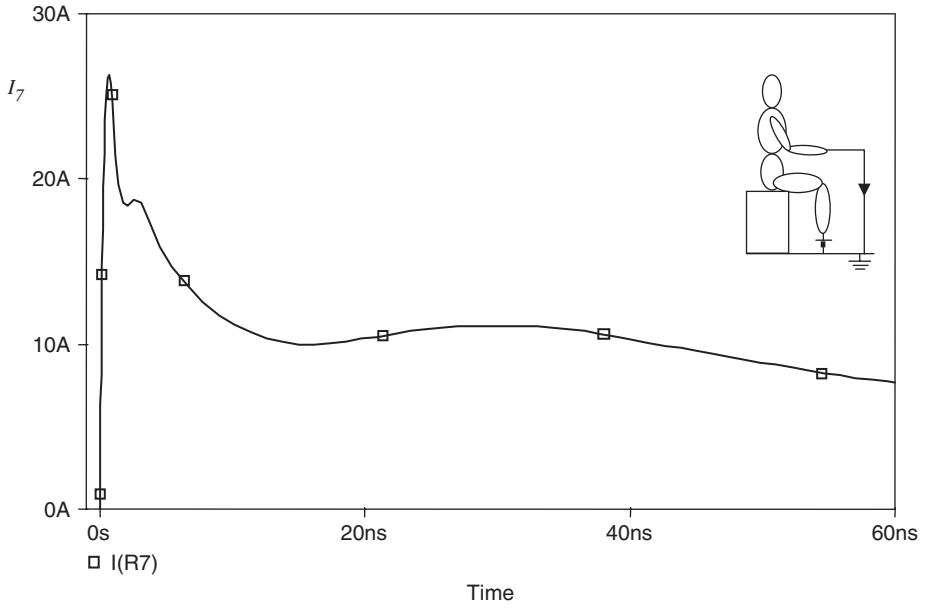
Fig. 6.12. As Fig. 6.6, but seated man.
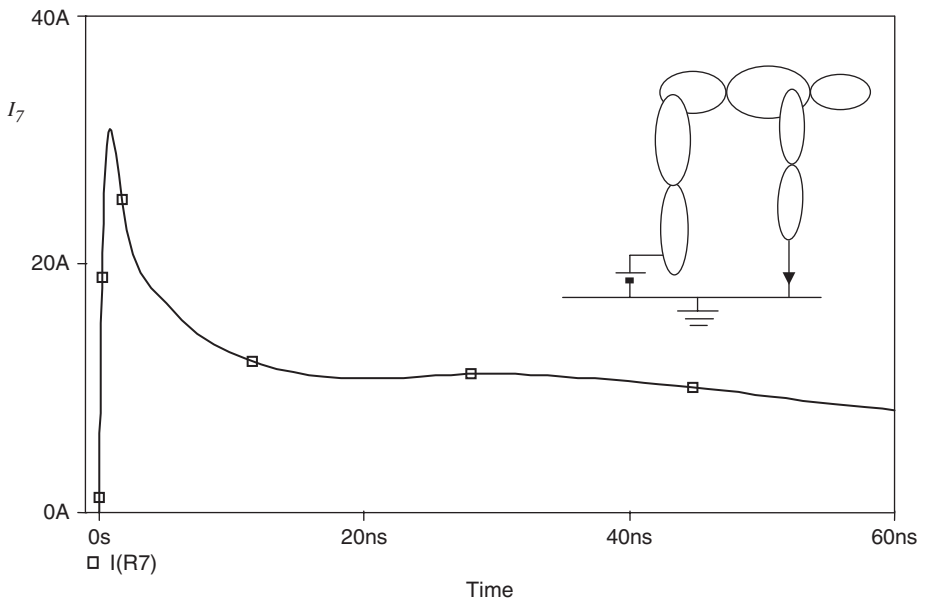
Fig. 6.13. Bent man. Additional data as Fig. 6.6.

The presence of a victim represented by an earthed 0.25 m radius sphere (elevated at 0.15 m above the plane) is considered in Fig. 6.14. The PSPICE model of the victim earthed by a connecting wire consists in the pair of serial parameters R_c and L_c set equal to 1 or 10 Ω and 8.0 nH, respectively. The inductance of the large victim is neglected. In spite of the presence of an object very close to the operator, the parameters of the waveshapes reported in Fig. 6.14 are slightly different from those of Fig. 6.6. Rather, reducing the ratio R_c/L_c causes the appearance of a smoothed oscillation superimposed on the original tracing. Figure 6.15 reintroduces the example of Fig. 6.14 but with a larger nearby victim represented by a spheroid of semi-axis 0.24 m and 0.75 m. As expected, only the peak value of the curves is increased because of the larger coupling surface of the victim. On the contrary, if the victim is isolated from the earth, strong changes in the current waveshape occur. In Fig. 6.16 (relative to the same man-victim system of Fig. 6.15), the victim is floating and charged at two values of the voltage $V_s = 1\,\text{kV}$ and 7 kV. The current oscillograms are very different from the standard waveshape of Fig. 6.6, especially when V_s approaches the man's voltage V_o.

Observing the amount of figures here reproduced, it seems that the current waveforms invariably tend to slightly depart from the standard upright-man case, thus irrespective of the HB posture and surrounding scenario. As a consequence it seems reasonable to presume that the current waveform is the subject of an undetermined topological property of invariance distinctive of the networked system under examination.
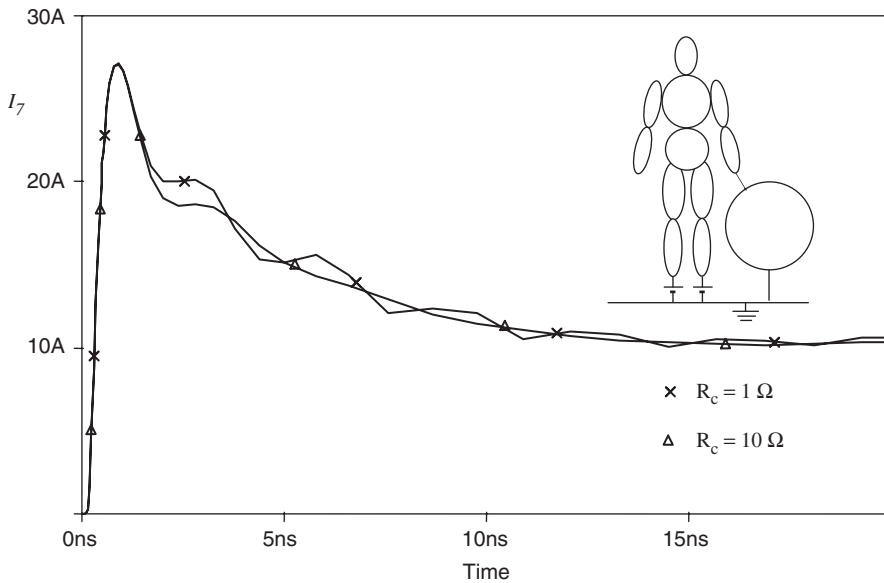
Fig. 6.14. As Fig. 6.6, earthed large victim included. The electrical parameters of the earthing connection are: resistance $R_c = 1$ and 10 Ω; inductance $L_c = 8$ nH. The 0.25 m radius sphere is centred on a point of coordinates $y = 0.5$ m and $z = 0.4$ m.
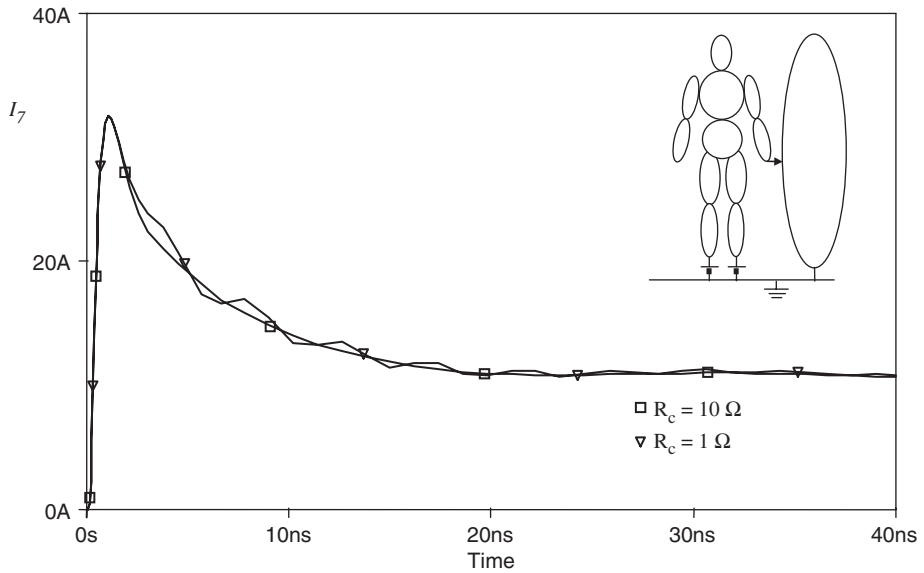
Fig. 6.15. As Fig. 6.14, but the victim is simulated by a spheroid of 0.24 m and 0.75 m semi-axes; centre coordinates: $y = 0.55$ m, $z = 0.8$ m.
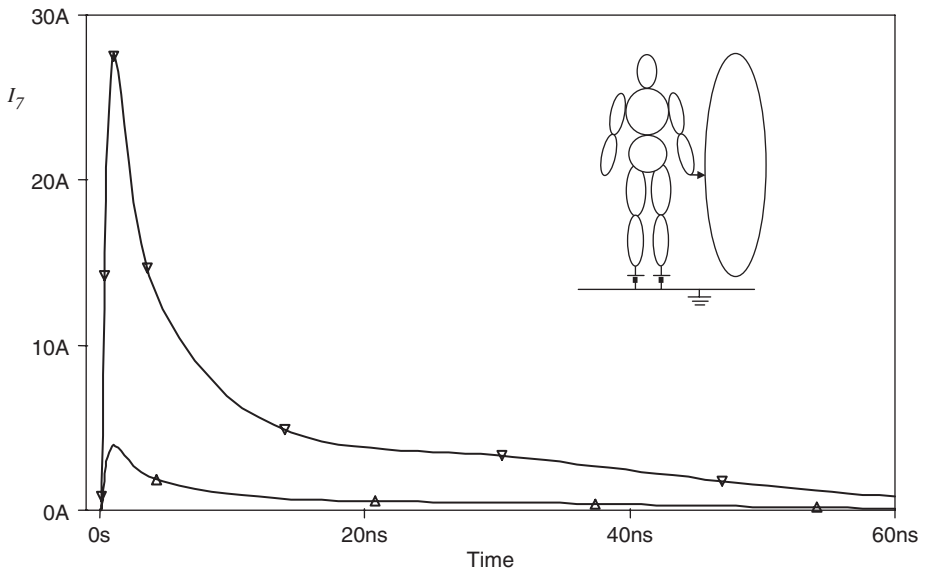
Fig. 6.16. Man's posture and proximity to the victim as Fig. 6.15; floating victim case; ∇ Spheroid floating voltage $V_s = 1$ kV: $I_{peak} = 27.19$ A; $t_r = 0.96$ ns; $I_{30} = 3.33$ A; $I_{60} = 0.83$ A; $\triangle$ Spheroid floating voltage $V_s = 7$ kV: $I_{peak} = 3.87$ A; $t_r = 0.96$ ns; $I_{30} = 0.47$ A; $I_{60} = 0.12$ A.

6.3.5 Air discharge mode

The case of air discharge, where $V_o = 5$ kV and different arc lengths g are established, is examined in Fig. 6.17. For comparison purposes, this example is similar to that treated by Pommerenke and Aidam (1996) (see therein the corresponding Fig. 5). Even the Rompe and Weizel arc model (Craggs, 1978) is likewise adopted. The arc connects the body to an earthed non-disturbing filament. Such an unrealistic circumstance has again been considered to investigate HB discharging features virtually decontaminated by influencing external causes but the plane.

According to Rompe and Weizel's model, the time-varying arc resistance $R_a(t)$ assumes the general form

$$R_a(t) = \frac{Bg}{\left[\int\limits_0^t i(\tau)^2 d\tau \right]^{1/2}} \qquad (6.23)$$

where g and $i(t)$ express arc elongation and current expressed in metres and amperes, respectively; the constant B is assumed to be equal to 71 $Vs^{1/2}$/m, as suggested by Pommerenke (1996). Such a non-linear law is derived from the "energy balance" approach applied to sparking channel studies. This approach is supported in Pommerenke (1995) by convincing counterdeductions to any residual critique to the above formula.
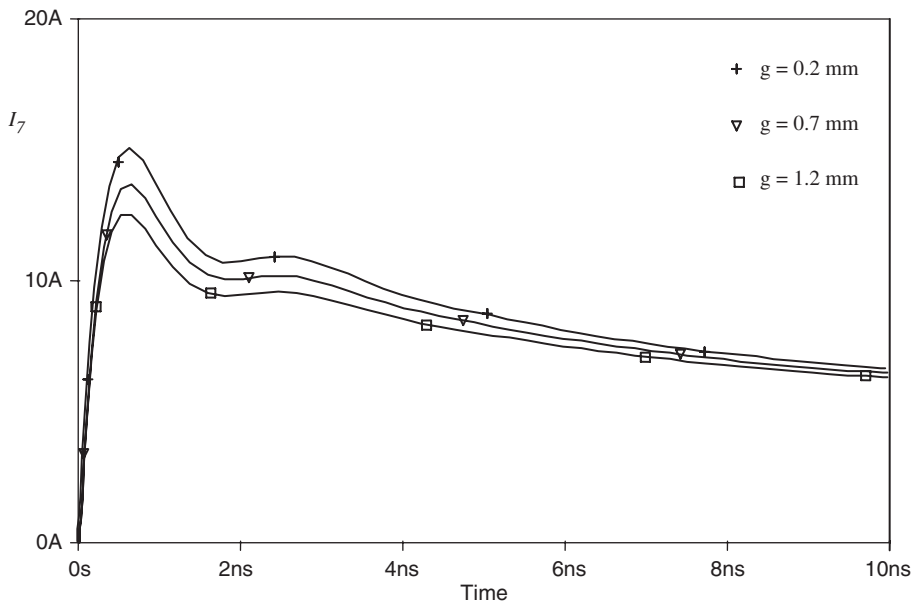
Fig. 6.17. Arc-discharge case (g: arc length). Man's posture as in Fig. 6.6 and voltage $V_o = 5$ kV.

As shown in Fig. 6.17, even in the present case the arc length g causes noticeable changes, especially in the first instants of the current wave shape. Note how the smoothing action exerted by the arc resistance is proportional to the gap extension, as intuitively expected. However, a restricted amount of the initial peak is discovered here to remain even at the largest arc elongation compatibly with the charge voltage. This result seems to be consistent with the discussed features of a discharging man, in the sense that a sharp peak is invariably expected, thus irrespective of the outer electrostatic couplings and connection conditions occurring at the body terminal. The latter condition, however, could contribute to shape the peak significantly. In fact, if the discharge occurs through a hand-held pair of tweezers (this is the example assigned to Fig. 5 in Pommerenke, 1996), the sharp peak tends to disappear as the arc elongates. Indeed, as claimed elsewhere (Amoruso and Lattarulo, 1994), the diakoptic-based model needs in specific cases to be accomplished by some refinements taking into account the surface sharp protrusions, which could cause local field overstresses affecting the discharge.

6.4 Conclusions

In this chapter, the essential performances of the diakoptic approach, with special application to EMC problems involving HB, have extensively been tested. The behaviour of the HB, intended either as a victim exposed to ELF electric fields or a source of ESD effects, results ultimately as described by an analogical lumped-parameter network. The dependence of the RLC components on shape, size and electrical properties of the large 11 elements in which the HB has ideally been partitioned, is extensively investigated. With particular reference to the electrostatic model of man, the representative set of 11 partial capacitances, given as a function of pre-established HB attitudes and positions of earthed/floating nearby conductors, carefully accommodate mutual electrostatic influences. The evaluation of the current distribution pervading the HB is affected by an error less than 10%, a conservative estimation corroborated by the available experimental and theoretical data. The latter category of databases derive from the models sophistication degree which are far exceeding that of the low-partitioning method examined here. Therefore, the diakoptic method turns out to be especially recommended for resolving the above class of engineering problems since the computational errors are safely expected being within the uncertainty affecting the simulation at work. Incidentally, it should be remarked that, as far as the result precision is concerned, the diakoptic and Maxwell's methods are quite equivalent, provided that the simplified multi-element electrostatic model and its partitioning *a priori* assumed are the same. The methods under comparison differ only for the fact that the former, contrary to the latter, directly involves capacitances instead of Maxwell's coefficients. This estimable feature plays in favour of the diakoptic technique since practising engineers rather prefer to manage capacitive parameters and, through them, arrive at the physical interpretations of the results for design and measurement purposes. Incidentally, even mutual capacitances (which are unimportant for the applications illustrated here, but important in general) among the disconnected conducting systems can be obtained, as suggested by Amoruso *et al.* (2001), by an extended version of the above technique.

Appendix A

Sphere above a plane

Let the geometric centre of a conducting sphere of radius r be positioned at height h above an earthed plane. The input capacitances needed for performing the diakoptic procedure could be $C_1 = C_2 = 4\pi\varepsilon_0 r$ and $C_{12} = 4\pi\varepsilon_0(2h)$, where suffix 2 is relative to the electrostatic image of the real sphere. Note that the above roughly established quantities correspond to those expressed in Table 6.2 for ellipsoidal bodies. In fact, C_1 represents the capacitance of an isolated sphere, while the formula adopted for C_{12} is in general applicable only if $2h \gg r$, a condition quite neglected here. In spite of being rather affected by first-order errors, the above quantities are deliberately involved here in the calculation to give

$$[Z^*] = \frac{1}{4\pi\varepsilon_0\omega} \begin{bmatrix} 1/r & 1/(2h) \\ 1/(2h) & 1/r \end{bmatrix}; \quad [M] = \begin{bmatrix} 1 \\ -1 \end{bmatrix}$$

which represent the solving matrices for this uncomplicated case study. According to Eq. 6.7,

$$[Z] = Z = \frac{1}{\omega C} = \frac{1}{2\pi\varepsilon_0\omega}\left(\frac{1}{r} - \frac{1}{2h}\right) \tag{6.24}$$

easily results since $[Z]$ is reduced here to a matrix of dimensions 1×1. An eloquent argument in favour of the present method is that Eq. 6.24 exactly reproduces the approximate formula proposed somewhere, for several engineering applications, even if r and h become comparable (see, for example, Deno and Zaffanella, 1975). Consider that the capacitance C embodied in Eq. 6.24 can also be derived by truncating the first two terms the exact series expansion given by Smythe (1968). This explanatory example permits immediate appreciation of the diakoptic method since C is given with a second-order approximation even though the chosen entries C_1, $C_2 = C_1$ and C_{12} are affected by first-order errors. Incidentally, Eq. 6.24 could represent the imaged version of the capacitance early calculated by Chow and Yovanovich (1982) for odd-shaped conductors in isolation. In fact, such authors show that an arbitrarily shaped body and a sphere, both assumed being conductors in isolation, present the same capacitance provided that their own total surface areas are equal. The equivalence in capacitance is ensured with an error not exceeding 10%. According to the diakoptic method, it is worth considering that the same maximum error substantially affects Eq. 6.24 provided that the difference $h - r$ does not vanish.

References

Amoruso V., Helali M., Lattarulo F., "An improved model of man for ESD applications", J. Electrostat., **49** (2000) 225.

Amoruso V., Helali M., Lattarulo F., "Human-generated ESD: investigation on the direct discharge to a victim", Proc. EMC Zurich, 2001, 193.

Amoruso V., Helali M., Lattarulo F., "Man-victim capacitive coupling effects on the ESD current", Proc. EMC Europe, 2002, 805.

Amoruso V., Helali M., Lattarulo F., "Multibody model of man applied to the quasi-static ESD analysis", Proc. of the 4th Int. Conf. on Applied Electrostatics, Dalian, China, 2001, 47.

Amoruso V., Lattarulo F., "ELF electric-field induced currents in the human body", Alta Frequenza, special issue on "Biological effects of electromagnetic fields and safety standards", **4** (1989) 385.

Amoruso V., Lattarulo F., "Diakoptics for electrostatics", IEE Proc.-S.M.T., **141** (1994) 317.

Barnes H.C., McElroy A.J., Charkow J.H., "Rational analysis of electric fields in live line workings", IEEE Trans. Power App. and Systems, **86** (1967) 482.

Bayer A., Brinkmann J., Wittke G., "Experimental research on rats for determining the effect of electrical AC fields on living beings", Elektrizitaeswirtschaft, **76** (1977) 77.

Chen K.M., Chuang H.R., Lin C.J., "Quantification of interaction between ELF-LF electric fields and human bodies", IEEE Trans. Biomed. Eng., **33** (1986) 746.

Chiba A., Isaka K., Kitagawa M., "Application of finite element method to analysis of induced current densities inside human model exposed to 60-Hz electric field", IEEE Trans. PAS., **103** (1984) 1895.

Chow Y.L., Yovanovich M.M., "The shape factor of the capacitance of a conductor", J. Appl. Phys., **53** (1982) 8470.

Chuang H.R., Chen K.M., "A numerical method for computation of induced currents inside 3D heterogeneous biological bodies", IEEE Trans. Biomed. Eng., **36** (1989) 628.

Craggs J.D., "Spark channels", in J.M. Meeks and J.D. Craggs, Eds., *Electrical breakdown of gases*, John Wiley & Sons, New York, 1978.

Dawson T.W., Stuchly M.A., "High-resolution organ dosimetry for human exposure to low-frequency magnetic fields", IEEE Trans. Magnetics, **34** (1998) 708.

Deno D.W., "Current induced in the human body by high voltage transmission line electric field – measurements and calculation of distribution and dose", IEEE Trans. PAS, **96** (1977) 1517.

Deno D.W., Zaffanella L.E., "Field effects of overhead transmission lines and stations", in *Transmission line reference book 345 kV and above*, F. Weiner, New York, 1975.

Durand E., Ed., *Electrostatique*, Masson, Paris, 1964.

Gandhi O.P., Chen J.Y., "Numerical dosimetry at power-line frequencies using anatomically based models", Bioelectromagnetics Supp., **1** (1992) 43.

Gonzales C., Peratta A., Poljak D., "Current density induced in the human body due to low frequency electric fields using the boundary element method", Proc. SoftCOM 2005, 2005.

Goubau G., Puri N.N., Schwering F.K., " Diakoptic theory for multielement antenna", IEEE Trans. A.P., **30** (1982) 15.

Greason W.D., *Electrostatic discharge in electronics*, John Wiley & Sons, New York, 1992.

Hart F.X., Marino A.A., "ELF dosage in ellipsoidal models of man due to high voltage transmission lines", J. Bioelec., **1** (1982) 313.

Henry J., Les interconnexions en electronique, Masson, Paris, 1970.

ICNIRP, "Guidelines for limiting exposure to time-varying electric, magnetic, and electromagnetic fields (up to 300 GHz)", Health Phys., **74(3)** (1998) 494–522.

IEC Standard 61000-4-2, Electromagnetic Compatibility (EMC), Part 4, testing and measurement techniques – section 2: Electrostatic discharge immunity test, 1995.

IEEE Std C95.6- IEEE Standard for safety levels with respect to human exposure to electromagnetic fields, 0–3 kHz, 2002.

Kaune W.T., Forsythe W.C., "Dosimetric comparison of human, rat, and pig models exposed to power frequency electric fields", Proc. of the 1983 US/USSR Workshop on Biological Effects of Physical Factors in the Environment (topic 3.2), National Institute of Environmental Health Science, 1983.

Kaune W.T., Forsythe W.C., "Current density measured in human models exposed to 60 Hz electric fields", Bioelectromagnetics, **6** (1985) 13.

Kaune W.T., Phillips R.D., "Comparison of the coupling of grounded humans, swine, and rats to vertical 60 Hz electric fields", Bioelectromagnetics, **1** (1980) 117.

King R.W.P., "Fields and currents in the organs of the human body when exposed to power lines and VLF transmitters", IEEE Trans. Biomed. Engin., **45** (1998) 520.

Lattarulo F., Mastronardi G., "Equivalence criteria among man and animals in experimental investigations of high voltage power frequency exposure hazards", Appl. Math Modelling, **5** (1981) 92.

Li L.W., Kang X.K., Leong M.S., *Spheroidal wave functions in electromagnetic theory*, John Wiley & Sons, New York, 2002.

Lin C.J., Chaung H.R., Chen K.M., "Steady-state and shock currents induced by ELF electric fields in a human body and a nearby vehicle", IEEE Trans. EMC, **32** (1990) 59.

Mahdi A.B., Anis H.I., "Field exposure modeling using charge simulation", Proc. Fifth Int. Symp. on H.V. Eng., Braunschweig, 1987, paper No. 33.20.

Maruvada P.S., Hylten-Cavallius, N., "Capacitance calculations for some basic high voltage electrode configurations", IEEE Trans. PAS, **94** (1975) 1708.

Miller D.L., "Miniature-probe measurements of electric fields and currents induced by a 60-Hz magnetic field in rat and human models", Bioelectromagnetics, **12** (1991) 157.

NRC (National Research Council), *Possible health effects of exposure to residential electric and magnetic fields*, National Academy Press, Washington, DC, 1997.

Okoniewska E., Stuchly M.A., Okoniewski M., "Interactions of electrostatic discharges with the human body", IEEE Trans. M.T.T., **52** (2004) 2030.

Okoniewski M., Hagness S., "FDTD in bio-electromagnetics", Proc. EMC Zurich, 2001, 57.

Pickles J.H., "Monte-Carlo calculation of electrically induced human-body currents", IEE Proc., Pt. A **134** (1987) 705.

Poljak D., Peratta A., Brebbia C.A., "A 3D BEM modelling of human exposure to extremely low frequency (ELF) electric fields", Proc. Boundary Element XXVII, 2005, 441.

Pommerenke D., "ESD: transient fields, arc simulation and rise time limit", J. Electrostatics, **36** (1995) 31.

Pommerenke D., Aidam M., "ESD: waveform calculation, field and current of human and simulator ESD", J. Electrostatics, **38** (1996) 33.

Ramo S., Whinnery J.R., Van Duzer T., *Fields and waves in communication electronics*, John Wiley & Sons, New York, 1984.

Repacholi M.H., Greenebaum B., "Interaction of static and extremely low frequency electric and magnetic fields with living systems: health effects and research needs", Bioelectromagnetics, **29** (1999) 133.

Schwering F.K., Puri, N.N., Butler C.M., "Modified diakoptic theory of antennas", IEEE Trans. A.P., **34** (1986) 1273.

Smythe W.R., *Static and dynamic electricity*, McGraw-Hill, New York, 1968.

Spiegel R.J., "ELF coupling to spherical models of man and animals", IEEE Trans. Biomed. Eng., **23** (1976) 387.

Spiegel R.J., "High-voltage electric field coupling to humans using moment method techniques", IEEE Trans. Biomed. Eng., **24** (1977) 466.

Stuchly M.A., Dawson T.W., "Interaction of low-frequency electric and magnetic fields with the human body", Proc. IEEE, **88** (2000) 643.

CHAPTER 7

New Power Quality Assessment Criteria for Harmonic Disturbances

M. Marinelli, V.G. Monopoli, and A. Dell'Aquila

Abstract

In recent years power quality issues have captured the attention of many researchers, energy suppliers and customers. The problem of controlling power quality is becoming more relevant because of the widespread use of non-linear and time-varying single-phase or three-phase loads that increasingly affect the operation of distribution networks in residential, commercial and industrial areas. Power quality deterioration is due to transient disturbances (voltage sags, voltage swells, impulses, etc.) and steady-state disturbances (harmonic distortion, unbalance, flicker). The main causes of such disturbances as well as the detrimental effects they have on the electrical systems are described. Among these issues, harmonics are investigated more accurately in this chapter. Some definitions relevant to non-sinusoidal systems are provided in order to deeply understand the solutions proposed in the remainder. An outline of IEC and IEEE Standards guidelines, which deals with harmonic disturbances is presented. A topic such standards deal with and several researchers are interested in is that non-linear loads should not be considered the only cause of the detrimental effects related to power systems in these conditions. The responsibility for the power quality deterioration should be shared between the supplier and the customer. This kind of information could be provided by indices in a straightforward and simple way. The traditional indices used by the international standards cannot satisfy these specifications. To this purpose, a new index to evaluate the above-mentioned harmonic distortion phenomena in the supply electrical networks is more deeply discussed.

7.1 Introduction about Power Quality

Electricity is an essential aspect of today's society. In fact, most of the utilities present in industrial as well as domestic environments rely on this kind of energy. That is why such a valuable product rules the majority of the political and strategic choices. Moreover, the industrial and economical development of a country has to be sustained by an adequate amount of electricity produced. To some extent, electricity is the "first" product to be produced. Notwithstanding, over the last few years, the analysis of operation of the electrical systems has proved that the electrical energy should not be considered in terms of "quantity" alone. The "quality" of the supply is a serious issue to be addressed as well (Dugan *et al.*, 1996; Arrillaga *et al.*, 2000). In fact, like other industrial products, electrical energy is required to meet some quality requirements: the reliability of the supply must be known in terms of the continuity of service and the parameters to be kept within some specified standards. On the other hand, unlike other products, electrical energy can undergo a lot of changes starting from where it is produced to the point where it is delivered. In fact, it is generated far from the point of use, is fed to the grid by a variety of generators and arrives to the point of use via several transformers and through many kilometres of overhead and underground cabling. Additionally, in a deregulated scenario, networks are managed and maintained by a number of different suppliers. Therefore, it is evident that the quality of the delivered electrical energy is not an easy task to be accomplished.

The situation is even more complicated if we consider that there is a lack of exhaustive statistical data on the quality of power the customer can access. Moreover, the idea that suppliers and customers have about the level of quality to be achieved as well as the opinion about the responsibility in power quality deterioration is different. In fact, in most of the cases, customers complain about the bad quality of supply causing expensive interruption of the production processes. On the other side, electricity suppliers argue that critical customers have to be directly involved in the hard task of ensuring the quality of power. The supplier should not be expected to deliver high-quality energy to every customer anytime and anywhere on the network. All this would mean huge costs to strengthen the network that only a few customers (in numerical, not consumption, terms) could take advantage of. In fact, there are some aspects that cannot be kept under control by the provider such as weather conditions causing damages and the characteristics of the customer loads which can be responsible for power quality deterioration phenomena. Therefore, the customer should co-operate in guaranteeing a high-quality electrical power flowing through the network.

So, what should we mean by the term "power quality" and what aim should be pursued by all the subjects involved in this matter? An ideal power supply would be the one that is always available, always within voltage and frequency tolerances, and has a pure noise-free sinusoidal wave shape. Notwithstanding, electrical grids are normally not capable of providing a supply fulfilling these requirements. In fact, power quality deterioration is usually due to transient disturbances (voltage sags, voltage swells, impulses, etc.) and steady-state disturbances (harmonic distortion, unbalance, flicker). Each of these power quality problems has a different cause. Some problems are strictly related to the shared nature of the electrical grid. For example, a fault on the network may cause a dip that will affect some customers connected to the grid, and the more severe the fault,

the larger the number of users involved. Other problems, such as harmonics, arise from the customer loads and may or may not propagate onto the network and so affect other customers.

In most of the cases, industrial customers complain about evident power defects such as interruptions (which range from a few seconds to several hours) and voltage dips or sags where the voltage drops to a lower value for a short duration. In fact, long power interruptions are a problem for all users, but many operations are very sensitive to very short interruptions. Examples of such sensitive operations are the continuous processes, where even short interruptions can lead to the loss of synchronisation among different machineries and then stop all production processes. Another example of delicate process is the multi-stage production where disturbances on the electrical supply may lead to the loss in value of the earlier operations.

Although majority of the customers are more sensitive to transient disturbances, since immediate economical losses are involved, there are more underhand problems affecting electrical power such as harmonics and unbalance. In fact, the effects of harmonics on power system apparatus include resonance, reduced operating life of rotating machines, malfunctioning of power system protection devices, errors in power measurements, additional losses, etc. Moreover, unbalance phenomena should also be well monitored, detected and corrected. A machine operating under an unbalanced supply will draw a current with a degree of unbalance several times that of the supply voltage. As a result, the three-phase currents might differ considerably and a rise in temperature would take place in the machine. Motors and generators, particularly the large and more expensive ones, may be fitted with protection to detect extreme unbalance and to trip the machine. The behaviour of multiphase converters, is also affected by an unbalanced supply; this causes an undesirable ripple component on the DC side and non-characteristic harmonics on the AC side. Moreover, the presence of an unbalanced load creates unbalanced current components that cause voltage drops across the source impedance and hence generate harmonic powers flowing backward from the load to the network.

Taking into consideration the above-mentioned aspects, the following section is focused mainly on harmonics whose effects could become more evident in the future.

7.1.1 Different kinds of disturbances

It is possible to define some characteristic parameters in order to assess the quality of power delivered from the supply (Dugan *et al.*, 1996; Arrillaga *et al.*, 2000):

- frequency;
- amplitude;
- waveform;
- symmetry of the voltage system.

These characteristics may vary during the normal operation of the electrical system because of load changes, disturbances introduced by user apparatus and fault occurrence. As a consequence, such characteristics may be time variant at each point where energy is delivered and for a given instant they may not be equal at different points in the network. In most of the cases, statistical evaluation of such phenomena may represent an important means to collect information about power quality.

7.1.2 Frequency variations

Large generators switch-off or important load commutation may lead to transient variations of the frequency, which are quickly compensated through the primary regulation of the generators. Then the power exchanged among interconnected grids is balanced by the generation station, which has to perform the secondary regulation. The primary regulation achieves a null average value for the power exchanges among interconnected grids due to frequency variations. Grid frequency affects the behaviour of motors (speed variations), the performance of some electronic devices where it is used for synchronisation purposes, the losses in magnetic materials and the usefulness of filters to suppress harmonics. Frequency variations are defined in terms of percentage deviation from the nominal frequency.

7.1.3 Voltage amplitude variations

Voltage variations   The grid voltage continuously changes because of the commutation of the electrical devices connected to the grid. The voltage variation may be slow or quick depending on whether an overall load progressive change or a step change for a large load is happening. The grid impedance deeply affects the amount of voltage variations as a consequence of load change: the higher the impedance, the larger the variation.

Voltage fluctuations   A set of quick voltage variations is referred to as voltage fluctuation. The limit between slow and quick variations is not so definite and can range from a few seconds to one minute. Slow variations are assessed through the average value calculated over contiguous intervals of ten minutes.

Rapid variations may be single or repetitive and their amplitude usually does not exceed 6–8% of the nominal voltage. Usually electrical apparatus are able to work even in the presence of this kind of disturbance (in most of the cases corrected by voltage regulation) unless initial voltage is too low. These kinds of variations are caused by variable loads such as welding machines, arc furnaces and mills. Rapid variations of over 10% amplitude irrespective of the duration, are considered voltage dips.

Flicker   The term flicker is referred to as a systematic or casual variation of the voltage amplitude ranging from 0.9 to 1.1 p.u.. Sometimes the terms flicker and voltage fluctuations are interchangeably used. Notwithstanding, the term flicker is strictly related to the impression of instability of the visual sensation produced by a light whose intensity and

spectral distribution are time variant. The amplitude of the voltage variations is usually less than 10% and the behaviour of the electrical apparatus is not affected. Notwithstanding, these small disturbances can result in lightning variations which may affect the human eye. This sensitivity is strictly dependent on the frequency of the phenomena reaching its peak value around 7–10 Hz. In this range, even a 0.3% variation of the rms voltage feeding an incandescent lamp may be perceived. The flicker can be measured through the following two quantities:

- P_{st}: short time severity;
- P_{lt}: long time severity.

Although voltage variations are usually caused by large load commutation, some kind of residential low-voltage apparatus may cause flicker. It is worth noting that voltage fluctuations caused by large industrial loads may affect different users connected to the same grid. Since the impedance of electrical networks varies according to the point which is being considered, voltage fluctuation produced by an electrical apparatus may considerably differ depending on the point the apparatus is connected to.

A perfect flicker compensation is not possible, but an attenuation of this phenomena can be achieved through:

- an increase of the short circuit power;
- a reduction of the reactive power flux;
- a limitation of the motor starting currents.

Voltage dips – short interruptions   Voltage dips are bi-dimensional electromagnetic distortions which are characterised by the amplitude and duration. Voltage dip means that energy is not properly provided to loads during this event and this could result in different consequences depending on the kind of load. According to International Electrotechnical Commission (IEC) standards, voltage dips are referred to as a sudden reduction of voltage affecting a point of the distribution network below 90% of the reference voltage. This reduction has to be recovered within 60 s. Whenever the voltage falls down to zero the event is classified as a short interruption.

The duration of a voltage dip is the interval between the instant when the voltage falls below the threshold value and the instant when the voltage rises again above the threshold. The depth of a voltage dip is the difference between the reference and the residual voltage.

The starting of large loads and faults on the network are the main causes of voltage dips. Dips caused by starting currents are less deep and longer (up to a few seconds) than the ones caused by faults on the grid (less than one second).

When large loads are switched on, the starting current could be much higher than the steady-state current. Since the feeders and the cable of a distribution system are designed for steady-state operation, the high current value is responsible for a considerable voltage drop.

7.1.4 Waveform variation

Harmonics   If an electric quantity is distorted and periodical it can be split into three terms: the mean value calculated over one period of the considered signal, the fundamental component having the same frequency of the considered signal and the sum of the harmonic components. The amplitude of the harmonics decreases with the frequency. The representation of such amplitudes is referred to as spectrum.

As regards symmetrical waveforms (perfectly matching of the positive and negative half-waves), the even harmonics are nihil. This type of harmonics were common when half-wave rectifiers were used.

Power suppliers provide a 50 Hz sinusoidal voltage, but the current drawn by a load is not always sinusoidal. The current is not sinusoidal anymore when the load impedance varies during one period T (the load voltage/current characteristic is not linear). Such type of loads is referred to as non-linear loads. For example, the magnetising current of a transformer is deformed by a third-order harmonic because of the non-linear magnetisation curve of the machine. Rectifiers (battery chargers, welding machines, etc.), inverters, electronic starters, adjustable speed drives, switching power supplies, discharge lamps are other examples of non-linear loads.

A distorted current causes distorting voltage drops so that the resulting voltage supplying a circuit will not be sinusoidal anymore. The voltage provided is the transformer voltage minus the voltage drop across the feeder. Thus, the voltage distortion depends on the distance from the transformer and on the line impedance. In short, the voltage distortion affecting the grid at a certain location depends on the value of the short-circuit current of that point. Also, once the grid voltage is distorted a linear load absorbs a distorted current. The presence of such harmonics on the grid is responsible for detrimental effects. At higher frequencies the capacitive reactance decreases making the current absorbed by capacitors to increase with consequent danger of damage and resonance. Moreover, at higher frequencies, iron losses (hysteresis losses and eddy current losses) as well as the losses in the cables increase. Finally, electronic equipments may experience failures due to the presence of harmonics.

Another aspect which should not be neglected is the resonance issue related to the presence of harmonics in electrical networks. In fact, in this case the amplitude of a specific harmonic may rise up to several times that of normal operation. Consequently this high-value current may seriously damage capacitors and equipments connected to the grid.

In order to prevent this kind of event, the resonance frequency of the grid at a certain point has to be known and, additionally, the insertion of well-fitted anti-resonance coils may be considered to damp the oscillatory phenomena.

Interharmonics   Interharmonics are particular harmonics whose frequency is not an integer multiple of the fundamental frequency. The analysis of such interharmonics has attracted increasing interest over the last few years since the massive use of power electronic equipments has caused an increment in their amplitude. They can be observed

where there is at least a part not pulsating synchronously with the fundamental power system frequency. There are many loads introducing voltage or current interharmonics such as arc furnaces, welding machines and cycloconverters.

The term "subharmonic" is used to indicate interharmonics whose frequency is lower than the fundamental. With respect to the harmonics, the interharmonic order is given by the ratio between the interharmonic frequency and the fundamental frequency.

The following scheme provides simple mathematical definitions:

Harmonic	$f = h \times f_1$, where h is an integer > 0
DC	$F = 0$ Hz
Interharmonic	$f \neq h \times f_1$, where h is an integer > 0
Subharmonic	$f > 0$ Hz and $f < f_1$.

where f_1 is the fundamental power system frequency.

Unbalance   A three-phase system is symmetrical and balanced when voltages and currents have the same amplitude in each phase and 120° phase shifted. To assess the degree of unbalance of a three-phase system it should be split into a positive sequence component, a negative sequence component and a zero sequence component. The ratio between the positive sequence and the negative sequence component provides useful information about the unbalance:

$$u_U = \frac{U_p}{U_n} \times 100 \ (\%).\tag{7.1}$$

Normally, the voltages produced are perfectly balanced because of the characteristics of the synchronous generator. Also, the effect of some geometrical asymmetries in the delivery electric system could be neglected. So, it is possible to state that unbalanced loads drawing unbalanced currents can be considered as the main cause of unbalanced voltages.

7.2 Electromagnetic Compatibility: Standards

The electromagnetic compatibility standards are necessary to assure that the customers of the same electrical network are not affected by other customers. The importance of such standards is increasing because of the restructuring of the electrical companies, the world over.

In the past, electrical utilities were integrated and their role was to monitor electrical networks in order to assure correct operation and to decide what it could be connected to the network.

Nowadays, in a free electricity market, customers seek convenience disregarding the impact on the network operation and on other customers. In this atmosphere, the standards fix requirements for a good operation of the entire system.

The standards are of vital importance in determining the level of power quality of any electrical distribution system in order to assure that the customer does not suffer unwanted interactions or does not undermine the integrity of the electrical network. The electromagnetic compatibility standards establish operational characteristics, tolerances, and limits which, when met, will allow facilities containing power sensitive and power disturbing loads to operate on electrical system with a minimum of interference to utility equipment or customer loads. Utilities and customers can use these standards to properly design, install, maintain and operate facilities containing power disturbing loads or sensitive equipment requiring a high degree of power quality.

7.2.1 IEC harmonic standards

International standards in the electrical and electronic area are the activity results of the IEC, a leading worldwide organisation in the field of standardisation. Such international standards provide a basis for national standardisation and for drafting international tenders and contracts.

IEC standards are divided into:

- *basic standards*, that specify the general conditions or rules necessary for achieving electromagnetic compatibility;

- *generic standards*, that define the generic limits of emission and immunities for industrial, commercial and domestic environments; these standards are for products operating in one of these particular Electromagnetic Compatibility (EMC) environments but for which no specific EMC standards exist yet;

- *product standards*, that refer to specific products and families of products, such as electricity meters and printed circuit boards, or to a group of products that have common general characteristics, that may operate in the same environment and have neighbouring fields of application. Medical devices, IT equipments (ITEs) and low-voltage household equipments are examples of product families.

The technical committee (TC) which deals with EMC is TC 77, which prepares basic and generic EMC publications specifying electromagnetic environments, emissions, immunity, test procedures, measurement techniques, etc. It is divided into three subcommittees:

- SC 77A dealing with low-frequency phenomena (≤ 9 kHz);

- SC 77B dealing with high-frequency continuous and transient phenomena;

- SC 77C covering high-power transients phenomena.

The subcommittee which considers the problems of power quality is SC 77A, whose main tasks in this field are the description of electromagnetic environments, the definition of

permissible harmonic and interharmonic current limits and the definition of appropriate procedure for the immunity tests, with regard to the equipment connected to supply systems, the preparation of guidelines for the connection of large disturbing loads to supply system and the definition of measurement parameters of power quality.

The contents of some major standards developed by SC 77A and concerning harmonics are outlined in the following:

IEC 61000-3-2 (2005) deals with the limitation of harmonic currents emission for electrical and electronic equipments having an input-rated current less than or equal to 16 A per phase, to be connected to public low-voltage network. This standard defines classification of equipments under test, measurement requirements, AC power source requirements and limits of harmonic components of the input current which may be produced by such equipment. Compliance to this standard ensures that tested equipment will generate harmonic currents at levels that do not affect the AC public supply voltage considerably.

IEC 61000-3-12 (2004) deals with the limitation of harmonic currents emission for electrical and electronic equipments having an input-rated current from 16 to 75 A inclusive, per phase, to be connected to public low-voltage network. In contrast to other standards, conformity with this standard can be verified through validated simulations and the methods for type tests and simulations have also been defined in this standard.

IEC 61000-2-2 (2002) is concerned with conducted disturbances in the low-frequency range, with an extension to the mains signalling systems. The compatibility levels specified in this standard apply at the point of common coupling (PCC) of public low-voltage AC distribution systems.

Compatibility levels are specified for the electromagnetic disturbances widespread in public low-voltage power supply systems, which are:

- voltage fluctuations and flicker;
- harmonics;
- interharmonics;
- voltage dips and short supply interruptions;
- voltage unbalance;
- transient overvoltages;
- power frequency variation;
- DC components;
- mains signalling.

The aim of this standard is to provide information about the disturbance levels that can be expected in the public low-voltage distribution systems. This standard provides

guidance for experts and utilities who have to define emission limits and for IEC product committees who have to define the immunity levels of specific products.

IEC 61000-2-4 (2002) is concerned with EMC levels of low-frequency conducted disturbances which affect industrial and non-public power distribution systems with nominal voltages up to 35 kV. Such compatibility levels are to be applied at any in-plant point of coupling. Additionally, they provide a guidance for the definition of emission limits into industrial power supply systems and for the choice of immunity levels of the equipments to be used within these systems.

IEC 61000-4-7 (2002) deals with the methods and instrumentations to be used for the measurement of harmonic and interharmonic components in the frequency range up to 9 kHz. It is a basic standard applicable for testing the accordance between individual items of equipment and emission limits given in some other standards, such as, for example, the IEC 61000-3-2, as well as for measuring harmonic currents and voltages in actual supply systems.

IEC 61000-4-30 (2003) defines the methods for in situ measurement of parameters which define power quality in transmission and distribution electrical systems, but does not set limits. Two classes of instruments are defined and, for each of them, measurement methods, accuracy, results processing and evaluation criteria are defined. The aim of this standard is to obtain reliable, repeatable and comparable results. All instruments that meet the Class A performance requirements of this standard, when connected to the same signals, will produce the same results. Instruments that meet the Class B performance requirements will produce useful, but not necessarily accurate, results.

The power quality parameters considered in this standard are power frequency, magnitude of the supply voltage, flicker, supply voltage dips and swells, voltage interruptions, transient voltages, supply voltage unbalance, voltage and current harmonics and interharmonics, mains signalling on the supply voltage and rapid voltage changes.

In addition to standards, SC 77A develops technical reports. Some of these publications, which deal with power quality and harmonics particularly, are outlined in the following:

IEC 61000-3-6 (1996) deals with the assessment of emission limits for distorting loads which are intended to be connected to MV and HV power systems. The aim of this technical report is to provide a practical guidance for ensuring a satisfactory level of voltage quality for all connected customers, in relation to planning levels. Such objective is reached by limiting the injection into the system of harmonic currents which results in harmonic voltages. Moreover, the control and limitation of harmonics voltages aim in the reduction of communication interferences.

IEC 61000-3-4 (1998) is concerned with the limitation of harmonic current emission due to electrical and electronic equipments having an input-rated current of more than 16 A per phase, to be connected to public low-voltage network. In this technical report, in contrast to other standards which concern limitation of harmonic emissions (for example, IEC 61000-3-12), equipment is intended to be a complex of components (for example, speed variable fan), and not a single component (for example, converter). The content

of this technical report is concerned with providing the supply authority the necessary information to evaluate the possibility of allowing equipment to be connected to the supply system, from the point of view of harmonic distortion.

7.2.2 IEEE Harmonic standards

Societies of the Institute of Electrical and Electronics Engineers (IEEE) and the Standards Coordinating Committees of the IEEE Standards Board provide standards that are formulated by working groups composed of volunteers representing varied viewpoints and interests to achieve the final product. IEEE standards documents tend to cluster in the fields of information technology, telecommunications energy and power.

There are three main standards developed by IEEE with harmonics as their main goal.

IEEE Std 1531-2003 is a guidance for application of passive shunt harmonic filters. It provides specification about components, protection and control of filters to be installed on low- and medium-voltage electric power system. Moreover, this guidance provides some considerations about the design and location of harmonic filters.

IEEE Std 1159-1995 provides a guidance for monitoring network power quality and measurement of electromagnetic disturbances, giving definitions relevant to power quality and depicting the impact of poor power quality on utility and customer equipment. The aim of this standard is to guarantee more uniformity in the monitoring and processing of power quality data, in order to properly understand the obtained results.

IEEE SM 519-1992 aims to provide criteria for the design of power systems in the presence of linear and non-linear loads. The standard defines harmonic voltage limits and harmonic current limits that the utilities and the customers, respectively, have to comply with at the PCC. Moreover, this guide describes how harmonics affect the operation of some electrical equipments and provides an overview about the most common harmonics sources, above all converters. The problems involved in the harmonic control and reactive compensation of such converters are addressed, and an application guide is provided.

7.2.3 Comparison of IEC and IEEE standards harmonic limits

The goal of both the IEC and IEEE harmonic standards is to guarantee the voltage quality through the control of harmonic currents injection into the network. However, the approaches of the IEC and IEEE in setting the limits to production of customer harmonic currents are different. The IEEE standard assigns the limits on the basis of the short circuit value at the PCC of the network. Consequently, the more robust the network is, the more will be the ability to tolerate higher levels of harmonics. The idea is that if voltage distortion problems occur while all customers comply with their current limits, the utility is responsible for them and it is liable to restore voltage quality. On the other hand, the IEC standard assigns the limits according

to the type of equipment connected to the network. Such limits derive from rigorous voltage quality targets and are designed to ensure that if all customers comply with their individual limits, then voltage quality problems related to harmonics will not occur.

Both standards also provide voltage limits. In IEEE, the individual voltage harmonic limits are constant across all frequencies whereas they decrease with frequency in IEC. In addition to individual voltage harmonic limits, the voltage total harmonic distortion (THD) limits are defined in both standards, but the limits are more restrictive for IEEE.

7.3 Harmonic Distortion Level Monitoring

As can be observed from earlier sections, in the last fifteen years power quality assessment standards have assumed great importance.

Harmonic distortion levels of current and voltage in electrical primary and secondary distribution networks have increased. Consequently, studies on harmonic pollution have become an important aspect of power system analysis and design, and harmonic distortion measurements are important to quantify the distortion in voltage and current waveforms. The aim of quality monitoring is also to verify if electromagnetic perturbations are below or above the limit fixed by standards. Besides, the knowledge of the composition and characteristics of non-linear loads present in a particular area is essential for an accurate determination of their impact on the resultant voltage waveform, in order to carry out an effective power quality management applying a prevention and/or a correction strategy. The first could be the use of converters with a control that aims at a low level of harmonics injected into the network, while the second could be the interposition between the source and the loads of active filters that compensate the harmonics produced by the loads, as will be better described in the following chapters.

7.3.1 Evaluation of the voltage and current distortion

To assess the impact due to the presence of voltage and current harmonics, the use of some indices is suggested by international standards. The most common harmonic index is the total harmonic distortion (THD) which can be applied to a voltage and current waveform. Such parameter is defined as follows:

$$\text{THD} = \sqrt{\sum_{n=2}^{N} \left(\frac{A_n}{A_1}\right)^2}, \tag{7.2}$$

where A_n is the amplitude of the nth order harmonic, A_1 is the amplitude of the fundamental and N is the maximum harmonic order to be considered.

Another harmonic index expounded by standards and applicable for voltage and current is the individual harmonic distortion (IHD), which can characterise the level of each harmonic with respect to the fundamental:

$$\text{IHD}_n = \frac{A_n}{A_1}. \tag{7.3}$$

Since the value of the current THD can be high even for a low power load, whose impact on the power system can be negligible, for current distortion evaluation the use of the total demand distortion (TDD) is preferable. It is defined as:

$$\text{TDD} = \frac{\sqrt{\sum_{n=2}^{N} I_n^2}}{I_L}, \tag{7.4}$$

where I_L is the maximum demand load current (15 or 30 min demand) at fundamental frequency at the PCC calculated as the average current of the maximum demands for the previous twelve months. The TDD value will give more realistic information about the level of disturbance caused by the load under test.

Voltage harmonic limits for a distribution power system are defined both by IEC and IEEE standards. The former fixes the maximum level of acceptable voltage THD at 8% for public low voltage AC distribution systems and suggests a maximum interharmonic voltage level of 0.2% of the fundamental voltage. The latter fixes the maximum level of acceptable voltage THD at 5% and does not address interharmonics limits. On the other hand, current harmonic limits are defined by IEC and IEEE standards also, but a maximum level of current THD is not fixed.

The determination of current and voltage THD gives information about the quality of their waveform, but nothing can be said about the assignment of the responsibility in the power quality deterioration process. A relationship between voltage and current distortion can always be observed, but what disturbance influences the other is not clear, because the measured parameters are not able to establish whether voltage distortion is due to the load under test or due to the interconnected power systems.

7.3.2 The need for new indices

Recently, many studies about the behaviour of power systems under non-sinusoidal conditions have appeared in scientific literature. Unfortunately, in spite of the fact that this discussion has involved researchers for decades, there is still no consensus on the numerous definitions (i.e. definition of powers) and many issues continue to be subjects of debate (IEEE Working Group, 1996). One of these issues concerns the search for parameters capable of assessing power quality phenomena in terms of harmonics.

An issue most researchers agree on is that non-linear loads should not be considered as the only cause of the detrimental effects related to power systems in these conditions. The responsibility for the power quality deterioration should be shared between the supplier and the customer (Cristaldi and Ferrero, 1994; Swart *et al.*, 1994; Srinivasan, 1996; Muscas, 1998; Srinivasan and Jutras, 1998; Mustafà *et al.*, 2000). This kind of information could be provided by indices in a straightforward and simple way. Such indices should be able to identify a non-ideal load (non-linear or time-varying); additionally, the value of these indices must increase with the level of harmonic distortion introduced by the load. Furthermore, they must be easy to calculate and are accurate.

The traditional indices used by the European and American Standards, such as THD, cannot satisfy these specifications (Dell'Aquila *et al.*, 2000). Nevertheless, the introduction of the new electricity market is going to revolutionise the power distribution above all regarding the interaction among the increased number of subjects involved.

Official agreements among all parties of this new market could definitely include limits to be respected regarding power quality issues, for example, harmonic distortion, transients, flicker, etc. Failures from any side in fulfilling the agreed power quality requirements could be punished with administrative penalties or simply by much higher bills in the case of users and contractors. The staff in charge of the network regulation will have to deal, as well, with different interests and needs of the entities connected to the network. It will not be an easy task to solve eventual disputes among contractors, distributors, private producers, etc. regarding the responsibilities on quality issues especially in the absence of a clear, efficient and unquestionable assessing technique.

Therefore, it will become strictly necessary to have a sort of standard method to identify the sources of electrical power quality deterioration, quantify the amount of unwanted effects introduced and evaluate accurately the actual proportion of responsibility of each of the market player involved. This need was also underlined by the activity of CIGRE Working Group 36.07 which was formed with the aim of discussing power quality indices and objectives (Beaulieu *et al.*, 2002).

Recently, a few studies dealing with new quality indicators able to identify and quantify the responsibility of suppliers and customers for the power quality deterioration due to the presence of harmonics in power systems have appeared in scientific literature (Wilsun Xu and Yilu Liu, 2000; Kandil *et al.*, 2001; Dell'Aquila *et al.*, 2004). Unlike the classical performance factors, they identify a non-ideal load pointing out whether the load or supply is mainly responsible for the current waveform distortion and indicating its level of non-linearity.

In the following, the authors present a new approach to evaluate the level of non-linearity of a distorting load based on the sole measurement of voltage and current waveforms at the PCC (Dell'Aquila *et al.*, 2004). Indices obtained only from these two quantities avoid complicated classifications of the harmonic active powers that some of the existent indices are based on (Cristaldi and Ferrero, 1994; Muscas, 1998).

7.4 New Power Quality Assessment Criteria for Supply Systems under Non-Sinusoidal Conditions

7.4.1 Basic assumptions

Power quality deterioration due to harmonics can originate simultaneously at several points in a network. Current and voltage waveforms measured at the PCC are the combined effects of the numerous deforming devices connected to the network in different places. Therefore, it is not possible to locate just one source of this problem. Instead, it is possible to separate the contribution to harmonic distortion due to the load under investigation connected to the considered PCC, while the rest is due to the supply side including all the other loads.

The first step in defining indices that satisfy the requirements mentioned above is to fix the ideal load conditions. Any load that shows a linear and balanced behaviour represents an ideal load condition. In fact, if the loads under test were linear, then the supply system alone would be responsible for harmonic distortion at the PCC.

Initially it is necessary to identify which current waveform would be drained if an *equivalent linear load* was present instead of the real one. Furthermore, the term *equivalent linear load* must be understood. Such a load can be defined as the linear load that absorbs from each phase an active power at the fundamental frequency equal to the fundamental active power actually flowing through the PCC. It also absorbs a reactive power at the fundamental frequency equal to the absolute value of the fundamental reactive power actually flowing through the PCC. So the *equivalent linear load* represents the ideal load. It drains a distorted current but it is not responsible for this distortion. In this case, the mains alone is responsible for distortion.

Three identical R–L series circuits have been considered in order to model the ideal three-phase linear load. These seem to be more suitable choices than parallel circuits, because there is no need to make a distinction between active and reactive current. Furthermore, it is not necessary to establish which part of the whole reactive power at the fundamental frequency is due to inductive elements and which due to capacitive ones. In fact by considering a load with a predominantly inductive reactance, as it usually is, then the important factor is that the current component should lag the voltage component at the fundamental frequency. In other words, a positive or zero reactive power at the fundamental frequency will always be expected.

By evaluating the parameters R and L of this ideal model, the part of the real load that represents the equivalent linear load not influencing the power quality can be identified. So whatever is at the load side, it is always possible to estimate a part of the whole load in terms of passive elements (R–L series) that does not affect distortion. This part of the real load drains a *linear current* that is the ideal current and represents only a part of the total current flowing through the PCC. If the linear current approximates the total current, then the load would not be responsible for the distortion problems.

7.4.2 New criterion for harmonic distortion evaluation

At the PCC, each harmonic of the current drawn by a non-linear and/or time-varying load depends on every harmonic component of the voltage. Since this voltage is also determined by network operative conditions, as explained in Section 7.2, the current is affected by the network also. Therefore, the existing indices, usually dependent on voltage and current, are deeply influenced by network conditions, so they are highly variable and hence not suitable to characterise the nature of the load.

On the basis of this observation, a new current index, to assess the power quality in terms of harmonic distortion, has been introduced. It is less sensitive to the network operative conditions than the traditional ones, such as, for example, the current total harmonic distortion (THDi). This means that if the load is fixed and the network alone is responsible for voltage harmonic content variation, the new index value is almost constant.

The parameters R and L of the *ideal and balanced load* have been estimated on phase A according to the following procedure. The same method can of course be applied to phases B and C. If Z_{1A} is the impedance of the phase A R–L series circuit at the fundamental frequency, it results:

$$|Z_{1A}| = \frac{V_{1A}}{I_{1A}} \tag{7.5}$$

$$\angle Z_{1A} = |\theta_{1A} - \phi_{1A}| = \varphi_{1A}, \tag{7.6}$$

where V_{1A} and I_{1A} are the fundamental rms values of the phase A voltage and current at the PCC, and θ_{1A} and ϕ_{1A} are the phase angles of the same quantities. Therefore we have:

$$R_A = |Z_{1A}| \cos \varphi_{1A} \tag{7.7}$$

$$X_{1A} = |Z_{1A}| \sin \varphi_{1A} \tag{7.8}$$

$$L_A = \frac{X_{1A}}{2\pi f_0}, \tag{7.9}$$

where X_{1A} represents the ideal R–L series reactance at the fundamental frequency f_0 and R_A and L_A are the expected parameters. The values of the reactance at the frequencies of the voltage harmonic components are:

$$X_{kA} = 2\pi k f_0 L_A \qquad k = 1, 2, \ldots, n \tag{7.10}$$

If the skin effect is neglected and the value of R_A is not influenced by frequency then:

$$|Z_{kA}| = \sqrt{R_A^2 + X_{kA}^2} \tag{7.11}$$

$$\varphi_{kA} = \text{arctg}\left(\frac{X_{kA}}{R_A}\right) \qquad k = 1, 2, \ldots, n, \tag{7.12}$$

where n represents the order of the last significant voltage harmonic component. For most applications, it is sufficient to consider the harmonic range between the 2nd and the 25th ($n = 25$), but most standards specify up to the fiftieth ($n = 50$).

The current that the ideal linear load on phase A should drain can be expressed as:

$$i_{\text{lA}}(t) = \sum_{k=1}^{n} \frac{\sqrt{2} V_{kA}}{|Z_{kA}|} \sin \left(2\pi k f_0 t + (\theta_{kA} - \varphi_{kA})\right). \tag{7.13}$$

This is the *linear current* and the supply system is the only cause of its distortion.

The difference between the measured real current and the calculated ideal current can be defined as the *non-linear current*:

$$i_{\text{nlA}}(t) = i_A(t) - i_{\text{lA}}(t). \tag{7.14}$$

The non-linear current expresses how much the real load on phase A differs from the ideal one in terms of harmonic distortion. This current could contain some harmonic components not present in the voltage.

We can therefore define a non-linear current index that provides reliable information about the distortion attributable to the customer, as follows:

$$\frac{I_{\text{nlA}}}{I_A} \times 100 \ (\%), \tag{7.15}$$

where I_{nlA} and I_A are rms values:

$$I_{\text{nlA}} = \sqrt{\sum_{k=1}^{l} I_{k\text{nlA}}^2} \tag{7.16}$$

$$I_A = \sqrt{\sum_{k=1}^{m} I_{kA}^2} \tag{7.17}$$

$I_{k\text{nlA}}$ and I_{kA} are the corresponding rms values of the harmonic components of $i_{\text{nlA}}(t)$ and $i_A(t)$, while $l = m = n$.

7.4.3 Simulation results

In order to evaluate the performance of the proposed index, simulation tests on a three-phase four-wire circuit have been carried out. Two different situations have been simulated, where the analysis has been limited to one phase.

The first case aims to verify whether this index assumes a constant and near-zero value when a non-distorting linear load is under test. A low-voltage bus-bar (230 V_{rms}) feeding

a 5 kW load with a cos $\varphi = 0.9$ has been considered. Various tests have been carried out considering a supply voltage with an increasing harmonic content and comparing the behaviour of the proposed index with the current THDi and with an index based on the definition of the conforming and non-conforming currents (Srinivasan and Jutras, 1998). The expressions for these currents on each phase are respectively:

$$i_c(t) = \sum_{k=1}^{n} \left(\frac{I_1}{V_1} \right) \sqrt{2} V_k \sin (k\omega t + \theta_k + k (\phi_1 - \theta_1)) \tag{7.18}$$

$$i_{nc}(t) = i(t) - i_c(t), \tag{7.19}$$

where V_1 and I_1 are the fundamental rms values of voltage and current at the PCC, θ_1 and ϕ_1 are the phase angles of the voltage and current, θ_k is the phase angle of the kth harmonic voltage component and $i(t)$ is the instantaneous current drawn by the load. This index is therefore:

$$\frac{I_{nc}}{I} \times 100 \ (\%), \tag{7.20}$$

where I_{nc} is the rms of Eq. 7.19.

As Fig. 7.1 shows, the THDi and the index of non-conforming current are non-constant as the voltage total harmonic distortion (THDv) varies. In this way, one of the starting requirements is not satisfied. The index of non-linear current, instead, shows the best behaviour since it assumes a constant near-zero value for different levels of supply voltage distortion.

The second simulated case aims to verify that the index of non-linear current assumes a constant non-zero value when a non-linear load is under test. For this reason, a model
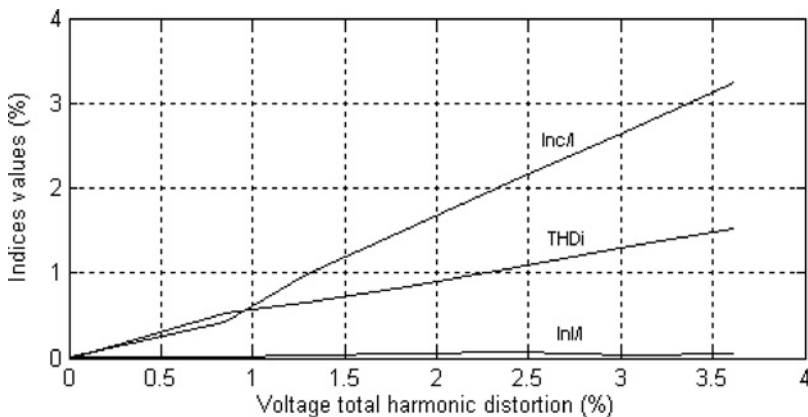
Fig. 7.1. Simulated indices values vs. voltage total harmonic distortion (THDv) in the case of linear load.
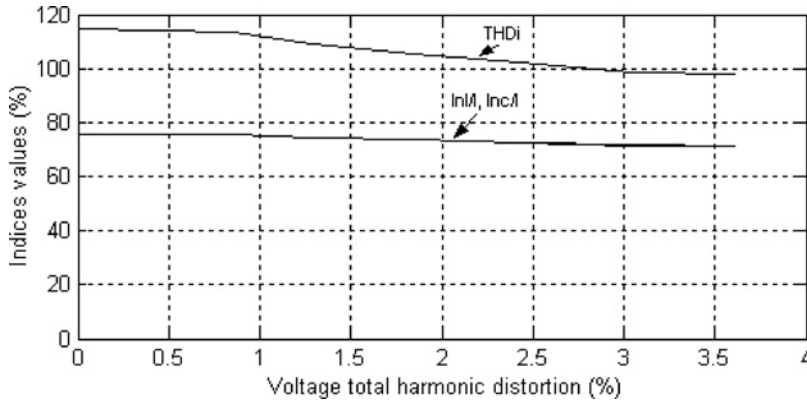
Fig. 7.2. Simulated indices values vs. voltage total harmonic distortion (THDv) in the case of non-linear load.

of a computer with a single-phase diode rectifier as front-end has been used. It is only necessary to consider a 200 W computer with $\cos \varphi = 0.7$ connected to the bus-bar since the value of the index considered depends on the nature of the load and is independent of the power absorbed at the PCC. Figure 7.2 shows that, as the THDv increases, the THDi has a non-constant trend, while the index of non-linear current is, again, almost invariant.

7.4.4 Experimental results

A dedicated measurement system has been set up in order to experimentally assess the theory and the results obtained from the simulations. It consists of a 16 single-ended channels AT-MIO 16E National Instruments plugged in board and a conditioning system. This last component, comprising three voltage and three current transducers, has been designed to adapt the measured signal voltage levels to the range allowed by the board input. This system has also been arranged to acquire six signals of voltage and current simultaneously without introducing any phase-shifting that would affect the accuracy of the measurements.

For data acquisition and processing, a virtual instrument developed in LabVIEW and MATLAB environment has been employed. This instrument stores the instantaneous values of each phase voltage and line current, as the block scheme of Fig. 7.3 shows for one phase.

The values of the main parameters that define the measurements may be selected via software by the user. The main user-selectable parameters are: number of channels and gain on each channel, sampling frequency, harmonics to be measured, rectangular window duration and total observation time. These main technical features of the virtual instrument follow the recommendations in IEC 61000-4-7. In fact, since the signal under test contains quasi-stationary harmonics, a window width of 0.1 s (equal to 5 cycles of
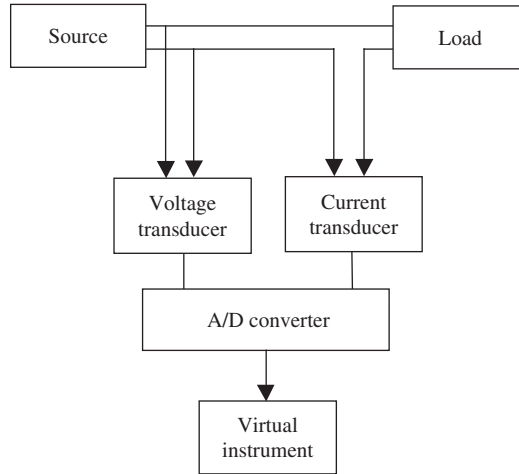
Fig. 7.3. Scheme of the measurement system on each phase.

the fundamental component) and a sampling frequency of 10 kHz have been imposed. This is more than double the frequency of the highest significant harmonic component of the signal, in order to avoid aliasing and leakage errors.

To investigate the effectiveness of the non-linear current index, experimental tests have been carried out on a typical balanced highly distorting non-linear load consisting of two computers on each phase (400 W, $\cos \varphi = 0.7$). The supply voltage and the drained current on phase A have been measured throughout a day, at regular intervals of one hour. In this way, it has been possible to evaluate the performances of the index of non-linear current in the case where a fixed load is fed by a supply voltage with variable harmonic content.

Like the simulations, the experimental results have proved that the proposed index has a better behaviour, compared to the THDi, in evaluating the real harmonic distortion generated by the load and in assessing the responsibilities between the customers and distributors.

Figure 7.4 shows that, though the THDv variation on phase A (shown in Fig. 7.5) is small ($\cong 1\%$), the THDi variation is remarkably high ($\cong 25\%$), as would be expected. The high value assumed by the proposed index means that in this case it is the load that is mainly responsible for the distortion phenomena observed at the PCC.

Moreover, as Fig. 7.6 shows, the non-linear current index varies less with the THDv than the non-conforming current index. This means that the proposed index is able to characterise the distorting nature of the load under test in a more accurate way.

To test the effectiveness of the proposed non-linear current index to assess the harmonic distortion even in the presence of an unbalanced load, some experimental tests have been
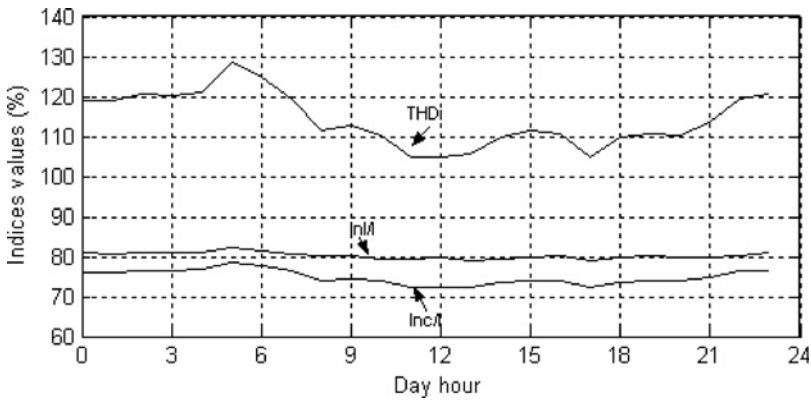
Fig. 7.4. Daily trend of measured indices values.
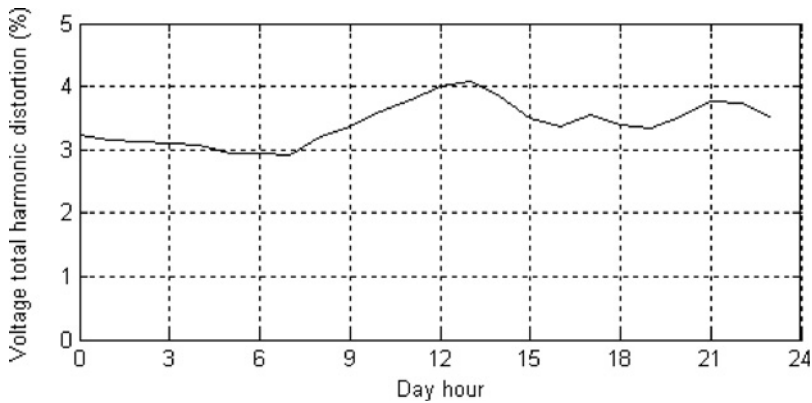
Fig. 7.5. Daily trend of voltage total harmonic distortion (THDv).
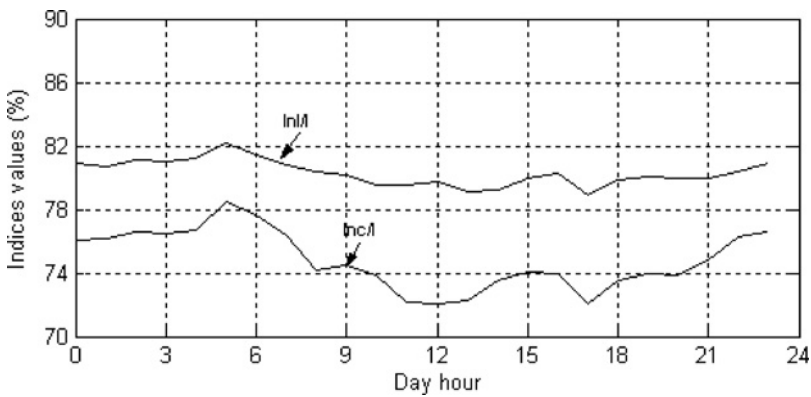
Fig. 7.6. Zoom of the daily trend of measured indices values.

carried out with a three-phase non-linear and unbalanced load. It consists of one computer on phase A (200 W, $\cos\varphi = 0.7$), three computers on phase B (600 W, $\cos\varphi = 0.7$), four computers (800 W, $\cos\varphi = 0.7$) and a resistive load (1 kW) on phase C. The three supply voltages and the three line currents at the PCC have been measured throughout a day, at regular time intervals of one hour. In this way, a constant load is connected to the network and undergoes all the daily variation of THDv and unbalance. Figure 7.7 shows, in this case, the trend of the THDv during the whole day on each phase, while Figs 7.8–7.10 show the daily trend of THDi and of non-linear current index for each phase.

It can be seen that the non-linear current index is more invariant than the THDi. It tends, like the THDi, to assume lower values as the load is less distorting like on phase C.
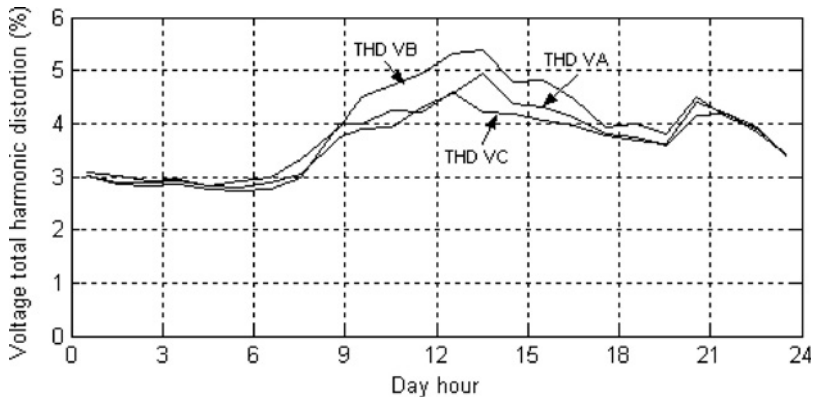
Fig. 7.7. Daily trend of voltage total harmonic distortion (THDv) (phases A, B and C).
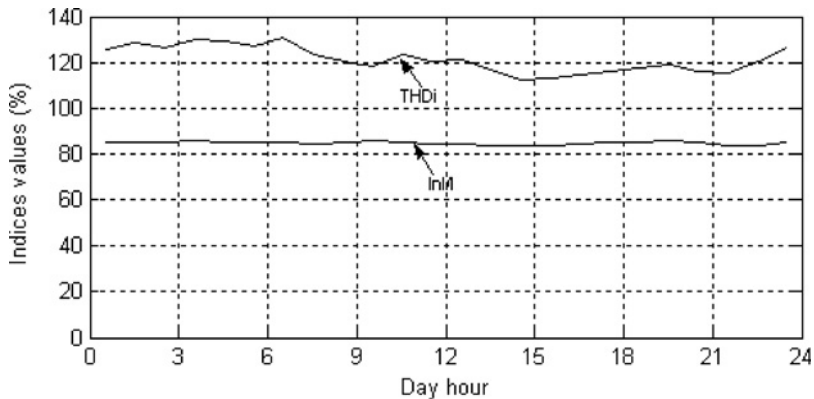
Fig. 7.8. Daily trend of current non-linear index and current total harmonic distortion (THDi) (phase A).
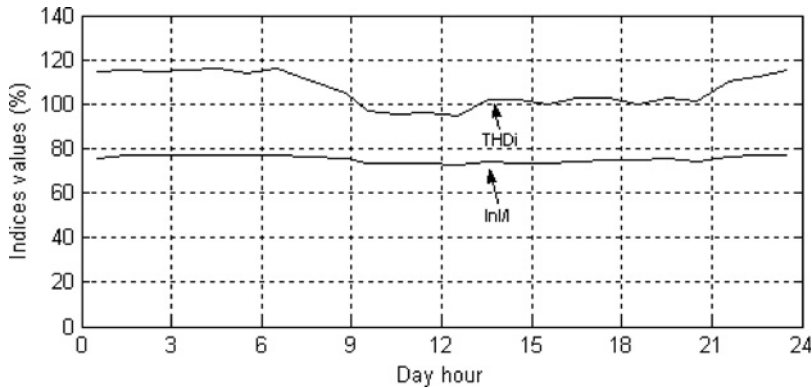
Fig. 7.9. Daily trend of current non-linear index and current total harmonic distortion (THDi) (phase B).
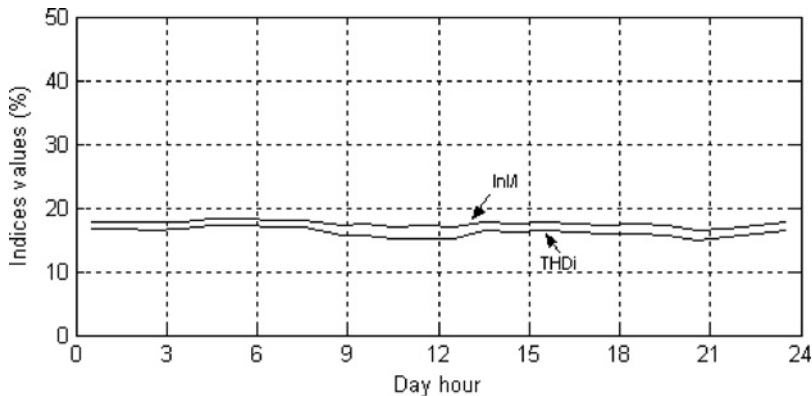
Fig. 7.10. Daily trend of current non-linear index and current total harmonic distortion (THDi) (phase C).

In this way, the evaluation of the harmonic distortion generated by the load is hardly influenced by network conditions.

Moreover, it can be pointed out that the index has approximately the same value on phases A and B since there is same kind of load on both phases. So the index value is almost independent from the load entity and expresses only the capability of the load to affect harmonic distortion at the PCC.

Since the aim of the proposed index is to evaluate the conformity of the real load to the ideal one without considering the effect that each harmonic can introduce into the network, all the harmonics are equally weighted. Additionally, it is worth noting that in the presence of distortion and unbalance, a single index, factor or

parameter can no longer be expected to carry complete information about the system conditions.

7.5 Conclusions

In this chapter, an overview of the main disturbances affecting the electrical power system operation has been presented. Harmonic issues have been more deeply investigated and the contents of the major international standards related to this topic have been briefly mentioned. Additionally, monitoring and evaluating the power quality from the point of view of harmonic disturbances have been introduced. The necessity to have a standard method to identify the sources of electrical power quality deterioration, to quantify the amount of unwanted effects introduced and to evaluate accurately the actual proportion of responsibility of each of the players involved has been underlined.

To this purpose, a new index to evaluate current harmonic distortion phenomena in the electrical supply networks has been defined and experimentally tested. Unlike the classical performance factors, it identifies whether the load or supply is mainly responsible for the deterioration of power quality in terms of harmonic distortion. Therefore, it can suggest how to share the responsibilities between the distributors and the customers. Simulation results and experimental tests have proved that this index can identify distorting loads on a network, provide reliable quantitative information about the level of harmonic distortion and separate the responsibilities of suppliers and users.

Acknowledgement

References

Arrillaga J., Watson N.R., Chen S., *Power system quality assessment*, John Wiley, Chichester, England, 2000.

Beaulieu G., Bollen M.H.J., Malgarotti S., Ball R., "Power quality indices and objectives. Ongoing activities in CIGRE WG 36-07", Proc. IEEE Power Eng. Soc. Summer Meeting, **2**, 2002, pp. 789–794.

Cristaldi L., Ferrero A., A digital method for the identification of the source of distortion in electric power systems. IEEE Trans. Instrum. and Meas., **44** (1994) 14–18.

Dell'Aquila A., Marinelli M., Menolascina E., Zanchetta P., "Power quality long term monitoring in non-sinusoidal conditions", Proc. 4th Eur. Symp. on Electromagnetic Compatibility, 2000, pp. 145–150.

Dell'Aquila A., Marinelli M., Monopoli V., Zanchetta P., New power quality assessment criteria for supply systems under unbalanced and non-sinusoidal conditions. IEEE Trans. Power Delivery, **19** (2004) 1284–1290.

Dugan R.C., McGranaghan M.F., Beaty H.W., *Electrical power systems quality*, McGraw-Hill, USA, 1996.

IEC 61000-2-2, Electromagnetic compatibility (EMC) – Part 2-2: environment – compatibility levels for low-frequency conducted disturbances and signalling in public low-voltage power supply systems, 2002.

IEC 61000-2-4, Electromagnetic compatibility (EMC) – Part 2-4: environment – compatibility levels in industrial plants for low-frequency conducted disturbances, 2002.

IEC 61000-3-2, Electromagnetic compatibility (EMC) – Part 3-2: limits – limits for harmonic current emissions (equipment input current ≤16 A per phase), 2004.

IEC 61000-3-12, Electromagnetic compatibility (EMC) – Part 3-12: limits – limits for harmonic currents produced by equipment connected to public low-voltage systems with input current >16 A and ≤75 A per phase, 2004.

IEC 61000-4-7, Electromagnetic compatibility (EMC) – Part 4-7: testing and measurement techniques – general guide on harmonics and interharmonics measurements and instrumentation, for power supply systems and equipment connected thereto, 2002.

IEC 61000-4-30, Electromagnetic compatibility (EMC) – Part 4-30: testing and measurement techniques – power quality measurement methods, 2003.

IEC/TR 61000-3-6, Electromagnetic compatibility (EMC) – Part 3: limits – Section 6: assessment of emission limits for distorting loads in MV and HV power systems – basic EMC publication, 1996.

IEC/TS 61000-3-4, Electromagnetic compatibility (EMC) – Part 3-4: limits – limitation of emission of harmonic currents in low-voltage power supply systems for equipment with rated current greater than 16 A, 1998.

IEEE SM 519-1992, Recommended Practices and Requirements for Harmonic Control in Electrical Power Systems.

IEEE Std 1159-1995, Recommended Practice for Monitoring Electric Power Quality.

IEEE Std 1531-2003, Guide for Application and Specification of Harmonic Filters.

IEEE Working Group on Nonsinusoidal Situations, Effects on Meter Performance and Definitions of Power, "Practical definitions for powers in systems with nonsinusoidal waveforms and unbalanced loads: a discussion", IEEE Trans. Power Delivery, **11** (1996) 79–101.

Kandil M.S., Farghal S.A., Elmitwally A., "Refined power quality indices", Proc. Inst. Elect. Eng., Gen., Trans. Dist., **148** (2001) 590–596.

Muscas C., "Assessment of electric power quality: indices for identifying disturbing loads", Eur. Trans. Elect. Power Eng., **8** (1998) 361–368.

Mustafà A.A., Moussa A.M., El-Gammal M.A., "Separation of customer and supply harmonics in electrical power distribution systems", Proc. 9th Int. Conf. Harmonics and Quality & Power 2000, pp.1035–1040.

Srinivasan K., "On separating customer and supply side harmonic contributions", IEEE Trans. Power Delivery, **11** (1996) 1003–1012.

Srinivasan K., Jutras R., "Conforming and non-conforming current for attributing steady state power quality problems", IEEE Trans. Power Delivery, **13** (1998) 212–217.

Swart P.H., Case M.J., van Wyk J.D., On techniques for localization of sources producing distortion in electric power network. Eur. Trans. Elect. Power Eng., **4** (1994) 485–489.

Wilsun X., Yilu L., "A method for determining customer and utility harmonic contributions at the point of common coupling", IEEE Trans. Power Delivery, **15** (2000) 804–811.

CHAPTER 8

Design of Line Front-End Converter Systems under Real Line Conditions

Marco Liserre and Antonio Dell'Aquila

Abstract

The aim of this chapter is to investigate the design of line front-end converter systems and their control in view of their steady-state and transient behaviour. After a brief review of the applications, the basic functions, the operating limits and the mathematical models of the voltage source front-end converters are discussed. Some basic and advanced control techniques are reviewed with specific attention to the possible design criteria. Then the influence of the non-ideal conditions (grid unbalance, converter dead-time and presence of unmodelled delays in control and measurement) is discussed.

8.1 Introduction

As mentioned in the previous chapter, the flow of current harmonics is one of the power quality problems affecting the electric grid. Several kinds of loads may be considered as harmonic sources, such as consumer electronic equipments and variable speed drives. Their front-end stage could be a converter that drains (injects) non-sinusoidal currents from (to) the mains thus causing an increase in current rms value, a general overheating of cables and, depending on the grid topology, a wide spread of harmonic pollution both in currents and in voltages. In order to limit the amplitude of produced harmonics and to meet international standards on power quality such as IEEE 519 and IEC/EN 61000-3-2, the use of bulky, expensive and sometimes inefficient filters, should be required on the AC side of a passive rectifier stage. Moreover, these filters are generally tuned for a certain cut-off frequency and load conditions, thus causing limitations on the dynamic performance of the system. Several alternatives have been introduced to face harmonic pollution problem, such as active harmonic compensators; the installation of an active filter in a proper location could be a viable solution, as shown in Chapter 11 of this book. However in many industrial applications, such as industrial process AC drive connected
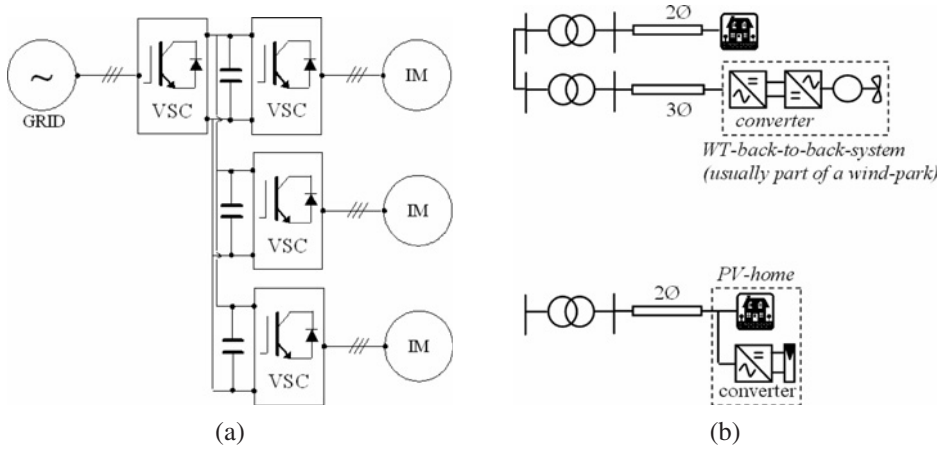
Fig. 8.1. Industrial process AC drive connected on the same DC link (a) and distributed generation systems (b).

on the same DC link (see Fig. 8.1(a)), and in many distributed generation systems (mainly photovoltaic and wind turbine, see Fig. 8.1(b)) the line-commutated polluting stage could be efficiently replaced by an active front-end converter offering the capacity of compensation of reactive power and bidirectional function (Kolar and Ertl, 1999; Jahns and Blasko, 2001). Thus the active front-end converter (Fig. 8.2) is the preferred solution not only in applications such as drives that work frequently in regenerative mode like crane, elevator, centrifuge, braking of large inertia or wind turbine (Jahns and
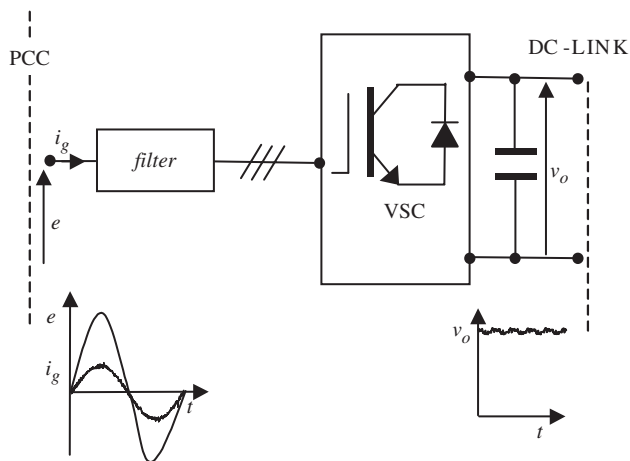
Fig. 8.2. Voltage source converter (VSC) used as active front-end with a sketch of the desired grid current i_g in phase with the grid voltage e and of the desired DC voltage v_o.

Blasko, 2001; Liserre *et al*., 2003), but also in distributed generation systems (Blaabjerg *et al*., 2004).

The inherent limitations of the active front-end converter are in the number of switches (six transistors with antiparallel diodes for three-phase systems, Fig. 8.3(a), or four transistors with antiparallel diodes for single-phase systems, Fig. 8.3(b)) and in the control complexity required. However, the quick evolution and progressive decrease in the cost of both switching devices with turn-off and bidirectional-current capabilities, and Digital Signal Processor (DSP)/microcontroller systems, have worked in the direction of reducing the limitations mentioned.

The basic requirements of a good design of an active front-end converter are: approximately sinusoidal line current; resistive fundamental line side behaviour; fixed reference value control of the output voltage; and high power density.

Besides reducing the effects on the grid, the active front-end converter also gives (as compared to the line-commutated rectifier systems) the possibility of a highly dynamic control of the power flow, the generation of an output voltage being constant independent

(a)

(b)
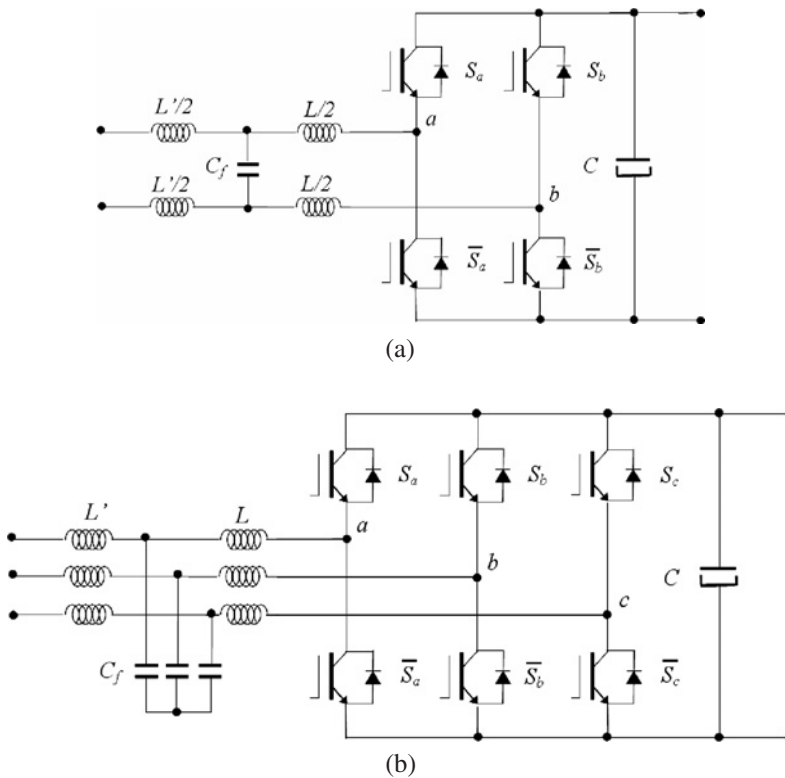
Fig. 8.3. Single-phase (a) and three-phase (b) voltage source converter (VSC).

of the grid voltage and load. Furthermore, a reduction in the rated power and in the weight of the rectifier unit can be achieved. The constant output voltage feature also gives the possibility of an adjustment to a wide input voltage region and a maximum utilisation of the rated power of a converter connected in series on the DC side for two-stage rectifier systems.

8.2 Basic Function, Operating Limits and Mathematical Models

An ideal three-phase power line, can be modeled as ideal: three sinusoidal phase voltages with constant amplitude $\sqrt{2}E$ and 120° displacement among them. The active front-end converter is a boost converter: the average DC voltage V_o can be controlled to be higher than the natural DC link voltage (the diode bridge one $\sqrt{6}E$):

$$V_o = \sqrt{6}E \cdot k_{boost} \quad \text{with } k_{boost} > 1 \tag{8.1}$$

The main objective of the active front-end converter is to obtain sinusoidal input currents, unity power factor and controllable DC voltage in each physically possible working condition, i.e. for each value of the chosen output voltage that is compatible with the value of the grid voltage.

If these requirements are actually fulfilled, the active front-end converter can be modelled as a black box with imposed sinusoidal input currents in phase with the grid voltages and constant output voltage. This means that it is seen as a resistor from the grid (the ideal active front-end converter does not introduce any phase displacement) and like an ideal voltage source from the load. In other words, the ideal active front-end converter exchanges only fundamental harmonic active power with the grid and fixed DC power with the DC side. Then the grid active power flow can be studied, as shown in Fig. 8.4.

When the DC side is absorbing power then the active front-end converter works in rectifying mode and a part of the grid power is dissipated by losses. When the DC side is generating power then the active front-end converter works in generating mode and a part of the DC side power is dissipated. In both these conditions, the DC voltage is controllable, exchanging a part of this power with the DC capacitor and making it charge or discharge. In the following sections, these two processes of power balance rectifying/generating and charge/discharge are discussed. Then the operating limits of these processes are clarified and some mathematical models are described for the control design purposes.

The two operating modes (rectifying and generating) and the two processes (charge and discharge of the capacitor) can be explained using the space vectors to deal with the AC side analysis:

$$\bar{y}(t) = \frac{2}{3}\big(y_a(t) + \alpha \cdot y_b(t) + \alpha^2 \cdot y_c(t)\big) \tag{8.2}$$

with $\alpha = \exp{(j2\pi/3)}$.
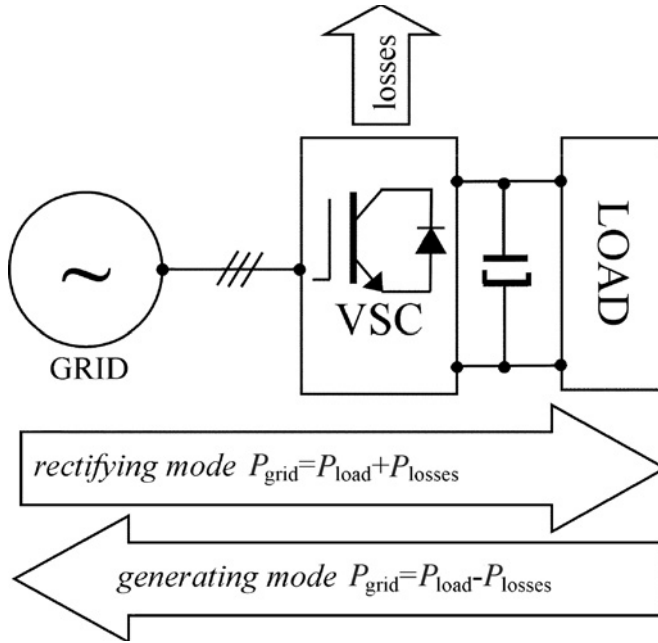
Fig. 8.4. Active front-end converter operating modes.

To obtain the ideal behaviour of the converter (sinusoidal input current, unity power factor, controllable DC voltage) the voltage source converter (VSC) should work as a voltage source on the grid side and as a current source on the load side.

On the grid side, according to Kirchoff's law two voltage sources should not be connected directly, therefore an inductor is inserted between the supply line and the active front-end converter. The presence of the inductive element on the AC side allows the voltage source $\bar{v}(t)$ to control the grid current $\bar{i}(t)$ against the grid voltage source $\bar{e}(t)$:

$$\bar{i}(t) = \frac{\bar{e}(t) - \bar{v}(t)}{j\omega L}, \tag{8.3}$$

where ω is the angular speed of the grid voltage vector. The model is shown in Fig. 8.5: $\overline{v_d}(t)$ is the voltage drop across the inductance.

By modulating the phase and amplitude of the converter voltage $\bar{v}(t)$ it can control the grid current. If the converter voltage matches the grid voltage exactly, no current will flow in the grid. If the amplitude of the converter voltage is slightly decreased, a purely inductive current will start flowing into the converter (assuming that the inductor to have no resistance). The direction of power flow can be controlled by changing δ; If $\bar{v}(t)$ is leading $\bar{e}(t)$, the converter is operated in a generative mode. When $\bar{v}(t)$ is lagging $\bar{e}(t)$, the converter is rectifying (Fig. 8.6).
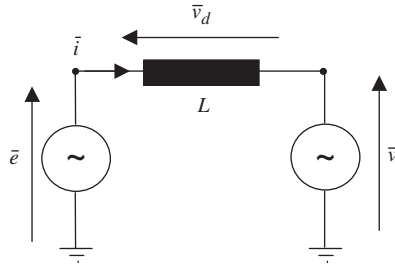
Fig. 8.5. Equivalent circuit for the grid current control.

(a) (b)
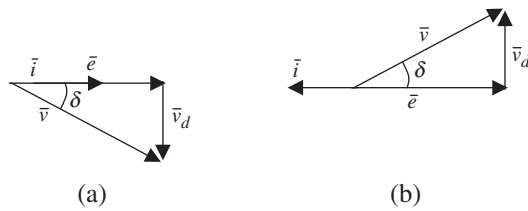
Fig. 8.6. (a) Rectifying and (b) generating modes.

On the load side, according to Kirchoff's law two current sources should not be connected directly. Therefore a capacitor is inserted between the load and the active front-end converter. The presence of capacitive element on the DC side allows the active front-end converter current source $i_o(t)$ to control the DC current source $i_{DC}(t)$, the load voltage $v_o(t)$:

$$\frac{dv_o(t)}{dt} = \frac{i_o(t) - i_{DC}(t)}{C} \tag{8.4}$$

The scheme is shown in Fig. 8.7.

If the converter current matches the load current exactly, the DC voltage will remain unchanged. If the amplitude of the converter current is slightly increased or decreased,
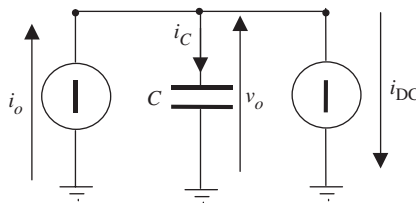
Fig. 8.7. Equivalent circuit for the load voltage control.

a capacitive current will start flowing into the capacitor. The direction of power flow can change the DC voltage level. If $i_o(t)$ is higher than $i_L(t)$, the DC voltage will increase (charging process):

$$i_o(t) > i_{DC}(t) \Rightarrow i_o(t) - i_{DC}(t) = \frac{dv_o(t)}{dt} > 0 \qquad (8.5)$$

When $i_o(t)$ is lower than $i_L(t)$, the DC voltage will decrease (discharging process):

$$i_o(t) < i_{DC}(t) \Rightarrow i_o(t) - i_{DC}(t) = \frac{dv_o(t)}{dt} < 0 \qquad (8.6)$$

The rectifying/generating process and charge/discharge process are summarised in Fig. 8.8.
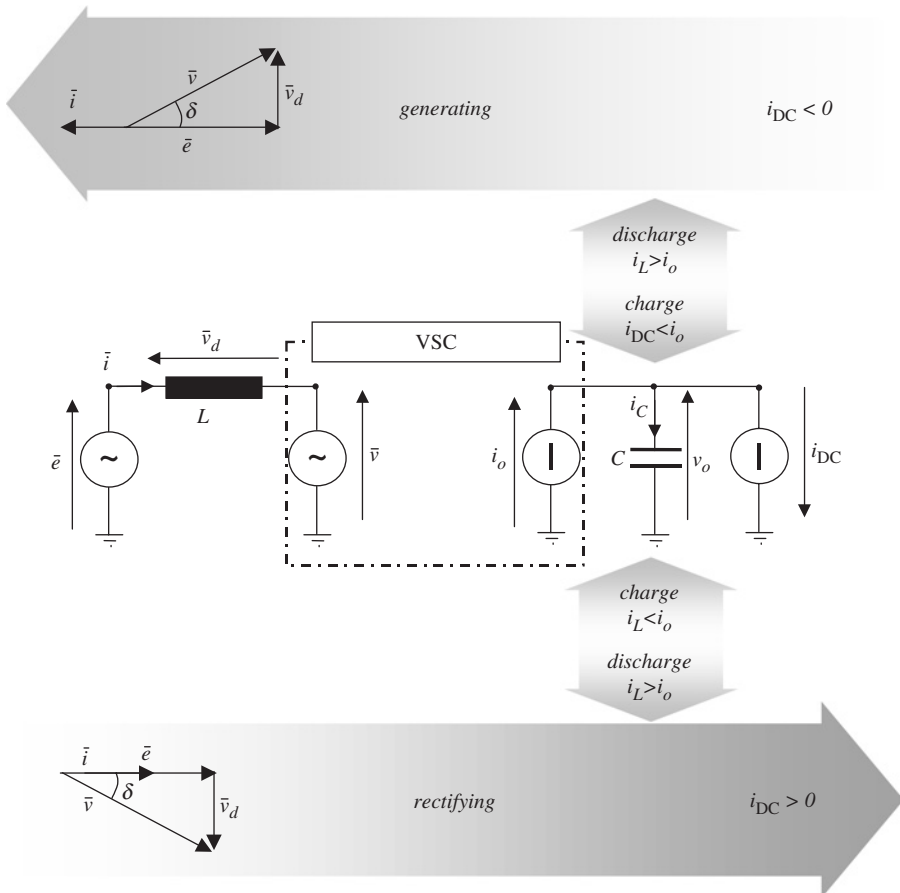
Fig. 8.8. Power balance of the active front-end converter (the arrows simulate the direction of the power flow).

The *AC current control* (that allows passing from rectification to generation) and the *DC voltage control* (that allows regulating the DC bus level through the charge or discharge of the capacitor) interact with each other. Usually if a proper sampling frequency is adopted the two controls could be designed to have different time constants in such a way that it does not influence each other. But the presence of harmonics, that has been neglected at the beginning of this analysis, makes the two processes to interact. In fact if the DC voltage ripples consequently the converter voltage, result of the pulse width modulation of the DC voltage, also ripples and so does the AC current. This will propagate back the harmonics in the DC voltage following a vicious circle that produces low-order harmonics both in the input and in the output. One cause of this situation is the unbalance of the AC phases or the unbalance and distortion of the grid voltages. Another cause is the presence of dead time in the switching devices commutation and other non-linearities.

The harmonics create different types of powers. On the AC side there are the first-order active power and the other harmonic active power, both deliver energy to the DC side. There are also all the harmonic reactive power that do not deliver energy to the DC side and increase the value of the input current amplitude with a consequent need for overrating of the converter. On the DC side there is the DC power and a fluctuating power related to the presence of harmonics that affect the DC bus quality. Moreover, the VSC is essentially based on the switching of its devices thus there will be switching ripple both on the grid side and on the load side that can cause improper operation of sensitive equipment connected.

Not only non-ideal conditions affect the performances of active front-end converter, but also the use of a particular filter for the input such as a LCL filter, if it is not properly considered in the design could lead to decrease in the power factor and resonance.

In conclusion, all the elements should be properly considered in the design and the non-ideal conditions should be overcome if it is possible.

8.3 Basic Control

Low- and high-frequency models, as well as the use of coordinate transformation and small-signal linearisation for control purposes, are needed in order to design the basic controls such as phase control and current control of the active converter.

8.3.1 Phase control

One of the first type of control developed for active rectifier was the "phase control". The rectifier is operated at a fixed modulation index, close to unity, and power transfer is controlled through pattern phase-shifting by maintaining line and rectifier input voltage amplitudes equal. Since the rectifier is operated at an almost fixed modulation index with a value near unity, optimised switching patterns with reduced switching frequency can be used (Zargari and Joos, 1995; Fig. 8.9).
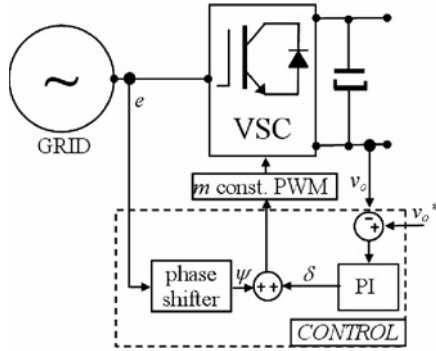
Fig. 8.9. Phase control based on the shift of the front-end AC voltage.

8.3.2 AC current control

The AC current control has been considered more suitable because the current-controlled converter exhibits, in general, better safety, better stability and faster response.

This solution ensures several additional advantages. The feedback loop also results in some limitations, such that fast-response voltage modulation techniques must be employed, like Pulse Width Modulation (PWM). Optimal techniques, which use pre-calculated switching patterns within the AC period, cannot be used, as they are not oriented to ensure current waveform control (Kazmierkowski *et al.*, 2002).

The use of an AC LCL filter could make the current control unstable, if a proper damping is not adopted (Liserre *et al.*, 2005).

8.3.3 Two axis-based current control

Figure 8.10 shows a *dq* frame that rotates at an angular speed ω (where $\omega = 2\pi f$ and f is the fundamental frequency of the power grid voltage waveform). The space vectors expressing the converter electrical quantities are projected on the *d* axis and *q* axis. As a consequence if a space vector with constant magnitude rotates at the same speed of the frame, it has constant *d* and *q* components while if it rotates at a different speed it has pulsating components.

The model of a three-phase system under study in a synchronous frame rotating at ω speed is:

$$\begin{cases} \dfrac{di_d(t)}{dt} - \omega i_q(t) = \dfrac{1}{DC}\left[-Ri_d(t) + e_d(t) - \dfrac{1}{2}p_d(t)v_o(t)\right] \\ \dfrac{di_q(t)}{dt} + \omega i_d(t) = \dfrac{1}{DC}\left[-Ri_q(t) + e_q(t) - \dfrac{1}{2}p_q(t)v_o(t)\right] \\ \dfrac{dv_o(t)}{dt} = \dfrac{1}{C}\left\{\dfrac{3}{4}\left[p_d(t)i_d(t) + p_q(t)i_q(t)\right] - i_{DC}(t)\right\} \end{cases} \quad (8.7)$$

Electromagnetic Compatibility in Power Systems
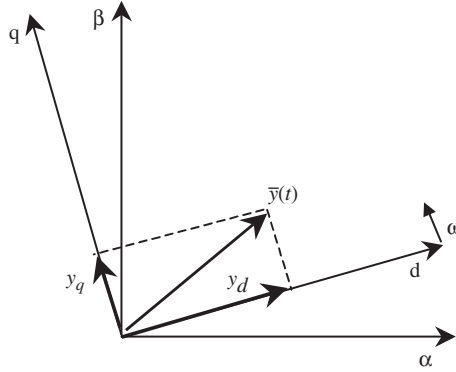
Fig. 8.10. Stationary $\alpha\beta$ frame and rotating dq frame.

Equation 8.7 shows how in the *dq* frame the *d* and *q* differential equations for the current are dependent due to the cross-coupling terms $\omega i_q(t)$ and $\omega i_d(t)$.

8.3.4 Use of averaging and linearisation

The AC current controllers are designed on the basis of an average model (Krein *et al.*, 1990) of the active front-end converter based on a continuous switching vector whose components are the duty cycle of each converter leg $-1 \leq s_j(t) \leq 1 (j = \text{a, b, c})$:

$$\bar{s}(t) = \frac{2}{3}\left(s_\text{a}(t) + \alpha \cdot s_\text{b}(t) + \alpha^2 \cdot s_\text{c}(t)\right) \tag{8.8}$$

Thus the average version of Eq. 8.7 becomes:

$$\begin{cases} \dfrac{\mathrm{d}i_d(t)}{\mathrm{d}t} - \omega i_q(t) = \dfrac{1}{L}\left[-Ri_d(t) + e_d(t) - \dfrac{1}{2}s_d(t)v_\text{o}(t)\right] \\[2mm] \dfrac{\mathrm{d}i_q(t)}{\mathrm{d}t} + \omega i_d(t) = \dfrac{1}{L}\left[-Ri_q(t) + e_q(t) - \dfrac{1}{2}s_q(t)v_\text{o}(t)\right] \end{cases} \tag{8.9}$$

In other words, the current controllers calculate the desired *d* and *q* components of the switching vector ($s_d(t)$ and $s_q(t)$) and a modulator select the converter switching states and their time of applications. Equation 8.9 can be linearised considering $v_\text{o}(t) = V_\text{o}$ with V_o constant:

$$\frac{\mathrm{d}}{\mathrm{d}t}\begin{bmatrix} i_d(t) \\ i_q(t) \end{bmatrix} = \begin{bmatrix} -\dfrac{R}{L} & \omega \\ -\omega & -\dfrac{R}{L} \end{bmatrix}\begin{bmatrix} i_d(t) \\ i_q(t) \end{bmatrix} + \begin{bmatrix} -\dfrac{V_\text{o}}{2L} & 0 \\ 0 & -\dfrac{V_\text{o}}{2L} \end{bmatrix}\begin{bmatrix} s_d(t) \\ s_q(t) \end{bmatrix} + \begin{bmatrix} \dfrac{1}{L} & 0 \\ 0 & \dfrac{1}{L} \end{bmatrix}\begin{bmatrix} e_d(t) \\ e_q(t) \end{bmatrix}$$
$$\tag{8.10}$$

Then Eq. 8.10 can be written in the form $\mathbf{i} = \mathbf{A} \cdot \mathbf{i} + \mathbf{B} \cdot \mathbf{s} + \mathbf{C} \cdot \mathbf{e}$, where the matrix $\mathbf{B}$, does not depend on the system state thus it is linear.

If instead of the continuous switching vector the average converter voltage is used such as:

$$\begin{cases} v_{d,\text{av}}(t) = \dfrac{V_o}{2} s_d(t) \\ v_{q,\text{av}}(t) = \dfrac{V_o}{2} s_q(t) \end{cases} \tag{8.11}$$

then Eq. 8.10 can be rewritten in this form:

$$\frac{d}{dt} \begin{bmatrix} i_d(t) \\ i_q(t) \end{bmatrix} = \begin{bmatrix} -\dfrac{R}{L} & \omega \\ -\omega & -\dfrac{R}{L} \end{bmatrix} \begin{bmatrix} i_d(t) \\ i_q(t) \end{bmatrix} + \begin{bmatrix} -\dfrac{1}{L} & 0 \\ 0 & -\dfrac{1}{L} \end{bmatrix} \begin{bmatrix} v_{d,\text{av}}(t) \\ v_{q,\text{av}}(t) \end{bmatrix} + \begin{bmatrix} \dfrac{1}{L} & 0 \\ 0 & \dfrac{1}{L} \end{bmatrix} \begin{bmatrix} e_d(t) \\ e_q(t) \end{bmatrix} \tag{8.12}$$

Also, the DC voltage controller is designed on the basis of the vector $\bar{s}(t)$ thus on the average version of Eq. 8.8, i.e.:

$$\frac{dv_o(t)}{dt} = \frac{1}{C} \left\{ \frac{3}{4} \left[s_d(t) i_d(t) + s_q(t) i_q(t) \right] - i_{\text{DC}}(t) \right\} \tag{8.13}$$

If the current is supposed to be equal to its reference value $i_d(t) = i_d^*(t)$ and $i_q(t) = i_q^*(t)$ and $s_d(t) = S_d$ and $s_q(t) = S_q$ it is also possible to linearise Eq. 8.13 obtaining:

$$\frac{dv_o(t)}{dt} = \frac{1}{C} \left\{ \frac{3}{4} \left[S_d i_d^*(t) + S_q i_q^*(t) \right] - i_{\text{DC}}(t) \right\} \tag{8.14}$$

Thus if a cascade controller is used, the DC voltage control could be performed through the selection of the input current value $i_d^*(t)$ as explained in the following sections.

8.3.5 The voltage oriented control

The voltage oriented control (VOC) of the rectifier is based on the use of a *dq* frame rotating at a speed ω and oriented such as the *d* axis is aligned on the grid voltage vector (Kazmierkowski *et al.*, 2002). The space vector of the fundamental harmonic has constant components in the *dq* frame while the other harmonic space vectors have pulsating components. The main purpose of the active front-end converter is to generate or to absorb sinusoidal currents; thus the reference current components in the *dq* frame are DC quantities.

The reference current *d* component (i_d^*) is controlled to perform the regulation of DC voltage while the reference current *q* component (i_q^*) is controlled to obtain a unity power factor. To have the grid current vector in phase with the grid voltage vector, i_q^* should be zero. These two control tasks are summarised in Fig. 8.11.

The control structure is defined as "cascade" because the DC voltage controller calculates the reference value for the *d* axis current controller. The general structure is shown in Fig. 8.12.
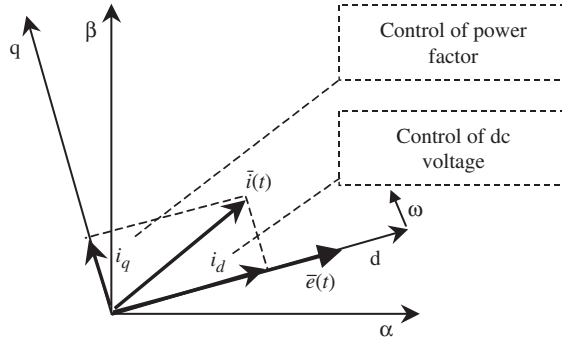
Fig. 8.11. *dq* frame and control aims.
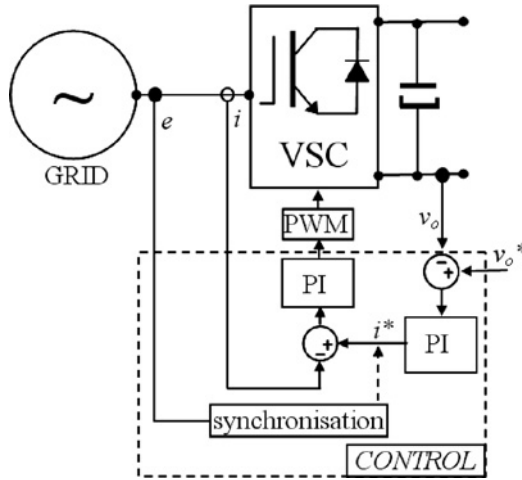
Fig. 8.12. Basic scheme of a cascade controller.

8.4 Advanced Control Techniques

Many advanced control techniques have been presented in the literature to guarantee optimum active front-end performances, some of them are briefly reviewed in the following sections:

8.4.1 Sensorless control techniques

An interesting alternative to the feedback current control is the so-called feedforward control where the current sensors are not used as depicted in Fig. 8.13. A formula is used to predict the switching space vector on the basis of the current error and of the DC voltage (Komurcugil and Kukrer, 1999). The main problems are related to the need for
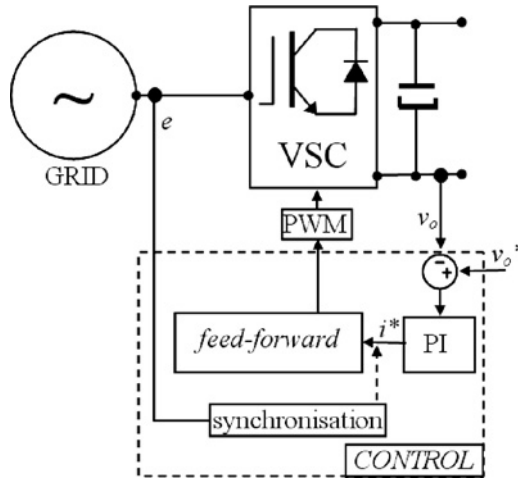
Fig. 8.13. Grid-current sensorless control.
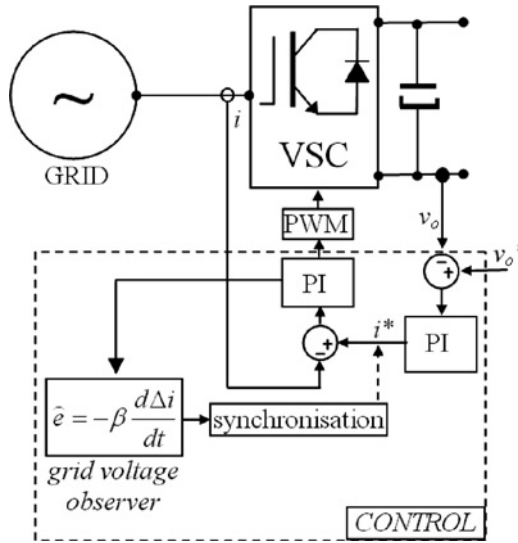
Fig. 8.14. Grid-voltage sensorless control.

protection against overcurrent. A fuzzy-logic version of the current-sensorless controller has been proposed by Cecati *et al*. (2003) and its implementation issues are discussed in Cecati *et al*. (2005).

On the other hand, it has been considered more reliable to avoid the use of grid voltage sensors rather than of grid current sensors. In Agirman and Blasko (2003) an algorithm to estimate the position of line voltage vector is presented (Fig. 8.14). The proportional-plus-integral current regulator is modified to obtain the angle error signal
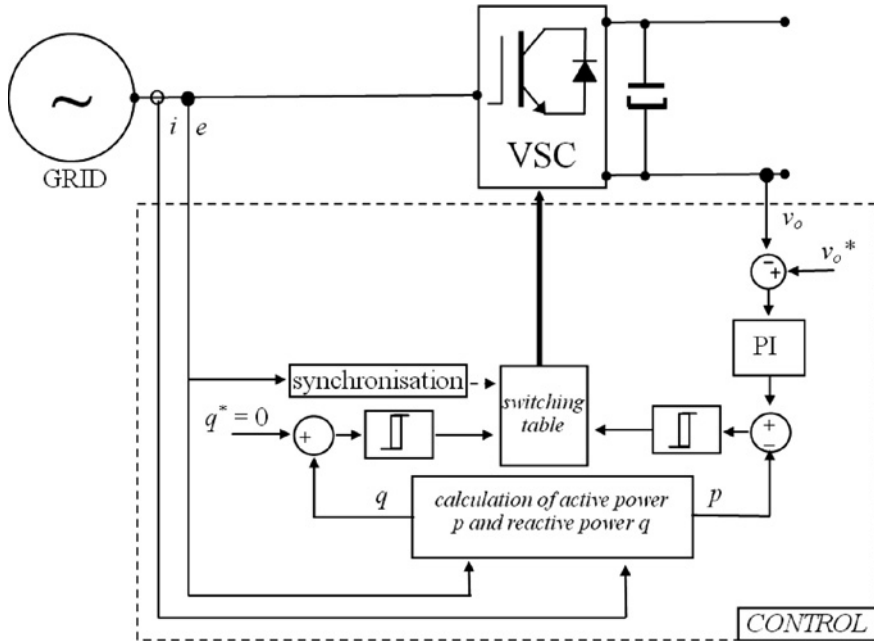
Fig. 8.15. Direct power control based on the active and reactive power calculation.

driving an observer, similar in structure to a phase-locked loop, which provides the angle of line voltages.

8.4.2 Direct power control

In recent years, the most interesting emerging technique has been the direct power control (DPC) developed in analogy to the well-known direct torque control used for drives. In DPC, there are no internal current loops and no PWM modulator block because the converter switching states are appropriately selected by a switching table based on the instantaneous errors between the commanded and estimated values of active and reactive power (Ohnishi, 1991; Kazmierkowski *et al.*, 2002; Fig. 8.15). The main advantage of the DPC is in its simple algorithm and the main disadvantage is in the need for high sampling frequency required to obtain satisfactory performances.

8.5 Design Criteria for PI-Based Current Controller

To design a PI-based current controller Eq. 8.12 is used:

$$
\frac{\mathrm{d}}{\mathrm{d}t}\begin{bmatrix} i_d(t) \\ i_q(t) \end{bmatrix} = \begin{bmatrix} -\dfrac{R}{L} & \omega \\ -\omega & -\dfrac{R}{L} \end{bmatrix}\begin{bmatrix} i_d(t) \\ i_q(t) \end{bmatrix} + \begin{bmatrix} -\dfrac{1}{L} & 0 \\ 0 & -\dfrac{1}{L} \end{bmatrix}\begin{bmatrix} v_{d,\mathrm{av}}(t) \\ v_{q,\mathrm{av}}(t) \end{bmatrix} + \begin{bmatrix} \dfrac{1}{L} & 0 \\ 0 & \dfrac{1}{L} \end{bmatrix}\begin{bmatrix} e_d(t) \\ e_q(t) \end{bmatrix}
$$

$$(8.15)$$

The *dq* currents $i_d(t)$ and $i_q(t)$ can be controlled by means of the right choice of the *dq* converter side voltages $v_{d,\text{av}}(t)$ and $v_{q,\text{av}}(t)$.

In Eq. 8.15, there are some terms to be considered before doing the design of the current controllers:

(1) The cross-coupling terms $\omega L i_d(t)$ and $\omega L i_q(t)$ that make the two current equations not independent; and

(2) The grid voltage *dq* components $e_d(t)$ and $e_q(t)$.

For both the cases, a feedforward compensation could be performed following the scheme of Fig. 8.16. Indicating with $u_d(t)$ and $u_q(t)$ the outputs of the two regulators, the applied voltages are:

$$\begin{cases} v_{d,\text{av}}(t) = u_d(t) + e_d(t) + \omega L i_q(t) \\ v_{q,\text{av}}(t) = u_q(t) + e_q(t) - \omega L i_d(t) \end{cases} \tag{8.16}$$

Substituting Eq. 8.16 in Eq. 8.15:

$$\begin{cases} u_d(t) = -R i_d(t) - L p i_d(t) \\ u_q(t) = -R i_q(t) - L p i_q(t) \end{cases} \tag{8.17}$$

Once the compensation of the grid influence and of the cross-coupling effects is completed, the controllers for both *d* and *q* axis can be designed on the basis of the following plant transfer function:

$$G(s) = -\frac{1/R}{1 + Ts} \tag{8.18}$$
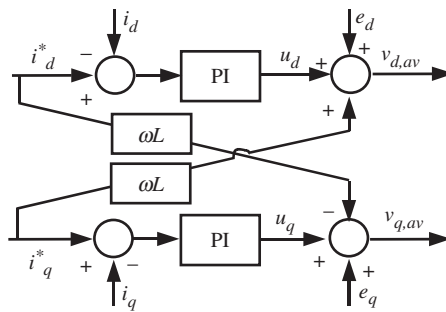
Fig. 8.16. AC current control in *dq* rotating frame.

The two current loop controllers could be designed on the basis of the same time constant $T = L/R$. Two PI-based controllers can be used to perform the control action. They have the following form in the S domain:

$$D(s) = -\frac{k_P (1 + T_I s)}{T_I s} \qquad (8.19)$$

with k_P proportional gain and T_I time constant of the integrator. The minus sign in Eq. 8.19 comes from Eq. 8.18, in fact a positive voltage makes the current to decrease.

The other terms of the current control loop (Fig. 8.17) are: the pulse width modulator $M(s)$ and the antialiasing filter on the feedback current $F(s)$.

The modulator $M(s)$ has a time constant that is usually settled at half of the sampling period ($T_M = T_s/2$) because this is the average time of the modulator to produce the desired voltage (chosen by the controller) (Blasko and Kaura, 1997). In fact, the modulator applies in a sampling period a sequence of inverter states that should produce an average voltage equal to the reference one. The problem is when to consider this average voltage applied: at the beginning of the sampling period, before the selection of the states, is unrealistic and at the end is too conservative; thus the centre seems a suitable approximation that leads to half a period delay in the current loop.

The filter $F(s)$ could be made analogue or digital. An antialiasing filter should be used because the sampling theorem says that: one can recover a signal from its samples, if the sampling frequency is at least twice the highest frequency in the signal. Thus, once the sampling frequency is chosen, the harmonic content of the sampled signal should be zero for frequencies up to twice that of frequency. However, usually in the current spectrum there are harmonics around several multiples of the switching frequency thus a filter should be designed. This filter, in its easiest implementation, introduces a number of delays dependent on its cut-off frequency: the lower is the cut-off frequency the higher is the number of delays. Fortunately, if a symmetrical switching function is adopted by the modulator the sampled signal is free of switching harmonics. Thus the sampling theorem can be complied with a high cut-off frequency such that the delay introduced is a negligible fraction of the sampling period.

The variations in the grid voltage and uncompensated non-linearities have been modelled with the disturbance w. The processing delay T_s and one sampling period due to the
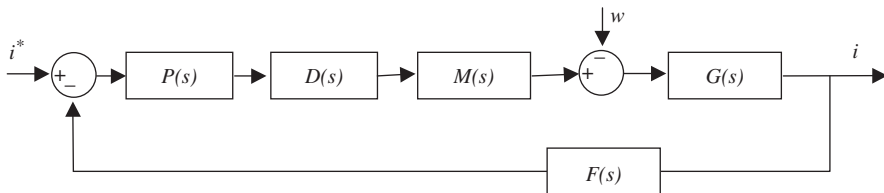
Fig. 8.17. Current control loop in S domain.

microcontroller or DSP is taken into account with the first-order transfer function $P(s)$:

$$P(s) = \frac{1}{1 + T_s s} \tag{8.20}$$

One block is substituted with two blocks with the smallest time constants ($M(s)$ and $P(s)$) that are grouped together. Its time constant is the sum of the $M(s)$ and $P(s)$ time constants. The current loops used for the PI design in S domain are shown in Fig. 8.18.

The digital version of the current loop (Fig. 8.18) in the Z domain is shown in Fig. 8.19: z^{-1} is the processing delay, $D(z)$ is the digital version obtained with the backward rule of the controller $D(s)$, $G(z)$ is the zero-order hold (ZOH) equivalent of the system $G(s)$ that includes also the effects of the modulator as explained later and $F(z)$ is the filter.

The PI-based regulator obtained with the backward discretisation rule is:

$$D(z) = -k_P \frac{(1 + (T_s/T_I))z - 1}{z - 1} \tag{8.21}$$

The plant $G(z)$ is the ZOH equivalent of the plant transfer function $G(s)$. This is justified by the fact that the zero-order hold (also called "step invariant transformation") is a suitable model of the analogue to digital (A/D) conversion:

$$G(z) = (1 - z^{-1})Z \left\{ \frac{G(s)}{s} \right\} \tag{8.22}$$

However, the ZOH introduces half the sampling period delay that is exactly how much should be considered to take into account the influence of the modulator. Thus the ZOH
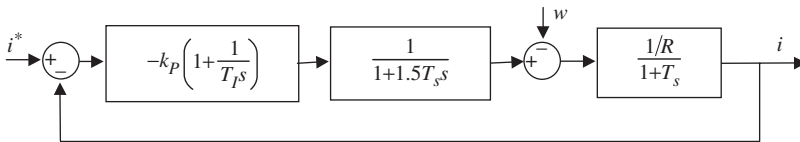
Fig. 8.18. Current control loop in S domain.
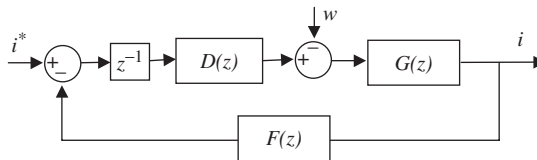
Fig. 8.19. Current control loop in Z domain.
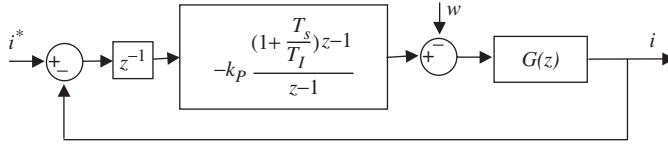
Fig. 8.20. Current control loop in Z domain.

equivalent of the $G(s)$ also takes into account the delay due to the modulation process. This is the reason in Fig. 8.14 as the modulator block is absent, but as explained, its effects have been taken into account. The current control loop in Z domain is shown in Fig. 8.20.

The PI controller can be designed both in the S domain and in the Z domain. The first approach offers a better mathematical basis for the design procedures, the second approach offers an easier verification in the Z plane of the desired dynamic performances and stability margins. Moreover, one should consider that in view of digital implementation of the controller it is always better to verify the controller with a Z plane analysis. The best approach seems to be a mixture of the two procedures: make a rough design in the S domain and then use the Z plane to verify the obtained controller and maybe to adjust it to filter the processing delays. Moreover, the step response will also be used to verify overshoot and settled time and the presence of undesired oscillations that can come from the presence of undamped poles. Then the Bode plot of the closed loop transfer function allows us in calculating the bandwidth of the controller.

As first step let us consider the steady-state accuracy in the Z domain. The use of a PI controller guarantees a zero error for a step reference, in fact $D(1) \to \infty$ from Eq. 8.21 thus:

$$e\left(\infty\right) = \lim_{z \to 1}\left[(z-1) \cdot \frac{z}{(z-1)} \cdot \frac{1}{1+z^{-1}D(z)\,M(z)\,G(z)} \right] = \frac{1}{1+D(1)\,M(1)\,G(1)} = 0 \tag{8.23}$$

 On the contrary the error for a ramp reference is:

$$e\left(\infty\right) = \lim_{z \to 1}\left[(z-1) \cdot \frac{T_{s}z}{(z-1)^{2}} \cdot \frac{1}{1+z^{-1}D(z)\,M(z)\,G(z)} \right] = \frac{1}{k_{\mathrm{v}}}, \tag{8.24}$$

where the velocity constant k_{v} is larger as the closed loop poles are farther from $z = 1$. Thus as the poles approach the circle the error for a ramp reference increases. This outlines the need for a balance between a small steady-state error and a fast transient response. However, in the case of current control of active front-end converter if the controllers are designed in a rotating frame the reference signal is usually a step.
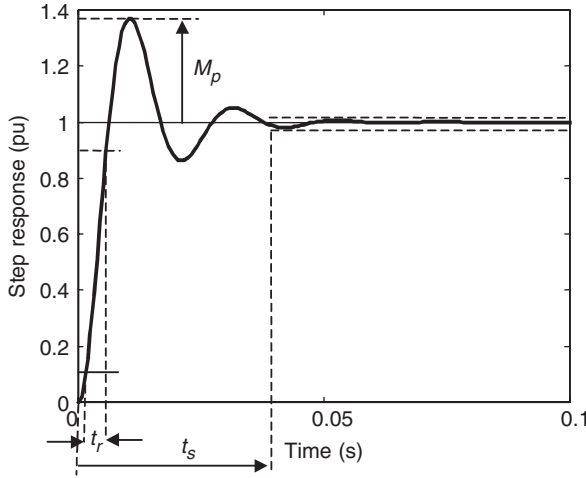
Fig. 8.21. Step response of a second-order system with the parameters that characterise the transient accuracy.

With respect to the transient accuracy, the overshoot M_p, the rising time t_r and the settling time t_s can be considered; they are defined as follows (Fig. 8.21):

(1) M_p is the maximum amount the system overshoots its final value, divided by its final value and expressed as a percentage;

(2) t_r is the time that takes the system to pass from 10 to 90% of the new set point; and

(3) t_s is the time it takes the system transients to decay in a range around the set point that could be 1, 2 or 5%.

A second-order system can be described in the S domain as:

$$H(s) = \frac{\omega_n^2}{s^2 + 2\zeta\omega_n s + \omega_n^2} \tag{8.25}$$

Thus $H(s)$ is characterised by the damping factor ζ and by the natural pulsation ω_n. The previously defined parameters for the transient can be defined as functions of ζ and of ω_n:

(1) $M_p = e^{-\pi\zeta/\sqrt{1-\zeta^2}}$;

(2) $t_r \cong \frac{1.8}{\omega_n}$ considering that all the curves rise in roughly the same time and taking as an average $\zeta = 0.5$;

(3) $t_s = \frac{4.6}{\zeta\omega_n}$ in 1% band;

Thus with the S domain analysis it is possible to calculate a formula to design the controller in view of the desired dynamic behaviour. Choosing the PI integrator time constant T_I equal to the plant time constant T, the current closed loop transfer function in S domain is:

$$H(s) = \frac{2k_P/3T_s L}{s^2 + (2/3T_s)s + (2k_P/3T_s L)} \tag{8.26}$$

This means that:

$$\omega_n^2 = \frac{2k_P}{3T_s L}$$

$$\zeta\omega_n = \frac{1}{3T_s} \tag{8.27}$$

Choosing to have a system critically damped (i.e. with a 5% overshoot) leads to $\zeta = 0.707$ thus to:

$$k_P = \frac{L}{3T_s} \tag{8.28}$$

Once the PI controller parameters are chosen it is possible to verify the desired damping of the system poles in the Z plane. Then the step response allows knowing in how many samples the system will settle in a fixed band and if the obtained overshoot is equal to the calculated one.

Finally with the closed loop Bode plot, the bandwidth of the controller is calculated. The term bandwidth is often used to roughly specify the quality of a control loop: the frequency at which the gain of the closed loop is reduced to -3 dB, and the phase delay becomes larger than $45°$ (assuming that closed-loop behaviour can be approximated by a first-order delay element). In reality, a closed loop transfer function is seldom a first-order element, and reduction of -3 dB and phase to $-45°$ does not happen at the same frequency. The conservative approach is to specify the lowest of the frequencies corresponding to these conditions as the bandwidth. In a system with the sampling delay approximated with a first-order element and all the small time constants being lumped together into an equivalent time constant, the phase becomes $-45°$ at a frequency lower than the frequency at which the gain reduces to -3 dB.

If the current control loop is adjusted to be optimally damped, the following first-order approximation can be useful to calculate the bandwidth of the system:

$$H_c(s) \approx \frac{1}{1 + 3T_s s} \tag{8.29}$$

and the bandwidth frequency f_{bi} is:

$$f_{bi} = \frac{1}{6\pi T_s} \approx \frac{1}{20T_s} \tag{8.30}$$

8.5.1 PI-based current control design example

Let us consider a system with $R = 0.3\,\Omega$ and $L = 8$ mH and sampling frequency equal to 5 kHz. If the design of the PI controller is made following the procedure previously described then $k_P = 13.3$ and $T_I = 0.03$.

The Z plane (Fig. 8.22) allows us to verify that the two complex conjugate poles that determine the dynamic are on logarithmic line for which the damping is 0.7 so the system is optimally damped. Therefore the step response (Fig. 8.23) has an overshoot of 5%. Moreover from the step response it is clear that the system has a rising time of 4 samples and a settling time of 11 samples in a band of 1% around the set point.

From the closed loop Bode plot of Fig. 8.24, it is possible to calculate the bandwidth that is expected for a system to be optimally damped at 1/20 of the sampling frequency, thus resulting in a frequency of 250 Hz. The calculated value from Fig. 8.24 is 200 Hz.

This kind of analysis allows us also in testing the effects of unmodelled delays. If in the system there are delays not considered for the calculation of the PI parameters, the desired stability and the dynamic performances can be seriously compromised. For example, let us consider two frequent situations of unmodelled delays:

If the elaboration time of the algorithm takes more than one sampling period, the modulator input cannot be refreshed at the end of the period. Thus if the system has been designed to refresh the duty cycle every sample period, one additional T_s is introduced in the loop in the position shown by Fig. 8.25. The effects are clear by Figs. 8.26(a) and 8.27(a) in terms of decrease in stability margin (the poles are only 0.3 damped), increase
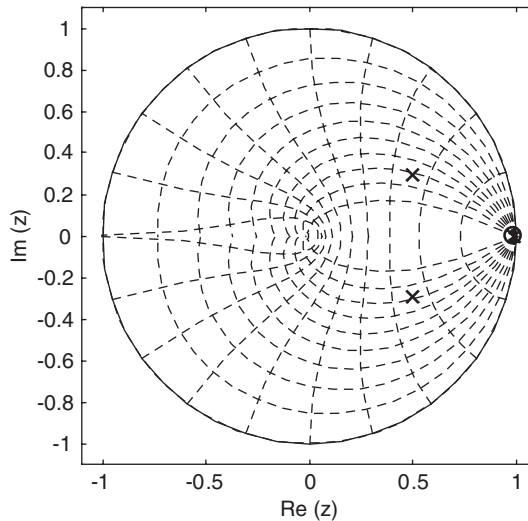
Fig. 8.22. Z plane root locus of the system with the two poles optimally damped, i.e. $\zeta = 0.7$.
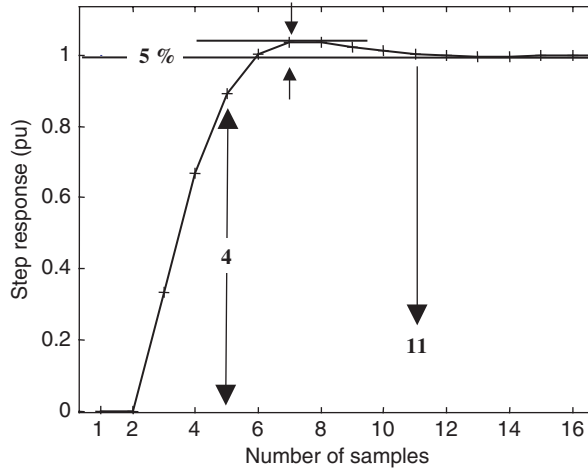
Fig. 8.23. Step response of the system with 4 samples of rising time, 11 of settling time in 1% band and 5% overshoot.
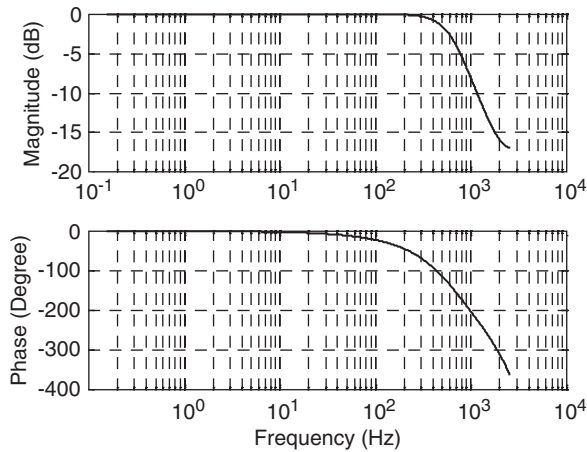
Fig. 8.24. Bode plot of the current controlled system.

in the overshoot (from 5 to 35%); but with $k_P = L/5T_s$ the poles are again critically damped as Figs. 8.26(b) and 8.27(b) show.

If there is a filter on the feedback current to cut-off the switching frequency ripple and the filter has a cut-off frequency of 2.5 kHz it will introduce approximately two T_s delays in the feedback loop in the position shown by Fig. 8.28. The effects are clear by Figs. 8.29(a) and 8.30(a) in terms in decrease of stability margin (the poles are only 0.1 damped), increase in the overshoot (from 5 to 70%). But by changing $k_P = L/7T_s$ the poles are again critically damped as Figs. 8.29(b) and 8.30(b) show.
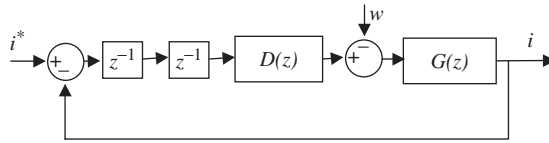
Fig. 8.25. Current control loop in the Z domain with one additional more caused by the microcontroller elaboration delay time.
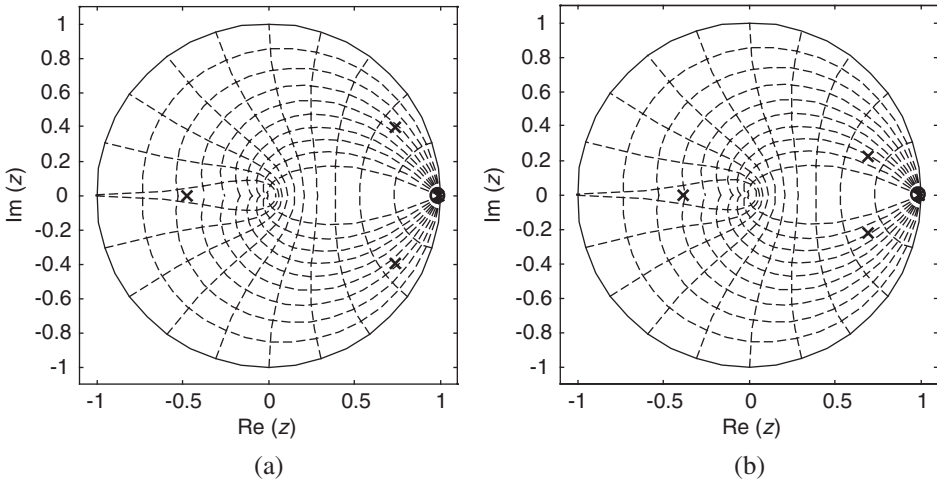
Fig. 8.26. Z plane root locus of the system if there is one additional delay in the feedback loop: the two poles damped 0.3 (a) and then damped again to 0.7 due to the change in k_P (b).
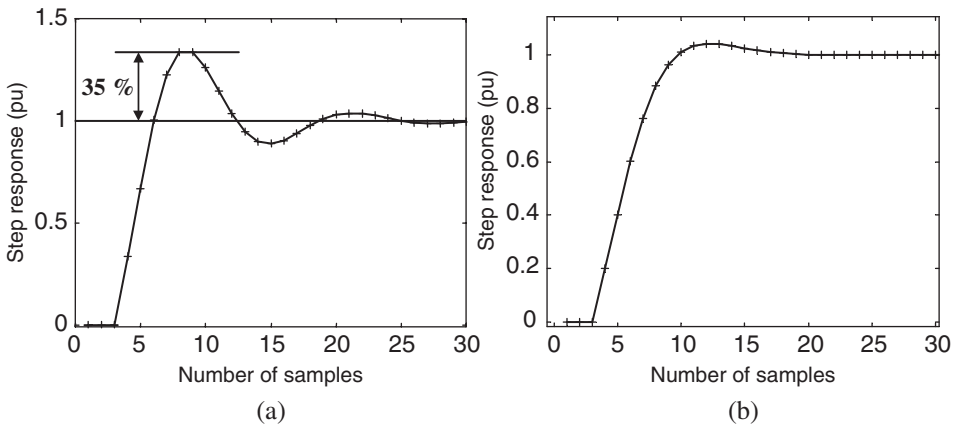
Fig. 8.27. Step response of the system if there are two additional delays in the feedback loop: 3 samples of rising time, 30 of settling time in 1% band and 35% overshoot (a) and 5 samples of rising time, 15 of settling time in 1% band and 5% overshoot with the new value of k_P (b).
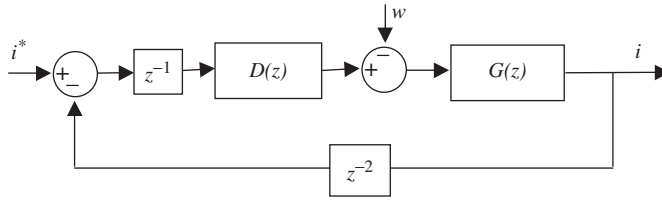
Fig. 8.28. Current control loop in the Z domain with two additional delays in the feedback loop.

(a)   (b)
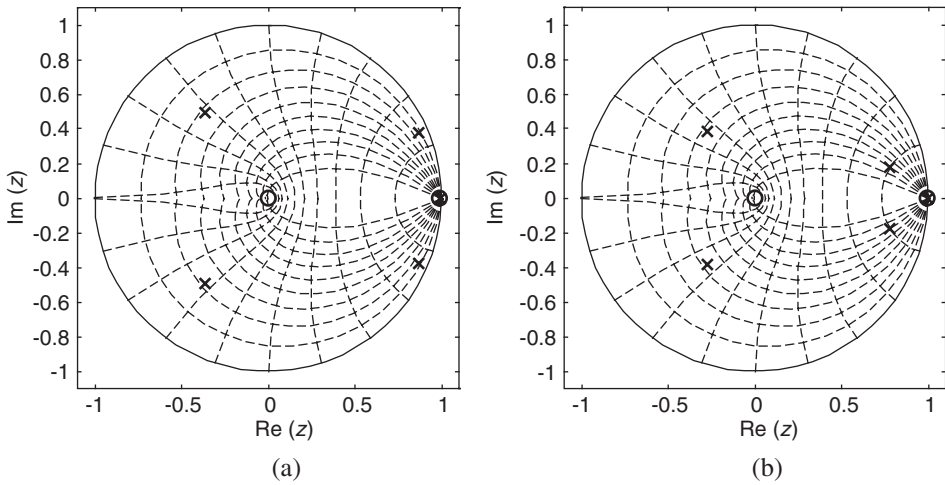
Fig. 8.29. *Z* plane root locus of the system if there are two additional delays in the feedback loop: the two poles damped 0.1 (a) and then damped again to 0.7 due to the change in k_P (b).

(a)   (b)
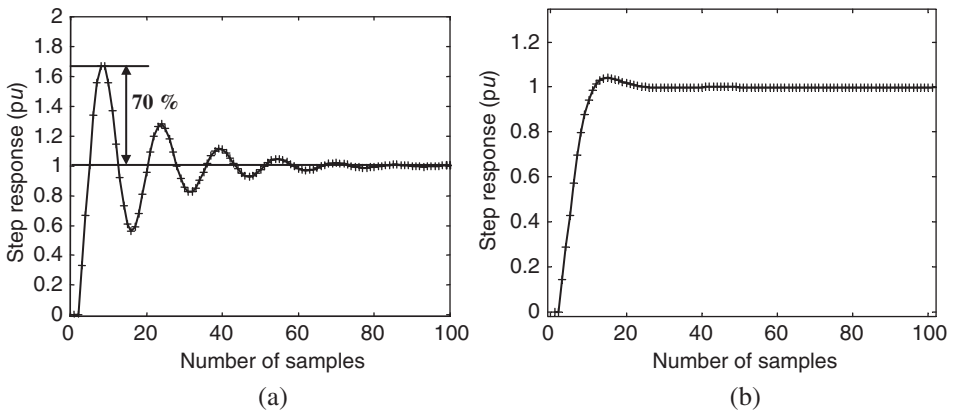
Fig. 8.30. Step response of the system if there are two additional delays in the feedback loop: 2 samples of rising time, 100 of settling time in 1% band and 70% overshoot (a) and 7 samples of rising time, 25 of settling time in 1% band and 5% overshoot with the new value of k_P (b).

8.6 Design Criteria for DC Voltage Control

In the active front-end converter system, both change in the load current and in the load voltage reference cause transient-operating conditions. Positive or negative variations of the voltage reference result in charge or discharge processes of the output capacitor. The increase in the load current results in voltage undershoot while its decrease results in voltage overshoot. So, from the point of view of the output voltage control, load current changes result in voltage variations that should be compensated by charge or discharge processes.

The DC voltage control is achieved through the control of the power exchanged by the converter. The increase or decrease in the DC voltage level is obtained, draining more or less power from the grid with respect to that one required by the DC side, thus changing the value of the reference for the AC current control loops.

Thus the voltage loop is the outer loop and the current loops are inner loops. These internal loops are designed to achieve short settling times. On the other hand, the main goals of the outer loop are optimum regulation and stability thus the voltage loop could be designed to be somewhat slower. Therefore, the internal and the external loops can be considered decoupled, and thereby, the actual grid current components can be considered equal to their references when designing the outer DC controller. However, during the active front-end converter start-up and under unbalance conditions (that lead to undesired low-frequency harmonics) this kind of decoupling is not valid and the inner and outer loops interact.

This interaction can cause high current overshoot that should be limited as much as possible. In fact, the current and voltage ratings of power devices for PWM converter are mainly chosen considering efficiency and safety operations. Hence, it is important to fully utilise the device capability to avoid under-utilisation that results in a non-cost-effective converter. On the other hand, the switch current cannot exceed the maximum current rating of the device because it can result in severe faults.

8.6.1 PI-based voltage control

Let us consider Eq. 8.13 with $i_q^*(t) = 0$:

$$\frac{dv_o(t)}{dt} = \frac{1}{C}\left\{\frac{3}{4}\left[S_d i_d^*(t)\right] - i_{DC}(t)\right\} \tag{8.31}$$

The DC voltage is controlled by means of the current $i_d^*(t)$. Instead the load current i_L could be seen as a disturbance signal, thus the plant of the system can be individuated as:

$$G(s) = \frac{3S_d}{4}\frac{1}{Cs} \tag{8.32}$$

The closed DC voltage loop is shown in Fig. 8.31.
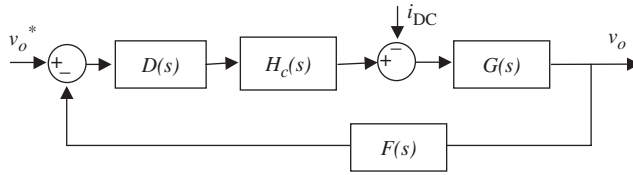
Fig. 8.31. Voltage control loop in S domain.

$F(s)$ is the filter that will be neglected now and considered at the end of the analysis. $H_c(s)$ is the current control closed loop transfer function. If the current controller is designed following the technical optimum, the transfer function can be approximated as:

$$H_c(s) \approx \frac{1}{1 + 3T_s s} \tag{8.33}$$

The controller can be written as:

$$D(s) = \frac{k_P (1 + T_I s)}{T_I s} \tag{8.34}$$

Thus the control loop can be redesigned as shown in Fig. 8.32.

The design of the PI controllers is done using the zero/pole placement in the Z plane aiming to obtain a better compromise possible between high dynamic performance of the DC output voltage and reduction in the AC current overshoot.

The method of "symmetrical optimum" (Leonhard *et al.*, 1997) is a standard design procedure for transfer functions containing a double integration when the controller is included such is the case of the DC voltage control open-loop transfer function:

$$H_{ov}(s) = \frac{3k_P(1 + T_I s)}{4S_d T_I s(1 + 3T_s s)\, Cs} \tag{8.35}$$

The main idea is to choose the cross-over frequency at the geometric mean of the two corner frequencies, in order to obtain maximum phase margin ψ which in turn will result in optimum damping of the DC voltage loop. Thus the Bode diagram shows symmetry with respect to the cross-over frequency ω_c.
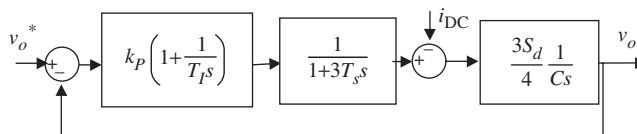
Fig. 8.32. Voltage control loop in S domain.

The cross-over frequency and the phase margin ψ are related by the following:

$$\omega_c = \frac{1}{3aT_s}$$

$$a = \frac{1 + \cos\psi}{\sin\psi} \quad (8.36)$$

$$a = \sqrt{\frac{T_I}{3T_s}}$$

The gain of the PI regulator at the cross-over frequency ω_c is given as:

$$k_P = \frac{4C}{9aS_dT_s} \quad (8.37)$$

Thus given the phase margin ψ or the constant a, the parameters of the PI controller are determined. The closed loop transfer function of the system is:

$$H_v(s) = \frac{(1 + T_I s)}{(3aT_s s + 1)\left(9a^2T_s^2 s^2 + 3(a-1)aT_s s + 1\right)} \quad (8.38)$$

The pair of complex poles of $H_v(s)$ result in a slightly underdamped response $\zeta = 0.7$ for $a = 2$. Thus:

$$k_P = 0.19 \cdot \frac{C}{S_dT_s}$$

$$T_I = 17 \cdot T_s \quad (8.39)$$

The bandwidth is expected to be:

$$f_{bv} = \frac{\omega_c}{2\pi} = \frac{1}{6\pi aT_s} \approx \frac{1}{50T_s} = \frac{f_s}{50} \quad (8.40)$$

due to the double integrating term in the open-loop transfer function, the closed DC voltage loop exhibits zero control area or zero voltage error. This means that the step response is characterised by considerable overshoot even though the transients are well damped. In order to eliminate this effect which is caused by the lead term of the PI controller, a corresponding lag term could be added on the reference signal:

$$H_v(s) = \frac{1}{1 + T_I s} \quad (8.41)$$

8.6.2 PI-based voltage control design example

Let us consider a system with $R = 0.3\,\Omega$, $L = 8$ mH on the AC side, $C = 500\,\mu\text{F}$ on the DC side and sampling frequency equal to 5 kHz, 700 V reference for the DC bus,

5.5 A of rated DC current. It is assumed that the current control poles are optimally damped.

If the grid phase voltage has a maximum amplitude of 310 V and the input filter causes approximately a voltage drop of 10%, in rated conditions the average converter voltage will be 280 V which means that S_d is 0.8. If the design of the PI controller is made following the rules expressed in the Section 8.6.1. then $k_P = 0.59$ and $T_I = 0.003$. With these values the cross-over frequency should be 100 Hz, the phase margin 40° and the open-loop Bode plot should be symmetric, as shown in Fig. 8.33.

The system step response is shown in Fig. 8.34(a). Usually the DC voltage is kept constant so the overshoot can be a problem only at start-up. In that case some special procedures can be adopted like limiting the rate of change of the DC voltage reference. However, introducing the lag network of Eq. 8.41 the overshoot reduces to 5%, as shown in Fig. 8.34(b). The closed loop Bode plot (Fig. 8.35) shows that the bandwidth is 100 Hz as it could be predicted with Eq. 8.40.

If a filter on the feedback voltage with a cut-off frequency of 2.5 kHz is adopted without considering it in the controller design, the system experiences a higher overshoot and an oscillatory transient, as shown in Fig. 8.36(a). If the delay in the period for the 6 samples introduced by the 2.5 kHz filter is considered in the design this leads to $T_I = 0.01$ modifying Eq. 8.36. The result is shown in Fig. 8.36(b) with the 40% overshoot but with a slow down of the system.
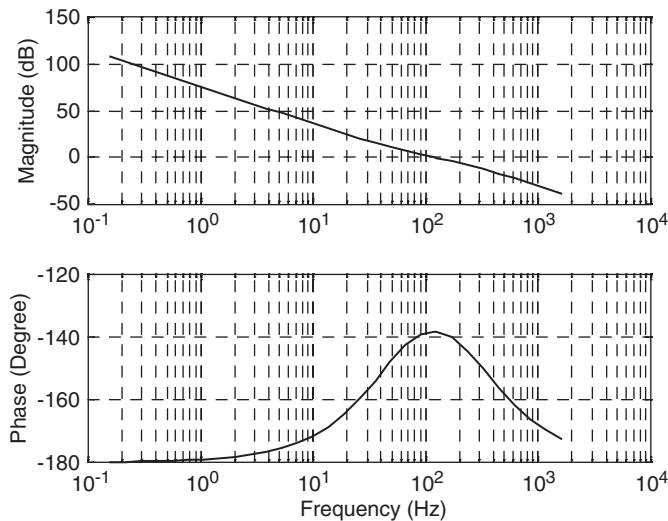
Fig. 8.33. Bode plot of the voltage open loop.
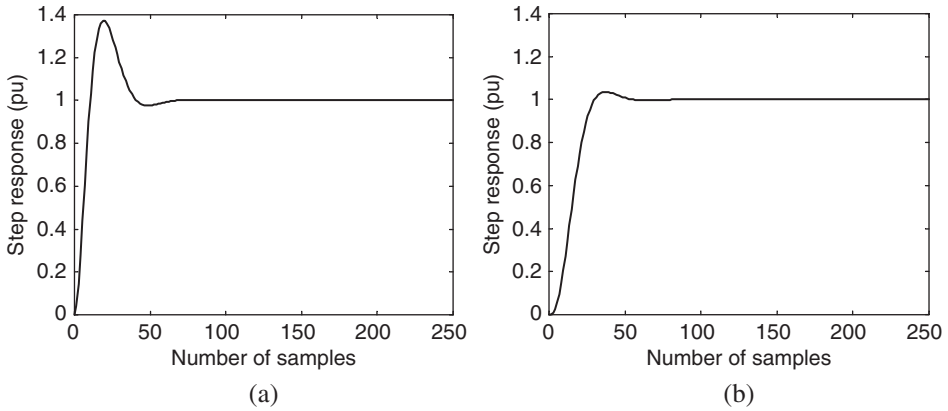
Fig. 8.34. Step response of the system without (a) and with (b) a lag network on the reference signal.
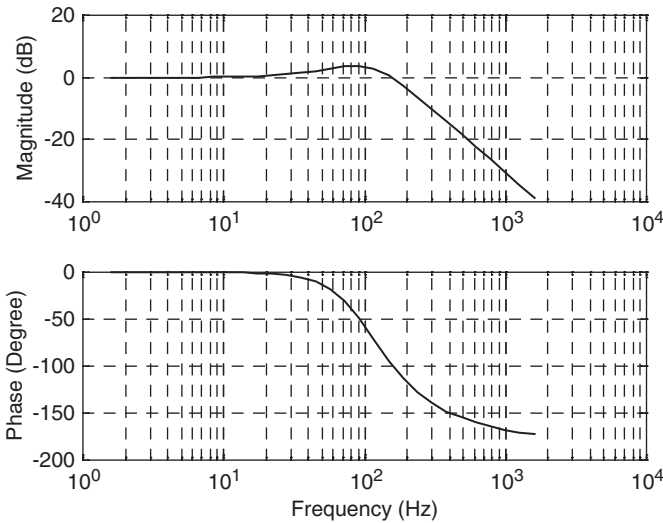
Fig. 8.35. Bode plot of the voltage closed loop.

8.7 Non-Ideal Operating Conditions

The non-ideal operating conditions lead to the generation of harmonics that influence both the active front-end converter input and output thus both AC and DC controls. Generally, these low-frequency harmonics become particularly dangerous because the design of the loops is based on the hypothesis that they are decoupled, due to the difference in the time constants, and thus it is possible to linearise them.
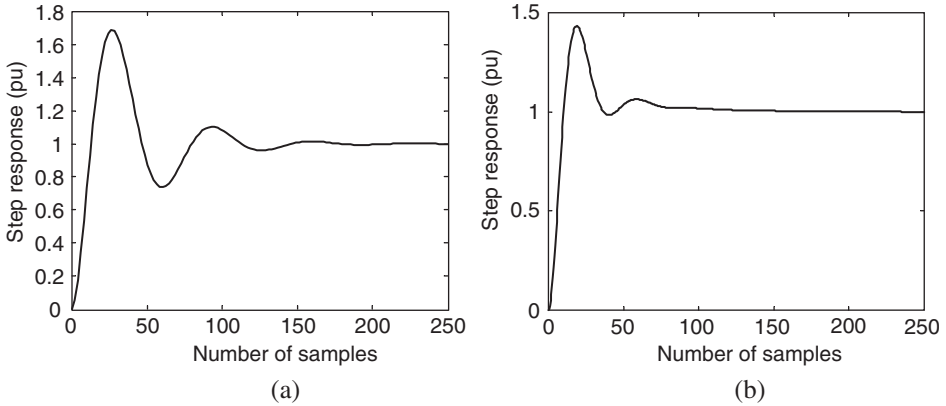
Fig. 8.36. Step response of the system with 80% overshoot and oscillations due to the filter (not considered in the design) on the feedback signal (a) and 40% overshoot if the filter is considered in the design (b).

The current control loop is designed considering constant DC voltage due to the slowness of the voltage loop. Moreover, the load changes produce transients in the voltage loop suffering only a little the consequent transient of the current loop that is faster. However, low-order harmonics contradict both of these considerations. In fact if the DC voltage has a low-frequency ripple it cannot be considered constant for the current loop design. In the following sections, each of the phenomena considered is analysed.

8.7.1 Delays

The presence of delays in the control loops is quite common and can be caused by too long computation time or the presence of filters on the feedback signals. Generally, if a symmetrical PWM modulation is adopted the sampled currents during zero vector on-time are ripple-free. Thus the filters adopted on the currents are only needed to cut high-frequency spikes and they introduce only little delays. On the contrary, if the elaboration time of the algorithm takes more than one sampling period the modulator input cannot be refreshed at the end of the period. Thus, if the system has been designed to refresh the duty cycle every sample period, one additional T_s is introduced in the loop (Fig. 8.25). The effects are decrease of stability margin and increase of the overshoot.

8.7.2 Grid unbalance

The grid voltage unbalance can be modelled considering an inverse sequence in the grid voltages that generate an inverse sequence in the grid current (Moran *et al.*, 1992). Balanced grid voltages and unbalance phase impedances can also cause this effect. Thus:

$$\bar{i}(t) = \bar{i}_p(t) + \bar{i}_n(t), \tag{8.42}$$

where the subscripts "p" and "n" address the positive and negative sequences of the electrical quantities.

Starting from the positive and negative sequences in the input AC currents one can demonstrate the presence of even harmonics in the DC current that create even harmonics in the DC voltage.

Let us introduce the switching functions:

$$p_a(t) = \sum_{m=1}^{\infty} A_{ma} \cos[m(\omega t + \varphi_a)]$$

$$p_b(t) = \sum_{m=1}^{\infty} A_{mb} \cos\left[m\left(\omega t - \frac{2\pi}{3} + \varphi_b\right)\right] \tag{8.43}$$

$$p_c(t) = \sum_{m=1}^{\infty} A_{mc} \cos\left[m\left(\omega t + \frac{2\pi}{3} + \varphi_c\right)\right]$$

If the VSC is driven in order to generate balanced voltages then:

$$A_{ma} = A_{mb} = A_{mc} = A_m \tag{8.44}$$

Moreover to have the maximum output DC voltage:

$$\varphi_a = \varphi_b = \varphi_c = 0 \tag{8.45}$$

The current fed by the VSC on the DC side is:

$$i_o(t) = \frac{3}{4}\text{Re}\left\{\bar{p}(t)\,\overset{\vee}{\bar{i}}(t)\right\} = i_o^p(t) + i_o^n(t), \tag{8.46}$$

where

$$i_o^p(t) = \frac{3}{4}\text{Re}\left\{\bar{p}(t)\,\overset{\vee}{\bar{i}}_p(t)\right\}$$

$$i_o^n(t) = \frac{3}{4}\text{Re}\left\{\bar{p}(t)\,\overset{\vee}{\bar{i}}_n(t)\right\} \tag{8.47}$$

then substituting Eqs. 8.42 and 8.43 in Eq. 8.46 and considering the effect of the interaction of the first harmonic of the switching function with the positive and negative sequences of the grid current:

$$i_o(t) = I_o + I_{o2}\cos(2\omega t + \varphi_n), \tag{8.48}$$

where

$$I_o = \frac{3}{4}\sqrt{2}A_1 I_p \cos\varphi_p$$

$$I_{o2} = \frac{3}{4}\sqrt{2}A_1 I_n$$

the second part of Eq. 8.48 is one of the most dangerous low-frequency harmonics in $i_o(t)$. This second harmonic comes from the interaction of the fundamental component of the switching vector $\bar{p}(t)$ and the fundamental component of the inverse current. Assuming a linear DC load, if the DC current $i_o(t)$ has a second-order harmonic also the DC voltage ripples at the same frequency:

$$v_o(t) = V_o + V_{o2}\cos(2\omega t + \varphi_2). \tag{8.49}$$

However the grid current is also a function of the DC voltage. The interaction of the fundamental component of the switching vector $\bar{p}(t)$ with the second-order harmonic of the DC voltage creates a third-order harmonic in the reflected input voltage, which allows a third-order (not zero sequence) harmonic current to flow into the grid.

In fact, the converter AC side voltage due to the first harmonic of the switching function is:

$$v_a(t)|_{p_{a1}} = \frac{1}{2}v_o(t)A\cos(\omega t) \tag{8.50}$$

from Eqs. 8.49 and 8.50:

$$v_a(t)|_{p_{a1}} = \frac{1}{2}V_o A\cos(\omega t) + \frac{1}{4}V_{o2}A\cos(3\omega t + \varphi_3) \tag{8.51}$$

The second part of Eq. 8.51 produces a third harmonic also in the grid current.

8.7.3 Position of the grid sensors

If the grid voltage that is used for the *dq* frame orientation is measured after a not negligible reactance, the grid current produces a voltage drop. Consequently, a derivative action is inserted in the system leading to oscillations characterised by even harmonic content in the current and odd harmonic content in the DC voltage.

8.7.4 Passive damping of the LCL filter

If a LCL filter is used on the AC side, the use of a passive damping in series with the capacitors leads the poles of the current closed loop to be more damped thus the system suffers a slow down. Moreover also a low-frequency oscillation both in the AC current and in the DC voltage is produced.

8.8 Conclusions

The main advantages of the active front-end are sinusoidal input current, unity power factor, regenerative operation, active and reactive power control, controllability of the DC link and also a limited voltage sag ride-through capability.

Non-ideal operating conditions, such as the presence of acquisition filters, AC grid unbalance and passive damping if a LCL filter is used, can substantially decrease active front-end performances. The phenomena generated by these conditions are generally non-linear. In short the effect of delays due to filters is dangerous current overshoot, the effects of unbalance are an increasing ripple in the DC voltage and the effects of passive damping are reduced efficiency and dynamics. These problems can be solved with more complex controllers or they can be reduced by increasing the value of the DC capacitor and adapting the parameters of the PI controllers. Moreover, the size of the capacitive storage in the DC link increases the load ride-through protection during utility voltage dip events.

In conclusion, main drawbacks in the use of the active front-ends are: higher costs with respect to line-commutated front-end solutions; lower reliability due to the complexity of the device compared to a conventional rectifier; residual low-frequency harmonics and inter-harmonics in the case of inadequate control; odd harmonics on the AC side and even harmonics on the DC side in grid unbalance conditions.

Acknowledgement

References

Agirman I., Blasko V., "A novel control method of a VSC without AC line voltage sensors," IEEE Trans. Ind. Appl., **39** (2003) 519–524.

Blaabjerg F., Chen Z., Kjaer S.B., "Power electronics as efficient interface in dispersed power generation systems," IEEE Trans. Power Elect., **19(5)** (2004) 1184–1194.

Blasko V., Kaura V., "A new mathematical model and control of a three-phase AC-DC voltage source converter," IEEE Trans. Power Elect., **12** (1997) 116–123.

Cecati C., Dell'Aquila A., Liserre M., Ometto A., "A fuzzy logic-based controller for active rectifier," IEEE Trans. Ind. Appl., **39(1)** (2003) 105–112.

Cecati C., Dell'Aquila A., Lecci A., Liserre M., "Implementation issues of a fuzzy-logic-based three-phase active rectifier employing only voltage sensors," IEEE Trans. Ind. Elect., **39** (2005) 378–385.

Jahns T.M., Blasko V., "Recent advances in power electronics technology for industrial and traction machine drives," Proc. IEEE, **89** (2001) 963–975.

Kazmierkowski P., Krishnan R., Blaabjerg F., *Control in power electronics*, Academic Press, 2002.

Kolar J.W., Ertl H., "Status of the techniques of three-phase rectifier systems with low effects on the mains," Proc. INTELEC'99, **14(1)** 1999.

Komurcugil H., Kukrer O., "A novel current-control method for three-phase PWM AC/DC voltage-source converters," IEEE Trans. Ind. Elect., **46** (1999) 544–553.

Krein P.T., Bentsman J., Bass R.M., Lesieutre B.L., "On the use of averaging for the analysis of power electronics systems," IEEE Trans. Power Elect., **5** (1990) 182–190.

Leonhard W., *Control of electrical drives*, Springer, New York, 1997.

Liserre M., Blaabjerg F., Hansen S., "Design and control of an LCL-filter based active front-end converter," IEEE Trans. Ind. App., **41** (2005) 1129–1135.

Moran L., Ziogas P.D., Joos G., "Design aspects of synchronous PWM rectifier-inverter system under unbalanced input voltage conditions", IEEE Trans. Ind. Appl., **28** (1992) 1286–1293.

Ohnishi T., "Three phase PWM converter/inverter by means of instantaneous active and reactive power control" Proc. IECON, **91** (1991) 819–824.

Zargari N.R., Joos G., "A near unity power factor input stage with minimum control requirements for AC drive applications," IEEE Trans. Ind. Appl., **31** (1995) 1129–1135.

CHAPTER 9

Adjoint Network Theory to Analyse the Power Converters with Respect to their Line-side Behaviour

Silvano Vergura, Marco Liserre, and Francesco Vacca

Abstract

The aim of this chapter is to offer a straightforward approach for the sensitivity analysis of the line-side connected converters with respect to the variation of their parameters. The sensitivity analysis is carried out based on the adjoint network theory which allows to study the variation of an electrical quantity with respect to the perturbation of any circuit parameter, considering only one circuit (just the adjoint network) besides the one assigned. As the control of a converter plays an important role in the propagation of the harmonics in the circuit, it is necessary to implement a detailed model of the controller too. Starting from the requirements of the digital controller, an analogue circuit (the so-called virtual circuit), able to represent the behaviour of the controller, is synthesised. Substituting the controller with the virtual circuit, an analogue network, representing the power converter and its control, is obtained. This homogenous model allows a rigorous and straightforward sensitivity analysis.

9.1 Introduction

The front-end power converter stage of the most widely used line-connected systems in industrial and consumer applications has always been a line-commutated converter. The main effects of such converters on the line have been the production of low frequency harmonics and the low power factor.

As a consequence to the introduction of more stringent standards, recommendations and codes on the maximum allowable low frequency disturbances, these systems have been
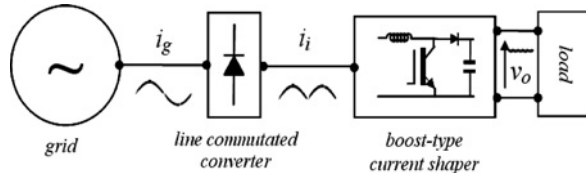
Fig. 9.1. Boost-type power factor corrector.

modified, replaced or compensated with other devices. In the first case, more common in low power consumer applications, a second power converter stage has been added with the aim to shape the drained current of the overall equipment and to make it compliant with standards. This is the case of the so-called Power Factor Corrector (PFC) (Fig. 9.1). In the second case (Fig. 9.2(a)), the line-connected stage has been replaced by a self-commutated power converter, called "active rectifier" due to its capability to be more immune to disturbances). In the third case (Fig. 9.2(b)), a shunt or series connected converter, called "active filter", has been added in order to compensate the disturbances. The converters adopted in these cases, often employing PWM modulation, were already used in applications such as industrial motor drives, robotics, air conditioning and electric vehicles (Bose, 2001).

Therefore in the last ten years, voltage source and current source PWM converters have been considered also as prime candidates in line front-end applications. However the use of current source inverters has been quite limited because they require several devices producing a large amount of conduction losses, sluggish transient response and high cost (Bose, 2001). There has been a clear preference for the voltage source configuration with respect to the current source one in a wide range of applications. The attention of the researchers in the field of voltage source converters, has been recently focused
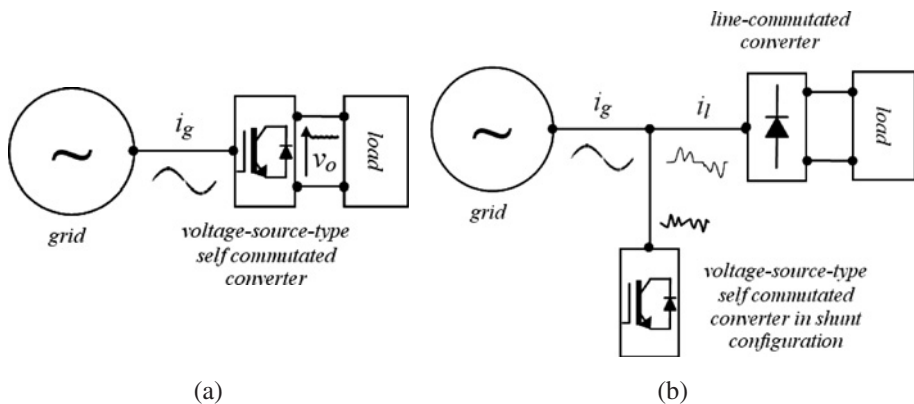
Fig. 9.2. Active front-end solution: (a) substitution of the polluting stage; (b) compensation of the polluting stage.

on the converter control respect to the AC filters. The main topics are: short-circuit and over-load protection, stability, low dependence of the performances on the system parameters and low switching frequency emission not to disturb other EMI sensitive loads connected to the line.

Particularly the AC Current Control (CC) has been considered suitable for all the applications of voltage source converters because the current controlled converter exhibits, in general, better safety and stability performance and faster response (Kazmierkowski *et al.*, 2002). Moreover the CC is crucial especially in applications like active rectifiers and active filters, where current should be regulated to obtain the desired active and reactive power and to minimise and/or compensate the line power factor and the current harmonics.

On the other hand, the DC voltage control is a key topic especially for active filters and rectifiers where the DC bus is not generally fed by a power converter stage as in classical diode-rectifier front-end-type PWM-VSI induction motor drive. There are only few exceptions like active filters connected directly to the DC bus of the polluting drive. Unfortunately, the DC voltage control cannot be treated as a separate topic with respect to the CC because the two control strategies interact.

The use of an AC filter claims a proper design procedure and deep dynamic and stability analysis (Liserre *et al.*, 2004). In applications where active rectifiers and filters are present, the use of a line side LCL-filter reduces the possibility of interference, caused by the PWM ripple, with other EMI-sensitive parallel connected loads. But the LCL-filter can also become a key point in the tracking capability of the active filter and so, in the CC performance improvement.

In conclusion, both AC current/DC voltage control and AC filter topics are appropriate subjects with a wide range of applications of the three-phase voltage source converter. They need advanced design and control techniques.

This chapter introduces a global approach to the analysis of the line behaviour of the current controlled PWM voltage source type self-commutated converter using the circuit theory (Blaabjerg *et al.*, 2004). The proposed approach can be easily adopted for a wide range of applications (active rectifier, active filter, front-end stage of distributed generation systems). This approach is straightforward but it does not neglect anything of both the physical system and the digital controller. In fact two different models are usually used for the evaluation of the CC of the converter (the capacitor of the LCL-filter is neglected) and for the LCL-filter effectiveness (line voltage is neglected). Then through simulations, the interaction between the two models is evaluated. On the contrary, with the proposed approach, a virtual circuit is combined with the real one and a sensitivity analysis can be done with respect to the controller as well as with respect to the filter parameters.

9.2 VSC Power Converters Connected to the Line

In Fig. 9.3, the system under investigation is reported: a Voltage Source Converter (VSC) employing six bidirectional switches (each one with turn off capability
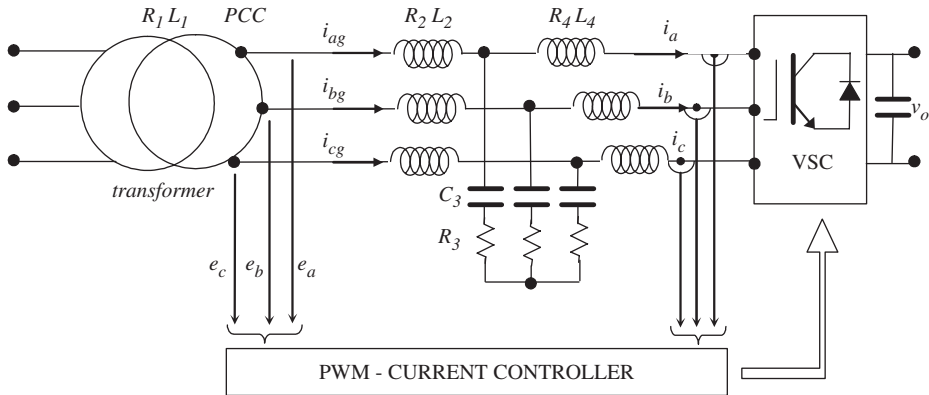
Fig. 9.3. Three-phase active rectifier with LCL-filter.

and anti-parallel diode) works as an active rectifier feeding a DC-bus, the voltage of which is v_0; the VSC is connected on its AC side to a transformer at the Point of Common Coupling (PCC) through an LCL-filter.

There are two passive stages on the AC side and on the DC side, respectively. The AC passive stage has mainly a filtering function while the DC passive stage has both the storage function and the filtering function.

In Fig. 9.3, only the PWM current controller of the VSC is highlighted: the PWM signal is generated by the controller on the basis of the line voltages across the PCC and of the currents flowing through the converter (the current sensors are usually embedded in the industrial converters).

It should be noted that:

- only the most relevant physical nature of the passive elements has been highlighted (for example the resistive nature has been neglected);

- the common mode EMI filters (usually some capacitors) have been omitted; and

- in the DC stage, some inductive elements could also be present but their role could be neglected with respect to the main capacitive element.

For the analysis developed in the chapter it will be assumed that:

- the passive elements are Linear Time Invariant (LTI);

- the converter switches are ideal; and

- the connections are ideal.

9.3 Modelling of the Current Controlled Voltage Source Converter with the "Virtual Circuit" Approach

The voltage source converter generates a voltage $v'(t)$ resulting from the control $v(t)$ and a term $v_{PWM}(t)$ expressing the harmonics generated by the switching. In the following, the first term $v(t)$, which depends on the line voltage $e(t)$ and by the converter current $i(t)$, will be modeled by means of a "virtual circuit" with R–L–C elements and controlled sources.

The first step is to analyse the control structure reported in Fig. 9.4 in the S-domain.

The line voltage $E(s)$ measured at the PCC, once filtered through $1/(1 + nT_s \cdot s)$ (T_s being the sampling period of the digital control and n the number of sampling periods), is used as a template to generate the reference current. In fact, $E(s)/R_b$ is the desired current that the converter has to absorb in order to have unity power factor and the highest possible efficiency, whereas R_b is the base resistance of the system and corresponds to the rated power:

$$R_b = E_n^2/P_n \qquad (9.1)$$

here E_n and P_n are the AC-rated voltage and AC-rated power respectively.

Then all the following analysis has been conducted under rated conditions but it can be easily extended to other load conditions such as 1/3 or 2/3 of the rated power by simply substituting the terms $E(s)/3R_b$ or $2E(s)/3R_b$ for $E(s)/R_b$.

The feedback current $I(s)$, also filtered through $1/(1 + nT_s \cdot s)$ is subtracted from the reference current in order to have the current error which feeds the PI controller (k_P and k_I are the proportional and the integral gain, respectively). The filtered line voltage is summed to the output of the PI controller in order to have a feedforward compensation of the line voltage neglected in the plant of the system used to tune the PI (Liserre *et al.*, 2005). It should be noted that the filter $1/(1 + nT_s \cdot s)$ takes also into consideration one sampling period delay, due to the calculation of the digital system, and half period delay, due to the PWM modulation (Blasko and Kaura, 1997); thus the cut-off frequency
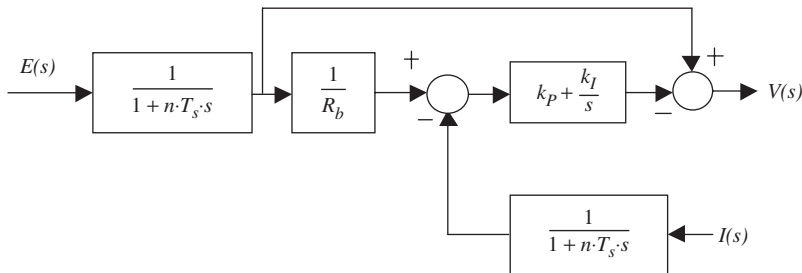
Fig. 9.4. Block diagram representation of the control system for the active rectifier.

of the filter is approximately $1/[(n-1.5)\,T_s]$. Once fixed, the sampling frequency of the controller and once tuned, for the filters, the proportional and integral gains can be calculated in order to have the "technical optimum" for the current control loop (Liserre *et al.*, 2005).

In Fig. 9.4, $V(s)$ and $I(s)$ are the S-transformed converter voltage and current, respectively, related as

$$V(s) = E(s) \cdot \frac{1}{1 + n \cdot T_s \cdot s} - \left(k_P + \frac{k_I}{s}\right) \cdot \frac{1}{1 + n \cdot T_s \cdot s} \cdot \left[\frac{E(s)}{R_b} - I(s)\right] \quad (9.2)$$

Equation 9.2 can be considered as KVL (Kirchhoff Voltage Law) applied to a bipolar component.

The first addendum of the right-hand side in Eq. 9.2 can be modeled as a voltage divider; particularly, if an R–L series bipolar component (with $R = 1[\Omega]$ and $L = n \cdot T_s\,[H]$) is considered in conjunction with a voltage source $E(s)$, it represents the voltage across the 1-ohm resistor, $E_f(s)$. Moreover the voltage source $E(s)$ is the voltage at the PCC. Hence, the first addendum of Eq. 9.2 can be considered as the voltage across the resistor R of an R–L series fed by a voltage-controlled voltage source.

The second addendum of Eq. 9.2 can be modeled as the voltage drop across an impedance to be synthesised, in which the current $[(E(s)/R_b) - I(s)]$ flows.

In order to synthesise the impedance

$$\dot{Z}(s) = \left(k_P + \frac{k_I}{s}\right) \cdot \frac{1}{1 + n \cdot T_s \cdot s} \quad (9.3)$$

the general theory on the synthesis of the driving-point function of the passive networks (Kendall, 1996) can be applied.

Rearranging Eq. 9.3, it is easy to obtain

$$\dot{Z}(s) = \frac{(k_P/n \cdot T_s) \cdot s + (k_I/n \cdot T_s)}{s \cdot (s + (1/n \cdot T_s))} \quad (9.4)$$

and then

$$\dot{Z}(s) = \frac{1}{(n \cdot T_s/k_P) \cdot s + (n \cdot T_s/k_P) \cdot \left(\dfrac{h \cdot s}{(k_P/n \cdot T_s) \cdot s + (k_I/n \cdot T_s)}\right)} \quad (9.5)$$

where $h = (k_P/n \cdot T_s) \cdot (1/n \cdot T_s) - (k_I/n \cdot T_s)$.

The denominator of Eq. 9.5 is clearly an admittance; the first addendum, representing an $n \cdot T_s/k_P$ – i.e. a value equal to capacitor C_{1C}, is in parallel with the second addendum.

Equation 9.5 can be re-written as

$$\dot{Z}(s) = \frac{1}{C_{1C} \cdot s + \dot{Y}_1(s)} \tag{9.6}$$

$\dot{Y}_1(s)$ can be re-arranged as

$$\dot{Y}_1(s) = \frac{1}{(1/h) \cdot (k_P^2/n^2 \cdot T_s^2) + (1/h) \cdot (k_I \cdot k_P/n^2 \cdot T_s^2) \cdot (1/s)} \tag{9.7}$$

The denominator of Eq. 9.7 is clearly an impedance; first addendum, representing a $(1/h) \cdot (k_P^2/n^2 \cdot T_s^2)$ – i.e. a value equal to resistor R_{1C}, is in series with an $h \cdot (n^2 \cdot T_s^2/k_I \cdot k_P)$ – i.e. the value of capacitor C_{2C}.

This procedure in synthesising the analogue filter is noted as *Cauer 1-realization* (Kendall, 1996) and the subscript of the synthesised components indicates just this realisation procedure. Figure 9.5 reports the synthesised impedance, whereas Table 9.1 reports the formulae which allow to obtain the values of the analogue components from the values of the controller parameters.

Finally, connecting in series the two previously synthesised components, a simple analogue circuit (Fig. 9.6), representing the overall control system, is obtained and it represents the *virtual circuit* introduced earlier.

At this point, the voltage source $V(s)$, can be substituted with that from the previous model (Fig. 9.7). The *virtual circuit* obtained by the synthesis can be easily interpreted. The current $I(s)$ absorbed by the active rectifier is the sum of a term which depends on the line voltage and a term which depends on the difference between the line voltage and the converter voltage.

Table 9.1. Bipolar component parameters.

R_{1C}	C_{1C}	C_{2C}
$\dfrac{k_P^2}{k_P - n \cdot T_s \cdot k_I}$	$n \cdot \dfrac{T_s}{k_P}$	$\dfrac{k_P - n \cdot T_s \cdot k_I}{k_P \cdot k_I}$
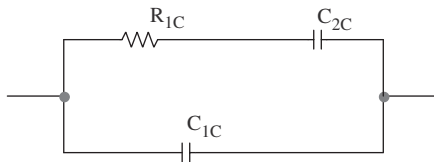
Fig. 9.5. Synthesised impedance of second addendum of Eq. 9.2.
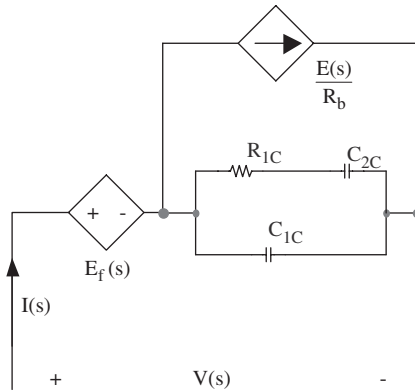
Fig. 9.6. *Virtual circuit* representation of the control system.

In greater detail, the first one is $E(s)/R_b$ which, as previously highlighted, is the ideal current that the converter should absorb; the other current is due to the current control dynamics and it results in $V(s) - E_f(s)$, i.e. by the difference between the two voltage sources present in the circuit. It is interesting to note that the core of this action is the impedance synthesised with the Cauer approach and reported in Fig. 9.5 and it depends not only on the PI parameters but also on the load conditions. Even if the bipolar component acts on the dynamics of the system, it is a filter and then it has also an important role in the propagation of the harmonics in the circuit as will be shown by the following analysis.
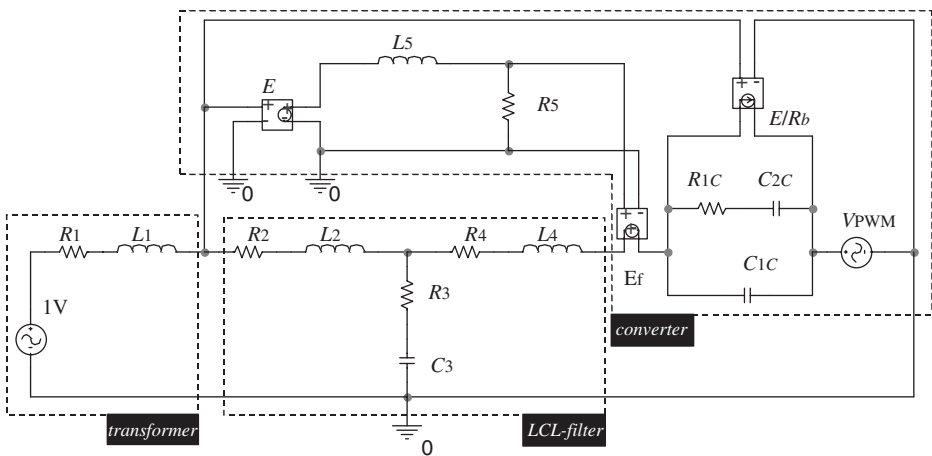
Fig. 9.7. Circuit for sensitivity analysis: the virtual circuit of Fig. 9.6 has been inserted in the role of voltage source converter.

9.4 Sensitivity Analysis in the Frequency Domain

9.4.1 Basic definitions

It is very important to know the effects on the system performances due to the variations of some system parameters (Chua and Lin, 1975). In the case of lumped, linear, time-invariant networks, a significant measure of this correlation can be expressed as "sensitivity" of the output variable with respect to the assigned parameter. This is usually called *absolute sensitivity* or *sensitivity coefficient* and is indicated as:

$$S_p = \frac{\delta Y}{\delta p} \tag{9.8}$$

where Y and p are the values of the output variable and of the parameter, respectively. Nevertheless, to compare several sensitivities it is of major interest to consider the *relative* (*or normalised*) *sensitivity*:

$$S_p^Y = \frac{(\delta Y/Y)}{(\delta p/p)} = \frac{p}{Y} \cdot \frac{\delta Y}{\delta p} \tag{9.9}$$

By observing Eqs. 9.8 and 9.9, it is obvious that the simplest way to calculate the sensitivity (indifferently absolute or relative) is to extract the relationship between the output variable Y and the under-test parameter p, and then to calculate the derivative. Unfortunately this approach is applicable only for simple linear circuits; then, more efficient and robust methods must be considered.

At least two circuit analyses would be usually needed to compute one sensitivity (Chua and Lin, 1975; Litovski and Zwolinski, 1997). The former one is related to the *original circuit*, i.e. to the circuit with all nominal parameters; the latter one is related to the *perturbed circuit* in which the value of the under-test parameter is changed by Δp. This last circuit is called *incremental network*, whereas its response will be $Y(p + \Delta p)$. The sensitivity can be approximated by

$$S_p = \frac{Y(p + \Delta p) - Y(p)}{\Delta p} \tag{9.10}$$

provided that Δp is sufficiently small (approaching zero, theoretically) and that second-order effects can be neglected.

If a multi-parameter sensitivity is required (i.e. more than one parameter changes its value), $(k + 1)$ circuits have to be analysed. Obviously the first one is again the nominal circuit, whereas each one of the incremental k-circuits is used to evaluate $Y_k(p_k + \Delta p_k)$. Then by applying Eq. 9.10 for k times, k sensitivities will be obtained. This method is inefficient (k circuits to be analysed for k sensitivities to be computed) and inaccurate if Δp is not sufficiently small.

In this chapter, in order to overcome earlier drawbacks, the theory of the adjoint network (Director and Rohrer, 1969), based on Tellegen's theorem (Tellegen, 1952), is used.

This approach requires only one adjoint network to compute the sensitivity of the output variable with respect to each one of the circuit parameters.

Moreover, when steady state AC analysis of linear dynamic circuits is considered, complex-domain variables are used ($\overline{V}$ for voltages, $\overline{I}$ for currents, $\dot{Z}$ for impedances, etc.). Then both the absolute and relative sensitivities will also be complex.

9.4.2 Application of the adjoint network

The first step in applying the *theory of the adjoint network* is to determine the *topology* of the adjoint network and the *typology* of each one of its components. Let N and $\widehat{N}$ be the original and the adjoint network, respectively.

The topology of $\widehat{N}$ is the same as that of N; as a matter of fact Tellegen's theorem is just based on two circuits having the same topologies.

The typology of each component of $\widehat{N}$ is derived by N applying the following rules (Litovski and Zwolinski, 1997):

(1) zero-valued voltage sources (short-circuits) in $\widehat{N}$ have to be considered for the voltage sources in N, at the equivalent ports;

(2) zero-valued current sources (open-circuits) in $\widehat{N}$ have to be considered for the current sources in N, at the equivalent ports;

(3) passive elements remain the same, as indicated in Table 9.2;

(4) controlled-sources in $\widehat{N}$ (all four types) are obtained as indicated in Table 9.2.

The second step consists in determining the *excitation* of the adjoint network. Particularly:

- if sensitivity of an output voltage has to be computed, a 1-A current source is connected to the corresponding port in $\widehat{N}$;

- if sensitivity of an output current has to be computed, a (-1)-V voltage source is connected to the corresponding port in $\widehat{N}$.

Since the analysis of the line current sensitivity with respect to some parameters of the circuit in Fig. 9.7 is of concern, only the second one of the previous options will be considered.

Then the adjoint network of Fig. 9.7 can be easily obtained (Fig. 9.8).

Table 9.2 reports the corresponding components between the original and adjoint networks, whereas the last column represents the sensitivity coefficient in frequency-domain with respect to the parameter indicated as subscript. Obviously, the dot above the letter S indicates that it is a complex number.

Table 9.2. Components in original and adjoint network.

Original network	Adjoint network	Sensitivity coefficient
R $\square$—WW—$\square$	R $\square$—WW—$\square$	$\dot{S}_R = -\overline{I}_R \cdot \widehat{I}_R$
L $\square$—mmm—$\square$	L $\square$—mmm—$\square$	$\dot{S}_L = -j\omega \cdot \overline{I}_L \cdot \widehat{I}_L$
C $\square$—||—$\square$	C $\square$—||—$\square$	$\dot{S}_C = j\omega \cdot \overline{V}_C \cdot \widehat{V}_C$
V_{12}, $g_m V_{12}$	$g_m V_{34}$, V_{34}	$\dot{S}_{gm} = -\overline{V}_{12} \cdot \widehat{V}_{34}$
V_{12}, kV_{12}	$-kI_b$, I_b	$\dot{S}_k = \overline{V}_{12} \cdot \widehat{I}_b$
I_a, $r_m I_a$	$r_m I_b$, I_b	$\dot{S}_{rm} = \overline{I}_a \cdot \widehat{I}_b$
I_a, kI_a	$-kV_{34}$, V_{34}	$\dot{S}_k = -\overline{I}_a \cdot \widehat{V}_{34}$

Fig. 9.8. Adjoint circuit for sensitivity analysis.

9.5 Sensitivity Analysis Based on the Adjoint Circuit: Case Study

Table 9.3 reports the numerical values of the controller needed to synthesise the "virtual circuit", while Table 9.4 reports the numerical values of the passive components. Since the rated active power is 4.5 kW@230 Vrms, the base resistance will be $R_b = 35\Omega$ (Liserre *et al.*, 2005). The simulations have been carried out in PSpice-ORCAD®.

In a real situation, the line voltage could be considerably distorted due to the presence of other loads connected at the same PCC, or due to phase unbalance conditions that can result in the production of low frequency odd harmonics (Moran *et al.*, 1992) or due to converter non-linear phenomena. The first cause is due to the fact that if another load is connected to the same transformer draining a distorted current, this current generates a distorted voltage drop at the PCC. The second cause is more complex: the unbalance of the phases or of the line voltages causes an unavoidable ripple in the DC link composed by even harmonics (Moran *et al.*, 1992). It should be noted that both the first type of harmonics (due to other loads) and the second type of harmonics (due to unbalance) can be modeled with low frequency voltage sources, but their mathematical evaluation is complex and depends on the system parameters.

Thus the sensitivity analysis will be carried out highlighting the influence of the variation of some system parameters (both physical and digital ones) on the frequency response of the line current. This analysis allows to highlight some critical points of the frequency range which can lead to the propagation of the harmonics, generated by the causes mentioned above, in the complete plant.

9.5.1 Sensitivity of the line current with respect to the transformer inductance

By definition, the normalised sensitivity of the line current with respect to the transformer inductance is:

$$\dot{S}_{L_1}^{\bar{I}_g} = \frac{\partial \bar{I}_g}{\partial L_1} \cdot \frac{L_1}{\bar{I}_g} \tag{9.11}$$

Table 9.3. Numerical values of the controller.

$T_s = 1/f_s$ [s]	n	k_P	k_I
1/5000	4.8	13.3	0.07

Table 9.4. Numerical values of the passive components.

$R_1[\Omega]$	$R_2[\Omega]$	$R_3[\Omega]$	$R_4[\Omega]$	L_1[mH]	L_2[mH]	L_4[mH]	$C_3[\mu F]$	$R_{1C}[\Omega]$	$C_1C[\mu F]$	C_{2C}[F]
0.1	0.06	5	0.1	3	2	3	2.2	13.3	72	14.28

where the sensitivity coefficient $(\partial \overline{I}_g / \partial L_1)$ has the following expression:

$$\frac{\partial \overline{I}_g}{\partial L_1} = \frac{\partial \overline{I}_g}{\partial Z_{L_1}} \cdot \frac{\partial Z_{L_1}}{\partial L_1} = -j\omega \cdot \overline{I}_{L_1} \cdot \widehat{I}_{L_1} \tag{9.12}$$

as reported in Table 9.2.

Substituting Eq. 9.12 in Eq. 9.11, the following is obtained:

$$\dot{S}_{L_1}^{\overline{I}_g} = -j\omega \cdot \overline{I}_{L_1} \cdot \frac{L_1}{\overline{I}_g} = -j\omega L_1 \cdot \widehat{I}_{L_1} = -\widehat{V}_{L_1} \tag{9.13}$$

where $\overline{I}_{L_1} = \overline{I}_g$.

Figure 9.9 shows that the inductance of the transformer is relevant at low as well as at high frequencies, thus the line stiffness is demonstrated to be one of the most relevant parameters in the design. Particularly the sensitivity to L_1 has a peak around 200 Hz (4th harmonic).

9.5.2 Sensitivity of the line current with respect to the number of sample delays

In order to determine the sensitivity of the line current with respect to the number of sample delays n, some brief considerations are needed. The first one concerns the components affected by n. From Eq. 9.2 and Table 9.1, it is clear that the components dependent on the parameter n are the inductor L_5, the resistor R_{1C} and inductor L_5, the resistor R_{1C} and the capacitors C_{1C} and C_{2C}, as reported in Fig. 9.7. Then, in order to determine the sensitivity with respect to n, the contribution of each one of these components has to be considered. The second one concerns this specific case-study.
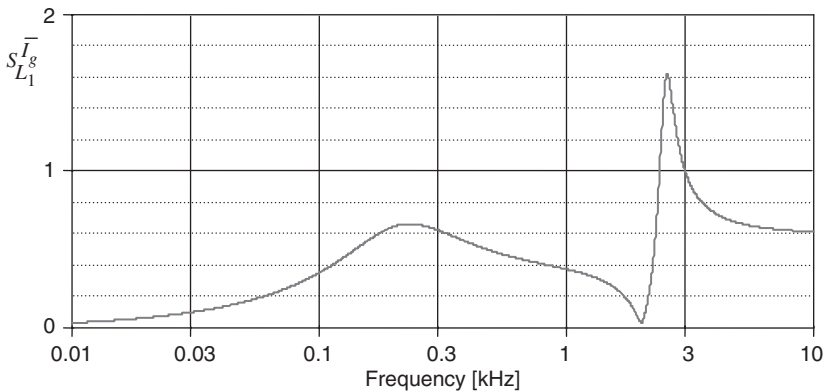
Fig. 9.9. Magnitude of the normalised sensitivity of the line current with respect to the transformer inductance L_1.

Substituting the values reported in Table 9.3 in the expressions of the components as reported in Table 9.1, it is observed that only the C_{1C} component, besides L_5, is really affected by the n-value, while the other components are very little sensitive to n and can be considered to be constant. Finally, the third one concerns the fact that the circuit in Fig. 9.7 is linear, thus the sensitivity can be obtained by summing all the contributions.

Bearing in mind all the earlier observations, it is possible to conclude that the sensitivity of the line current with respect to the number of sample delays n can be determined by summing two contributes: the former one is the sensitivity related to L_5 inductor and the latter one is the sensitivity related to C_{1C} capacitor.

In

$$\dot{S}_n^{\overline{I}_g} = \frac{\partial \overline{I}_g}{\partial n} \cdot \frac{n}{\overline{I}_g} \tag{9.14}$$

the sensitivity coefficient can be obtained as:

$$\frac{\partial \overline{I}_g}{\partial n} = \frac{\partial \overline{I}_g}{\partial L_5} \cdot \frac{\partial L_5}{\partial n} + \frac{\partial \overline{I}_g}{\partial C_{1C}} \cdot \frac{\partial C_{1C}}{\partial n} \tag{9.15}$$

Considering Tables 9.1 and 9.2 and the expression of L_5, it results as follows:

$$\frac{\partial \overline{I}_g}{\partial n} = -j\omega \cdot \overline{I}_{L_5} \cdot T_s + j\omega \cdot \overline{V}_{C_{1C}} \cdot \widehat{\overline{V}}_{C_{1C}} \cdot \frac{T_s}{k_P} \tag{9.16}$$

where the second member on the right-hand side will be subsequently justified.

Substituting Eq. 9.16 in Eq. 9.14, we get:

$$\dot{S}_n^{\overline{I}_g} = \left(-j\omega \cdot \overline{I}_{L_5} \cdot \widehat{\overline{I}}_{L_5} \cdot T_s + j\omega \cdot \overline{V}_{C_{1C}} \cdot \widehat{\overline{V}}_{C_{1C}} \cdot \frac{T_s}{k_P} \right) \cdot \frac{n}{\overline{I}_g} \tag{9.17}$$

and using the L_5 and C_1 definitions, it follows:

$$\dot{S}_n^{\overline{I}_g} = -\frac{\overline{I}_{L_5} \cdot \widehat{\overline{V}}_{L5}}{\overline{I}_g} + \frac{\overline{V}_{C_{1C}} \cdot \widehat{\overline{I}}_{C_{1C}}}{\overline{I}_g} \tag{9.18}$$

Figure 9.10 shows the sensitivity of the line current with respect to the number of sample delays n introduced by the filters: the influence is on the whole spectrum, being more relevant at low frequencies, and has two peaks.
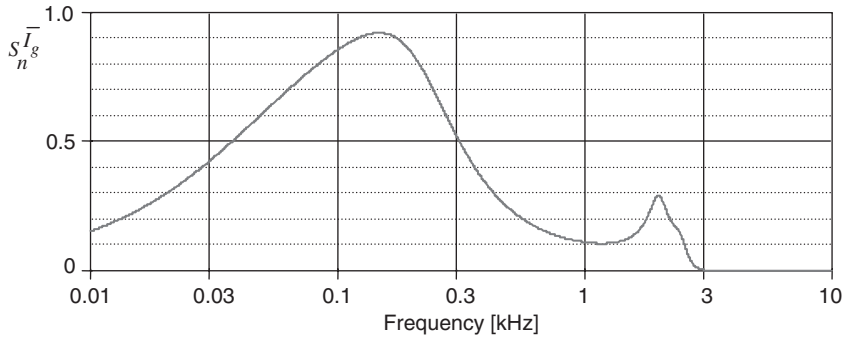
Fig. 9.10. Magnitude of the sensitivity of the line current to the number of sampling periods n introduced by the filters adopted on the signals.

9.5.3 Sensitivity analysis with respect to the LCL filter

Now, the sensitivity of the line current with respect to all the parameters of the LCL filter will be analysed, starting with the study of the influence of the damping resistor R_3. The normalised sensitivity of the line current to R_3 is defined as:

$$\dot{S}_{R_3}^{\overline{I}_g} = \frac{\partial \overline{I}_g}{\partial R_3} \cdot \frac{R_3}{\overline{I}_g} = -\overline{I}_{R_3} \cdot \widehat{\overline{I}}_{R_3} \cdot \frac{R_3}{\overline{I}_g} = -\frac{\overline{I}_{R_3} \cdot \widehat{\overline{V}}_{R_3}}{\overline{I}_g} \tag{9.19}$$

Figure 9.11 proves how the damping resistance R_3 has a relevant influence only around the resonance frequency.
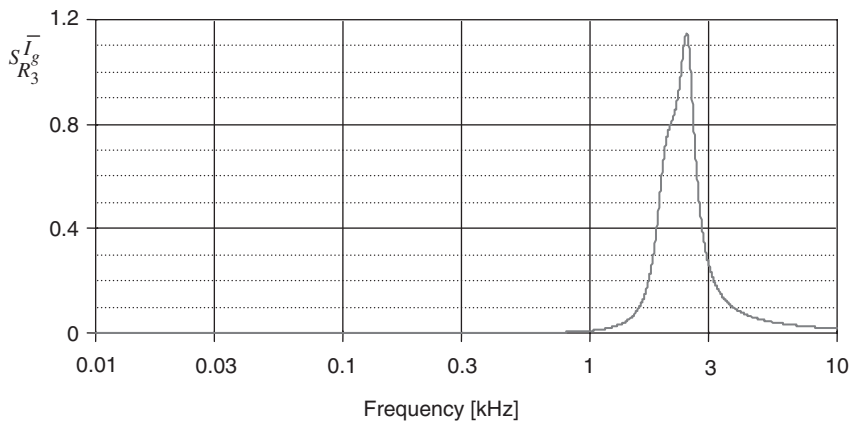
Fig. 9.11. Magnitude of the normalised sensitivity of the line current with respect to the damping resistance R_3.

At this point it is important to evaluate also the sensitivity of the line current to the capacitor C_3. This normalised sensitivity is defined as:

$$\dot{S}_{C_3}^{\overline{I}_g} = \frac{\partial \overline{I}_g}{\partial C_3} \cdot \frac{C_3}{\overline{I}_g} \tag{9.20}$$

where the sensitivity coefficient can be determined as:

$$\frac{\partial \overline{I}_g}{\partial C_3} = \frac{\partial \overline{I}_g}{\partial Y_{C_3}} \cdot \frac{\partial Y_{C_3}}{\partial C_3} = j\omega \cdot \overline{V}_{C_3} \cdot \widehat{\overline{V}}_{C_3} \tag{9.21}$$

Substituting Eq. 9.21 in Eq. 9.20, the following is obtained:

$$\dot{S}_{C_3}^{\overline{I}_g} = j\omega \cdot \overline{V}_{C_3} \cdot \widehat{\overline{V}}_{C_3} \cdot \frac{C_3}{\overline{I}_g} = \frac{\overline{V}_{C_3} \cdot \widehat{\overline{I}}_{C_3}}{\overline{I}_g} \tag{9.22}$$

Figure 9.12 demonstrates the C_3 capacitor influence around the resonance frequency; in order to appreciate its contribution in the whole spectrum, Fig. 9.13 reports the same waveform in logarithmic scale. In this way, it has been highlighted that the line current sensitivity to the C_3 capacitor value is relevant also at 100 Hz, although its magnitude is very small. However it is noted that the sensitivities to the C_3 and R_3 at the resonance frequency differ heavily.
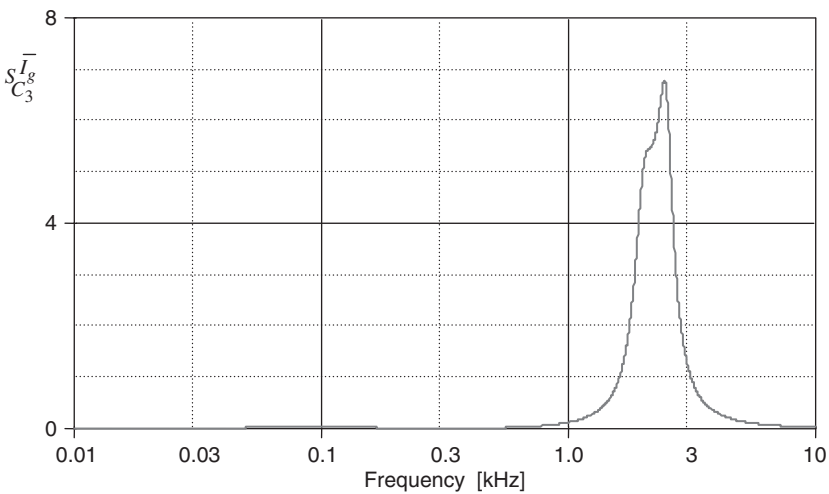
Fig. 9.12. Magnitude of the sensitivity of the line current with respect to the capacitor C_3.
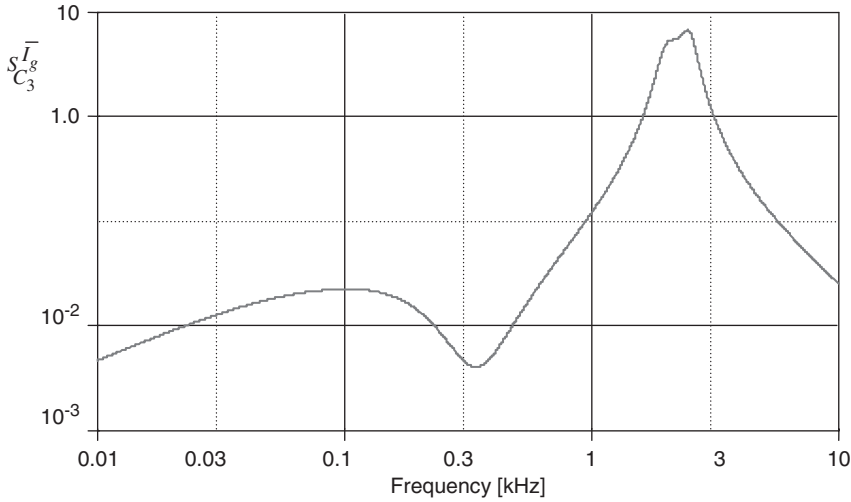
Fig. 9.13. Magnitude of the sensitivity of the line current with with respect to the capacitor C_3 in logarithmic scale.

Finally, by calculating the sensitivity of the line current to the inductors L_2 and L_4, the following expressions are obtained, respectively:

$$\dot{S}_{L_2}^{\overline{I}_g} = -j\omega \cdot \overline{I}_{L_2} \cdot \widehat{\overline{I}}_{L_2} \cdot \frac{L_2}{\overline{I}_g} = -\frac{\overline{I}_{L_2} \cdot \widehat{\overline{V}}_{L_2}}{\overline{I}_g} \tag{9.23}$$

$$\dot{S}_{L_4}^{\overline{I}_g} = -j\omega \cdot \overline{I}_{L_4} \cdot \widehat{\overline{I}}_{L_4} \cdot \frac{L_4}{\overline{I}_g} = -\frac{\overline{I}_{L_4} \cdot \widehat{\overline{V}}_{L_4}}{\overline{I}_g} \tag{9.24}$$

Figure 9.14 reports the normalised sensitivity of the line current with respect to the inductor L_2 of the LCL-filter, while Fig. 9.15 reports the normalised sensitivity of the line current with respect to the inductor L_4 of the LCL-filter. It is easy to observe that the inductor L_4 affects the line current at the resonance frequency much more than the inductor L_2.

By assembling Eqs. 9.19–9.24 in matrix form, the normalised sensitivity of the line current with respect to any component of the LCL filter, $\dot{S}_{\text{LCL}}^{\overline{I}_g}$, is obtained:

$$\dot{S}_{\text{LCL}}^{\overline{I}_g} = \begin{bmatrix} -\overline{I}_{R_3} \cdot \widehat{\overline{V}}_{R_3} & 0 & 0 & 0 \\ 0 & \overline{V}_{C_3} \cdot \widehat{\overline{I}}_{C_3} & 0 & 0 \\ 0 & 0 & -\overline{I}_{L_2} \cdot \widehat{\overline{V}}_{L_2} & 0 \\ 0 & 0 & 0 & -\overline{I}_{L_4} \cdot \widehat{\overline{V}}_{L_4} \end{bmatrix} \cdot \frac{1}{\overline{I}_g} \tag{9.25}$$
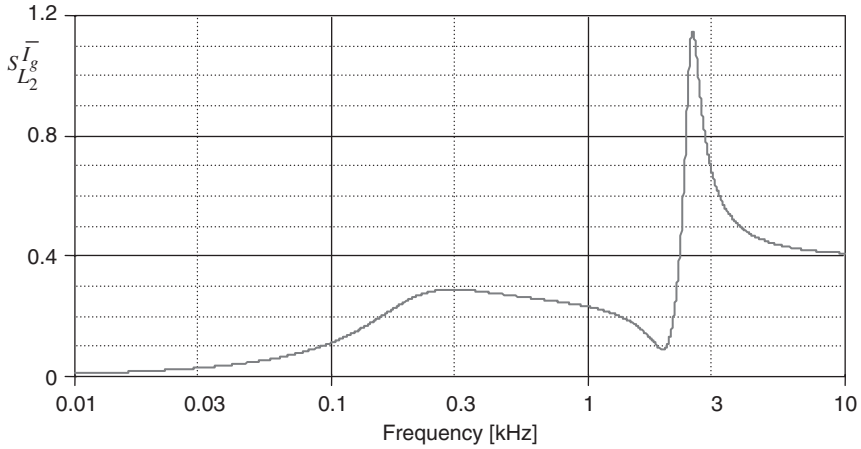
Fig. 9.14. Magnitude of the sensitivity of the line current with with respect to the inductor L_2.
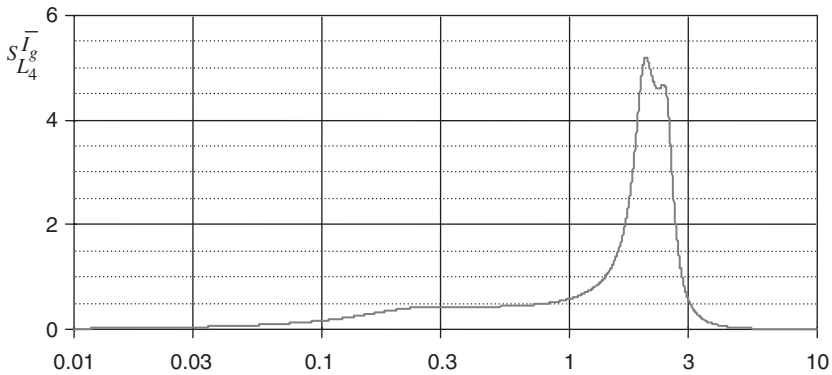
Fig. 9.15. Magnitude of the sensitivity of the line current with with respect to the inductor L_4.

In Eq. 9.25, the *ii*-th element belonging to the main diagonal represents just the *virtual power* (absorbed by the capacitor and supplied for both the resistor and the inductor) by the *ii*-th component. The term *virtual* implies that the power is not the actual power absorbed/supplied by the element, because the voltage and the current are referred to the same element but belong to different circuits, i.e. to the assigned one and to the adjoint one. Obviously, power does not have a physical sense and it is a direct consequence of the Tellegen's theorem application. Nevertheless, this concept allows to obtain a simplified form of the sensitivity matrix. It is worth noting that there is no difference in defining the virtual power of a certain component as the product between the voltage across the component of the assigned network and the current into the respective component of the adjoint one or vice versa.

For example, Eq. 9.19 gives:

$$\dot{S}_{R_3}^{\overline{I}_g} = \frac{\partial \overline{I}_g}{\partial R_3} \cdot \frac{R_3}{\overline{I}_g} = -\overline{I}_{R_3} \cdot \widehat{\overline{I}}_{R_3} \cdot \frac{R_3}{\overline{I}_g} = -\frac{\overline{I}_{R_3} \cdot \widehat{\overline{V}}_{R_3}}{\overline{I}_g} = -\frac{\widehat{\overline{I}}_{R_3} \cdot \overline{V}_{R_3}}{\overline{I}_g} \qquad (9.26)$$

and so Eq. 9.22 gives:

$$\dot{S}_{C_3}^{\overline{I}_g} = j\omega \cdot \overline{V}_{C_3} \cdot \widehat{\overline{V}}_{C_3} \cdot \frac{C_3}{\overline{I}_g} = \frac{\overline{V}_{C_3} \cdot \widehat{\overline{I}}_{C_3}}{\overline{I}_g} = \frac{\widehat{\overline{V}}_{C_3} \cdot \overline{I}_{C_3}}{\overline{I}_g} \qquad (9.27)$$

and so Eq. 9.23 gives:

$$\dot{S}_{L_2}^{\overline{I}_g} = -j\omega \cdot \overline{I}_{L_2} \cdot \widehat{\overline{I}}_{L_2} \cdot \frac{L_2}{\overline{I}_g} = -\frac{\overline{I}_{L_2} \cdot \widehat{\overline{V}}_{L_2}}{\overline{I}_g} = -\frac{\widehat{\overline{I}}_{L_2} \cdot \overline{V}_{L_2}}{\overline{I}_g} \qquad (9.28)$$

and so on.

Equation 9.25 highlights that the sensitivity of each component of the LCL-filter can be obtained by dividing the virtual power absorbed/supplied by each one of them by the line current $\overline{I}_g$. Then, Eq. 9.25 becomes:

$$\dot{S}_{\text{LCL}}^{\overline{I}_g} = \frac{\overline{A}_{\text{virtual}}}{\overline{I}_g} \qquad (9.29)$$

where $\overline{A}_{\text{virtual}}$ represents the diagonal matrix of the *virtual powers* and the upper line indicates that each power is complex.

9.6 Conclusions

The aim of this chapter was to offer a straightforward approach to the analysis of a self-commutated line-connected voltage source converter with respect to its line behaviour. It has used a *virtual circuit* approach, which consists of using passive elements to model the digital control. With the proposed approach it is straightforward to evaluate the problems of the use of the line-connected converter related to the propagation of harmonics in an industrial plant.

Acknowledgement

References

Blaabjerg F., Chiarantoni E., Dell'Aquila A., Liserre M., Vergura S., "*Sensitivity analysis of an LCL-filter-based three-phase active rectifier via a "virtual circuit" approach*", JCSC – Journal of Circuits, Systems and Computers, Vol 13, n. 4, August 2004, pp. 665–686 (doi:10.1142/S0218126604001489).

Blasko V., Kaura V., "A novel control to actively damp resonance in input LCL-filter of a three-phase voltage source converter", IEEE Trans. Ind. Appl., **33(2)** (1997) 542–550.

Bose, *Modern power electronics and A.C. drives*, 1st ed., Prentice Hall, 2001.

Chua L.O., Lin P.M., *Computer-aided analysis of electronic circuits: algorithms and computational techniques*, New Jersey, Englewood Cliffs, Prentice-Hall, 1975.

Director S.W., Rohrer R.A., "The generalized adjoint network and network sensitivity", IEEE Trans. Circuit Theory Appl., CT-**16** (1969) 318–323.

Kazmierkowski M.P., Krishnan R., Blaabjerg F., *Control in Power Electronics*, Academic Press, 2002.

Liserre M., Blaabjerg F., Dell'Aquila A., "Step-by-step design procedure for a line-connected three-phase PWM Voltage Source Converter", Int. J. Electronics, 2004.

Liserre M., Blaabjerg F., Hansen S., "Design and control of an LCL-filter based active front-end converter", in IEEE Trans. Ind. Appl., (2005) 1129–1135.

Litovski V., Zwolinski M., *VLSI circuit simulation and optimization*, Chapman & Hall, 1997.

Moran L., Ziogas P.D., Joos G., "Design aspects of synchronous PWM rectifier-inverter system under unbalanced input voltage conditions", IEEE Trans. Ind. Appl., **28(6)** (1992) 1286–1293.

Su Kendall L., *analogue Filters*, Chapman & Hall, London, (1996) 91–117.

Tellegen B.D.H., "A general network theorem with applications", Philips Res. Rep., **7** (1952) 259–269.

CHAPTER 10

Harmonic Load Flow Applications for Industrial Power Systems Design

E. De Tuglie and M. La Scala

Abstract

The harmonic pollution due to power electronic converters is a major problem in industrial power system. The classical techniques for studying harmonic propagation consider only the basic components and do not take into account the interactions among them through the electrical network. Harmonic Load Flow is a tremendous tool for assessing the propagation of harmonics on an industrial distribution system. The classical approach can be integrated with a probabilistic framework where the harmonic current spectrum at major sources of disturbance is measured and evaluated under actual operating conditions. The Probabilistic Harmonic Load Flow has been considered as a tool to quickly monitor the harmonic pollution and its effect in industrial power systems and calculate the probability that a harmonic index exceeds the limit fixed by technical standards. Passive harmonic filters are an effective mitigation method for harmonic problems. The passive filtering provides a tremendous tool to divert troublesome harmonic currents in the power systems. Optimisation algorithms can provide a useful tool to minimise cost in the synthesis of passive filters in industrial systems.

10.1 Introduction

Distortion of sinusoidal voltage and current waveforms caused by harmonics is one of the major power quality concerns in electric power industry. Considerable efforts

have been spent in recent years to improve the management of harmonic distortion in power systems. Harmonic standards provide useful preventive solutions to harmonics. International standards emphasise placement of limits on harmonic currents produced by nonlinear loads for customer and network bus harmonic voltage distortion for electric utilities.

The area of power system harmonic analysis has also experienced significant advancement. Many models have been proposed for representing harmonic sources as well as non-linear components. Various network harmonic solution algorithms have also been published.

In recent years, the analysis of the distortion of sinusoidal voltage and current waveforms caused by harmonics has assumed relevance due to the widespread proliferation of power electronic converters.

Many techniques have been developed for modelling and studying harmonic pollution. In a classical model, harmonics generated by converters of any pulse number may be evaluated according to $1/h$-rule model ($h = 1, 5, 7, \ldots$) where h is related to the pulse number of converter (Arrilaga *et al*., 1985; Chang and Xu, 1998a,b). Consequently, AC harmonic currents generated by a six-pulse converter include all odd harmonics except triplens.

The most commonly and efficiently adopted technique for studying harmonic propagation treats the power converter as a source of harmonic currents. The phase angles of the current sources, function of the supply voltage phase, are evaluated by means of fundamental frequency load flow solutions using a linear model for all power converters. The solutions are adjusted with the phase angle of the non-linear load harmonic source current spectrum. This is a computational efficient technique and the solutions can always be obtained directly without iterative approach. The limitation of this technique is the validity of the harmonic current vector representation.

In a power system with low distortion and a single dominant harmonic source, the distortion calculations can simply be performed making use of the admittance model for network representation (Chang and Xu, 1998a). For larger system and complicated harmonic loads, more formal Harmonic Load Flow (HLF) analysis methods are adopted (Arrilaga and Callaghan, 1991; Xu *et al*., 1991; Chang and Xu, 1998a; Carpinelli *et al*., 2001). The HLF algorithm combines the current source methodology with the conventional load flow algorithm.

Obviously, the harmonic current vector should be known for each power converter. This might be a drawback because the harmonic current spectrum is not always reliable. In fact, a theoretical harmonic source current spectrum considers only the basic components and does not take into account the interaction among power converters and electrical network due to non-typical operating modes as partial loading, excessive harmonics voltage distortions and unbalanced network conditions. These operating conditions could be usual in the industrial power system (Jalali and Lasseter, 1994; Currence *et al*., 1995; Ellis, 1996). A way to overcome the mentioned drawback is

the adoption of a probabilistic analysis (Carpinelli *et al.*, 2001; Morrison, 2002; Testa *et al.*, 2002).

In this chapter, a review of the basic notions about harmonics and harmonic load flow is summarised.

A brief mathematical formulation of a Probabilistic Harmonic Load Flow (PHLF) is reported with an application to industrial systems. The test case is based on a real-world experience.

It is shown how harmonic load flow can be integrated with the harmonic current spectrum of each converter obtained through adequate measurements on industrial power systems. The harmonic current spectrum is evaluated by taking into account the actual operating conditions of power converters and their mutual influences (Sutherland, 1995; Simpson, 1998; Grady, 1999). Real-time recorded data allow probabilistic distribution functions of current spectra to be determined under actual operating conditions and for different configurations.

The PHLF and measured current spectra at converter bus terminals permit to assess the harmonic propagation at each bus of the power system on the basis of few points of measurements with a consequent gain in terms of equipment to be used in large distribution networks.

In the final section, the optimal allocation of passive filters is addressed.

10.2 Power System Response to Harmonics

Harmonic-producing equipment represents a significant portion of the total connected load of modern industrial systems. The effect of harmonics can be noticeable in many ways such as voltage and current distortion, low voltage notching, communication systems interference and high voltages and currents in case of resonance. Harmonics may cause relay misoperations, PLC interference, equipment failures, capacitor fuse interruptions and high overall system losses.

Harmonic study analysis must be conducted at the engineering design stage of all industrial systems that include harmonic-producing equipment, alongside load flow and short circuit studies. The interaction between load flow and harmonic study should lead to the best system configuration design, optimal operating conditions and proper size and location of power factor correction capacitors. Although the installation of power factor correction capacitors in industrial systems as one of the most effective ways to reduce energy consumption and utility bills allows the usage of transformers and feeders at full capacity and are easy to install and cheap to maintain, they can be the most troublesome element in the whole plant when installed in the presence of harmonics in the system.

Power system modelling for harmonic studies still requires a trade-off between a sufficient level of accuracy and a fair level of complexity in system representation taking into

account the cost (time and money) involved in obtaining the necessary data for parameter identification. Improved models are specifically needed for transformers, loads, harmonic sources and utility equivalents.

In electrical engineering studies, harmonic analysis must be conducted and accommodated within budget and time constraints. Therefore, system modelling should be as simple as practical that would provide reasonably accurate results for design purposes.

Harmonic Sources   Harmonic-producing equipment such as variable speed and DC drives, arc furnaces and welders and any other non-linear loads are harmonic sources. Typically, harmonic sources are modeled as current source with magnitude and phase angle for each harmonic frequency. This model provides reasonable results for power systems with no resonance at or near generated harmonic frequencies.

When system impedance contains both inductive and capacitive elements, which is usually the case for industrial systems, the simple current source model produces unrealistically high estimates of harmonic voltages, current and distortion factor in case of parallel or series resonance at or near one of the generated frequencies.

Simulating harmonic sources as current sources with an infinite shunt impedance means that harmonic parameters can reach any value without limitations. In fact every harmonic source is limited by its internal circuit. Therefore harmonic sources must be modeled by their Norton's or Thevinin's equivalents in order to limit harmonic voltage and current rises in case of resonance.

The harmonic-producing equipment supplier should provide harmonic currents (magnitude and angle) to be used in simulation studies. In most cases, it is necessary to measure harmonic currents since they are significantly different from theoretical values given in text books, standards or vendor documentation.

Loads   Passive loads are modeled by their equivalent impedance based on MW, Mvar and rated voltage. Motor loads are represented by their subtransient and locked rotor impedance for synchronous and asynchronous motors respectively.

Several detailed motor models are proposed for harmonic studies. In practice, when detailed models are used in a typical industrial system of several hundred motors, the task of harmonic study analysis becomes unbearable due to budget and time constraints. Furthermore, the effect of low voltage loads on the system impedance–frequency response is only marginal and falls within 10–15% for example. Therefore, loads can be generally neglected at low voltage levels. Only in special cases when filters are considered at low voltages, should loads be included to size filter elements.

When medium voltage capacitors (2.4–13.8 kV) are considered, load modelling becomes more significant and may be included. Here again, the simple model of sub-transient and locked rotor impedance models are acceptable for motors.

Transformers, Transmission Lines and Cables   For low frequency harmonics up to 1.5 kHz, transformers, transmission lines and cables can be safely represented by their

equivalent short circuit impedance. For higher harmonic calculations, these models become inaccurate and may produce misleading results.

Detailed models have been proposed but again with so many transformers in industrial systems, it becomes impractical to use detailed models unless studying the performance of a few or a single transformer in the system. This situation arises when calculating the telephone influence at the point of service with utility. It is important in this case to model tie transformers and associated cables in more detail including their internal capacitance which becomes effective with higher harmonic frequencies.

Utility Equivalent   The utility equivalent short circuit impedance is generally used to represent the utility system at the point of service. This model can be used with a good degree of accuracy in the following cases:

- No series or shunt capacitors are connected to the transmission line or nearby substation serving the system under study;
- Calculation of low frequency harmonics up to 1.5 kHz; and
- No other customers close by producing harmonics and sharing the same line with the studied system.

In most cases, the above conditions are not satisfied since the utilities worldwide are still striving in the implementation of standards such as the IEEE standard 519 which recommends specific limits for harmonic distortion and telephone interference. Consequently, close-by capacitor banks and other harmonic-producing customers must also be included in the model.

It is important that both utilities and their customers share responsibilities and join efforts to meet the specific limits of the standard.

Summing up, in harmonic studies, power system components can be classified as:

- Linear loads and devices;
- Devices with non-linear voltage–current relationship;
- Line commutated converters.

Linear and non-linear loads can be modeled by their voltage–current characteristics as follows:

$$I_i^h = f_i\left(V_i^1, \ldots, V_i^h, \ldots, V_i^n\right) \tag{10.1}$$

where I_i^h represents the generic h-th harmonic current injected by the load at bus i, V_i^h represents the generic h-th harmonic voltage at the bus i which is connected to the load, and n is the total number of harmonics under investigation.

For line commutated converters, it is assumed that the behaviour of these devices have no commutation overlap and balanced three-phase operation. In this case, it can be shown that the magnitude of the harmonic injected current is

$$
\begin{cases}
I_i^h = \dfrac{I_i^1}{h} \\[2mm]
\vartheta_i^h = -\left[h\vartheta_i^1 + (h+1)\dfrac{\pi}{2}\right]
\end{cases}
\qquad h = pm \pm 1
\tag{10.2}
$$

where m is any integer, p is the pulse number of the converter and ϑ_i^h is the phase angle of the h-th harmonic current with regard to the h-th harmonic voltage at the same i-th bus. For the ideal case, converter harmonic current magnitudes decrease according to $1/h$ rule.

The current I_1 can be obtained by power flow analysis at the fundamental frequency. Consequently I_1 is a function of V_1.

Denoting N as the total number of buses and assuming the following vectors representing the generic h-th harmonic current and voltage at each bus of the system:

$$
V^h = \left[V_1^h, V_2^h, \ldots, V_N^h\right]^T
\tag{10.3}
$$

$$
I^h = \left[I_1^h, I_2^h, \ldots, I_N^h\right]^T
\tag{10.4}
$$

The linear network can be represented by the following relationship:

$$
I^h = Y^h V^h
\tag{10.5}
$$

where Y^h represents the matrix admittance evaluated at the h-th harmonic.

The following relationships hold for the overall system:

$$
f^h\left(V^1, \ldots, V^h, \ldots, V^n\right) = Y^h V^h \quad h = 1, \ldots, N
\tag{10.6}
$$

Equations 10.6 can be rewritten in a more compact form as follows:

$$
F(V) = 0
\tag{10.7}
$$

where

$$
V = \left(V^1, \ldots, V^h, \ldots, V^n\right)
$$

$$
F = \left[f^1 - Y^1 V^1, \ldots, f^h - Y^h V^h, \ldots, f^N - Y^N V^N\right]
\tag{10.8}
$$

Equation 10.7 represents the mathematical formulation of the harmonic power flow. The entire set of equations is solved iteratively (Arrilaga *et al.*, 1985; Sharma *et al.*, 1991; Xu *et al.*, 1991) using either Newton or Gaussian methods, giving rise to an extremely complex and powerful technique. Loads can be modeled with a desired complexity depending on the required accuracy of the solution. When a closed-form solution for the non-linear load current harmonics can be obtained as a function of voltage, it is possible to represent the load harmonics directly in the frequency domain. In many cases, this closed-form solution can not be obtained and a combination time- and frequency-domain technique is employed.

From a HPF analysis, it is possible to evaluate typical variables such as:

- Harmonic voltages at buses of concern;
- Harmonic currents at branches of concern;
- Total harmonic distortion factors (THD for voltage and current); and
- Telephone interference factor.

Usually, harmonic analysis needs computer programs to calculate the above parameters for mid-size and large industrial systems. Results of computer programs must be used with caution for the obvious modelling limitation. Field measurements are always necessary to verify the theoretical computer simulation results. Furthermore, a hybrid approach, which employs both measurements and HPF analysis, can be adopted to extend the information which can be derived when using few measurement equipments as it will be shown later in the case study.

Various system equipment ratings must be checked for possible overload and/or over stress due to excessive harmonic currents and voltages. Power factor correction capacitors are particularly vulnerable to high harmonic voltages and currents due to system resonance. Capacitor total RMS voltages and currents, including harmonics, can be checked against standard maximum rated capacity limits.

In harmonic analysis, there are several important indices used to describe the effects of harmonics on power systems components and network. These indices are used to measure the deviation of a periodic waveform containing harmonics from a perfect sinewave.

In the following developments, we adopt the Total Harmonic Distortion (THD), the Total Demand Distortion (TDD) and the ratio between harmonic current and fundamental frequency current (IHD). These quantities are defined as:

$$\text{THD}_I = f(I) = \frac{\sqrt{\sum_{i=2}^{\infty} I_i^2}}{I_1} \tag{10.9}$$

$$\text{THD}_V = g(I) = \frac{\sqrt{\sum_{i=2}^{\infty} V_i^2}}{V_1} \tag{10.10}$$

$$\text{TDD}_I = h\,(I) = \frac{\sqrt{\sum_{i=2}^{\infty} I_i^2}}{I_\text{L}} \tag{10.11}$$

$$\text{IHD}_i = \frac{I_i}{I_1}, \tag{10.12}$$

where:

– i denotes the i-th harmonic;

– I_1 and V_1 are, respectively, order current and voltage at fundamental frequency;

– I_L is the maximum demand load current (15- or 30-minute demand) at fundamental frequency at the Point of Common Coupling (PCC) calculated as the average current of the maximum demands for the previous twelve months.

The total voltage harmonic distortion factor $\text{THD}_V\%$ is a very significant measure to verify the performance of system equipment. Acceptable limits for harmonic distortion are given in the IEEE standard 519-1992 for different voltage levels.

Impedance Calculation   Another set of results which can be obtained by a harmonic study is the so-called impedance calculation.

It consists in exploring resonance conditions through impedance versus frequency calculations. A typical industrial system with distributed capacitors and various harmonic sources requires computer calculations.

Generally, if the system exhibits resonance at or near any of the system potential harmonics, mainly at the 5, 7, 11 or 13th harmonic, in the presence of harmonics and medium voltage capacitor banks (2.4–13.8 kV), then the safest thing to do is to tune the capacitor banks to eliminate any possibility of resonance at each capacitor location. Impedance–frequency plots are very helpful to visualise potential resonance for different system configuration and corrective measures. Frequency steps should be small enough to detect sharp resonance (0.1–0.5 pu).

Harmonic Measurements   Simulation results could be far from reality and therefore must be verified by field measurements to ensure proper system performance. On the other hand, measurements of harmonic voltages and currents through typical system voltage and current transformers are subject to limitations and can only be trusted up to 1.5–2 kHz. This may be enough to identify potential harmonic problems due to system resonance in the range of 5th to 13th harmonics. For the purpose of telephone interference measurements which highly depend on the higher harmonic frequencies, special measurement devices are required. Voltage harmonic distortion measurements using spectrum analyser may be misleading in the presence of deep short notching in the system, especially at the harmonic source bus.

It is important that harmonic currents injected into the system from all harmonic sources be measured and compared with theoretical values used in the simulation. Harmonic filters and capacitor banks should also be targeted for harmonic current measurements to ensure proper performance.

The basic equipment required for harmonic measurements is spectrum analyser and/or oscilloscope with data recorder. This equipment is enough for industrial plant harmonic measurement purposes. High frequency harmonic filters are required for telephone interference and IT product measurements.

10.3 Probabilistic Formulation

In this section, it will be shown as a hybrid approach based on measurements, simulation and probabilistic analysis consent to circumvent all the difficulties connected with the use of only one of these methodologies. A real-life example will help in showing this assumption. In fact, in real-life network parameter, the exact nature of nonlinearities, the time dependence of non-linear loads and converter harmonic injections can not be known in advance with sufficient accuracy. A probabilistic approach can be proposed to take into account these aspects.

The ideal solution would be to measure harmonics at each node but this is often not practicable. Even in this case, the computer solution through simulation is still necessary to forecast the effects and the distribution of harmonics throughout the grid when some new components are added or different network configurations are taken into account during the design phase of the industrial plant when new apparatus and systems should be added to the existing plant layout. Furthermore, during operations network topology may change and in particular conditions (perhaps not so likely) may give rise to resonant circuits. These conditions, although characterised by a very low likelihood, may give rise to very severe conditions characterised by the possibility to stop a critical process (such as, for example, cracking in a petrochemical plant, etc.). Thus, although the occurrence probability is very low, the risk may be high if the economical or safety value of the effects is high.

For these reasons, it is important to consider a probabilistic framework to the deterministic harmonic analysis as an additional tool which should be taken into account every time accuracy of results or uncertainties of data require it.

As shown in the previous section, the harmonic pollution in an industrial power system can be studied by adopting a current injection method in conjunction with load-flow computations. Mathematically, the approach involves the solution of the network equation for each harmonic, written as in Eqs. 10.5–10.7.

A fundamental frequency load flow permits to evaluate the state of the system. Subsequently, harmonic components are evaluated on the basis of measured or typical harmonic spectrum for the harmonic-producing devices. Through providing the network harmonic admittance and harmonic injected currents, the total harmonic current and voltage distortion at each bus can be determined. Obviously, a measured harmonic

spectrum takes into account the actual operating condition and the mutual influences among devices.

We propose to solve the harmonic analysis by means of a probabilistic approach, where random variables consist in the harmonic current spectrum at major converter buses.

The records of current measurements for each converter permit the construction of specific harmonic spectrum and the evaluation of the standard deviation for each harmonic component. The measurement can be obtained by positioning the instrumentation close to the harmonic sources. Obviously, the time duration for the measurements must be significant from a statistic and probabilistic viewpoint.

Under the assumption of Gaussian distribution, for the i-th harmonic current I_i, it is possible to describe this random variable with two moments, namely, the mean value μ_{I_i} and standard deviation σ_{I_i}.

Synthetically, the random variable I_i can be written as:

$$I_i = N\left(\mu_{I_i}, \sigma_{I_i}\right) \tag{10.13}$$

where N denotes Gaussian distribution.

The resulting spectra are utilised in a Probabilistic Harmonic Load Flow (PHLF) in order to calculate the current and voltage distortion and evaluate the harmonic propagation at different buses in the system.

By means of a probabilistic approach, we can model the harmonic sources as random variables and as a function of actual system conditions. It is possible to obtain deviations of voltages around their respective mean values on the basis of random fluctuations of source currents.

Under the assumption of small random fluctuations and Gaussian distribution, it is possible to obtain the covariance matrix of voltages as a function of covariance matrix of current harmonic sources:

$$E\left(\Delta V_i \Delta V_i^T\right) = Y_i^{-1} E\left(\Delta I_i \Delta I_i^T\right)\left(Y_i^T\right)^{-1} = Y_i^{-1} \mathrm{cov}\left(\Delta I_i\right)\left(Y_i^T\right)^{-1} \tag{10.14}$$

where E denotes expectation operator.

Since all the variables in the network can be obtained through the assessment of nodal voltages, it is possible to evaluate for each current and voltage in the network its random distribution on the basis of nodal voltage distributions.

Since measured currents I_i at harmonic sources are assumed randomly distributed, THD$_I$ itself can be considered normally distributed. Under the assumption of small deviations around the mean values, it is possible to linearise Eq. 10.9. If we also assume statistically

independent measurements, the mean and the standard deviation are:

$$\mu_{\text{THD}_I} = \frac{\sqrt{\sum_{i=2}^{\infty} \mu_{I_i}{}^2}}{I_1} \tag{10.15}$$

$$\sigma_{\text{THD}_I}^2 = \left(\frac{\partial \text{THD}_I}{\partial I_1}\right)^2 \sigma_{I_1}{}^2 + \cdots + \left(\frac{\partial \text{THD}_I}{\partial I_n}\right)^2 \sigma_{I_n}{}^2 \tag{10.16}$$

Therefore, the previous moments may be evaluated by knowing the harmonic spectrum and the standard deviation of each harmonic component.

Probabilistic harmonic load-flow permits the assessment of the mean and the covariance matrix associated to nodal voltages.

The standard deviation THD_V at each node can be directly obtained by covariance matrix (Eq. 10.14) through linearisation of (Eq. 10.10). Since currents across the components of the network can be derived by voltages obtained through harmonic load-flow analysis, the standard deviation of IHD_i, THD_I and TDD_I can be assessed by linearisation and standard manipulations of covariance matrix (Eq. 10.14).

Furthermore, the harmonic load flow permits to study in advance different configurations of the system.

From a power quality viewpoint, by means of a probabilistic approach, it is possible to calculate the probability that, for each i-th topological condition, a generic harmonic index h_i exceeds, among those expressed in Eqs. 10.9 – 10.12, a limit L fixed by a specific technical standard:

$$\rho_i = \text{prob}(h_i > L) \tag{10.17}$$

Each possible configuration C_i is characterised by a different occurrence probability. Industrial system operators keep track of major events on the grid and maintenance scheduling. Thus, it is possible to assess the likelihood of each configuration and to combine this information with the results obtained by probabilistic harmonic load flow.

Therefore, on the basis of the total probability theorem (Anders, 1990) assuming disjoint events, the total probability $P(L)$ to exceed a specific limit is given by

$$P(L) = \sum_{i=0}^{n} P(L/C_i) P(C_i) \tag{10.18}$$

where:

$P(L/C_i)$ denotes the conditional probability to exceed the generic limit L assuming a particular configuration C_i;

$P(C_i)$ is the occurrence probability of each configuration C_i; and

C_0 denotes the base case, i.e. normal operating condition.

This analysis permits to assess the harmonic pollution (according to a particular index) considering all the possible operating conditions that the industrial system can experience during its lifetime.

It should be noted that this result can be obtained through load-flow analysis and data measured at harmonic source buses on a time period sufficiently long to take into account the different configurations experienced by the industrial system. Different behaviour of harmonic sources in presence of different topological conditions can be captured by the random fluctuations of measured current.

10.4 Case Study

In order to better explain the proposed approach, a test case is shown to study harmonic pollution in a real industrial power system. In Fig. 10.1, a base configuration C_0 of the industrial system under study is reported.

There are seven generators whose maximum power generation is 290 MW. The total load is 140 MW and the power exported to the external grid is about 150 MW.

There are four adjustable speed electrical power drives for a total of 45 MW, equal to 32% of total load.

The main characteristic of the power drives are illustrated in Table 10.1.

By means of four oscilloperturbographs, positioned at power drives busbars, a wide harmonic analysis has been carried out. The measurements are permitted to individuate non-typical operating modes as overloads, excessive harmonic voltage distortions and unbalanced network conditions. The data were acquired for about two weeks in different periods of the year. The harmonic analysis has been conducted by referring to Standard IEEE 519-1992 (IEEE, 1993) and EN 60146-1-1 (EN, 1997).

As an example, the measured currents for each phase in PD 1 power drive is reported in Fig. 10.2. Table 10.2 shows the measured average current μ and the standard deviation σ for odd frequencies.

Table 10.3 shows the percent harmonic content for odd frequencies with respect to fundamental frequency for each power drive.

The harmonic distortion has been compared with the limits defined by IEEE Standard 519-1992 (IEEE, 1993). These limits are dependent on the nominal voltage V_n and on the ratio I_{SC}/I_L, where I_{SC} and I_L are, respectively, the short circuit current and the load current.
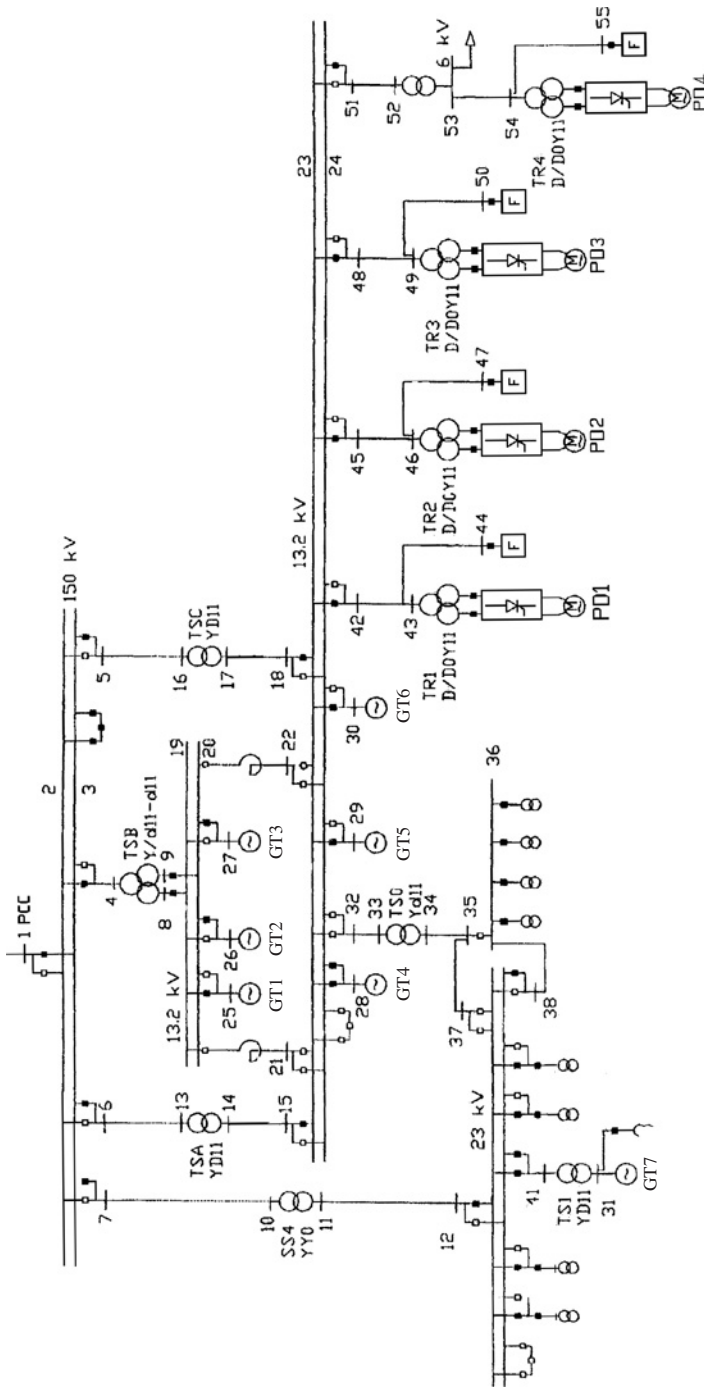
Fig. 10.1. Case Study – Power System of a petrochemical plant.

Table 10.1. Main characteristic of adjustable speed electrical power drives.

Power drive	Vn [kV]	Pn [MW]	DPF	Number of pulse
PD 1	13.2	11	0.858	12
PD 2	13.2	15	0.858	12
PD 3	13.2	15	0.858	12
PD 4	6	4	0.858	12
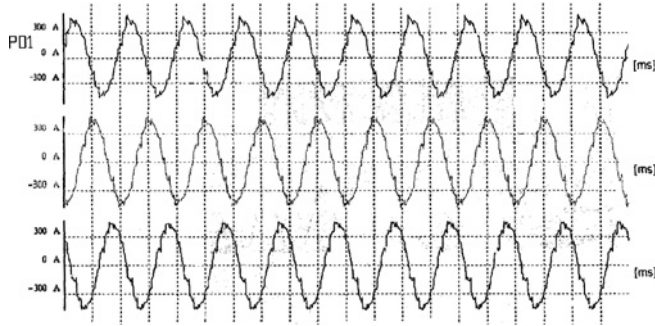
Fig. 10.2. Measured currents for each phase in PD1 power drive.

Table 10.2. Measured data for PD 1 power drive.

Moment	Harmonic						
	1st	3rd	5th	7th	9th	11th	13th
μ [A]	380.4	2.035	3.156	1.042	4.291	16.13	2.016
σ [A]	3.46	0.121	0.105	0.156	0.256	0.256	0.204

Table 10.3. Harmonics in the power drives.

Power drive		IHDi [%]						
		3rd	5th	7th	9th	11th	13th	15th
PD 1	μ	0.53	0.83	0.27	1.10	4.15	4.24	0.53
	σ	0.03	0.03	0.04	0.02	0.08	0.07	0.02
PD 2	μ	0.35	1.06	0.21	0.87	3.98	4.91	0.14
	σ	0.02	0.08	0.04	0.05	0.08	0.09	0.01
PD 3	μ	0.69	2.28	0.23	1.62	4.11	5.90	0.49
	σ	0.04	0.10	0.03	0.06	0.09	0.11	0.02
PD 4	μ	0.29	1.43	0.29	0.13	6.48	6.13	0.14
	σ	0.03	0.06	0.01	0.03	0.12	0.10	0.01

Table 10.4. Harmonic limits on the basis of IEEE standard 519-1992.

Power drive	Vn [kV]	I_{SC}/I_L	IHDi [%] limit	
			$i < 11$th	11th$\leq i < 17$th
PD 1	13.2	113	14.1	7.7
PD 2	13.2	89	16.9	6.3
PD 3	13.2	89		
PD 4	6	51		

It should be considered that the electrical power drives under investigation are characterised by 12 pulse converters whereas the IEEE Standard is referred to 6-pulse converters. Consequently, the limit reported in Table 10.4 takes into account the corrective factor $q = \sqrt{12/6} = 1.414$.

From a deterministic viewpoint, it can be observed that only the 11th harmonic for PD 4 is slightly violated. The knowledge of standard deviations of harmonic currents permits to evaluate the probability that the previous indices exceed the standard limits.

In particular, the probabilities that the 11th harmonic current of PD 3 and the 13th harmonic currents of PD 3 and PD 4 to overcome the limit are:

$$\text{prob}\left(\text{IHD}_{11}^{\text{PD4}} > 6.3\right) = 93.3\%$$

$$\text{prob}\left(\text{IHD}_{13}^{\text{PD3}} > 6.3\right) = 0.014\%$$

$$\text{prob}\left(\text{IHD}_{13}^{\text{PD4}} > 6.3\right) = 0.45\% \tag{10.19}$$

We observe that although the mean of 13th harmonic currents of PD 3 and PD 4 are lower than the limit there are, respectively, 0.014 and 0.45% of the probability to exceed the limit. For other harmonics, the probability that IHDi overcomes the limit is negligible.

For the base case, the harmonic pollution at the Point of Common Coupling (PCC) has been evaluated. The current and the harmonic distortion obtained through PLF are shown in Fig. 10.3 and in Table 10.5, respectively.

The values reported in Table 10.5 confirm the respect of IEEE Standard limits. Even considering random fluctuations, the probability to exceed the threshold is negligible.

In order to illustrate the potentials of the proposed approach, we have performed the probabilistic analysis by considering the main topological configurations of
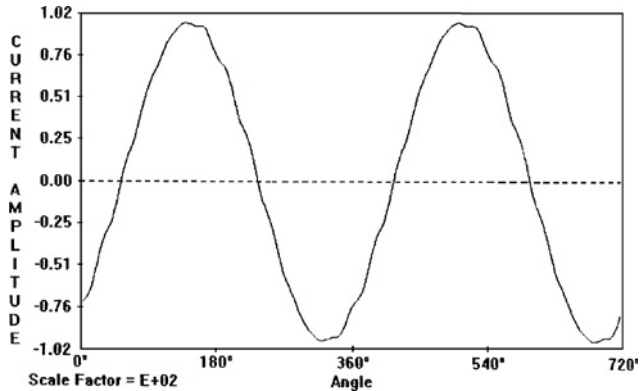
Fig. 10.3. Current at point of common coupling.

Table 10.5. Harmonic analysis at the Point of Common Coupling (PCC).

Moment	IHD11 [%]	IHD13 [%]	IHD15 [%]	THD_V [%]	TDD_I [%]
μ	0.28	0.74	0.11	1.0	1.7
σ	0.02	0.03	0.01	0.01	0.04
Limit	1.75	1.75	1.75	2.5	4.0

the system:

C0: base case

C1: isolated system and GT6 out of service;

C2: GT1, GT2, GT3 and GT6 out of service;

C3: GT2, GT3, GT5 and GT6 in service;

C4: GT4, GT5 and GT6 out of service; and

C5: only GT6 in service and power imported through PCC.

This analysis has been conducted to check if the converters operate under the limit associated to their immunity class defined in EN 60146-1-1 (CENELEC, 1994). The steady state limit of harmonic distortion is equal to 10%.

As an example, we show in Table 10.6 the THD_V and THD_I at power drives for different system configurations. By applying the procedure proposed in Section 10.2, we evaluate that the total probability of exceeding the limits is negligible.

The same approach can be carried out to evaluate the consequence of harmonic pollution on functional features of other components such as condensers and transformers.

Table 10.6. Harmonic analysis for different configurations.

Configuration	Index	Power drive			
		PD 1	PD 2	PD 3	PD 4
C0	THD_V	0.95	0.95	0.82	1.64
	THD_I	7.95	6.81	7.27	8.24
C1	THD_V	1.19	1.18	1.19	1.86
	THD_I	7.47	6.86	7.45	7.68
C2	THD_V	1.22	1.22	1.23	1.64
	THD_I	7.68	7.45	8.01	8.21
C3	THD_V	1.10	1.08	1.18	2.02
	THD_I	7.10	7.23	8.55	8.25
C4	THD_V	1.16	1.18	1.20	1.87
	THD_I	7.25	7.22	8.14	8.23
C5	THD_V	1.18	1.19	1.21	1.90
	THD_I	7.31	7.28	8.15	8.22

Table 10.7. Probabilistic analysis for currents in PD 4 filters.

Moment	C0	C1	C2	C3	C4	C5
μ	1.28	1.31	1.29	1.26	1.35	1.43
σ	0.009	0.010	0.009	0.008	0.010	0.011
prob($I_{eff}/I_1 > 1.3$) [%]	1.30	84.1	13.35	0	99.34	100

For example, the condensers must be able to operate until $I_{eff}/I_1 = 1.3$, where I_{eff} is the r.m.s. of current and I_1 is the current at the fundamental frequency (Xu *et al.*, 1991).

In Table 10.7, we report the mean of I_{eff}/I_1, its standard deviation and the probability that the previous ratio exceeds 1.3 in the case of filters connected to power drive PD 4 for each topological configuration. The table shows severe violations of current limit.

By taking into account the probabilistic results reported in Table 10.7 and the likelihood of each configuration, we estimate the total probability P that the ratio I_{eff}/I_1 exceeds 1.3 is:

$$P(I_{eff}/I_1) = \sum_{i=0}^{5} P((I_{eff}/I_1)/C_i) P(C_i) = 5.49\% \tag{10.20}$$

10.5 Passive Harmonic Filters

Passive harmonic filters are an effective mitigation method for harmonic problems. The passive filter is generally designed to provide a path to divert the troublesome harmonic currents in the power system (Arrilaga *et al.*, 1985).

Providing a phase shift between non-linear loads on different branches can also reduce harmonic currents in power systems. One popular method is the so-called phase multiplication (Mohan *et al*., 1995).

Active filtering techniques (Grady *et al*., 1990) have drawn great attention in recent years. These approaches provide effective filtering of harmonics and elimi-nate some adverse effects of passive filters such as component aging and resonance problems.

Even today, when the active filters have started to emerge as the most effective means of power quality preservation technique, consulting engineers dealing with harmonic mitigation prefer the passive to the active filters for their favorable economic outlook. The main thrust on recent filter research seems to be shifting toward hybrid filters that hold the promise of a more affordable unit cost, while retaining the performance characteristics of the active filter.

The engineering literature abounds on studies that describe the basic design and applica-tions of tuned power filters (Bornits *et al*., 1958; Adamson and Hingorani, 1960; Iliceto *et al*., 1964; Ainsworth, 1965; Steeper and Stratford, 1976; Brewer *et al*., 1996). The problem of minimum filter cost was addressed in Arrilaga (1985) and Kimbark (1971). In these studies, the cost of each filter was considered individually. In Kawann and Emanuel (1996), a cost comparison study between filter centers connected on the MV and LV side is presented, giving that, for non-linear loads exceeding 1 MVA it is more economical to use filter centers connected on the medium voltage side. Based on this consideration, in this chapter a new procedure able to minimise the harmonic reduction filters costs is presented. The main feature of the approach is to treat the amount of MVA installed filters as unknowns of an optimisation problem and confine them in a domain based on admissible harmonic requirements.

The approach is presented for the same case study presented in the previous section and is based on an actual industrial power system. For purpose of lucidity, the synthesis of passive filters has been performed only from a deterministic viewpoint without lack of generality.

10.6 Minimal Cost Design for Harmonic Reduction

In this section, we show how an optimisation methodology is helpful to treat the problem of the economic cost associated to the filter centers and the integration with equality and inequality constraints. The constraints are the harmonic load flow and the harmonic limits. Harmonic standards (IEEE, 1993; EN, 1997) provide the voltage and current harmonic limits.

The design of the filter centers can be formulated as an optimisation procedure where:

- – the economic cost of the filters is minimised;
- – inequality constraints ensure the satisfaction of the voltage and current harmonic limits in a power system;

– equality constraints derive from the power system representation i.e. from the HPF.

The basic elements of the procedure are defined as follows.

Independent variables The variables that need to be adjusted in order to minimise the economic cost are:

$$\boldsymbol{u} = \left[Q_1, \ldots, Q_j \ldots, Q_{N_c} \right]^{\mathrm{T}}, \tag{10.21}$$

where Q_j represents the capacitive reactive power injected by the filter center connected to generic jth bus and N_c is the number of the controlled bus, i.e. the buses which the filters are connected. We assume that the location of filters is known.

Objective function The main objective of the procedure is to minimise the total economic cost due to the filter centers. For this purpose, the following objective function is assumed:

$$C(\boldsymbol{u}) = \sum_{j=1}^{N_c} k_j Q_j, \tag{10.22}$$

where k_j represents the MVAr cost of installed filters.

Equality constraints The main index used to describe the effects of harmonics in power system is the well-known Total Harmonic Distortion THD. For voltages, THD can be defined as:

$$\mathrm{THD}_i^V = \frac{\sqrt{\sum_{h=2}^{\infty} V_h^2}}{V_1}, \tag{10.23}$$

where the subscript i denotes that THD is evaluated at the i-th bus. Analogously a THD for currents can be defined as:

$$\mathrm{THD}_i^I = \frac{\sqrt{\sum_{h=2}^{\infty} I_h^2}}{I_1} \tag{10.24}$$

Previous equations can be rewritten in the following compact form, evaluated for the overall system, performing the harmonic related equality constraint:

$$\mathbf{THD} - \mathbf{g}(\mathbf{V}) = 0, \tag{10.25}$$

where:

$$\mathbf{THD} = \lfloor \mathrm{THD}_1^V, \mathrm{THD}_1^I, \ldots, \mathrm{THD}_i^V, \mathrm{THD}_i^I, \ldots, \mathrm{THD}_{N_c}^V, \mathrm{THD}_{N_c}^I \rfloor \tag{10.26}$$

The other equality constraints involve the harmonic Power Flow equations:

$$F(V, \boldsymbol{u}) = 0 \tag{10.27}$$

Harmonic inequality constraints The main constraint in designing filter centers in power system is the ability of these devices to minimise the harmonic voltages and current magnitudes to acceptable levels as defined in (IEEE, 1993; EN, 1997).

In our formulation, the harmonic constraints are defined as follows:

$$\text{THD}_i \leq \alpha_i \qquad i = 1, \ldots, N_c \tag{10.28}$$

where α_i represents the limit imposed by the standards at the same bus.

Under the previously illustrated assumptions, the overall optimisation problem can be formulated as:

$$\min_{\mathbf{u}} C(\boldsymbol{u}) \tag{10.29}$$

subject to:

$$F(\boldsymbol{V}, \boldsymbol{u}) = 0$$
$$\mathbf{THD} - \boldsymbol{g}(V) = 0$$

and

$$\text{THD}_i \leq \alpha_i \quad i = 1, \ldots, N_c.$$

10.7 Optimisation Algorithm

By the use of the "penalty factor method", the problem formulated in Section 10.3 can be treated as a minimisation problem in presence of the sole equality constraints by the use of Lagrange multipliers (Dommel and Tinney, 1968; El-Abiad, 1983).

To take into account inequalities related to **THD**, the following penalty function is defined:

$$C_p(\mathbf{THD}) = \sum_{k=1}^{N_c} w_k(\text{THD}_k - \alpha_k)^2 \tag{10.30}$$

where

$$w_k = \begin{cases} 0 & \text{if} \quad \text{THD}_k \leq \alpha_k \\ 1 & \text{otherwise} \end{cases}$$

By applying the optimisation method of Lagrangian multipliers to the evaluation of the minimum of the function $(C + C_p)$, it is possible to determine the solution of the problem

stated above. In fact, introducing as many auxiliary variables as equality constraints and minimising the unconstrained Lagrangian function:

$$L = C(\boldsymbol{u}) + C_{\mathrm{p}}(\mathbf{THD}) + \lambda^T \boldsymbol{F}(\boldsymbol{V}, \boldsymbol{u}) + \mu^T (\mathbf{THD} - \boldsymbol{g}(\boldsymbol{V})) \tag{10.31}$$

where λ and μ, are Lagrangian multiplier vectors of dimensions $2N_p$ and N_c respectively.

From Eq. 10.31, the set of necessary conditions follows:

$$\frac{\partial \boldsymbol{L}}{\partial \boldsymbol{V}} = \lambda^T \frac{\partial \boldsymbol{F}}{\partial \boldsymbol{V}} - \mu^T \frac{\partial \boldsymbol{g}}{\partial \boldsymbol{V}} = 0 \tag{10.32}$$

$$\frac{\partial L}{\partial \mathbf{THD}} = \frac{\partial C_{\mathrm{p}}}{\partial \mathbf{THD}} + \mu^T = 0 \tag{10.33}$$

$$\frac{\partial L}{\partial \boldsymbol{u}} = \frac{\partial C}{\partial \boldsymbol{u}} + \lambda^T \frac{\partial F}{\partial \boldsymbol{u}} = 0 \tag{10.34}$$

$$\frac{\partial L}{\partial \lambda} = \boldsymbol{F}(\boldsymbol{V}, \boldsymbol{u}) = 0 \tag{10.35}$$

$$\frac{\partial L}{\partial \mu} = \mathbf{THD} - \mathbf{g}(\boldsymbol{V}) = 0 \tag{10.36}$$

To solve the set of first-order necessary conditions for optimisation, we adopted the Generalised Reduced Gradient method (GRG) (Dommel and Tinney, 1968; El-Abiad, 1983).

The algorithm stops if the modulus of the gradient vector is less than a fixed tolerance, otherwise the vector of the independent variables is updated as follows:

$$\boldsymbol{u}^{\mathrm{new}} = \boldsymbol{u}^{\mathrm{old}} + \chi \frac{\partial L}{\partial \boldsymbol{u}} \tag{10.37}$$

where χ is an accelerating factor which can be assessed on the basis of various algorithms or heuristic techniques.

10.8 Case Study

The case study is related to the previous example shown in Fig. 10.1. Double radial structure characterises the distribution network. The main harmonic sources are:

4 electronic power converters (12 pulse) with total active power of 45 MW;

several DC speed adjustable drives (5 MW);

fluorescent lamp (1 MW);

a miscellaneous of various non-linear loads.

Table 10.8. Iterative process.

Iter. #	C [million$]	THD 43 [%]	THD 46 [%]	THD 49 [%]	THD 54 [%]
0	0	37.6	37.7	37.7	38.6
2	1.22	15.9	16.2	16.2	11.9
4	1.49	8.3	9.4	9.4	8.3
6	1.78	3.4	3.6	3.7	3.4
8	1.62	4.8	4.9	4.9	4.9

Four filter centers are installed in proximity of the four power converters.

As reported in IEC (1994), the limit α_i is evaluated considering the I_{SC}/I_L ratio, where I_{SC} and I_L represent, respectively, the available short circuit current and 15 or 30 min (average) maximum demand current. Another parameter for fixing the THD limits is the range of the fundamental voltage magnitude, in order to apply standard (IEC, 1994).

For our tests, we used a DEC ALPHA SERVER 4100/400 characterised by a CPU type 21164 ALPHA 400 MHz, 4 MB L2 cache, 2 GB RAM and 16 GB RAID disk space.

In all simulations, the fundamental frequency was assumed equal to 50 Hz.

Since the pulse number of the converter was twelve, the filters were tuned for the 5-th and 11-th harmonic order.

The case under investigation refers to the worst case with regard to the harmonic levels. The configuration network in which the GT11 generating unit satisfies the entire load demand characterises this case.

Table 10.8 shows the behaviour of the iterative process in calculating the total cost and the THD for the bus nos. 43, 46, 49 and 54 on which the filters are connected.

From the table shown below, it is possible to observe how the methodology is able to adjust the system in terms of harmonic reduction. At the same time, the algorithm is capable of improving the economic cost. In fact, at the iteration 6, the THD at the selected buses decreases satisfying the limits fixed by standard referred into (IEEE, 1993; EN, 1997). The economic cost increases due to the low weight of this cost function C with regard to C_p. When the penalty function C_p vanishes, the economic cost is the sole concern of the optimisation. Consequently, this function decreases giving, when the algorithm stops, an economic cost of 1.62 million USD. A simple comparison between a design of the filter centers based on sole technical aspects, and this algorithm gives a gain of about 9% (compare iterations 6 and 8).

References

Adamson C., Hingorani N.G., *High voltage direct current power transmission*, Garraway Ltd., London, 1960, p. 168.

Ainsworth J.D., "Filters, damping circuits and reactive Volt-Amps in HVDC converters," in *High Voltage DC Convertors and Systems*, B.J. Cory, Ed. Macdonald, London, 1965, pp. 137–174.

Anders G.J., *Probability concepts in electric power systems*, John Wiley & Sons, New York, 1990.

Arrilaga J., Callaghan C.D., "Three phase ac-dc load and harmonic flow," IEEE Trans. Power Del., **6** (1991) 238–244.

Arrilaga J., Brandley D.A., Bodger P.S., *Power system harmonics*, John Wiley & Sons, New York, 1985.

Bornits E., Hoffmann M., Leiner G., "Harmonics in electrical system and their reduction through filter circuits," CIGRE Report No. 304, 1958.

Brewer G.L., Clarke C.D., Gavrilovic A., "Design consideration of AC harmonic filters," Conf. on HVDC Transmission, University of Manchester, Sept. 1996, pp. 277–279.

Carpinelli G., Esposito T., Varilone P., Verde P., "First order probabilistic harmonic load flow," IEE Proc. Generation Transmission and Distribution, **148** (2001) 541–548.

CEI 33-7 "Shunt capacitors for a.c. power system having a rated voltage above 1000V."

CENELEC, "Voltage characteristic of electricity supplied by public distribution systems," Standard, EN 50160, 1994.

Chang G., Xu W., "An overview of harmonics modeling and simulation," IEEE PES Tutorial on Harmonics Modeling and Simulation, TP-125-0 (1998a) 1–7.

Chang G., Xu W., "Modeling of harmonic sources: Power Electronic Converters," IEEE PES Tutorial on Harmonics Modeling and Simulation, TP-125-0 (1998b) 28–34.

Currence E.J., Plizga J.E., Nelson H.N., "Harmonic resonance at a medium-sized industrial plant," IEEE Trans. Ind. Appl., **31** (1995) 682–690.

Dommel H.W., Tinney T.F., "Optimal load flow solutions" IEEE Trans. Power Apparatus and Syst., Vol. PAS-87, 1968.

El-Abiad A.H., *Power system analysis and planning*, Hemisphere Publishing Corporation, USA, 1983.

Ellis R.G., "Harmonic analysis of industrial power systems," IEEE Trans. Ind. Appl., **32** (1996) 417–422.

EN 60146-1-1, 1997-09 "Semiconductor converters. General requirements and line commuted converters. Part 1-1: specifications of basic requirements," 1997.

Grady W.M., Instructions for performing Load Flow, short circuits and motor starting calculations (PCFLOH, PCFLO, HARMPLOT), 1999.

Grady W.M., Samotyj M.J., Noyola A.H., "Survey of active power line conditioning methodologies," IEEE Trans. Power Del., **5(3)** (1990) 1536–1542.

IEC, "Electromagnetic compatibility (EMC) – Part 2: Environment – Section 2: Compatibility levels for low-frequency conducted disturbances and signalling in public low-voltage power supply systems," Standard, IEC 61000-2-2, 1990.

IEC, "Electromagnetic compatibility (EMC) – Part 2: Environment – Section 4: Compatibility levels in industrial plants for low-frequency conducted disturbances, Standard, IEC 61000-2-4, 1994.

IEEE, "IEEE Recommended Practices and Requirements for Harmonic Control in Electrical Power Systems," Standard, IEEE 519-1992, New York, April 1993.

Iliceto F., Ainsworth J.D., Goodrich F.G., "Some design aspects of harmonic filters for HVDC transmission systems," CIGRE Report No. 405, 1964.

Jalali S.G., Lasseter R.H., "A study of non linear harmonic interaction between a single phase line-commuted converter and a power system," IEEE Trans. Power Del., **9** (1994) 1616–1621.

Kawann C., Emanuel A.E., "Passive shunt harmonic filters for low and medium voltage: a cost comparison study," IEEE Trans. Power Syst., **11(4)** (1996) 1825–1831.

Kimbark E.W., *Direct Current Transmission*, Vol. 1, John Wiley & Sons, New York, 1971.

Mohan N., Undeland T.M., Robbins W.P., *Power Electronics – Converters, Applications and Design*, John Wiley & Sons, New York, 1995.

Morrison R., Probabilistic analysis of harmonic currents in power systems, IEEE-PES Winter Meeting 2002, New York.

Sharma V., Fleming R.J., Niekamp L., "An iterative approach for analysis of harmonic penetration in power transmission network," IEEE Trans. Power Del., **6(4)** (1991) 1698–1706.

Simpson R.H., "Instrumentation, measurement techniques and analytical tools in Power Quality studies," IEEE Trans. Ind. Appl., **34** (1998) 534–548.

Sutherland P.E., "Harmonic measurement in industrial power systems," IEEE Trans. Ind. Appl., **31** (1995) 175–183.

Steeper D.E., Stratford R.P., "Reactive compensation and harmonic suppression for industrial power systems using thyristor converters," IEEE Trans. Ind. Appl., **IA-12(3)** (1976) 232–254.

Testa A., Castaldo D., Langella R., Probabilistic aspects of harmonic impedances, IEEE-PES Winter Meeting 2002, New York.

Xu W., Rose J.R., Dommel H.W., "A multiphase harmonic load flow solution technique," IEEE Trans. Power Syst., **6** (1991) 174–182.

CHAPTER 11

Shunt Active Filters to Mitigate Harmonic Propagation in Distribution Lines

Agostino Lecci, Marco Liserre, and Antonio Dell'Aquila

Abstract

The aim of this chapter is to treat the single-phase, three-phase and four-wire shunt active filters both with respect to control issues and implementation issues. In the first case, traditional control methods and innovative ones are discussed and in the second case the procedure to develop microcontroller algorithm is addressed. The chapter includes basic topologies and standard operation of shunt active filters; traditional control techniques (hysteresis and predictive); innovative control techniques (fuzzy-logic based and Nelder-and-Mead based); algorithms development on microcontroller.

11.1 Introduction

Several power converters can be effectively utilised to improve the quality of power supplied to the customers. An initial application of power electronics to power systems was through high voltage direct current (HVDC) transmission, while subsequently many devices were employed to achieve better operations in AC transmissions that were generally known as flexible AC transmission system (FACTS) controllers.

As regards distribution systems, power electronic devices can be utilised to increase the reliability and the quality of power supplied to the customers. Basically, it is possible to classify power quality enhancement devices into two types: network reconfiguring type and compensating type. The network reconfiguring equipments are often used for fast current limiting and current breaking during faults as well as for fast load transfer to an alternate feeder in case of problems in the supplying feeder. On the other hand, the compensating devices are used to filter out undesired components, to compensate for the

unbalanced loads, to raise the power factor, to regulate voltage level and to compensate for voltage dips and voltage sags.

It is possible to highlight outstanding devices in the compensating converter family at distribution level, where generally a voltage source inverter is the basic core:

Distribution STATic synchronous COMpensator (DSTATCOM): This is a shunt connected device that has the same structure as that of a STATCOM but generally it is made up of IGBTs instead of GTOs, mostly used in transmission applications. The DSTATCOM can perform load compensation, i.e. power factor correction, harmonic filtering and load balancing. It must be able to inject an imbalanced and harmonically distorted current to eliminate imbalance or distortions in the load current or the supply voltage.

Dynamic Voltage Restorer (DVR): This is a series connected device. The main purpose of this device is to protect sensitive loads from sag/swells i.e. interruptions in the supply side. This is accomplished by rapid series voltage injection to compensate the drop/rise in the supply voltage. Moreover, both reactive and active power injection into the grid can be carried out by means of proper regulation of control action.

Unified Power Quality Conditioner (UPQC): This is a versatile device that can inject current in shunt and voltage in series simultaneously in a dual control mode. Therefore, it can perform both the functions of the load compensation and voltage control at the same time.

Active filters (AFs): Originally proposed to compensate for harmonic distortion, these devices can be considered as a fully functional compensating device with respect to both reactive power and voltage.

11.2 Active Filters

Active filters are power converters utilised in order to compensate power quality disturbances. In order to meet quality enhancement constraints proper control of their power switches is needed. Several names have been introduced in the literature and in commercial implementations for these converters, that highlight different aspects of their compensation tasks. Some names and acronyms are:

- Active Filters (AFs);
- Active Power Filters (APFs);
- Active Power Line Conditioners (APLCs);
- Active Power Quality Conditioners (APQCs);
- Instantaneous Reactive Power Compensators (IRPCs);
- Power Quality Filters (PQFs);
- Shunt Active Filters (SAFs).

A major advance in the development of AFs has resulted from the electronics revolution. Initially the use of discrete analogue and digital components was introduced, then the focus has been addressed to microprocessors, microcontrollers, digital signal processors to recently reach programmable logic devices, FPGA and so forth. This development has made it possible to implement many control algorithms, ranging from the simpler hysteresis band and proportional integral ones, to variable-structure control, fuzzy logic, genetic algorithm and neural networks based ones, thus allowing the achievement of a large number of compensation tasks while keeping a fast control code execution and lowering systems costs. Several topologies serve as active compensators and thus are anyway considered active filters. As a consequence, a classification is needed. These converters can be classified according to several categories that range from converter type, to topology, and the number of phases. The converter type can be either current source inverter (CSI), or voltage source inverter (VSI) bridge structure while the topology of connection can be shunt, series or a combination of both. As regards the number of phases, active filters can be two-wire (single phase) and three- or four-wire three-phase systems. As regards the converter type, the current-fed inverter bridge behaves as a non-sinusoidal current source to meet the harmonic current requirement of the non-linear load and to compensate for undesired components. The other converter type is a voltage-fed inverter; a single-phase example of which is shown in Fig. 11.1. The single phase half bridge VSI has a self-supporting DC voltage bus with a large split DC capacitor. Several advantages made this topology interesting: it is lighter, cheaper and expandable to multilevel versions.
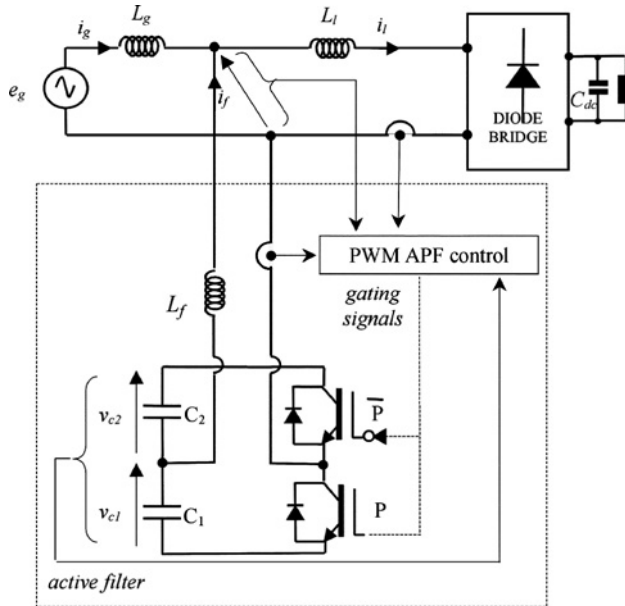
Fig. 11.1. Single-phase VSI-based SAF.

Active filters can also be classified based on the topology of their connection to the distribution system. They can be series or parallel connected to the grid thus being classified as series or SAFs, while a combination of both connections generally leads to a UPQC. Combinations of active and passive filters are known as hybrid filters. As already mentioned, Fig. 11.1 is an example of an SAF, which is generally used to eliminate current harmonics, to compensate reactive power and to reduce load unbalance in three-phase systems. It is generally connected at the load end, which is generally the source of harmonics components. The SAF generates compensating currents to cancel out harmonics and/or reactive components of the non-linear load current at the point of connection. On the other end, series AF is connected in series with the line, generally by means of a matching transformer, and it is used to eliminate voltage harmonics, balance and regulate the terminal voltage of the load or line. The use of hybrid topology have several advantages. The presence of passive components strengthening compensating action and withstanding lower order harmonics compensation, allows the adoption of solid-state devices of reduced size and cost.

The main topics related to the use of AFs are:

- Point of installation of the active filter. There are two main compensating approaches: load level or system level. Generally the load level approach is chosen by the consumer. In order to choose the better compensation, the type of polluting source should be classified as current harmonic or voltage harmonic source (Akagi, 1996; Peng, 1998). On the contrary the system level approach is chosen by the electric utility. In order to damp harmonic propagation and ensure stability the best point of installation and the best harmonic detection method should be chosen (Akagi, 1996);

- Design and control of the AF. A design procedure should be selected for the rating of the AF passive elements on the basis of distorting load characteristics such as the current amplitude and its maximum derivative value.

11.3 Identification of the Polluting Load

A typical polluting load is considered in the following analysis. The considered polluting load is a motor drive. The first stage of the power conversion process that links the grid to the motor is responsible for the harmonic distortion of the grid currents and consequently of the grid voltages at the point of common coupling (PCC) because of the inductance existing upstream of the PCC. In the majority of commercial drives, the first stage is a diode or thyristor rectifier connected to the grid with an essentially inductive filter. The size of the inductive filter influences the current harmonic pollution: a high inductance value allows a mitigation of the harmonic content. However, the nature of the filtering stage on the DC side is responsible for the kind of distorted current waveforms drained by the grid. In fact according to the impedance of the rectifier seen by the grid, the drive could be classified into two types of harmonic sources (Thomas *et al*., 1998). The first is the case when there is, in the DC side, a sufficient inductance, that produces a smoothing effect and therefore an almost constant DC current. In the low harmonic

spectrum the DC impedance is greater with respect to the one on the AC side:

$$\omega L_\mathrm{g} < \omega L_\mathrm{DC} \tag{11.1}$$

Thus the rectifier stage can be considered as a current source from the grid side. This is due to the fact that the produced current harmonic pollution depends mainly on the size of the DC side inductance rather than on the AC side.

This is usually the case of a big thyristor bridge that feeds a DC motor, as shown in Fig. 11.2. If the bridge works in continuous conduction mode the load currents are characterised by a THD lower than 40% (Fig. 11.3). The compensation with an SAF is not a highly demanding task as shown by many scientific publications and industrial applications (Dell'Aquila *et al.*, 1999). In fact if the motor drive is considered as a sum of sinusoidal current sources of different frequencies and phases, the connection in parallel of the current controlled SAF compensates exactly the non-fundamental frequency sources and the fundamental current phase displacement. This process is not influenced by the amount of inductance upstream and downstream the point of connection of the SAF, in fact generally, the polluting load impedance ωL_DC is much higher than the grid impedance ωL_g.

In the second case, instead, the DC side is characterised by the presence of a limited DC inductance and a DC smoothing capacitor allowing an almost constant DC voltage.

(a)

(b)
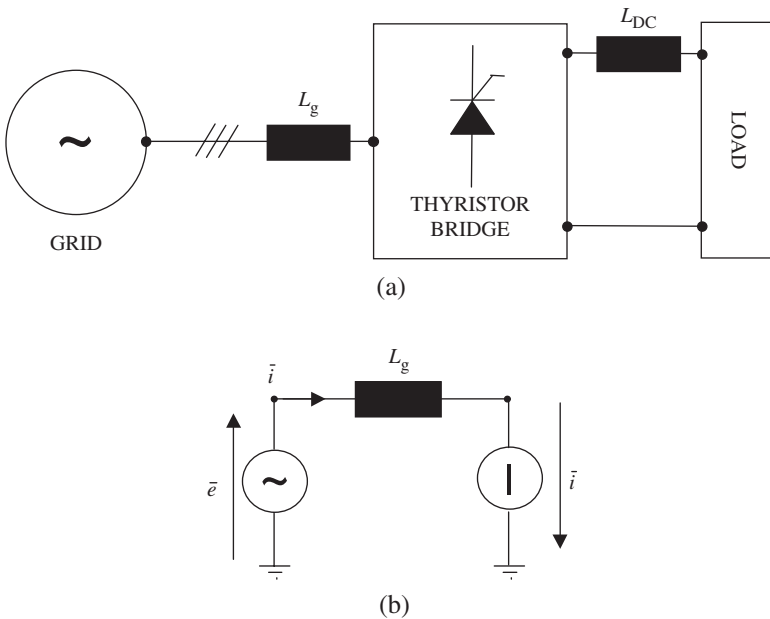
Fig. 11.2. (a) Grid-connected thyristor bridge and (b) its single phase equivalent if $\omega L_\mathrm{g} < \omega L_\mathrm{DC}$.
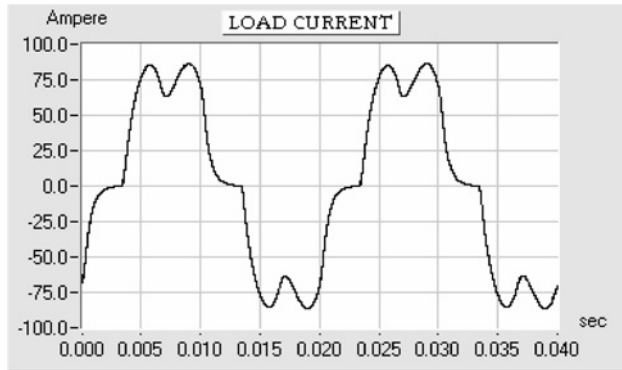
Fig. 11.3. Example of thyristor bridge polluting current.

In the low harmonic spectrum the DC impedance is limited with respect to the AC side one:

$$\omega L_g > 1/\omega C_{DC} \tag{11.2}$$

Thus, the rectifier stage can be considered as a voltage source from the grid side. This is due to the fact that the current harmonic pollution produced depends mainly on the size of the AC side inductance rather than that on the DC side.

This is usually the case of a diode bridge that feeds an inverter or a chopper, as shown in Fig. 11.4. The first is the classical diode-rectifier front-end-type PWM–VSI induction motor drive: depending on the size of the AC inductive filter the rectifier may work in discontinuous conduction mode determining a highly distorted grid current with a THD of 40–60% with a high level of fifth and seventh harmonics (Fig. 11.5).

The compensation with an SAF is a challenging task (Buso *et al.*, 1998). In fact the motor drive can be considered as a sum of sinusoidal voltage sources, of different frequencies and phases. Thus, the compensation due to the connection in parallel of the current-controlled AF depends on the amount of inductance upstream and downstream the point of connection of the AF. In fact the polluting currents depend on the impedance on the grid side because the DC link impedance is low. The parallel AF modifies the impedance that limits the polluting current. For a very low load side impedance the compensation becomes very difficult and the polluting current could become very high. Thus, the AF should have a very good control and may be overrated and consequently not economical.

11.4 Shunt Active Filters (SAFs)

The SAFs can be used to compensate several disturbances in power distribution systems. The main compensation action is generally the elimination of current harmonics flowing

(a)

(b)
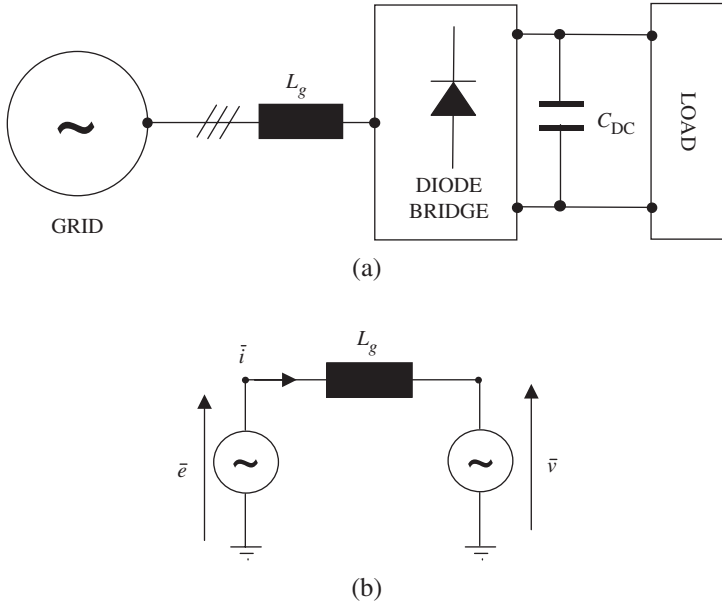
Fig. 11.4. Diode bridge: (a) seen as voltage harmonic source in the single phase equivalent and (b) ($\omega L_g < \omega L C_{DC}$).

Fig. 11.5. Example of diode bridge polluting current.

through the lines. The large diffusion of non-linear loads drawing distorted current waveforms causes the presence of stiff harmonic components in the spectrum of waveforms. Harmonic components in current have several consequences in electric equipments thus leading to economic losses. The use of an SAF can lead to the compensation of harmonic current components since it can generate compensating currents that sum up with damaging waveforms and as a result, reduce harmonic presence in the grid. The SAFs

may be controlled in order to solve many other problems in distribution systems. An example of further compensation by means of SAF is the reactive power compensation. Due to the possibility to synthesise a current waveform, it is possible to manipulate the AF to generate a current achieving a unity power factor. In three-phase systems, SAFs could be required to compensate for load current unbalance and for excessive neutral current.

The topology of SAF is directly related to its connection to the grid. In three-phase systems there is a difference in topology due to the presence or absence of neutral wire. The three legs of VSI output are connected to the three phases of electrical line. In case of neutral wire, it could be necessary to connect it to the SAF. The connection can be done directly to the middle point of VSI DC bus, i.e. the split capacitors, or to a fourth inverter leg. In single-phase systems full bridge or half bridge topologies are mainly used. Even a half-bridge topology can achieve interesting results in harmonics and reactive power compensation, as discussed in several studies (Al-Haddad and Joos, 1997; Bakhshai *et al.*, 2003; Dell'Aquila *et al.*, 2003; Wu *et al.*, 2005). The choice of the point of installation is a key feature in SAF design. One of the preferred solutions is the installation next to the harmonic source. One of the advantages of this choice is that when the filter is installed next to a highly polluting load, the shunt connection of non-linear load and active filter is equivalent to a virtual resistive component.

The control techniques studied for AFs have a cascade structure. Thus, there are two loops: an inner loop responsible for the AC current control and an outer loop responsible for the DC voltage control. However, the DC voltage controller calculates only the fundamental harmonics of the reference current, that should charge or discharge the capacitor, while the other harmonics of the reference current are calculated on the basis of the desired compensation. In other words, the outer loop decides which current should be injected by the AF to compensate the polluting load current and to ensure the DC link voltage level that is needed for the optimal operation of the AF.

In the following subsection, the AC current reference calculation and the AC current control will be addressed separately.

11.4.1 Reference current generation

In theory, this reference current can be obtained by subtracting the whole fundamental frequency line current from the distorted load current. However, the proposed voltage regulation system acts on the amplitude of the subtracted current with a gain k, in order to let a part of the fundamental frequency current to be fed or drained by the AF. The optimum amount of this fundamental frequency current is computed by a control loop which works by evaluating the voltage error amplitude and the slope of the average DC bus voltage. Figure 11.6 shows a block scheme of the control system. Active filter current control is performed by the block denominated in the same way, the output of which is the optimum duty cycle for inverter switches. The conversion duty-cycle/time-signals is achieved by the block denominated "PWM switching". The block "power circuit" includes the line, AF and load; the outputs derived from this block are those used as feedback signals and to obtain the reference waveforms.
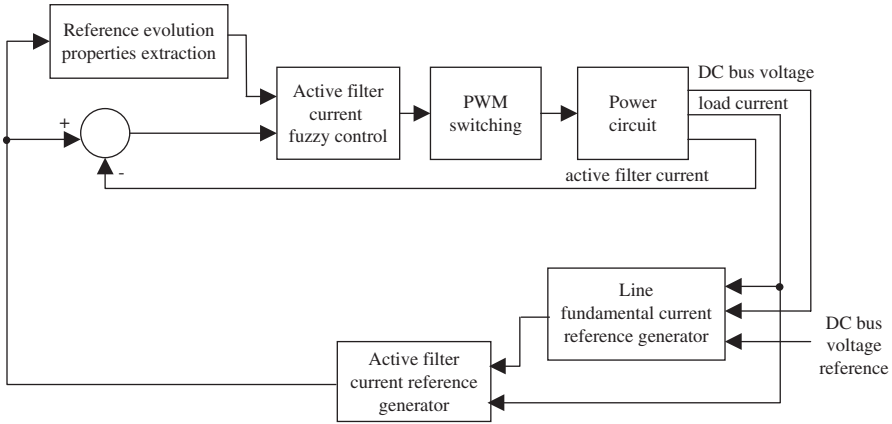
Fig. 11.6. Block scheme of the control system.
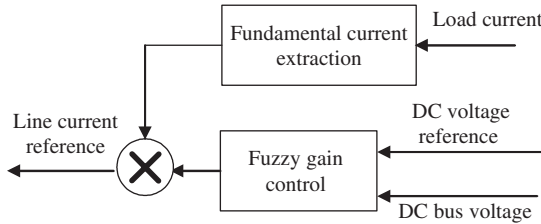
Fig. 11.7. Line fundamental reference generator block.

The DC bus voltage control, performed by the block named "Line fundamental reference generator" is described in detail in Fig. 11.7. It is made up of a block implementing the extraction of the fundamental load current, the amplitude of which is modulated by a gain k. The value of k is quite near unity; when k is above unity, more power is required by the line than that required by the load. Power in excess is drawn by the AF which lets the DC capacitor charge. When k is below unity, the DC bus voltage decreases. By power considerations it results that, neglecting the power exchanged with AF, the power fed by the line, P_S, is equal to the power absorbed by the load, P_L. Indicating with V_S is the line voltage peak value, while I_{L1} and I_S are the peak values of load fundamental current and line current, respectively, then we have:

$$P_L = \frac{3}{2} V_S I_{L1} \cos \varphi_{L1} = P_S = \frac{3}{2} V_S I_S \tag{11.3}$$

In order to charge the DC bus capacitor $P_S > P_L$ is required. This relation, applied to currents, results in:

$$I_S > I_{L1} \cos \varphi_{L1} \tag{11.4}$$

11.4.2 p–q method

The reference current for the control of the AF could also be calculated using the active and reactive power analysis in a stationary $\alpha\beta$ frame. Grid currents and phase voltages of a three-phase system expressed in $\alpha\beta$ frame are given by:

$$\begin{bmatrix} i_\alpha \\ i_\beta \end{bmatrix} = \sqrt{\frac{2}{3}} \begin{bmatrix} 1 & -\frac{1}{2} & -\frac{1}{2} \\ 0 & \frac{\sqrt{3}}{2} & -\frac{\sqrt{3}}{2} \end{bmatrix} \begin{bmatrix} i_a \\ i_b \\ i_c \end{bmatrix} \tag{11.5}$$

$$\begin{bmatrix} e_\alpha \\ e_\beta \end{bmatrix} = \sqrt{\frac{2}{3}} \begin{bmatrix} 1 & -\frac{1}{2} & -\frac{1}{2} \\ 0 & \frac{\sqrt{3}}{2} & -\frac{\sqrt{3}}{2} \end{bmatrix} \begin{bmatrix} e_a \\ e_b \\ e_c \end{bmatrix} \tag{11.6}$$

where i_a, i_b, i_c are the line currents and e_a, e_b, e_c are the three-phase grid voltages. The instantaneous real power and the instantaneous imaginary power absorbed by the load are, respectively, defined as follows:

$$p_l = e_\alpha i_\alpha + e_\beta i_\beta \tag{11.7}$$

$$q_l = e_\alpha i_\beta - e_\beta i_\alpha \tag{11.8}$$

p_l and q_l are made up of a DC and an AC component, so that they may be expressed by:

$$p_l = \bar{p}_l + \tilde{p}_l \tag{11.9}$$

$$q_l = \bar{q}_l + \tilde{q}_l, \tag{11.10}$$

where $\bar{p}_l$ and $\bar{q}_l$ are DC components while $\tilde{p}_l$ and $\tilde{q}_l$ are AC components.

Assuming that phase voltages do not contain harmonic components, $\bar{p}_l$ and $\bar{q}_l$ are due to fundamental currents, while $\tilde{p}_l$ and $\tilde{q}_l$ are due to harmonic currents.

In order to generate the current reference, a balance between instantaneous powers supplied by the grid and the AF and drained by the load is to be computed. If p_g and q_g are the real and imaginary instantaneous powers supplied by the main, while p_f and q_f are the real and imaginary instantaneous powers supplied by the APF, in order to compensate reactive power and eliminate harmonic currents, the grid should supply $p_g = \bar{p}_l$ and $q_g = 0$. The oscillatory component of p_l is to be fed by APF, while q_l must be fully fed by the APF because it is also possible in this way to achieve reactive power compensation. The oscillatory part of p_l is due to harmonic components, so if it is fed to the load

by the AF, grid current remains sinusoidal, while the load keeps on receiving the same amount of harmonic and fundamental current. Power balance yields:

$$p_g = \bar{p}_l$$
$$q_g = 0$$
$$p_f = p_l - p_g = p_l - \bar{p}_l = \tilde{p}_l \qquad (11.11)$$
$$q_f = q_l - q_g = q_l$$

Previous equations need to be modified in order to consider proper operation of the capacitor on the DC side of the inverter. The capacitor stores energy which is utilised as a power supply for the normal operation of the AF. More in detail, in normal operating conditions the APF does not feed active power because it should be able to supply $p_f = \tilde{p}_l$ and $q_f = q_l$ and so only reactive power is fed. For this reason, capacitor voltage level is constant during the steady state.

A control of voltage value is needed to regulate voltage level in the steady state and to limit the variability of voltage during transients and during start up. So the calculation of current reference wave should consider the need to move power balance in order to charge or discharge the DC side capacitor of the AF. In order to regulate DC voltage level, it is necessary to control active power balance among the grid, load and APF. When the load absorbs a precise quantity of power $\bar{p}_l$ and if $p_g > \bar{p}_l$ excess power is drawn by the APF, which increases the DC side voltage. If $p_g < \bar{p}_l$, since the load needs a precise amount of power, the APF feeds the remaining part in order to have $\bar{p}_g + \bar{p}_f = \bar{p}_l$ and hence the DC voltage level decreases. To control the proper amount of active power fed or drawn by the APF, it is necessary to introduce a gain factor 'k' (Dell'Aquila *et al.*, 2001) which is the amount of load active power fed by the grid, i.e. the ratio between $\bar{p}_g$ and $\bar{p}_l$:

$$k = \frac{\bar{p}_g}{\bar{p}_l} \qquad (11.12)$$

In normal conditions this gain is quite near unity, except for negligible losses in APF components. When DC capacitor charging is needed, the gain factor is above unity because grid must supply an additional amount of active power to the APF. When DC voltage level is too high, gain factor is regulated to values below unity, so a power less than $\bar{p}_l$ is required to the grid and the remaining part of $\bar{p}_l$ is fed to the load by the AF. Hence the instantaneous reference powers for the AF are:

$$p_f^* = \tilde{p}_l + (1 - k)\bar{p}_l$$
$$q_f^* = q_l \qquad (11.13)$$

A transformation from instantaneous powers to currents allows to generate proper reference waves for current control according to the following equation:

$$\begin{bmatrix} i_{f\alpha} \\ i_{f\beta} \end{bmatrix} = \begin{bmatrix} e_\alpha & e_\beta \\ -e_\beta & e_\alpha \end{bmatrix}^{-1} \begin{bmatrix} p_f \\ q_f \end{bmatrix} \tag{11.14}$$

11.4.3 APF AC current control

The AF current reference has a wide harmonic spectrum and the whole signal is dependent on the polluting load. If one wants to use traditional regulators, an on-site virtual instrumentation measurement and simulation campaign can be a good solution for a load-oriented tuning of the controllers (Dell'Aquila *et al.*, 1999). On the other hand, fuzzy current controllers can offer more flexibility in the design but a mathematical frame is needed in order not to lose too much time in the tuning process. Anyway the current control has to be fast and accurate, hence hysteresis and predictive controllers are the preferred solutions (Dell'Aquila *et al.*, 2003). Then the fuzzy-logic-based or Nealder-and-Mead-based algorithms can be used to optimise their behaviour.

11.4.3.1 Hysteresis current controller   The hysteresis current controller offers a good compensation action even for polluting currents characterised by high peaks. Hysteresis controllers are robust and achieve very fast dynamic response at the expense of poor steady-state performance, with current errors of up to twice the hysteresis band and a variable switching frequency. The use of a variable hysteresis band to control switching frequency is an approach to overcome the problems of the basic control strategy (Malesani *et al.*, 1997).

11.4.3.2 Predictive current control   Predictive controllers can be successfully adopted for AFs due to their fast response and to the simple algorithm, which allows a short execution time.

The dead-beat and predictive current control algorithms offer both fast dynamic response and good steady-state performance. When the choice of the switching pattern (driving duty cycle or asynchronous switching sequence) is made in order to nullify the error at the end of the sample period, the predictive controller is often called dead-beat controller. The dead-beat technique predicts at the beginning of each sampling period, the current error vector on the basis of the actual error and of the output side parameters. The switching status to be applied by the control during the next sampling period is thus determined, so as to minimise the forecast error. Hybrid current controls combining predictive and hysteresis techniques have also been proposed. Dead-beat technique suffers from sensitivity to parameter variations due to the circuit model utilised in the design of the controller and to the absence of the integrator action. Constant switching frequency predictive algorithm may be utilised to avoid switching problems typical of hysteresis control technique. In this case, the predictive algorithm calculates the duty cycle of driving signal once in every sample period. This will force the current waveform according to its command. In this case the current ripple is variable but the switching frequency

is fixed. The disadvantage of this algorithm is that it does not guarantee the inverter peak current limit.

11.4.3.3 Predictive current control in case of half-bridge SAF topologies Half-bridge topology is a variable structure system: there are two possible configurations, shown in Fig. 11.8 that can be individuated by the switch state variable "P". In the following a current control is introduced in order to choose the switch position P at the instant k.

The goal of current control is to lower the current tracking error $e(k)$. Tracking error is defined as follows:

$$e(k) = i_F^*(k) - i_F(k) \tag{11.15}$$

If in sample $k - 1$ the error is $e(k - 1)$, a good control should ensure the reduction of tracking error in the subsequent step:

$$|e(k)| < |e(k - 1)| \tag{11.16}$$

and this is the key equation of proposed digital control. The condition expressed by Eq. 11.16 should be ensured by the proper choice of $P(k)$ value. To perform the best choice, let us evaluate the error $P(k)$ as a function of the switch position:

$$(1) \quad \begin{aligned} |e(k)|_{P(k)=1} &< |e(k - 1)| \\ |e(k)|_{P(k)=0} &> |e(k - 1)| \end{aligned} \tag{11.17}$$

$$(2) \quad \begin{aligned} |e(k)|_{P(k)=1} &> |e(k - 1)| \\ |e(k)|_{P(k)=0} &< |e(k - 1)| \end{aligned} \tag{11.18}$$

$$(3) \quad \begin{aligned} |e(k)|_{P(k)=1} &< |e(k - 1)| \\ |e(k)|_{P(k)=0} &< |e(k - 1)| \end{aligned} \tag{11.19}$$

$$(4) \quad \begin{aligned} |e(k)|_{P(k)=1} &> |e(k - 1)| \\ |e(k)|_{P(k)=0} &> |e(k - 1)| \end{aligned} \tag{11.20}$$
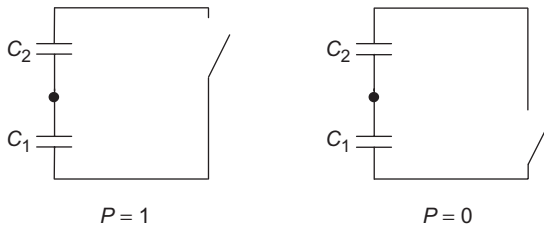
Fig. 11.8. Switch configurations.

In Case (1) undoubtedly $P(k) = 1$ will be applied since $P(k) = 0$ would increase the error in k step. In Case (2) similarly $P(k) = 0$ will be applied. In Case (3) either $P(k) = 0$ or 1 will make the error smaller. It is possible to choose any of them but it is convenient to choose $P(k) = P(k-1)$ in order to minimise the switching frequency. In Case (4) either $P(k) = 0$ or 1 will cause the growth of tracking error and this is an unpleasant condition; again $P(k-1)$ is applied in order to limit the switching frequency. The computation of $e(k)$ is a primary concern, since it is based on quantities to be evaluated in k step and so they are still unavailable. Evaluation of $e(k)$ should be based on quantity values in $k-1$ step; the error due to the assumption:

$$x(k) \cong x(k-1) \tag{11.21}$$

should be estimated. Since $e(k) = i_F^*(k) - i_F(k)$, first approximation to be introduced is:

$$i_F^*(k) \cong i_F^*(k-1). \tag{11.22}$$

In this case, introduced error is quite small since frequency of the highest harmonic order component in i_F^* is more than 10 times smaller than sampling frequency $1/T$. The evaluation of $i_F(k)$ is also based on a few approximations:

$$i_F(k) = i_F(k-1) - \frac{T}{L}e_g(k) + P(k)\frac{T}{L}v_{C1}(k) - (1 - P(k))v_{C2}(k) \tag{11.23}$$

The assumption $e_g(k) \cong e_g(k-1)$ does not introduce any significant error because e_g changes slowly during sampling period T. The assumption $v_{Ci}(k) \cong v_{Ci}(k-1)$ is affected by an error which is either 0 or $(T/C_i)i_F(k-1)$, depending on $P(k-1)$ value. This error is however tolerated in order not to increase equation complexity. So $i_F(k)$ assumes the following values:

$$i_F(k)_{P(k)=1} = i_F(k-1) - \frac{T}{L}v_S(k-1) + \frac{T}{L}v_{C1}(k-1)$$

$$\tag{11.24}$$

$$i_F(k)_{P(k)=0} = i_F(k-1) - \frac{T}{L}v_S(k-1) - \frac{T}{L}v_{C2}(k-1)$$

Equation 11.24 allows the evaluation of Eq. 11.16 and the application of proposed digital control, which may be quickly checked in Table 11.1.

Table 11.1. Proposed digital control switching table.

$|e(k)|_{P(K)=0} < |e(k-1)|$	$|e(k)|_{P(K)=1} < |e(k-1)|$	$P(k)$
0	0	$P(k-1)$
0	1	1
1	0	0
1	1	$P(k-1)$
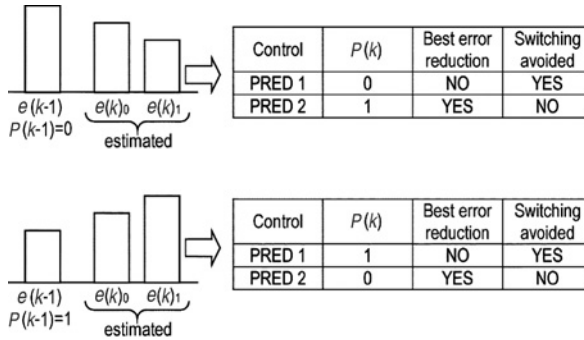
Fig. 11.9. Second predictive control solves the indefinite cases in order to reduce current error.

A different control technique is obtained if a comparison is carried out not only between the estimated and actual error but also between the estimated current errors. Without any need for computing or storing actual current error the following comparison leads to the decision on next step state.

$$|e(k)|_{P(k)=1} < |e(k)|_{P(k)=0} \Rightarrow P(k) = 1$$

$$|e(k)|_{P(k)=1} > |e(k)|_{P(k)=0} \Rightarrow P(k) = 0$$

(11.25)

Nevertheless, this control algorithm applies the state that ensures an error reduction higher than in the first predictive control case. Main difference between the two algorithms is in the first and fourth case shown in Table 11.1. The second predictive algorithm solves these cases in order to reduce current error even with the issue of a switching. Figure 11.9 shows the basic difference between the first and second predictive algorithm under two different conditions. In the hypothesis that both states will reduce the error in the successive step, the first algorithm will propose again $P(k-1)$ in order to avoid a switching. However, the best reduction of the current error will not be achieved. The same happens when the two estimated errors are larger than the actual one. The first predictive control will apply the same state as $P(k-1)$ thus avoiding a switching. The second predictive control will apply the state that better reduces error even while accepting the state change.

11.5 Optimisation Methods for SAFs

11.5.1 Introduction to fuzzy control

Fuzzy logic can easily implement human experiences and preferences via membership functions and fuzzy rules, from a qualitative description to a quantitative description that is suitable for microprocessor implementation of the automation process (van der Rhee, *et al.*, 1990; Neacsu and Stoica, 1993; Stobart, 1993; Wang, 1993). Fuzzy membership functions can have different shapes depending on the designer's preference

and/or experience. The fuzzy rules, which describe the control strategy in a human-like fashion, are written as antecedent–consequent pairs of IF–THEN statements and stored in a table. Basically, there are four modes of derivation of fuzzy control rules:

- Experience and control engineering knowledge;

- Behaviour of human operators;

- Derivation based on the fuzzy model of a process; and

- Derivation based on learning.

Due to the use of linguistic variables and fuzzy rules, the fuzzy controller can be made understandable to a non-expert operator. Moreover, the description of the control strategy could be derived by examining the behaviour of a conventional controller. The fuzzy characteristics make it particularly attractive for control applications because only a linguistic description of the appropriate control strategy is needed in order to obtain the actual numerical control values. Thus, fuzzy logic can be used as a general methodology to incorporate knowledge, heuristic or theory into a controller. In addition, fuzzy logic has the freedom to completely define the control surface without the use of complex mathematical analysis. On the other hand, the amount of effort involved in producing an acceptable rule base and in fine-tuning the fuzzy controller is directly proportional to the number of quantisation levels used, and the designer is free to choose the best trade-off between being able to create a large number of features on the control surface and not having to spend much time in fine-tuning the process. The general shape of these features depends on the heuristic rule base and the configuration of the membership functions. Being able to quantise the domain of the control surface using linguistic variables allows the designer to bypass the mathematical constraints and achieve a control surface which has more features and contours. Zadeh (1965) established the foundations of fuzzy set theory, which is a generalisation of conventional set theory, as a method of dealing with the imprecision of the real physical world.

Bellman and Zadeh wrote: "Much of the decision-making in the real world takes place in an environment in which the goals, the constraints and the consequences of possible actions are not known precisely". This imprecision or fuzziness is the core of fuzzy logic. Fuzzy control is the technology that applies fuzzy logic to solve the control problems. The advantages of using fuzzy control are more substantial when applied to non-linear and ill-defined systems. Several application of fuzzy control to power converters are available in literature (Dixon *et al*., 1997; Shoulaie *et al*., 1997; Valouch, 1997; Farrokhi *et al*., 2004), where fuzzy logic has been applied to compute reference signals for cascade controllers and to estimate load pollution, to compute duty cycles for PWM controllers, to control power balance among source, load and AF. The fuzzy model predictive algorithm is used in internal model control scheme to compensate for process disturbances, measurement of noise and modelling errors; and several advantages have been highlighted among them, by means of experimental campaigns:

- The fuzzy control has better dynamic behaviour than conventional PI control; and

- The fuzzy power control method is simple and little sensitive to the changes of parameters.
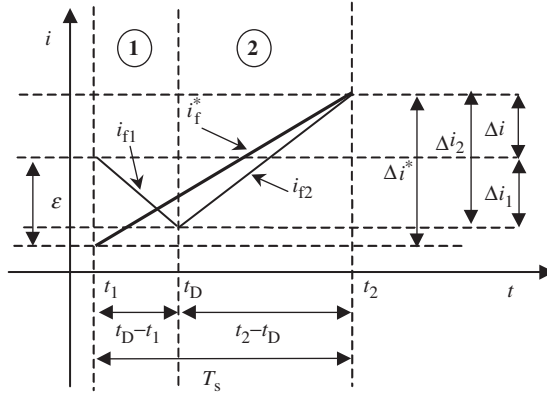
Fig. 11.10. Current evolution in one sampling period.

11.5.2 The fuzzy logic applied to the current control of SAFs

Considering the single-phase AF depicted in Fig. 11.1 and on the basis of Fig. 11.10 it is possible to calculate the duty cycle needed to nullify the current error at the end of a sampling period.

$$D = \frac{1}{2} + \frac{1}{v_{DC}} \left[e + L_f \left(s^* + \frac{\varepsilon}{T_S} \right) \right] \tag{11.26}$$

In the D function, the values of L_f, T_S and v_{DC} are fixed, while s^* (slope of the reference current) and ε (current error) vary in each period T_S. Moreover, e is the grid voltage. In case a four-wire SAF is considered, as reported in Fig. 11.11, the current evolution is as reported in Fig. 11.12 but Eq. 11.26 is valid again because the presence of the split capacitor makes the three switching legs virtually independent. This is not the case of a three-phase three-wire inverter where the absence of neutral connection makes the three current dependent and as a consequence the duty cycles too. In order to choose the main rules of the fuzzy inference system, the waveform of the reference current is detected and then the critical values of its slope and current error are measured and used in Eq. 11.26.

11.5.3 Introduction to the use of Nelder–Mead optimisation

In this section an optimisation algorithm, the algorithm of amoeba, is adopted to optimise two control parameters of a fuzzy controller. The fuzzy control is used to ensure fast reference current tracking. The amplitude of line third harmonic component in current is used as the function to be minimised and its minimisation becomes either the algorithm or the compensation goal. The Nelder–Mead algorithm was proposed (Nelder and Mead, 1965) as a method for minimising a real-value function $f(x)$ for $x \in \mathbb{R}^n$. The method
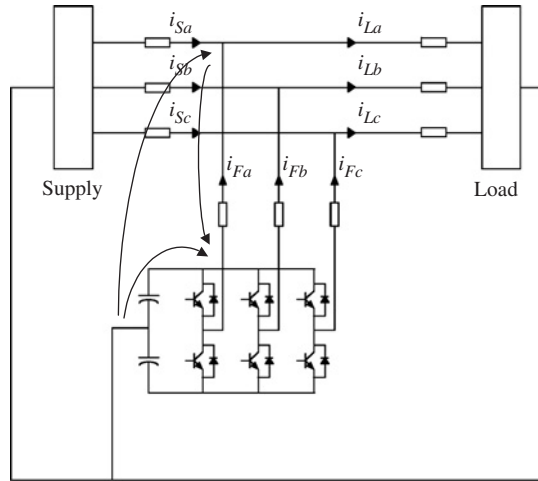
Fig. 11.11. Close path for inductance voltage drop computing in case of four wires SAF.
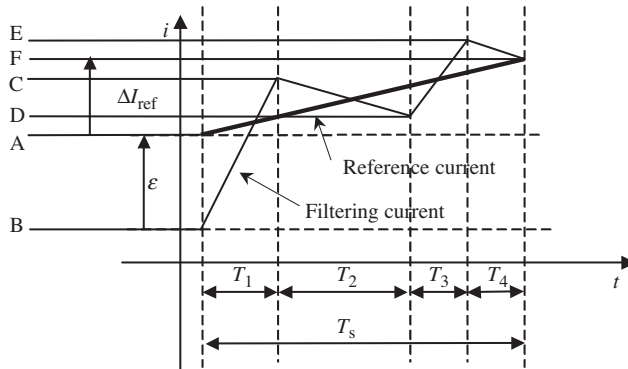
Fig. 11.12. Reference and filtering current during switching period T_S.

requires only function evaluations, not derivatives. It is not very efficient in terms of the number of function evaluations that it requires. Other methods such as Powell's method are almost surely faster in all likely applications. However, the downhill simplex method may frequently be the best method to use for a problem whose computational burden is small. The method has a geometrical aspect, which makes it delightful to describe or work through: a simplex is the geometrical figure consisting, in N dimensions, of $N+1$ points (or vertices) and all their interconnecting line segments, polygonal faces, etc. In two dimensions, a simplex is a triangle. In three dimensions it is a tetrahedron, not necessarily the regular tetrahedron. In general we are only interested in no degenerate simplexes, i.e. that enclose a finite inner N-dimensional volume. If any point of a no degenerate

simplex is taken as the origin, then the N other points define vector directions that span the N-dimensional vector space. In one-dimensional minimisation, it is possible to bracket a minimum, so that the success of a subsequent isolation is guaranteed. The algorithm is then supposed to make its own way downhill through the unimaginable complexity of an N-dimensional topography, until it encounters a minimum. The downhill simplex method must be started not just with a single point, but with $N + 1$ points, defining an initial simplex. If one of these points is the initial starting point P_0, then other N points are:

$$P_i = P_0 + e_i, \tag{11.27}$$

where the e_is are N unit vectors, and where λ is a constant. The downhill simplex method takes a series of steps, most of the steps just moving the point of the simplex where the function is largest, the highest point through the opposite face of the simplex to the lowest point. These steps are called reflections, and they are constructed to conserve the volume of the simplex hence maintain its no degeneracy. When it can do so, the method expands the simplex in one or the other direction to take larger steps. When it reaches a valley floor, the method contracts itself in the transverse direction and tries to ooze down the valley. If there is a situation where the simplex is trying to pass through the eye of a needle, it contracts itself in all directions, pulling itself around its lowest point. The routine name amoeba is intended to be descriptive of this kind of behaviour; the basic moves are summarised in Fig. 11.13. Termination criteria can be delicate in any multidimensional minimisation routine. Without bracketing, and with more than one independent variable, we no longer have the option of requiring a certain tolerance for a single independent variable. We can typically identify one cycle or step of our multidimensional algorithm. It is then possible to terminate when the vector distance moved in that step is fractionally smaller in magnitude than some tolerance. Alternatively, it is required that the decrease in the function value in the terminating step be fractionally smaller than some tolerance.
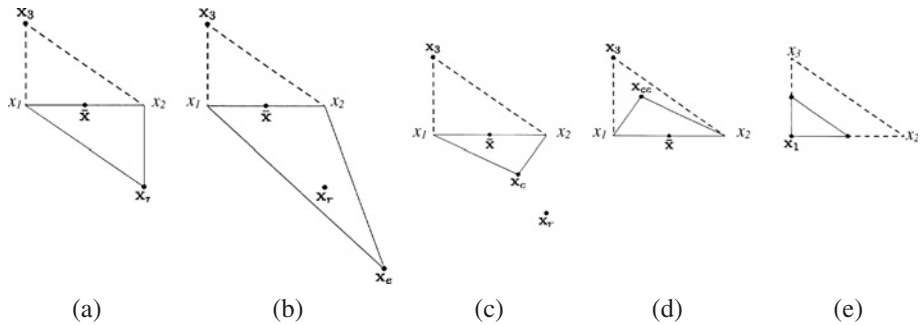
Fig. 11.13. Nelder–Mead simplex method (the original simplex is shown with a dashed line [x_1, x_2, x_3]): (a) reflection x_r, (b) expansion x_e, (c) outside contraction x_c, (d) inside contraction x_{cc} and (e) shrink.

Four scalar parameters must be specified to define a complete Nelder–Mead method:

Coefficients of *reflection* (ρ), *expansion* (χ), *contraction* (γ) and *shrinkage* (σ). According to the original Nelder–Mead article (Nelder and Mead, 1965), these parameters should satisfy

$$
\begin{aligned}
\rho &> 0 \\
\chi &> 1 \\
\chi &> \rho \\
0 &< \gamma < 1 \\
0 &< \sigma < 1
\end{aligned}
\tag{11.28}
$$

At the beginning of the kth iteration, a no degenerate simplex Δ_k is given along with its $n + 1$ vertices, each of which is a point in $\mathbb{R}^n$. It is always assumed that iteration k begins by ordering and labeling these vertices as $\mathbf{x}_1^{(k)}, \ldots, \mathbf{x}_{n-1}^{(k)}$, such that

$$
f_1^{(k)} \le f_2^{(k)} \le \cdots \le f_{n+1}^{(k)},
\tag{11.29}
$$

where $f_i^{(k)}$ denotes $f(\mathbf{x}_i^{(k)})$.

The kth iteration generates a set of $n + 1$ vertices that define a different simplex for the next iteration, so that $\Delta_{k+1} \ne \Delta_k$. Because we seek to minimise f, we refer to $\mathbf{x}_1^{(k)}$ as the *best* point or vertex, to $\mathbf{x}_{n+1}^{(k)}$ as the *worst* point, and to $\mathbf{x}_n^{(k)}$ as the *next-worst* point. Similarly, we refer to $f_{n+1}^{(k)}$ as the worst function value, etc. The result of each iteration is either a single new vertex, the *accepted point*, which replaces $\mathbf{x}_{n+1}$ in the set of vertices for the next iteration, or if a shrink is performed, a set of n new points that, together with $\mathbf{x}_1$, form the simplex at the next iteration. In the following, the algorithm steps are illustrated.

Order

Order the $n + 1$ vertices to satisfy

$$
f(\mathbf{x}_1) \le f(\mathbf{x}_2) \le f(\mathbf{x}_3) \le \cdots \le f(\mathbf{x}_{n+1})
\tag{11.30}
$$

using the tie-breaking rules given below.

Reflect

Compute the reflection point $\mathbf{x}_r$ from

$$
\mathbf{x}_r = \bar{\mathbf{x}} + \rho(\bar{\mathbf{x}} - \mathbf{x}_{n+1}) = (1 + \rho)\bar{\mathbf{x}} - \rho\mathbf{x}_{n+1},
\tag{11.31}
$$

where $\bar{\mathbf{x}} = \sum_{i=1}^{n} \mathbf{x}_i / n$ is the centroid of the n best points, all vertices except for $\mathbf{x}_{n+1}$

Evaluate $f_r = f(x_r)$.

If $f_1 \leq f_r < f_n$, accept the reflected point x_r and terminate the iteration.

Expand

If $f_r < f_1$, calculate the expansion point x_e,

$$x_e = \bar{x} + \chi(x_r - \bar{x}) \tag{11.32}$$

and evaluate $f_e = f(x_e)$. If $f_e < f_r$, accept x_e and terminate the iteration; otherwise accept x_r and terminate the iteration.

Contract

If $f_r \geq f_n$, perform a contraction between $\bar{x}$ and the better of x_{n+1} and x_r.

Outside

If $f_n \leq f_r < f_{n+1}$, perform an outside contraction: calculate

$$x_c = \bar{x} + \gamma(x_r - \bar{x}) \tag{11.33}$$

and evaluate $f_c = f(x_c)$. If $f_c \leq f_r$ accept x_c and terminate the iteration; otherwise, perform a shrink inside. If $f_r \geq f_{n+1}$, perform an inside contraction: calculate

$$x_{cc} = \bar{x} - \gamma(\bar{x} - x_{n+1}) \tag{11.34}$$

and evaluate $f_{cc} = f(x_{cc})$. If $f_{cc} < f_{n+1}$, accept x_{cc} and terminate the iteration; otherwise, perform a shrink.

Perform a shrink

Evaluate f at the n points $v_i = x_1 + \sigma(x_i - x_1)$, where $i = 2, \dots, n + 1$.

The vertices of the simplex at the next iteration consist of $x_1, v_2, \dots, v_{n+1}$.

Non-shrink ordering rule

When a non-shrink step occurs, the worst vertex $x_{n+1}^{(k)}$ is discarded. The accepted point created during iteration k, denoted by $v^{(k)}$ becomes a new vertex and takes position $j + 1$ in the vertices of Δ_{k+1}, where

$$j = \max_{0 \leq \ell \leq n} \left\{ \ell \mid f\left(v^{(k)}\right) < f\left(x_{\ell+1}^{(k)}\right) \right\} \tag{11.35}$$

all the other vertices retain their relative ordering from iteration k.

Shrink ordering rule

If a shrink step occurs, the only vertex carried over from Δ_k to Δ_{k+1} is $\mathbf{x}_1^{(k)}$. Only one tie-breaking rule is specified, for the case in which $\mathbf{x}_1^{(k)}$ and one or more of the new points are tied as the best point: if

$$\min\left\{ f\left(\mathbf{v}_2^{(k)}\right), \ldots, f\left(\mathbf{v}_{n+1}^{(k)}\right)\right\} = f\left(\mathbf{x}_1^{(k)}\right) \tag{11.36}$$

11.5.4 The Nelder–Mead optimisation of the third harmonic compensated by an AF

The algorithm of amoeba, Nelder–Mead, was used to optimise a couple of electrical and control parameters of simulation model of a half-bridge SAF. A fuzzy control has been used to ensure fast reference current tracking. However, two electrical parameters of both coupling filter and DC bus capacitors have been involved in optimisation. The amplitude of line third harmonic component in current has been used as the function to minimise, based on the values of inductance and sampling time. In the state diagram, the majority of the states consist of a calculation step, where the simplex is updated. Only one step is the simulation of electrical model using the new values of the parameters. The simulation allows computing the value of the third harmonic. When the third harmonic drops below a certain level and the parameters converge to a defined value, the optimisation can be considered completed, otherwise it continues until these termination criteria are met.

Figure 11.14 shows an optimisation process to minimise the third harmonic using a SAF.
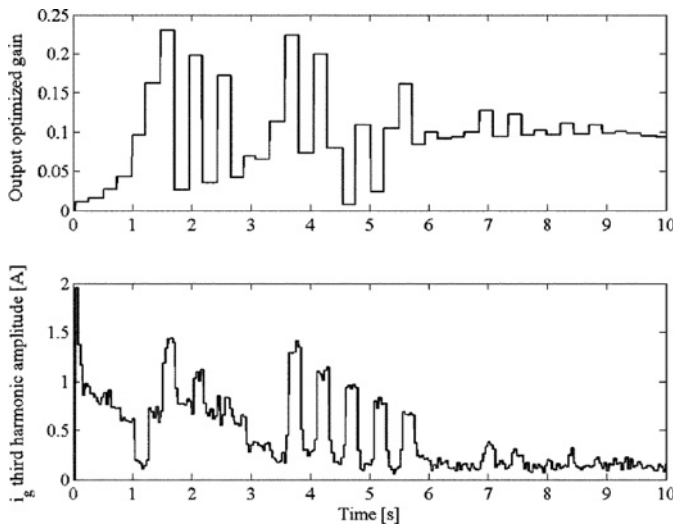
Fig. 11.14. Third harmonic variation as a consequence of Nelder–Mead algorithm.

11.6 Real-Time Control Implementation

11.6.1 Control code sections

A power converter is made up of several static switches that operate alternately in two states: on and off. The timely switching between the two states is the main goal of power converters control. In order to operate properly, the controlled power converters need continuous supervision. A dedicated microcontroller is the chosen solution to evaluate the control techniques that have been proposed in this chapter. The controller has been utilised to supervise the operation of the control loop. The microcontroller has several tasks to manage. It processes the feedback signals received from interface boards. Then it runs the control algorithm and soon after it computes proper command patterns for the converter switches. All these tasks must be run in a timely manner. Simulations on computer software represent the execution of control algorithms applied to a model of the reality based on several physical laws and equations. As a consequence, the results of simulations campaign can be quite near to the real operation if the complexity of the mathematical model of the simulated system is really high. The main disadvantage of a detailed model is the long computation time required. In many simulations, the elapsed time to simulate a dynamic system for a few milliseconds is measured in minutes or tens of minutes. Control in real-time cannot accept such long times. Computations on feedback measures must be executed as soon as possible in order to keep errors under desired level. In order to execute real-time simulations, much faster microcontrollers are required. Many microcontrollers are equipped with several peripherals, which can execute acquisition and modulating tasks without requiring processor supervision. The processor keeps on computing algorithm outputs without attending peripheral operation. Control code, run on such microcontrollers, is generally divided into two sections. The first is generally run once at the start of code execution. The second is run during real-time control operation. At the beginning of the code, there are initializations of the various constants utilised during the algorithm execution. In this section, there is the initialization of parameters and values relating to the electrical system, the parameters of controllers as well as the knowledge base of intelligent control algorithms such as fuzzy, genetic algorithm and neural networks. The successive section contains the initialization of microcontroller peripherals. Each microcontroller peripheral has several registers which require different settings based on the operation to enable. The control registers of the peripherals are set in the initialization phase. Moreover, some peripherals require the setting of a start bit in order to begin operation. The starting of peripherals operation is done in this section of control code.

After the initialization of parameters, the setting of the peripheral registers and the start of peripheral operation, the core of control algorithm is executed for an infinite number of times. The corresponding flow chart of a real-time control program is shown in Fig. 11.15.

The loop, that is shown in Fig. 11.15, can be created by means of the statements of loop control which are generally available in every high-level programming language. According to this solution, the control algorithm is repeated as soon as each previous execution has ended. There is no waiting time between the end of a cycle execution and the beginning of the next one. This solution has the advantage to use 100% of the time for control tasks, and in no instants the processor is halted to wait for external events.
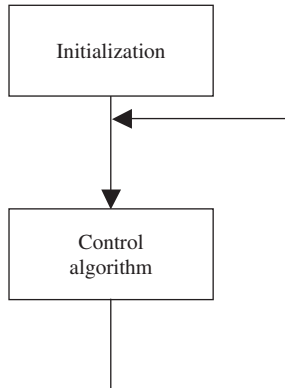
Fig. 11.15. Block diagram of a real-time control code.

```
main(){

        /* initialization code */

while(1){

        /* control algorithm code */

}
```

Fig. 11.16. Program structure of control code within "while" loop.

The main disadvantage is that the execution is asynchronous. The beginning of control execution is not issued at a precise time instant because the length of code execution varies, depending on the complexity of the control code. In other words, the control algorithm is written in a code loop and it is operated continuously, so a new control routine instance is processed as soon as the preceding one ends, as shown in Fig. 11.16.

In Fig. 11.17, a typical succession of control code executions is pointed out; typically different duration lengths are encountered, so it is not possible to schedule the start of algorithm execution.
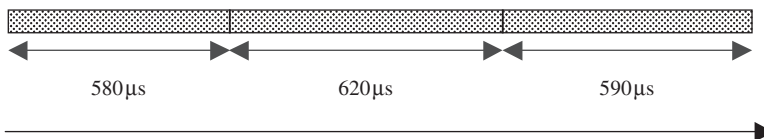
Fig. 11.17. Time diagram of control code execution when inserted in software loop statements.

An alternative solution consists in introducing a "not operation" loop after the initialization section and carrying out the execution of the control code in service interrupt routines, timely requested by timing peripherals (Fig. 11.20). In this case, the control code is started at the beginning of the interrupt routine, so it is started periodically with a fixed frequency. Timing diagram is shown in Fig. 11.18.

In this case, the processor is not fully utilised since there is a time interval, between the end of control execution and the next interrupt request, when the processor is waiting in "not operation" state, as clearly shown in block diagram of Fig. 11.19.

The advantage of this solution is that it is possible to use the timing start of control code to timely store signal samples. By means of equally spaced signal samples, it is possible to carry out a diagnosis process of the application developed.

Another severe inconvenience of running control code in an interrupt routine consists in the risk to jump a control cycle execution if the processor is still serving an interrupt when a new request arrives. This event is shown in Fig. 11.21. Every interrupt request has its own priority level, and this priority level is established in the initialization section of the code. The same interrupt request gets the microcontroller to run control code since this request is repeatedly launched by the same peripheral, but the processor cannot serve
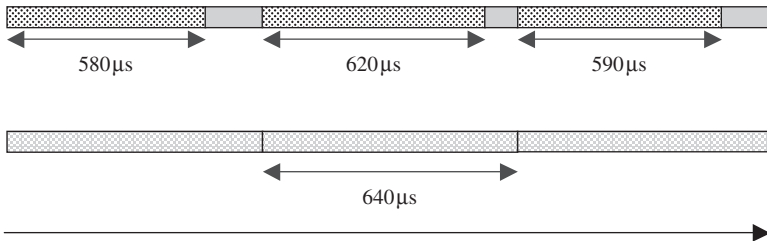
Fig. 11.18. Timing diagram of control code execution inserted in timely requested interrupt routines.
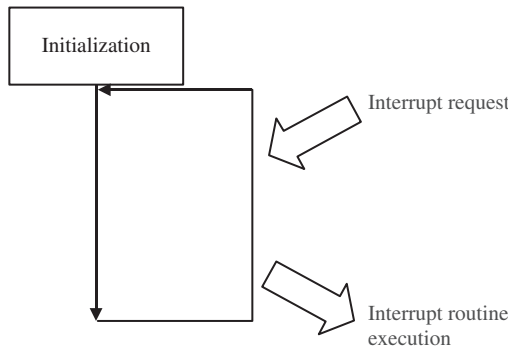
Fig. 11.19. An interrupt request reaches the microcontroller blocked in an NOP loop.

```
main(){

        /* initialization code */
while(1){

        /* nothing, not operation */
}
```

Fig. 11.20. Program code which blocks microprocessor in a NOP loop.
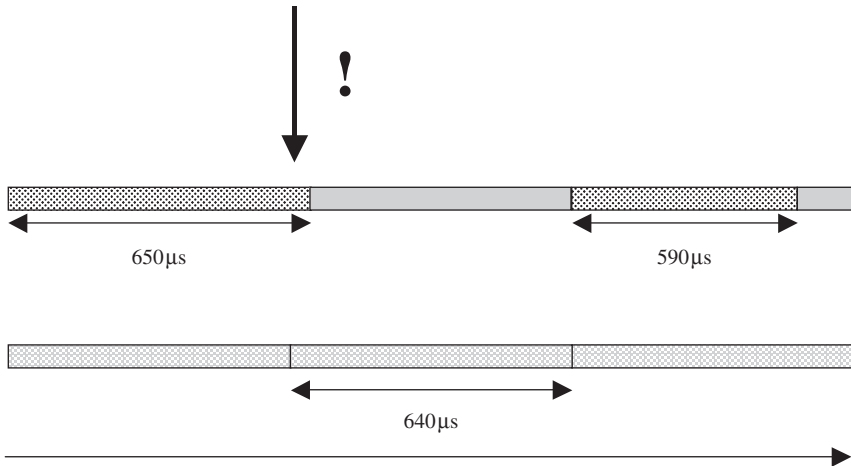
Fig. 11.21. The interrupt request is not served if the microcontroller is still serving an interrupt of the same priority level.

a level-i interrupt request if it is still serving it. This request has the same priority level and so it is masked and ignored.

11.6.2 Fuzzy algorithm software implementation

A typical fuzzy logic controller consists of a fuzzification module, fuzzy inference engine, defuzzification module and pre- and post-processing modules. A fast fuzzy logic controller must be used when the process to be controlled has relatively fast dynamics. In recent years, a number of hardware fuzzy inference systems have been implemented or proposed. A low-cost fuzzy logic controller can be implemented by means of a general-purpose microcontroller; even if the sampling interval is necessarily bigger than that with a direct hardware implementation. When a fuzzy algorithm is used, if all modules are treated conventionally employing all necessary arithmetical operations the performance is slowed down.

The computation of membership values for controller inputs is one of the slowest steps in the inference process. Even with triangular functions the computation of membership value is very time-consuming since each fuzzy set has at least four regions that are differently defined: they are the two regions where membership value is zero and the two regions with rising and falling slopes. Since in a computing algorithm the input–output relationship should be expressed by a mathematical function, a change in membership function slope causes the change of the mathematical expression that should be used. The different expressions are used depending on the value of input variable. In this way, the input range is divided into several regions where membership values are computed by means of different mathematical functions. As a consequence, if fuzzification process were implemented in such a way, many "if–then–else" structures should be utilised, thus increasing very much the computational load. In this case, many relational operators should be used and then would be many flow changes in software control code. If the goal is the reduction of computational load, fuzzy logic controller could be implemented by means of a large array of data.

A change in the way of thinking fuzzification is made. In previous solution the input variable, generally a floating point value, determines which mathematical function should be used to compute membership value; and the mathematical function is computed at input value in order to obtain the membership value. A different solution can be adopted. Fuzzy inputs are obtained directly from A/D converter as integer quantities. Therefore, these integer values can be used to access an array of membership values. Each value of the array is assigned to a defined integer input and consequently fuzzification of inputs does not require mathematical computation any more. Membership values are quickly available after accessing the arrays. They are read and assigned to membership variables. Moreover, each integer fuzzy input can be assigned an additional index that represents the number of fired fuzzy set. This index is successively utilised during inference process. The indexes of fired fuzzy sets become the indexes to access the table of fuzzy rules. In this way, "if–then–else" procedure is avoided in fuzzy inference also and fuzzy output computation is completed after a few algebraic operations between the fired rules values and weights. The main disadvantage of this method is the necessity of an amount of memory in order to store fuzzification data, fuzzy labels and fuzzy inference rules. After A/D conversion, inputs have been quantised by means of seven bit strings; therefore, membership lookup tables have only 128 entries, thus lowering memory requirements. In order to further reduce memory requirements output membership values range from 0 to 255. This range can be completely stored in an 8-bit variable, such as a "char"-type variable in C language, which is the smallest size among programming language variables. Even output fuzzy rules and weights are stored as integer values. The reason is that arithmetical operations between integer variables are computed much more quickly than operations between floating point numbers. Consequently, fuzzy logic control is really sped up. The proposed solution has a computational time that is quite independent from the number of fuzzy inputs and fuzzy sets. In fact for each value of inputs a membership value and a fuzzy set label are stored. Moreover, even if the two fuzzy inputs are organised by means of several fuzzy sets, during the inference process only fired rules are involved. In a fuzzy system with two inputs and only two membership functions overlapping, there are four fired rules even if the inputs are divided into a very large number of fuzzy sets. The execution of a fuzzy routine for the proposed current control which is based on two fuzzy inputs and a five per five fuzzy

knowledge base takes only 32 μs, on a microcontroller rated 40 MIPS (Mega Instructions Per Second).

11.7 Conclusions

The chapter gives a comprehensive approach to the control of SAFs. In fact how to design an advanced control (fuzzy-logic) using a predictive framework instead of a trial-and-error procedure is described. Moreover, the possibility to use an optimization algorithm (Nelder and Mead, 1965) to choose correctly the controller parameters is considered. Then some implementation issues in case a general-purpose microcontroller adopted are addressed.

Acknowledgement

The figures reported here are reprinted from:

References

Akagi H., "New trends in active filters for power conditioning", IEEE Trans. Ind. Applicat., **32** (1996) 1312–1322.

Al-Haddad K., Joos, G., "Implementation issues for half-bridge and full-bridge active filters in single phase applications", IEEE 1997 Canadian Conference on Electrical and Computer Engineering, **2(25–28)** (1997) 544–547.

Bakhshai A.R., Karimi H., Saeedifard M., "A new adaptive harmonic extraction scheme for single-phase active power filters", Vol. 3, Proceedings of the 2003 International Symposium on Circuits and Systems, ISCAS'03, 25–28 May, 2003, pp. III-268–III-271.

Buso S., Malesani L., Mattavelli P., "Comparison of current control techniques for active filter applications", IEEE Trans. Ind. Elect., **45** (1998) 722–729.

Dell'Aquila A., Liserre M., Loiudice F., Marinelli M., Zanchetta P., "Performance evaluation of active filters for compensation of distorted line currents produced by induction motor drives", Proc. ELECTRIMACS'99, **III**, (1999) 63–68.

Dell'Aquila A., Lecci A., Zanchetta P., Liserre M., "Fuzzy active filter performance in transient conditions", EPE (2001).

Dell'Aquila A., Lecci A., Liserre M., "Microcontroller-based fuzzy logic active filter for selective harmonic compensation", Vol. 1, 38th IAS Annual Meeting, Conference Record of the Industry Applications Conference, 12–16 October, 2003, pp. 285–292.

Dell'Aquila A., Lecci A., Liserre M., "A comparison between two predictive controllers for single-phase active filter", Vol. 3, The 29th Annual Conference of the IEEE Industrial Electronics Society, IECON'03, 2–6 November, 2003, pp. 2294–2299.

Dixon J., Contardo J., Moran L., "DC link fuzzy control for an active power filter, sensing the line current only", Vol. 2, 28th Annual IEEE Power Electronics Specialists Conference, PESC'97, 22–27 June, 1997, pp. 1109–1114.

Farrokhi M., Jamali S., Mousavi S.A., "Fuzzy logic based indirect current control of the shunt active power filter", Vol. 1, 39th International Universities Power Engineering Conference, UPEC 2004, 6–8 September, 2004, pp. 489–493.

Malesani L., Mattavelli P., Tomasin P., "High-performance hysteresis modulation technique for active filters", IEEE Transactions on Power Electronics, **12(5)** (1997) 876–884.

Neacsu D.O., Stoica A., "Fuzzy control for output current of a phase-controlled rectifier", Conference Record of the Power Conversion Conference, Yokohama, 19–21 April, 1993, pp. 683–688.

Nelder J.A., Mead R., "A simplex for function minimization", Comput. J., **7** (1965) 308–313.

Peng F.Z., "Application issues of active power filters", IEEE Ind. Appl. Mag. (1998) 21–37.

Shoulaie A., Ramezanpoor P., Amirkhani H., "Control of multilevel-inverters for active power filters using a fuzzy space-vector method", Vol. 2, Proceedings of the IEEE International Symposium on Industrial Electronics, ISIE'97, 7–11 July, 1997, pp. 279–282.

Stobart R., "Tutorial on fuzzy control", IEE Colloquium on Two Decades of Fuzzy Control – Part 1, May, 1993, pp. 1/1–1/6.

Thomas T., Al-Haddad K., Joos G., Jaafari A., "Design and performance of active power filters", IEEE Industry Application Magazine, (1998) 38–46.

Valouch V., "Fuzzy power control in PWM voltage-type rectifier", Vol. 3, Proceedings of the IEEE International Symposium on Industrial Electronics, ISIE'97, 7–11 July, 1997, pp. 1162–1167.

van der Rhee F., van Nauta Lemke H.R., Dijkman J.G., "Knowledge based fuzzy control of systems. IEEE Transactions on Automatic Control", **35(2)** (1990) 148–155.

Wang L.-X., "Stable adaptive fuzzy control of nonlinear systems", IEEE Transactions on Fuzzy Systems, **1(2)** (1993) 146–155.

Wu T.F., Nien H.S., Shen C.L., Hsieh H.M., Chen Y.M., "A half-bridge 1/spl Phi/2 W PV inverter system with active power filtering and real power injection", Vol. 1, Twentieth Annual IEEE Applied Power Electronics Conference and Exposition, APEC 2005, 6–10 March, 2005, pp. 428–434.

Zadeh L., "Fuzzy sets", Inf. Control, **8** (1965) 338–353.

This page intentionally left blank

Index

This page intentionally left blank